Experimental and Numerical Studies of Laser Riveting for Dissimilar Materials Joining

A thesis submitted for the degree of Doctor of Philosophy by:

Bowei Li

Department of Mechanical and Aerospace Engineering

Brunel University London

London

United Kingdom

Acknowledgement

This research project was sponsored by Brunel University London and TWI Ltd, and carried out in the Laser and Sheet Processing (LAS) section at TWI Ltd. The project was funded through TWI's Core Research Programme.

The PhD research is one of my most challenging experiences. All my research learnings and knowledge in these 3 years contributed to this thesis, and it accompanied me day and night. I am grateful to this PhD provides me with the principal research thinking and skills, which would be valuable spiritual wealth for my life and career. I would like to reflect on the people who have supported and helped me so much throughout this period.

Foremost, Also, I must express my very profound gratitude to my family for providing me with unconditional support and continuous encouragement throughout my years of study and through the process of this research. They are the fundamental faith of my life, and this accomplishment would not have been possible without them.

I also would like to express my deep and sincere gratitude to my supervision team: academic supervisor, Dr Bin Wang for the continuous support in my PhD study, for his patience, motivation, enthusiasm, and immense knowledge. His guidance helped me in all the time of research and writing of this thesis; Industrial supervisor, Dr Ali Khan, for providing my project setup, experimental support, and research guidance throughout my study in TWI; Previous industrial supervisor Dr Michelangelo Mortello for initially leading me into both academic and industrial research, who tutored me step by step from the most basic part. Their dynamic, vision, sincerity and motivation have deeply inspired me.

I would also like to take this opportunity to thank Dr Supriyo Ganguly and Dr Lorna Anguilano - my viva examiners, their valuable comments and suggestions improved this thesis to reach higher quality.

My colleagues and technicians in the LAS and TWI also provided me with great help during my PhD study. They are always very patient with me to deal with the questions

and support me since I joined. Special thanks go to my section manager Dr Paola De Bono for offering the best experimental conditions and invaluable supports in the section, she attentively took care of this project in every detail. Thanks to Dr Sullivan Smith for mechanical suggestions and corresponding strength tests support in the research, Dr Ren Yao for experimental advice and Dr Longjie Wang for numerical parts teaching. Finally, my appreciation also goes out to my friends for their encouragement and support all through my studies.

Declaration

The candidate confirms that the work submitted is his own and that appropriate credit has been given where reference has been made to the work of others.

This copy has been supplied on the understanding that it is copyright material and that no quotation from the thesis may be published without proper acknowledgement.

The right of Bowei Li to be identified as the author of this work has been asserted by him in accordance with the Copyright, Designs and Patents Act 1988.

Some parts of the work have been published in the following article:

Li, B., Khan, A., Wang, B. and De Bono, P., 2021. Feasibility study of dissimilar metal joining by laser riveting of Ti-6Al-4V to AA6061. Journal of Laser Applications, 34(1), p.012005.

Abstract

In the automotive and aerospace sectors, there is an increasing interest in lightweight structures by dissimilar joining, which enables the reduction of weights and enhances the frame performance by selecting the appropriate materials. Currently, for dissimilar joining, the widely used mature methods are mechanical fastening (riveting and bolting) and adhesive bonding, but they still have certain limitations in specific conditions. Therefore, laser riveting is designed and developed as an innovative technique, aims to improve the joining flexibility, applicability and productivity compared to traditional methods. Laser riveting consists of joining two heterogeneous materials by additively manufacturing a rivet to interlock them, the jointed rivet is produced by laser-based metal wire cylindrical deposition (LMwcD) as a building method.

A cylindrical feature was successfully built by LMwcD onto a Ti6Al4V substrate on a small scale (1mm-4mm), which proves the positive feasibility for laser riveting, followed by parametric optimization has allowed increased productivity almost 8 times. The cylindrical deposition showed a positive correlation with heat accumulation, and primary grain size with micro-hardness was increased with higher energy input.

LMwcD was applied for joining for Ti6Al4V substrate to AA6061 sheets in laser riveting (LR) processing, then a high-frequency laser washing is implemented as the additional post-process. The post-wash procedure significantly improves the wetting condition and the quality in the welding area. The rivet crown and welding areas improved by the post-wash process were directly reflected in the micro-hardness and shear tests, increased by up to 95% and 180% respectively, compared with those in unwashed rivet. For the further exploration of Ti6Al4V/ CFRP joining, compared to the direct LMwcD-LR, the post-processed depositions can maximally avoid contamination from CFRP degradation regarding optimized energy accumulation in process.

In addition, the experimental analysis has been combined with a finite element analysis for LMwcD and LR process. The calculated thermal-historical results show a maximum 10% related error by calibration through corresponding experiments. The

results indicate that the models have certain reliability to support understanding the fundamental experimental principle, and accurately predicting the thermal behaviour of the processing in the future research.

Contents

Nomenclature and definitions

Nomenclature	Definition	Units
$A\%$	Elongation to fracture	$\%$
ALE	Arbitrary Lagrangian-Eulerian method	
ALM	Additive layer manufacturing method	
AM	Added material	
BM	Base material	
Cp	Specific heat	
CAFE	Corporate Average Fuel Economy	
CFRP	Carbon-fibre-reinforced-polymer	
CNC	Computer numerical control	
CS	Continuous spiral deposition method	
CW	Continuous wave laser mode	
EBSD	Electron backscatter diffraction	
EDS	Energy dispersive spectroscopy	
FZ	Fusion zone	
D_{w1}	Weld diameter	mm
DOE	Design of experiments	
FEA	Finite element analysis	
FEM	Finite element method	
HAZ	Heat affected zone	

h_{HAZ}	Depth of fusion zone	mm
h_w	Wire offset height	
HE	High energy experiment	
HS	High speed deposition method	
HSS	High speed spiral deposition method	
HV	Vickers microhardness	VH
IMC	Intermetallic compound	
IT	The total time the laser beam interacts with the workpiece	s
k	values of wire feeding speed/travel speed	
K	Thermal conductivity	$W/(m.k)$
LE	Linear energy, Heat transferred to the material per unit distance	J/mm
LMD	Laser metal deposition	
LMwcD	Laser metal wire cylindrical deposition	
LMwD	Laser-based metal wire deposition	
LPD	Laser-powder deposition	
LR	Laser riveting	
NM	Normal laser wire cylindrical deposition method	
M_s	Martensite start temperature	℃
M2	Beam parameter product	
OM	Optical microscopy	

OSD	Offset spiral deposition	
P	Laser power	W
PD	Post-deposition laser riveting	
PS	Post-scanning laser riveting	
SEM	Scanning electron microscopy	
q	Heat flux	
Q	Heat source	W
R	Circular path radius	mm
SRA	Strategic Research Agenda	
t	Time	s
T	Temperature	℃
T_β	The β transus temperature	℃
T_{Diss}	Temperature of the dissolution start point for the α grains	℃
T_m	Melting temperature	℃
T_∞	Room temperature	℃
TS	Laser beam travel speed	mm/s
UTS	Ultimate tensile strength	MPa
V_{exp}	Volume of expected deposited material	$mm3$
VOF	Volume of fluid method	
WFS	Wire feeding speed	
YS	Yield stress	MPa

ρ	Density	Kg/m^3
ε	Emissivity	
σ	Stefan–Boltzmann constant	
η	absorptivity of laser power	

List of tables

List of figures

Chapter 1 Introduction

1.1 Background

In the transport sector, there has been a recent emphasis on the practice of 'light-weighting' in which engineers attempt to reduce the overall weight of structures to:

- Meet emission targets and standards as required by both national and international legislation and policy.
- Improve the fuel economy of the vehicle and reduce costs for the owner
- Meet the public's environmental expectations of the sector

Such desire is driven in part by European Regulations (No. 443/2009) and the USA Corporate Average Fuel Economy (CAFE) standard. Automotive and aerospace companies are increasingly trialing new carbon fibre composites to make savings of up to 50% on weight compared to metallic alternatives [1.1, 1.2]. Despite advancements, the eventual goal is unlikely to be 100% composite solutions. Designers continue to strive to use appropriate materials and greater emphasis is being placed on the use of multi-materials. Hence, optimum designs are likely to continue to include both composites and metals.

Metallic (titanium and aluminium alloys) and non-metallic materials (notably carbon-fibre-reinforced-polymers (CFRPs)) can be used in conjunction to create materials that are both lightweight and tailored to their purpose.

Regarding the joined material properties, the hybrid structure contributes to the demanded benefits include lower weight (such as composite and aluminum), high specific strength, and stiffness, as well as their resistance to corrosion and fatigue (titanium). Meanwhile, metals are praised for their temperature resistance, energy absorption, high-bearing load resistance, and (generally) lower costs [1.3-1.5]. Despite the benefits of integrating metallic and composite materials, there are several issues relating to the manipulation and joining of these very different materials [1.6, 1.12].

1.2 Motivation of the laser riveting research

1.2.1 Technical challenges in traditional dissimilar joining methods

In the fusion processing for aluminium and titanium joining, there remains a metallurgical difficulty. Research conducted has shown that numerous brittle intermetallic compounds (IMCs) may be formed in the thermal process, which weaken the mechanical strength of the joint [1.13-1.15]. As for metal to composite joining, the most commonly adopted techniques at present are mechanical fastens and adhesive bonding. Several drawbacks, such as stress concentrations at holes, poor long-term environmental resistance, limited inspection techniques, non-uniform stress distribution, and low production rates, can impact these joining methods (Figure 1.1).

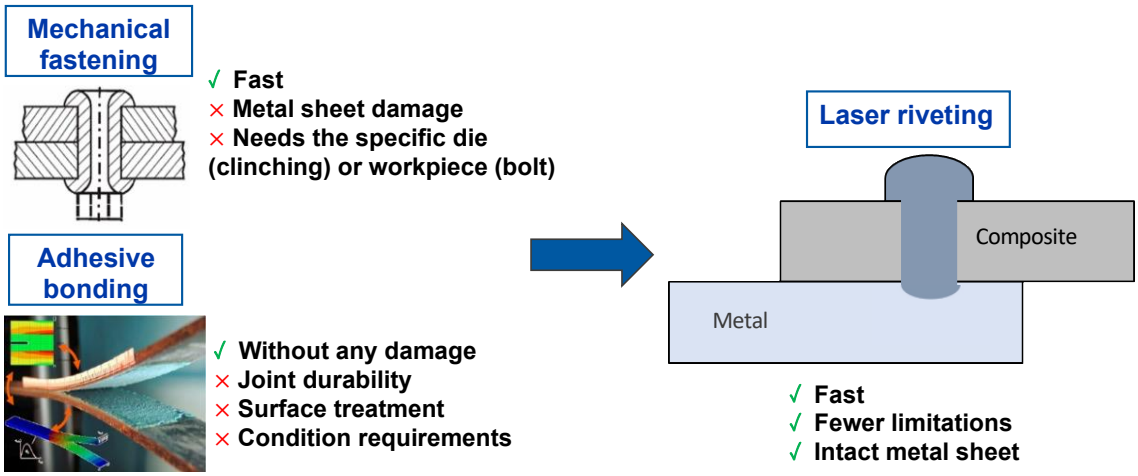

Figure 1.1 Motivation and benefits of laser riveting.

Woizeschke [1.8] noted that when joining CFRP elements to aluminium with traditional methods, an overlapping material is needed to realize the joint. This applies to mechanical joining (i.e., bolting and riveting) [1.9], combined joining [1.10], and sometimes adhesive bonding [1.11]. In addition, the drilling is required to install rivets can disrupt fibres and negatively impact load paths. Due to the localized application of force, the structures need to be strengthened or reinforced at the joint area. Failures can be arised due to issues with the fabrication, such as failures at the interfaces or defects at the edges. Finally, where the aluminium and carbon materials come into direct contact with each other, there will be accelerated corrosion [1.8].

1.2.2 Laser riveting process concpet

Laser riveting is an innovative technology in which the joint between metals and composite is achieved by additively manufacturing a rivet with a laser beam as energy source and metal wire as feedstock.

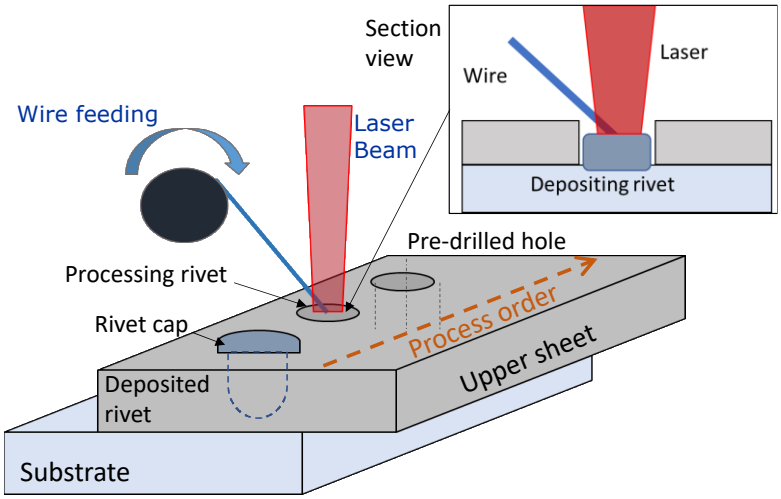

Figure 1.2 Laser riveting process concept.

The laser riveting procedures are shown in Fig 2.8, main phases of the process include:

1) First, make a hole in the composite. The hole could be made using a laser or by thermal assisted piercing.
2) Followed by controlled delivery of laser melted filler material through this hole to additively build a rivet. By overfilling the hole, a natural rivet can form between the metal and the composite.
3) The rivet will interlock the composite sheet to a metal surface underneath

A mechanized filler delivery system could improve consistency by making the process repeatable and reproducible [1.16]. Laser riveted joint processing can be enhanced using thermally assisted perforation (with multiple small holes rather than one large hole). Thus, by reducing the mass of the laser-melted metals which is required for the joints, the impact of otherwise high temperatures on the composite polymer matrix can be reduced.

The laser riveting technology presents some similarities with laser-wire additive manufacturing processes because it is laser-based and relies on the use of a wire feedstock to build 3D components.

1.2.3 Comparation between laser riveting and traditional joining

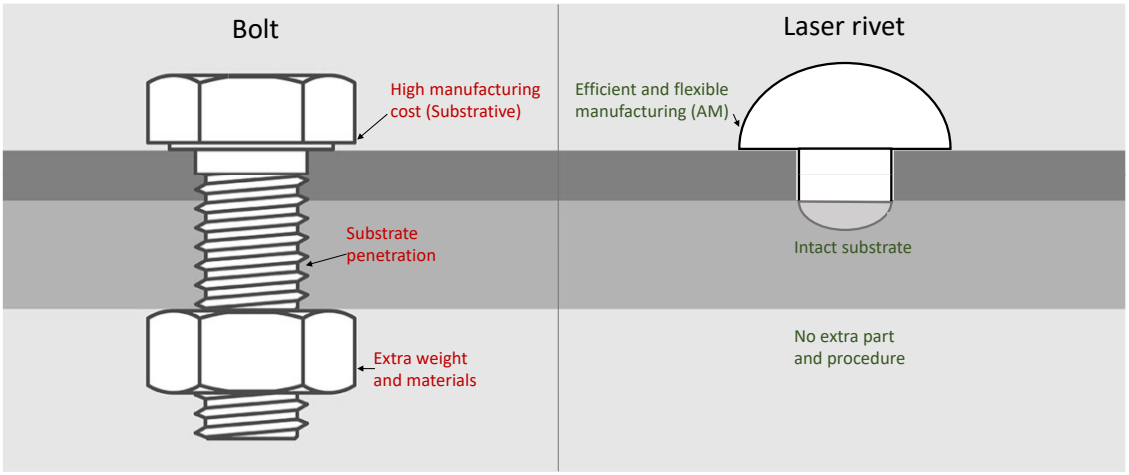

Figure 1.3 Benefits of designed laser riveted joints.

Currently the mechanical fastening and adhesive are the most common methods for titanium to dissimilar metal and composite joining, blind riveting is commercial used for aerospace titanium/aluminium joining and bolting is widely applied for the titanium to composite joining in wind turbine blade assemblies. Based on the previous discussion, it is clear that innovative, flexible, cost-effective, and quick techniques for joining composites to metal structures are desirable. For instance, as shown in Fig 1.3, compared with the traditional bolting method, the hypothetical laser riveting can take the benefits from following aspects:

Lower cost and more efficient manufacturing: the fabrication process for traditional rivet, pin and nuts for blind riveting and bolting is high cost and low efficient with subtractive manufacturing. In laser riveting, the additive manufacturing will be employed to fabricate the rivet joint, it can dramatically improve the material efficiency and cost. The advantage of laser riveting joint is especially remarkable for high-cost and difficult-to-machine materials.

Less damage to the substrate: the pre-drill hole and penetration on substrate are required in the traditional mechanical fasten joining, which causes the stress

concentration and leads to crack formation and propagation explained in facture mechanics, it is unexpected in the load-bearing structure. The laser rivet will be built onto the substrate by additive manufacturing without physical and mechanical damage of the base material, thus the new technology can further protect the structure integrity.

Lightweight: laser riveting not only can take the lightweight benefit from the hybrid structure with demanded materials, but also can reduce the residual weight by removing the extra parts compared to traditional blind rivet and bolt. As the example shown in the Fig 1.3, the excess part in bolt includes end of pin and nut, approximately take 35.9% of the total weight, the AMed laser rivet saves the material in each joint, and which vastly reduces the weight of the frame by a great number of alternative laser rivets.

Fewer limitations and higher flexibility: the rivet joint deposited by laser metal wire deposition (LMwD), compared with the existing adhesive joint, there are few or no environmental (temperature, humidity, and ageing) limitations for the joint. Compared with mechanical fastening, no specific die, and workpiece are required in the processing, which provides a more convenient set up in complex manufacturing situations.

Despite the benefits of laser riveting discussed above, the process still has some intrinsic issues in this novel technique. Broadly speaking, these issues come under four categories:

- Maintaining the structural integrity of the materials.
- Accuracy of the process: misalignments, alignment of the hole and contact point, processing parameters selection like input power, travel, and wire feeding speed.
- Distribution of the liquid metal over a limited area of the upper sheet and its wettability, the zoom is limited in the clearance hole located in the upper sheet, in the rivet deposition process.
- Control of thermal behaviours, the thermal gradients, and the degradation in composite processing, especially the melting and difference between titanium and composite.

1.3 Aims of the research on laser riveting as an innovative alternative technology

Laser riveting (LR) is an innovative technology in which joining between dissimilar materials is achieved by additively manufacturing a rivet with a laser beam and a wire feed material. The above technology will allow producing a riveting joint, tailored to each application and geometry. To achieve the aims of this thesis, this research will focus on the following main four specific phases and actions:

1. **Develop the empirical understanding of the laser riveting technique**, design the specific methodology, and develop the feasible producing experiment for this innovative technology.
   Action: Literature review is focused on the existing research and studies on laser wire deposition, dissimilar joining, and their numerical modelling, to determine the current gap for laser riveting technology both in the academic and industrial areas.
2. **Evaluate the effect of the key variables on the processing features** Demonstrate the capabilities of the process in comparison with preliminary results, optimize the processing procedure by parameter influence study.
   Action: Feasibility of LMwD riveting is checked by systematic investigation, which is conducted on the methodology of controllable design and development. A parametric study is conducted following the feasibility check to optimize processing quality and productivity of rivet building.
3. **Identify pre-treatment and post-treatment techniques,** microstructure analysis, and strength tests are required to evaluate and optimize the joint quality. **Develop further understanding of the process physics and be able to predict the process behaviours** under different conditions regarding the elaboration of an accurate numerical model.
   Action: Quality of the rivets produced is assessed through analytical measurements (microstructural analyses and mechanical tests).
4. **Develop finite element models to simulate the joining process,** which are calibrated by the experimental results and are used for parametric study.

Titanium, aluminium, and composite have been adopted during the experimental investigation for the industrial purpose of creating dissimilar joints. Moreover, several analytical frameworks are followed, including morphology, metallurgy, microstructural and strength analysis. Meanwhile, Laser Metal wire cylindrical Deposition (LMwcD) and LR ABAQUS simulations were applied for experimental assistance purposes.

1.4 Thesis outline

The research adopts a combined experimental and simulation approach and can be broadly divided into three parts as listed below. The first part is the preparation for both experimental developments and numerical modelling, with the research introduction, theoretical backup and experimental system setup. Then LMwcD and LR experiments will be conducted in second experimental part, they will be comprehensively investigated by feasibility and parametric studies and the results will be assessed by analytical measurements. Based on the experiments carried out in experimental part, the simulations will be developed in the numerical part, and the modelling will be validated by corresponding experiments.

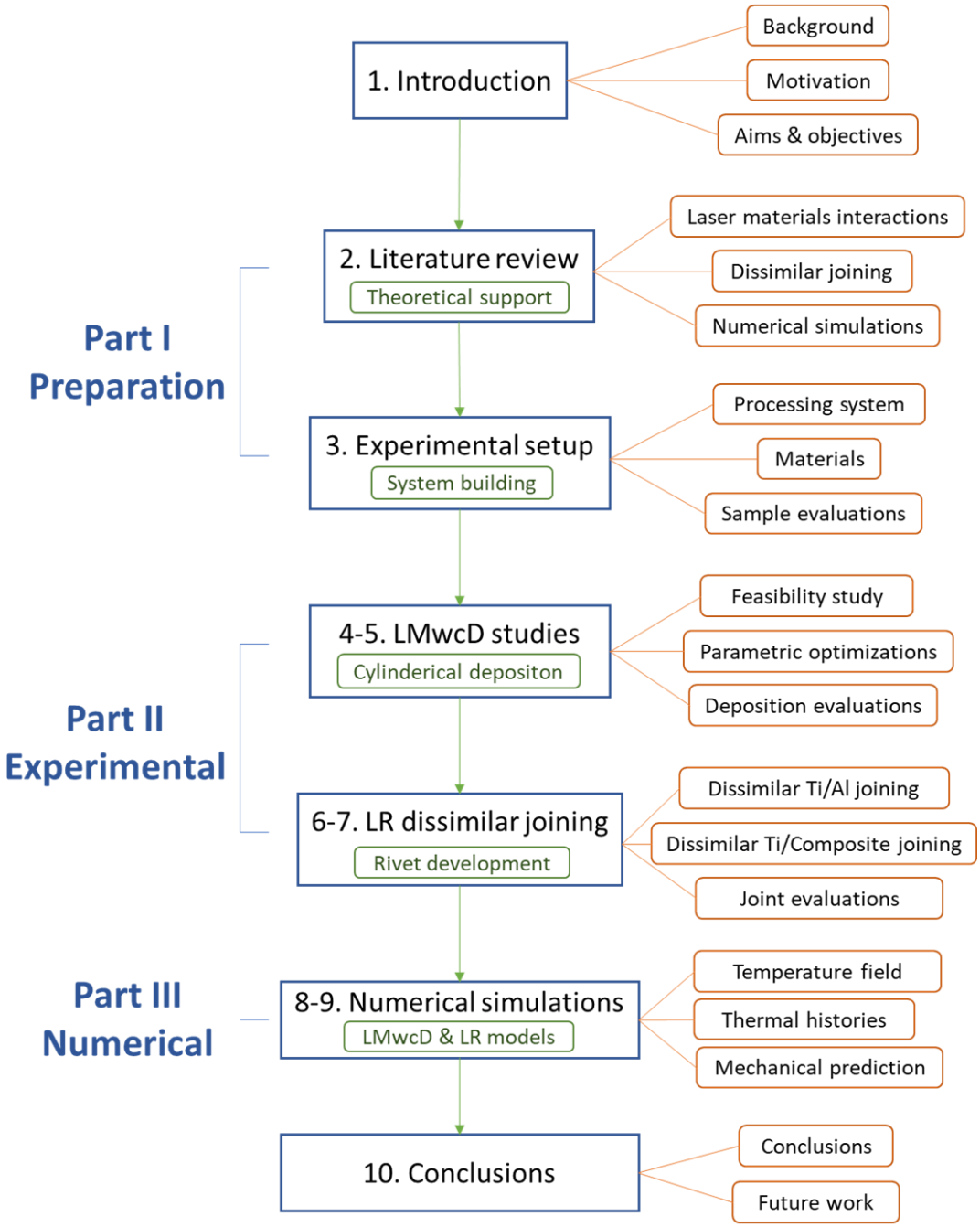

Figure 1.4 The research framework employed in the experimental and numerical studies on the LR dissimilar joining.

The general framework of this research is provided in Fig 1.4, this PhD thesis is divided into ten chapters, the detailed tasks, and contents of them are listed:

- **Chapter 1 Introduction**

The background, motivation, aims, and objectives were introduced.

- **Chapter 2 Literature review**

The literature review was completed in three parts, to explore the state of the art on the laser wire technology deposition, dissimilar joining, and numerical simulation. Hence, the literature review provides theoretical and technical starting background for the project activities.

- **Chapter 3 Experimental system set-up**

According to the acknowledge of previous LMwD and dissimilar joining studies and specific demand in methodology introduced in the literature review, a standard experimental system for laser riveting has been designed, components in the system were prepared and assembled to the LMwD system, the processing parameters and preparation and analyses of samples have been explained for following experiments.

- **Chapter 4 LMwcD feasibility study**

Two deposition track strategies were designed and developed to build up a single rivet onto the substrate, different process factors were varied to explore the process dynamics and down select the potential key performance indicators. The experiments included bead on plate trials on the base material, single layer deposition, and multiple layers deposition (which resulted in the production of an additively manufactured rivet onto the base substrate). The building process feasibility was demonstrated, and some basic processing parameter ranges were defined.

- **Chapter 5 LMwcD parametric study**

Based on the feasibility study, the parametric experiments were carried out to reduce the processing time which is the key factor in the potential industrial application, three deposition methods were developed and improved the productivity up to around 7 times compared to the initial deposition strategy. Meanwhile, further experiments for steel materials, cavities repair, and dissimilar joining were tested and explored.

- **Chapter 6 Ti6Al4V/AA6061 LR Joints development and evaluation**

For the laser riveting experiments, the AA6061 sheet was drilled and placed onto the Ti6Al4V metal substrate, to develop a LR joint utilizing laser riveting. Performance experiments will be carried out to facilitate understanding of the major performance variables that impact the laser riveting process, especially for the post-processing

parameters such as scanning time, wash speed, and power, couples of sound rivets have been successfully built up and were evaluated in morphological, microstructural and mechanical aspects.

- **Chapter 7 Ti6Al4V/CFRP LR Joints development and evaluation**

In further dissimilar joining experiments, the CFRP was used as the target upper joined sheet on the Ti6Al4V substrate to explore the LR feasibility for metal to composite joining. Several rivet deposition strategies were designed and conducted to mainly avoid the degradation of the epoxy. The morphologies and cross-sections microstructure of rivets were analyzed by SEM, and their strengths were measured by the shear test.

- **Chapter 8 LMwcD numerical modelling**

Corresponding to the LMwcD experiments, straightline-LMwD, NM-LMwcD, HSS-LMwcD numerical simulations of feasibility and parametric studies were developed to better understand the experimental result, assist with the investigation, and better predict how the process would be affected by different welding conditions. All the LMwcD and following LR models were compared to the experimental results in the thermal behaviour, subsequently predicting the mechanical performance for the samples.

- **Chapter 9 Ti6Al4V/AA6061 LR numerical modelling**

Same with the aim of LMwcD modelling, the numerical modelling of the Ti6Al4V LR experiment was developed as well to further simulate the processing behaviour in the LR experiment. The deposition and post-wash procedures were simplified to the experimental conditions and a new annular heat source was created to simulate the laser circular wash processing.

- **Chapter 10 Conclusions and recommendations**

The overall conclusions of the research were summarized, and recommendations were offered regarding future work.

Chapter 2 Literature review

In this chapter, the literature review is presented. The previous research on the state of the art of laser processing and dissimilar joining were conducted to find out what elements and what previous work can be exploited as a starting point for the experimental and numerical analysis targeted in the present work, moreover, provide the solid literature and technical knowledge base for the following experiments and simulations.

The chapter is divided into three main sections:
(1) The basic theory of laser metal wire deposition and processing system.
(2) Traditional dissimilar joining methods between metal and composite materials.
(3) Fundamentals on finite element analysis during laser deposition.

This section also guides the readers' understanding and provides an adequate background knowledge of the project.

2.1 Fundamentals of laser metal wire deposition

The whole review begins with basic laser theory, laser systems are introduced in this chapter as this can facilitate the fundamental understanding of the process. First, the laser as an energy source is introduced, then its principles, components, and properties are explained. This is followed by the phenomenon and theory of laser-material interaction, which is described to reveal the relationship between laser and material during processing. Finally, to introduce the laser-wire deposition conducted in the experiments, the dynamics in the laser-wire transfer are explained to transfer the knowledge to the LMwD processing in laser riveting explicitly stated.

2.1.1 The components of the Laser processing system

Based on different functions, the whole Laser processing system can be divided into five basic components. These are the laser source (generator), delivery system,

processing head and motion system. Their details are shown below in Fig. 2.1, which provides a schematic illustration of the laser equipment for material processing.

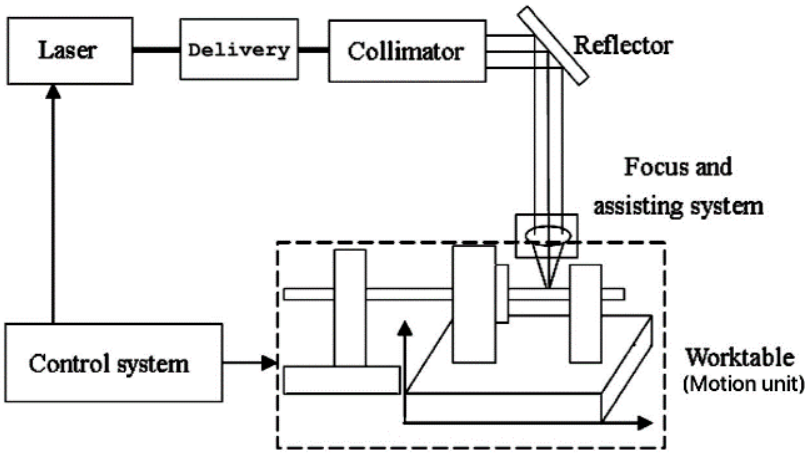

Figure 2.1 Laser system components [2.1].

(1) Laser generator

The laser source is responsible for generating the laser for the entire system. Moreover, it is the energy source in several manufacturing and processing systems that run off the laser method.

The laser wavelength is determined by the difference in energy as the excited species drops in energy level [, where h is Planck's constant $6.620 \times 10^{-34} Js$) and c is the light velocity ($3 \times 10^{8} ms^{-1}$)]. In general, quantum states are the molecular vibration levels of long-wavelength lasers. In other words, they are the electron orbit levels for visible laser radiation as well as the ionization effects associated with ultraviolet lasers [2.2].

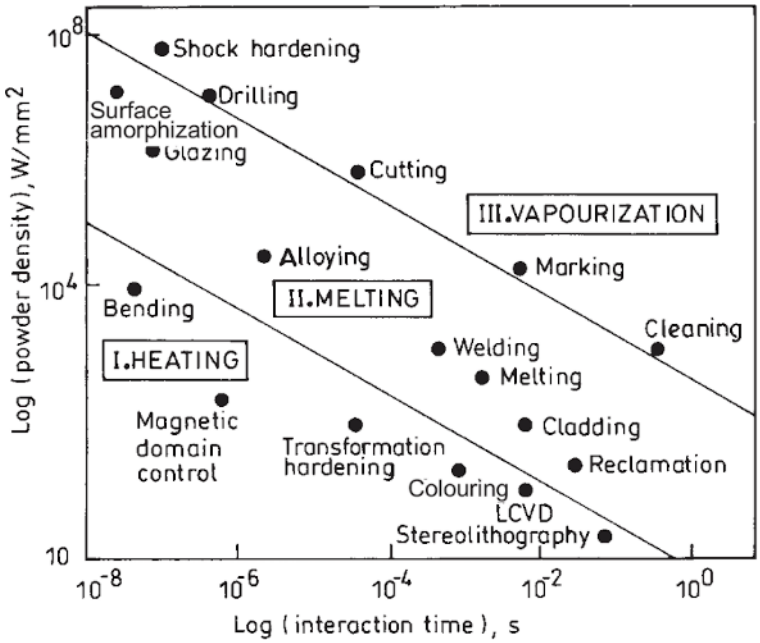

Figure 2.2 Process map showing laser power density as a function of interaction time for different laser material processes [2.3].

At present, CO_2 and Nd: YAG and fibre lasers are the most popular laser systems in material processing regarding their light sources receiving an increased attention. In Fig. 2.2, the ability of a single laser to perform several processes is shown for a low density and manipulated interaction time [2.3]. This partially explains the high popularity of lasers in flexible manufacturing systems. Therefore, the laser generator determines several factors in the laser processing, other parameters such as laser power, mode are also critical but can be adjusted during the processing procedures.

(2) Delivery system

In the laser system, the laser source is connected to the processing head through the delivery system, the main function of which is laser transmission. There are two main delivery systems: fibre optic which is used for Nd: YAG lasers and reflective optic used for the CO_2 lasers [2.4].

The processing head, which is mounted on the end of the delivery system, directly emits the laser onto the workpiece. Moreover, it consists of two principal components: the collimator and focusing lens.

A collimator is a device that narrows the rays of particles or waves. In this case, the collimator narrows the laser beam from the generator, and corrects them in a specific parallel direction.

In the processing head, the randomly directed lasers from the delivery system are reoriented. Then, in the processing head, these collimated lights go through the focusing lens and focus on the focusing plane, therefore, the focusing lens produces a high-energy laser that can interact with the workpiece.

(3) Motion unit

This part allows for the relative motion between the laser beam and the material on the workbench to be realized through one of two possible systems. These are:
(a) CNC (computer numerically control) system: the laser and its delivery system are fixed but the material is mounted on the workbench, which is ideal for processing small pieces. Meanwhile, large floor space is required for processing large pieces.
(b) Robot: the laser generator is immobile while its delivery parts are free, even though the material is also fixed. Generally, this involves a robot that contains the beam delivery elements. The greatest drawback of using a robot is the resultant change in the focused spot's size along the processed path following beam divergence and the increase in the beam size as it moves away from the laser output window. Hence, beam divergence needs to be minimized [2.5].

2.1.2 Laser processing parameters

The previous sections summarize the main laser processing parameter, which defines the characteristics of the laser energy delivery and is responsible for the features of the manufactured part [2.6]. This section will focus on continuous wave emission, being the form selected for the specific work desired.

(1) Energy and Power

In a solid-state pulsed system, the output is determined by the charging voltage for the power supply and the capacitors acting as the energy storage unit. High-intensity

flash lamps discharge the stored energy, thereby exciting the laser beam for stimulated emission.

The intensity of the laser beam (I) is typically taken to be the optical power per unit area, which is transmitted through an imagined surface that is perpendicular to the propagation direction. Units of intensity or light intensity are expressed as W/m^2 or (more commonly) W/cm^2.

(2) Wavelength

Wavelength is the spatial period of a plane wave. Lasing material wavelength greatly affects the extent to which the focused beam is absorbed by a material and converted into heat generation inside.

(3) Focusing and Spot Size

The laser beam propagates along a certain direction, which can be referred to as the propagation axis. The beam spot size is generally considered as the distance from the propagation axis at which the intensity has fallen to $1/e^2$ of its peak value.

The size of the beam spot varies along the propagation axis, describing a function called “caustic”. The caustic presents a waist, which consists of the focal position and beam distribution boundaries along the central axis. The caustic is made up of two main parts, which are the near-field divergence part (in the proximity of the waist) and a far-field divergence (further away from the waist), which in the case of Gaussian beams approximates a straight line.

The depth of focus is defined as the half-width of the range of longitudinal positions in which a focus to a film or image sensor is achieved.

The Raleigh length can be calculated as the distance along the propagation direction of a beam from the waist to the point at which the area of the cross-section is doubled.

In material processing, laser beam irradiance at the material surface is critical [2.7]. By focusing on a laser, it is possible to realize irradiances that are capable of melting or vaporizing any material. At the lens focal point, at which beam diameter is minimized, irradiance is maximized. At this focal spot, one can obtain irradiance in the billions. The obtained focal spot is limited in its size by optimal component imperfections and diffraction effects.

Focal spot size is determined by several factors. Firstly, incoming beam quality (quantifiable by beam divergence) is an important factor (Fig. 2.3). Weakly divergent laser beams can be focused onto a smaller spot than is possible for more divergent beams [2.8]. Secondly, diffraction is also important. When using a lens to focus a diffraction-limited laser beam, the higher the focal length, the greater the diameter of the focused spot. The diameter of the incoming laser beam influences focal spot largess. For certain optics, focal spot size can only be reduced by increasing the incoming laser beam diameter.

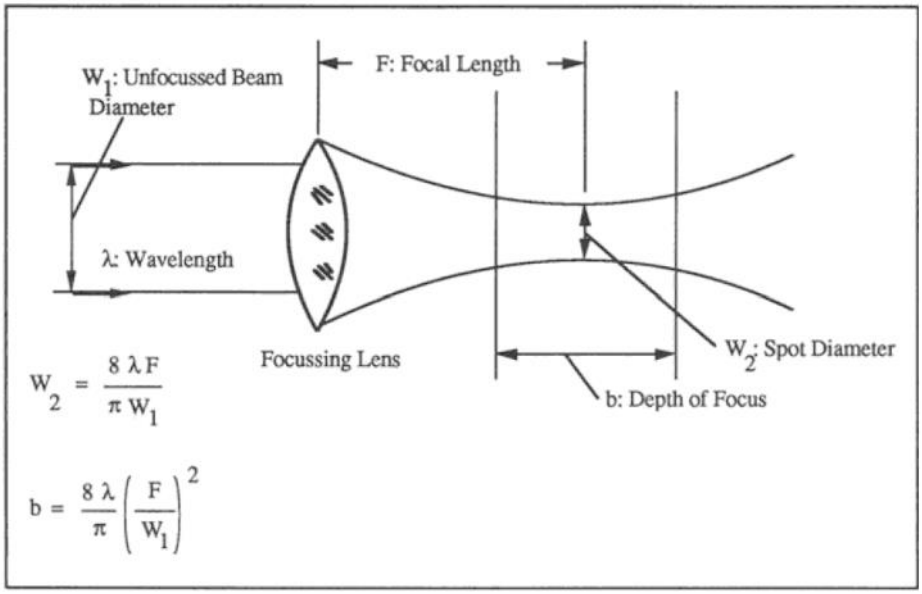

Figure 2.3 Calculating focal spot diameter and focus depth [2.8].

(4) Laser beam quality (M^2)

The M^2 (also referred to as the beam quality factor) represented the degree to which a beam varies from an ideal Gaussian beam [2.1]. To get the M^2, the ratio of the beam parameter product (BPP) of the beam to that of a Gaussian beam with the same

wavelength must be worked out. This related the beam divergence of a laser beam to the minimum beam spot that can be achieved.

(5) Set-up characteristics

The characteristics of the system arrangement are important to determine the laser beam emission needed. These characteristics depend on the laser machine and the optical arrangement.

Table 2-1 Laser beam parameters during laser processing

Beam Parameter	Symbol	Description/Function	Unit
Diameter of delivery fibre	$\emptyset_D$		mm
Focal length of collimator	f_c		mm
Focal length of focusing lens	f_f		mm
Half divergence angle	θ_d	Angle of the emerging beam	
M square	M^2	Beam quality $M^2 = \frac{(BPP)_{real}}{(BPP)_{gaussian}}$	
Beam Parameter Product	BPP	$BPP = \frac{BD_f \cdot \theta_d}{2}$	
Peak power intensity	I_{peak}	$I_{peak} = \frac{8P_0}{\pi BD^2}$	W/mm^2

Table 2-1 summarizes part of factors that are often adopted as basic process parameters when:

- Transferring the process conditions from one set-up to another has different laser machines and optical arrangements.

- Establishing the effect of process conditions on the features of the laser processed part. The relationship often involves a basic function rather than single parameters themselves.

Table 2-2 Laser system processing parameters

Parameter	Symbol	Description/Function	Unit
Interaction Time	IT	The total time the laser beam interacts with the workpiece	s
Travel speed	TS	The speed at which the laser beam travels $TS = \frac{BD_s}{IT}$	mm/s
Linear energy	LE	Heat transferred to the material per unit distance $LE = \frac{P}{TS}$	J/mm

2.1.3 Laser-material interaction in welding

The interactions between laser and matter are fundamental to defining the process regime and the fluid dynamics of the weld pool. In this thesis, metal is the main material that interacts with the laser beam. The degradation of the composite by direct laser beam irradiation will have to be avoided and prevented by tools, and the main effect of heat transfer has been fully investigated in Chapter 7. Thus, this section focuses predominantly on the interaction between laser beam and metal.

(1) Heating and melting

As light carries heat, the material processing laser beam carries considerable energy. Moreover, the low divergence of beam permits for energy to be concentrated in a small area. If the beam touches a material, light is both reflected and absorbed [2.8]. Thus,

the absorbed laser causes heat accumulation in the material to reach the point at which it begins to melt.

If the heating process is continuous, the heated solid changes state, with most materials melting except for graphite which vaporizes, and most polymers which decompose in composite material which will be shown and discussed in 7.1.

Even though the interaction mechanisms are similar, heat transfer is different to a certain extent. Hence, material melting can occur and is driven by the fact that temperature gradients give rise to surface tension changes [2.8].

(2) Laser welding mode

Whilst welding, a high-energy laser beam rapidly heats and melts the surface of the material being worked on. The energy from the laser subsequently evaporates and ionizes the melted material, which creates an expanding plume of plasma. The extent to which the plume expands depends on several factors, including the features of the laser beam, the properties of the material, the conditions in which the welding process takes place, the process parameters, and the surrounding atmosphere [2.8, 2.9]. Each of these variables can cause fluctuations in the ablation mechanisms which in turn affect the evolution of the plasma plume [2.10]. According to the extent of laser-metal interaction, there are two laser welding mechanisms: the conduction and the keyhole mode.

Conduction mode: typically, this welding mode is carried out with a relatively low power density laser. As such, the effects of plasma and vaporization are minimized, with the most prominent phenomena being localized heating and melting. The area which the laser beam irradiates on the workpiece becomes the source of the heating. A small area surrounding this point melts and the rest of the workpiece is heated by conduction as heat from the contact area spreads to the rest of the material. Subsequently, the weld pool increases, and other phenomena become relevant. This method results in large zones affected by heat with low penetration depth. Compared to the keyhole mode, another difference needs to be noted is that an excessive distortion and residual

stress is generated in a large part manufacturing with the conduction mode regarding the higher energy input with a longer interaction time.

Keyhole mode: normally, this mode is carried out with a high-power density laser. As such, a plasma cloud forms, and localized heating and melting occur. As the laser beam irradiates the top surface of the workpiece, vaporization occurs and a cavity form — referred to as a keyhole — consists of vapour and plasma. This keyhole is surrounded by molten materials which then fill the space left behind the beam as it advances along the welding line. The specific dynamics of this method depend on the various contributing forces [2.11, 2.12].

(3) Weld efficiency
In the laser material processing, weld efficiency i.e., energy absorption in the fusion manufacture needed to be identified, this ultimately allows providing the required efficiency of welding, quality of the produced welded joint, process stability and reproduction of its results [2.13]. The weld efficiency of laser cause material melting and evaporation of the material at the point of interaction, forming a cylindrical hole inside which expands through the whole sheet [2.14].

2.1.4 Laser-material interaction in metal wire deposition

In this case, for the rivet building part, the laser metal wire deposition technology is applied to melt the wire and rivet built in the hole of the upper sheet by multiple layers deposition. The laser-wire transfer condition the thermal behaviours are demonstrated, as its processing procedure is specific and relevant to the application experiment. Moreover, the recent research and basic wire-transfer modes and laser-wire deposition investigations are introduced in the following paragraphs.

2.1.4.1 Background

Additive manufacturing is a lucrative means of generating industrial devices that consist of material melting in the form of a powder or wire, with layer-by-layer adding ensuring that components are constructed. Alternatively, subtractive manufacturing methods could be used [2.15–2.18].

Among additive manufacturing techniques, there are strengths associated with metal part production during those instances in which directed energy deposition (DED) techniques are used. These strengths involve producing large parts, retroactively adding component features, using a single repair process, and efficient material use. The energy source and feedstock are used to determine the differences among processes [2.19]. Different combinations of the above have been investigated for their ability to additively produce metallic parts. The most explored is the use of a laser beam with powder feedstock [2.20]. Indeed, by using a laser beam, flexible operations are made possible in an ambient atmosphere with high precision based on the trade-off between competing energy sources [2.21].

Recent decades have seen the creation of several different additive manufacturing approaches. For wire-based approaches, specific layering is used by feeding a wire through a workpiece nozzle. Like powder injection approaches, inert gas shields the material during the molten state. Moreover, the surface area with powder-based processes is less than with wire-based approach, which increases the risk of atmospheric gases reacting. Hence, working in a closed chamber of inert gas is not required, thereby increasing the freedom available to wire-based applications [2.22]. Furthermore, additive manufacturing uses wire-feeding systems, the material is more efficiently used [2.17], deposited structure surface quality is improved [2.23] and deposition rates are higher compared to powder-feeding systems.

The laser-wire condition produces a deposition with a complex microstructure and several thermal sequences. Moreover, functionally graded materials can be produced using the composite material by following the laser-engineered net shaping process, [2.24]. Further study is still required to comprehensively understand the link connecting phase changes and temperature variations [2.25]. Numerical simulated the temperature fields for a multi-layer material with a 9-layers wall. Because of its poor convergence, it is difficult to calculate the stress field. Moreover, the work forms the riveting head using a laser metal deposition technique, involving filler wire and a laser.

2.1.4.2 Energy input and thermal behaviour

(1) AM processes involving complex multi-physics, non-equilibrium phenomena influenced by a set of variables such as power, scan speed, path strategy, deposition height, hatch spacing, etc. The difference between the powder bed fusion and DED processes lies in the significant differences in energy input and thermal behavior. The interaction between the power source and the filling material also depends on the absorptivity, the physical properties of material, and the particle scale and shape [2.26]. In these conditions, the input energy density E (in J/m^3) is regarded as a fundamental start for comparing additive processes. E is the absorbed energy density and has the following expression:

$$E = \frac{\alpha P}{v \cdot h \cdot t} \quad (1)$$

where P is the power (in J/s), v is the scanning speed (in m/s), h is the shaded spacing (in m), t is the path deposited height (in m), and α is the absorptivity. During the AM process, heat is radiated from the melt pool by downward conduction and by forced convection from the shielding airflow [2.27].

Regarding the layer-additive manufacturing characteristic of LMwD, different regions of the deposited material repeatedly undergo a complex thermal history. The temperature field of LMwD typically involves melting at relatively low temperatures and multiple reheating cycles [2.28]. Such a complex thermal behavior of the LMwD process leads to complex phase transitions and microstructure development in the material. Therefore, there are significant difficulties in the desired microstructure for the manufactured component [2.29, 2.30]. Besides, the well-focused laser is selected to achieve a fast-moving melt pool can lead to high solidification rates and melt instabilities in process. Because the thermal transients experienced during solidification, complex residual stresses are likely to be blocked in fabrication. [2.31] The presence of residual stresses can lead to deformation, or even form cracks in LMwD machined parts. Uncontrollable composition, microstructure and the generated residual stresses are considered to be the main challenges in LMwD. [2.20]

2.1.4.3 Wire-transfer modes

Abioye et al. (2013) demonstrated the three wire-transfer modes at several feed speed conditions. These are smooth deposition, droplet deposition, and stubbing deposition. In Fig. 2.4, typical example tracks deposited by the deposition process are visible. The three tracks are characterized by wire droplet, smooth wire transfer, and wire stubbing. When the wire transfers smoothly into the melting pool, the preferred scenario, whereby a track with high surface quality and tolerable measurements is produced by cladding conditions, materializes. During moments in which the wire tip melts close to where it meets the melting pool, the preferred scenario occurs. In the third quadrant of the process map, the processing conditions for smooth wire transfer are given [2.23].

Figure 2.4 Typical modes of wire-transfer: (a) droplet (b) smooth (c) stubbing deposition modes [2.23].

Intermittent wire dripping occurs when the wire feed rate drops far below the normal level for a given traverse speed and laser power. Hence, discontinuous tracks are deposited as given in Fig. 2.4. Meanwhile, the wire tip interacts with the laser beam for a long time that sufficient heat energy is absorbed to cause melting for a low wire feeding rate. The wire tip melts before the intersection with the melt pool, causing intermittent molten wire dripping during substrate traversal. When the energy per unit length of track exceeds the normal limit for a given wire deposition volume per unit length, the impact is similar. Moreover, the feed wire interacts for a short moment with the laser beam when the wire feed rate exceeds normal levels for given levels of speed and laser strength, consequently, the wire tip collides with the solid substrate at the melting pool base since the wire enters in a near solid state. However, the wire does

not melt when the wire feed rate is highly raised because the wire deposition volume per track length greatly exceeds normal levels given the energy per unit track length [2.23].

2.1.4.4 Thermal cycles and HAZ band formation in multilayer deposition

The previous LMD research stated the effect of laser speed on the thermal cycling nature of in-layer process, such as peak temperature, cooling and heating rate. A comprehensive study of the influence of process parameters of overheat input, component scale or path deposition has not been finished, regards to these processing values have not been reported for LMD of Ti-6Al-4V. Nevertheless, based on the current studies, the result of applied energy affects the nature of the process temerature cycle was revealed. The heat input is inversely proportional to the travel speed, thus, rising the power input at a constant speed will rise the cycle temperature histories, molten pool scale and processing time while lead to heating rate drop. The results show that the laser power input has the least effect on the cooling rate, but the cooling rate to reduce with higher heat input [2.32].

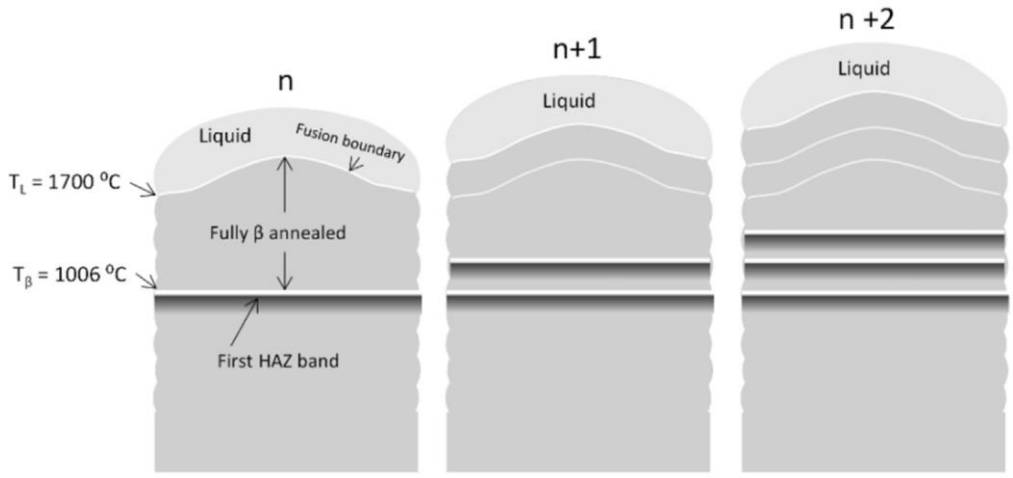

Figure 2.5 HAZ and segregation bands formation among layers in LMwD process, against melting and fully beta annealed temperatures.

In single thin-wall depositions, it is usually assumed that the final HAZ zone occurs below the interface between substrate and AM material, where the peak temperature increased is approximately equal to the β-transus point (T_β) [2.33, 2.34]. Simulations show that for the Ti6Al4V multilayer deposition, the isothermal heat generated by the energy input is similar curve appeared regarding the wide thermal range between the melting temperature and β transus point. The the initial HAZ zone below the area is

repeated into the β transus zone to five times, with the deposition of next layer, this new HAZ appears during the final layer when the process completed with a similar cooling rate at T_β [2.35]. The thermal cycle process is presented in Fig. 2.5, which schematically demonstrates the formation of the microstructure segregation band in the LMwD. When a new layer is deposited, the energy is accumulated, the area above the last heat affected zone is β-annealed to the very similar area with previous layer, and an following new heat affected zone is drawn on the fully β-annealed transition microstructure in the last path. In each weld pass, the energy input will accumulate vertically by a height equal to the increased layer thickness, thus the β-transus ground temperature produced by the energy input will increase the similar height, so that the vertical distance between HAZ bands is equal to the deposited material thickness [2.36].

2.1.4.5 Existed research on LMwD

In terms of laser wire deposition, Froend (Fig 2.6) [2.22] examines the different factors of the processing parameters, geometric shape, and microstructures obtained during the course of experimentation. In particular, Froend utilized a wire-based laser metal deposition process with the AlMg alloy EN AW-5087 as the wire and EN AW-5754 as the substrate material. Moreover, a systematic parametric study showed the connections between the specific process energy, wire feed rate, porosity, and the geometric shape of the deposited beads. Pre-heating the substrate helped to reduce porosity and cracking.

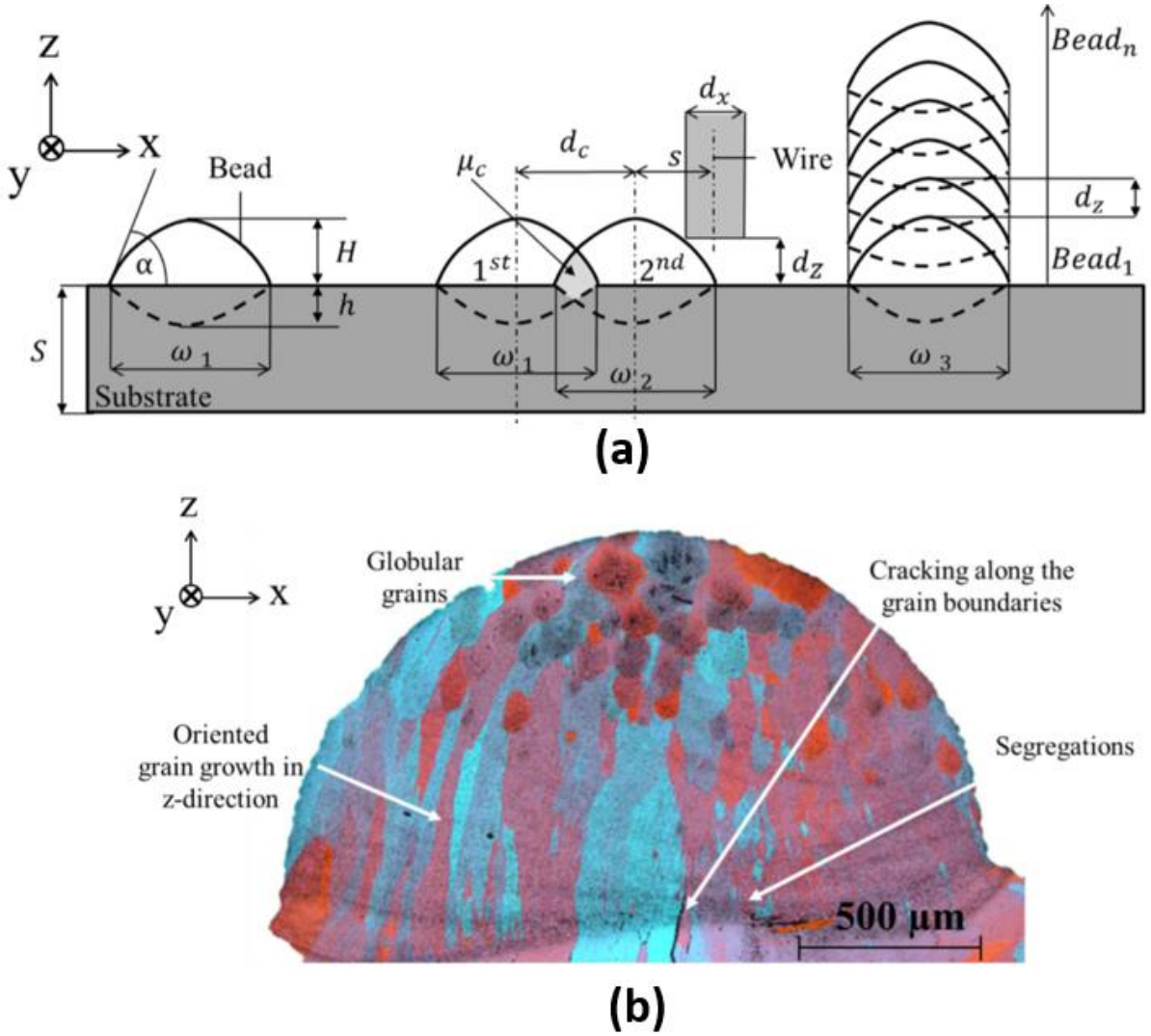

Figure 2.6 The (a) geometric and (b) microstructure of the laser-wire deposition bead [2.22].

According to the results, the deposited beads' geometric properties can be tailored by adjusting the process parameters. With such an alteration, the highly diluted, broadly expanded, and flat beads were deposited at a low side-angle through the utilization of highly specific energy densities and low wire feed rates. Given the expense of post-processing in AM, controlled layer geometries facilitate such a decline. Hence, the wire-based laser metal deposition (w-LMD) of aluminium alloys can be carried out. High deposition rates and controllable layer geometries allow for the processing of tall structures and coated surfaces. In terms of the temperature distributions, cooling rates, and features connected to heat transfer mechanisms, only assumptions could be made. Further research should be carried out using controlled temperature measurements so that temperature-related effects can be identified.

Meanwhile, Ali Gokhan Demir thoroughly investigated multiple layers, which is also known as the thin-wall structure [2.37]. Moreover, the microlaser metal wire deposition was developed, as wire-based DED processes require high deposition rates, while this paper attempts to reduce dimensions and improve geometrical tolerances using a laser-wire combination. These study trials the use of a dimensional resolution of wires that are 0.5 mm and constructed of AISI 301 stainless steel. The principal findings are as follows:

Firstly, at the single-layer level, high pulse energy and pulse duration lead the layer to increase in width and decrease in height. At the same time, dilution increases. Furthermore, due to the processing conditions, layer width may exceed twice the wire diameter, which should be subjected to regulation to maintain the micrometric dimensions. Secondly, while the amount of material deposited at high and low ranges may fall due to traverse speeds, at intermediate values, the process is likely to remain stable. Thirdly, it is possible to realize thin-walled structures with layer widths between 700 and 800 μm, which are maintained over 15 mm to provide an aspect ratio of 20. Fourthly, material efficiency is high when such a process is applied. Material use efficiency increases as fluence levels rise as a result of vapour and spark generation. Such phenomena do not occur when deposition conditions are stable. Fifthly, based on the relevant cases, the process can be used to additively manufacture different thin-walled shapes which feature wall inclinations and section changes (Fig 2.7) [2.37].

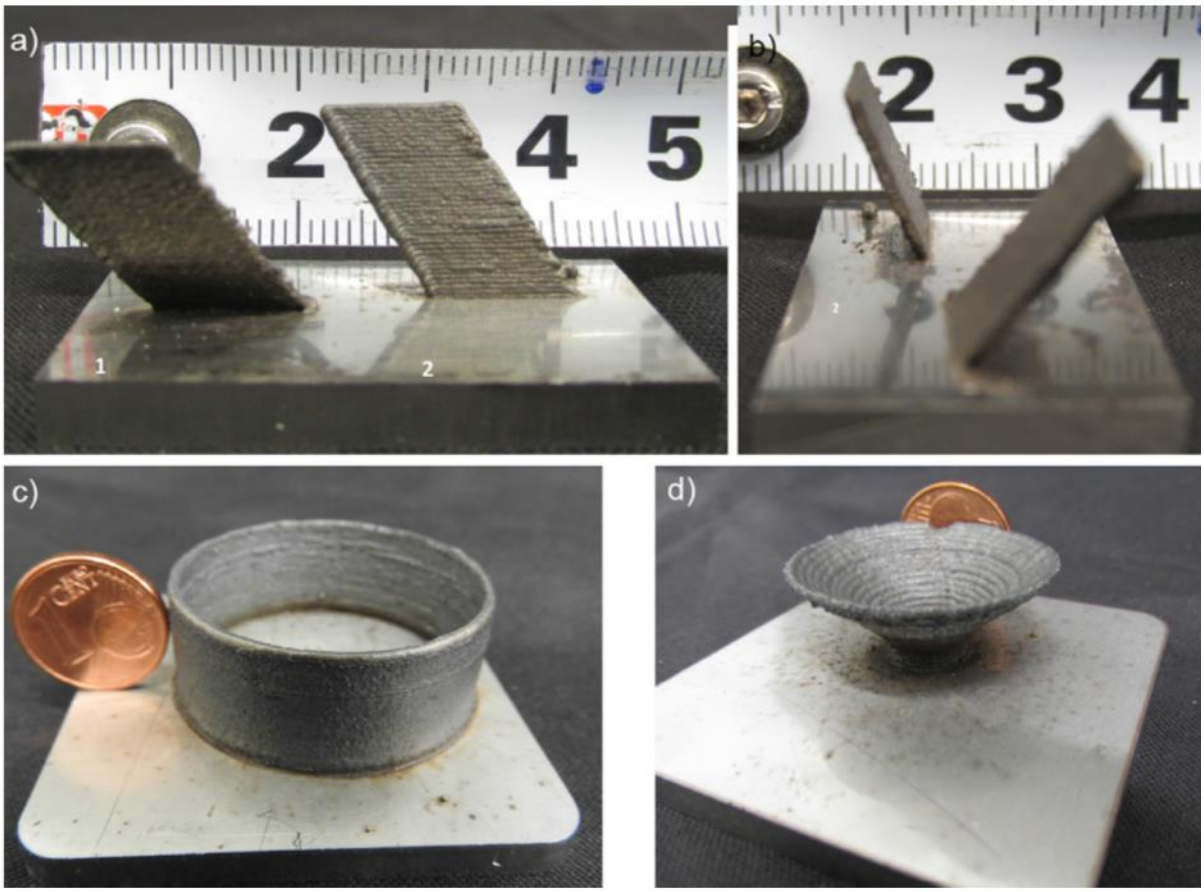

Figure 2.7 Laser wire additive manufacturing of AISI 316 steel thin-walled structures. (a, b) Inclined walls with a height of 13mm at inclination angles of 58 and 69 respectively relative to the substrate plane; (c) Tube with a height of 13mm and diameter of 35mm; and (d) Truncated cone with a height of 11.5mm in the range of 8-29.5mm [2.37].

2.2 Dissimilar materials joining

In the last section, the relative acknowledgements of laser processing are systematically reviewed but only based on the laser processing aspect. The relative materials and basic joining method are yet to be explained. Therefore, in this chapter, the industrial applications and metallic of joining techniques are introduced, and the advantages of hybrid structure are explained to justify the popularity of such techniques in the industry. Next, the challenges and opportunities of dissimilar joints in the industry are stated, with an emphasis on their shortcomings as these are of utility in this project. Finally, after introducing the metals in dissimilar joining, this review focuses on the composite materials joining given their promising properties. In the

experiment, the composite material used in dissimilar joining was investigated with regard to the laser riveting method.

Dissimilar materials can be described as ‘materials or material combinations that are difficult to join, either because of their chemical compositions or because of large differences in physical properties between the two materials being joined’ [2.38].

It is no mean feat of engineering and technology to join dissimilar materials [2.39], whereby at least two components are combined to make a multi-material hybrid joint to satisfy specific engineering requirements for specifically optimized versatility [2.40]. Dissimilar materials are often joined due to the needs of complex industrial applications [2.41, 2.42].

Hybrid have been made possible thanks to mechanical assembly, including screwing, riveting, roll bonding, and clinching [2.43–2.45]. In recent years, new welding techniques that avoid the need to transition from solid to liquid have been successfully implemented, including explosive welding and friction welding [2.44].

2.2.1 The use of dissimilar joints in the industry

2.2.1.1 The applications of dissimilar joints in the industry

Dissimilar-metal joints are extensively utilized across the industry for reasons both technical and economical. By adopting dissimilar-metal combinations, product flexible design can be efficiently realized based on material characteristics [2.45].

By bringing various materials together in a multi-material hybrid structure, it is possible to satisfy the desire for better, lighter, and superior structures, as well as the continued integration of additional functions into each component [2.46]. In other words, desired product performance is achieved by using the different properties inherent to distinct materials. This trend has been seen in several industries, including automobiles [2.47], aeronautics [2.48, 2.49], clothing [2.50], tooling [2.51], implants [2.52], power generation [2.53] and marine technology [2.54]. Material selection must be approached systemically given the mixing of new materials, which will interact in new

ways. Moreover, there may be requirements for new manufacturing systems, for which the simultaneous optimization of material selection and geometry will be necessary. Modern industrial developments on lightweight and recyclability encompass suggestions for multi-material design procedures [2.55] and optimal material choice [2.56], examples shown in the following.

The fields of nuclear energy and automobiles have adopted highly engineered materials where specific components require specific materials that possess unique attributes. In the field of dissimilar joining, the research seeks to integrate hybrid multi-material structures into the complex system manufacturing process, thereby leading to the optimization of performance and manufacturing [2.57]. In Fig. 2.8, the potential application of dissimilar assembly of light water reactors is exhibited in [2.58].

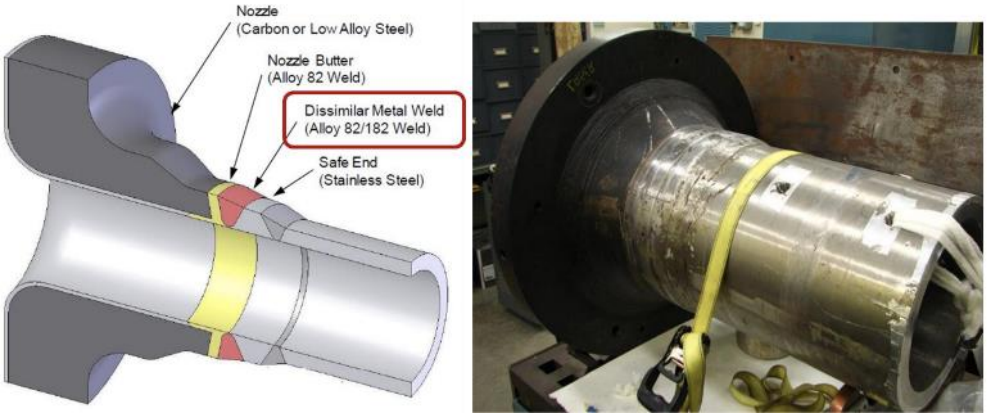

Figure 2.8 Dissimilar joining in light water reactors [2.58]

Similarly, in modern car bodies, it is possible to use high-strength steels in longitudinal beams for strength, aluminium alloys in bumper beams to reduce weight and protect against crashes and composite sheets in panels because they are lightweight. The EU FP6–project Superlight Car [2.59] illustrates how the combining of aluminium, steel, magnesium, and glass-fibre-reinforced thermoplastics can reduce mass (Fig 2.9).

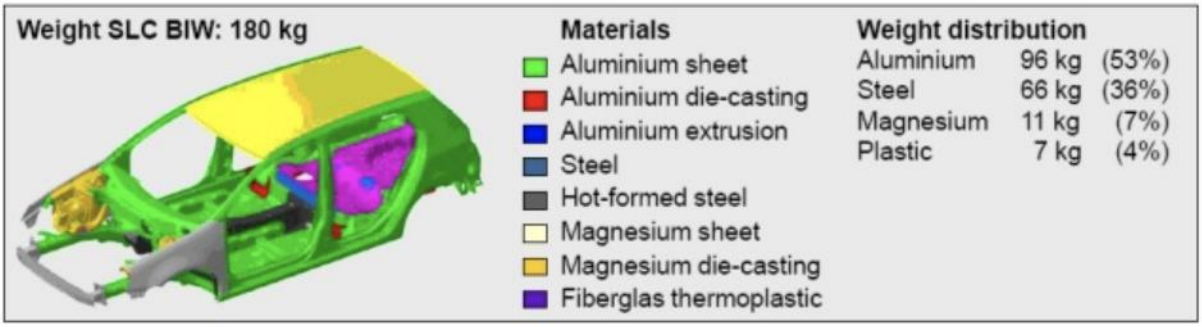

Figure 2.9 Material map for the superlight car [2.59]

2.2.1.2 The metal materials of dissimilar joints

Aluminium, titanium, and steel are highlighted in this section. Their outstanding properties in dissimilar joining across the industry, especially in aerospace applications, showcase their significant merits compared to other metals. The advantages of joints made of these three metals are as follows:

(1) Aluminium alloys are commonly used in aerospace and automotive construction because they possess a high strength-to-weight ratio and are low in density, corrosion-resistant, ductile and recyclable [2.60]. Moreover, since the 5000 series Al-Mg non-heat-treatable alloys possess deep drawing and sheet-forming characteristics, they are well suited for automotive tailored blanks [2.61–2.63].

(2) Titanium alloys are used extensively in aerospace, the petrochemical industry, and the transportation sector due to their strength and ability to withstand corrosion and high temperatures [2.64].

(3) Steel is also highly competitive given its price and performance. Moreover, the evolving needs of the automotive industry mean that new steel alloys are continuously in development. Different kinds of steels have been used in industry from low-strength high-elongation mild steels to the ultrahigh-strength low-elongation DP, TRIP, and MART series. By utilizing ultrahigh strength steels, to produce thinner gauges, it is possible to reduce weight, increase strength and enhance crashworthiness [2.65].

As illustrated above, aluminium, titanium, and steel are ideal materials across engineering and thus are investigated as the metal sheets of choice in this thesis.

2.2.2 Challenges and opportunities in dissimilar joining

While dissimilar joining technology presents many promising features, there are nonetheless certain drawbacks and challenges facing the field in both industry and academia. Fusion welding dissimilar materials can lead to problems, such as porosity formation, solidification cracking, and chemical reactions. However, proper welding can be achieved by paying attention to joint design and preparation, process parameters, and filler metals [2.66–2.69].

In the field of solid-state dissimilar joining welding, Kulkarni [2.70] shown that the issues present with fusion welds are less serious than with solid-state welded joints, even though most problems found in one are also found in the other. Nonetheless, certain strengths of solid-state welds compared to fusion welds have similarities held during dissimilar material weldings, such as their porosity and distortion. Given the higher temperatures used with fusion welding, using filler material normally produces a weld material with different metallurgical characteristics, mechanical features, and physical characteristics compared to the individual materials used.

2.2.2.1 In industry

The EU Manufuture Sub-platform on Joining [2.71] has created the Strategic Research Agenda (SRA) dedicated to industrial drivers, difficulties, and possibilities for joining in a variety of sectors. Several such difficulties concern contrasting materials [2.40, 2.71, 2.72].

(1) In the automotive sector, the SRA specifies joint dissimilar/hybrid materials containing aluminium, steel, high strength steel, composites, and thermoplastics. Electric cars need weakly electrically resistive joints, while hydrogen-powered vehicles require joints suitable for high-pressure hydrogen handling.

(2) In the energy sector, the SRA points out the joining of composite metals for use in turbine blades, solar panels, and ceramics. Meanwhile, the aerospace sector requires

innovation compared to joining polymer composites, metals, and high-temperature materials.

(3) In construction and transportation, the difficulties faced involving joint dissimilar/hybrid materials relate to aluminium, steel, high strength steel, polymer fibre composites, and thermoplastics. Meanwhile, electronics and nanotechnology are concerned with circuit boards and joining processes, such as miniaturized soldering, bonding, and joining copper to aluminium and metals to polymers.

(4) In the oil and gas industry, joining steel that comes from different grades and is of distinct thicknesses, as well as composites and metals, merits innovation.

2.2.2.2 In research

As mentioned above, several research problems exist. While innovative systems are in development, much research remains necessary to produce a profound understanding of existing processes [2.73-2.75]:

(1) By increasing our understanding of basic bonding mechanisms, the required input for calibrating FEM simulations and other numerical systems will be provided.

(2) The research community must further its knowledge to better locate crucial processes, material miss-match situations, and/or failure mechanisms, as these are vital in the design phase if structural failures are to be avoided.

(3) The gap between modelling scales from the atomic to macro scale must be bridged. Moreover, one must also bridge the gap between microstructures, continuum mechanics, and process modelling.

(4) In manufacturing, sensor-based process monitoring and control, as well as automated quality inspection, are extensively employed. Moreover, future manufacturing will rely heavily on sensor data from joining processes for their cyber-physical systems. Hence, it is necessary to continue research to better utilize the ability of novel sensors to respond to the issues facing joining dissimilar materials.

2.2.3 Thermal behaviors and potential damage in fusion joining

Due to the laser riveting involves a competitive high energy input and accumulation between the dissimilar materials during this fusion joining process, which results in the thermal, mechanical impacts and potential damage in the materials, and they will be further introduced in this section.

2.2.3.1 Heat treatment for titanium

(5) Ti6Al4V is heat treated to change its microstructure, improve strength and ductility, minimize the effect of residual stresses and promote mechanical performances [2.76]. A widely applied improvement is solution treatment followed by quenching and aging to improve the mechanical performance of titanium by transforming the β grains to α acicular grains [2.77]. Another common method is annealing to obtain an equiaxed-domain grain microstructure.

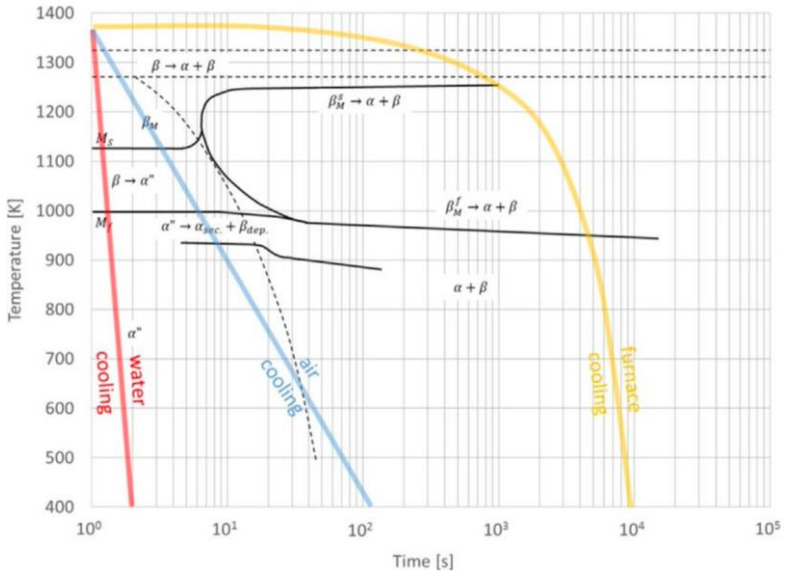

Figure 2.10 Microstructural phase transformation diagram for Ti6Al4V under different cooling conditions. [2.80].

The Ti6Al4V microstructure evolution with cooling rate is presented in Fig 2.10 [2.80]. Heat treatment including solution treatment with quenching and aging is an effective approach to obtain improved performances, optimized mechanical behaviors [2.78]. The thermal history of the solid solution treatment is consequential to obtain the desired microstructure and performances and is thus set $40 - 100℃$ below the β

transus point, aims to obtain some range of the alpha and beta phases by subsequent high cooling rate [2.79]. In addition to temperature, the cooling condition also is a significant variable affecting the microstructure formation and mechanical strength.

2.2.3.2 Laser welding for titanium to aluminium

Laser beam welding (LBW) can provide an outstanding flexibility and capability of welding and take benefits of higher heat input and accuracy in the process. This technology is receiving increasing interest in dissimilar materials joining. For Al and Ti alloys laser welding, one of the difficulties is the formation of the interfacial intermetallic compounds (IMC) which weakens the strength of joint [2.85], as shown in Fig 2.11, the IMC depends on the thermal history underwent in the welding process [2.83, 2.84].

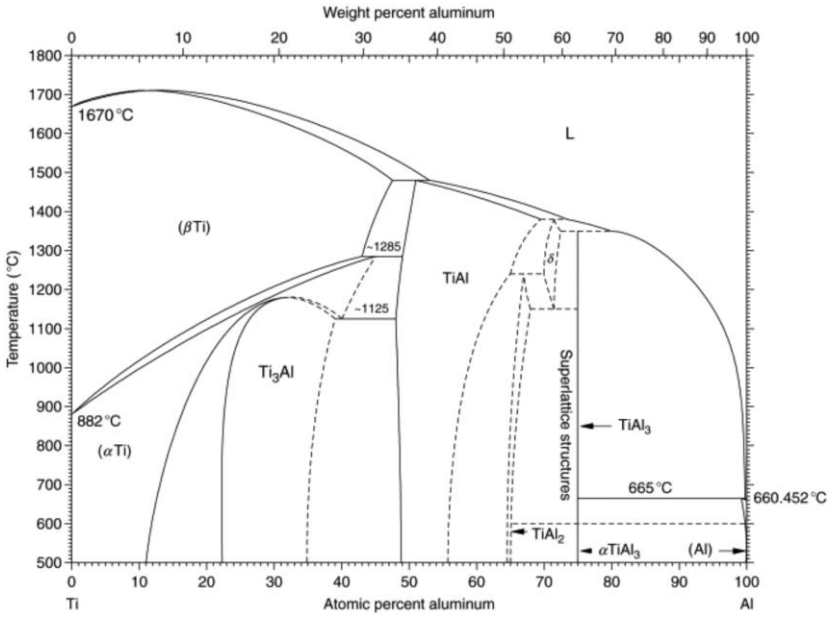

Figure 2.11 Binary titanium and aluminium phase diagram [2.82].

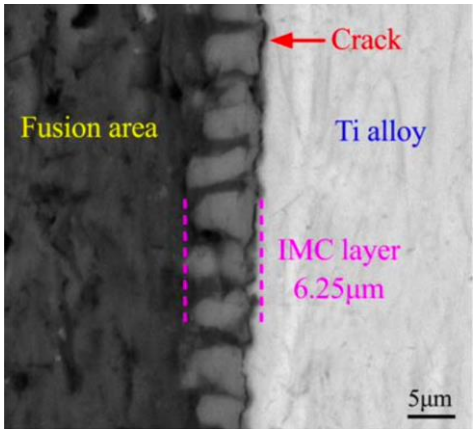

Figure 2.12 Microstructure diagram of IMC layer in Ti/Al welding- brazing butt [2.81].

Although the thermal behaviours are clearly related to non-equilibrium metallurgical phenomena, equilibrium phase diagrams of Al and Ti alloys need to be referred. The binary titanium and aluminium phase diagram is presented in Fig 2.12, it explains the phase transformation fundamentals. Near the Ti element axis, the solubility of Al is slightly decreased. The Al proportion in Ti above about 13% leads to the generation of Ti_3Al. As the Al element rises, compound such as TiAl and $TiAl_2$ are formed. Near the Al axis in the chart, the decreased solubility of Ti element results in the generation of the intermetallic phase TiAl3 in advance when the Ti element fraction above about 2%. According to thermodynamic hypotheses, the $TiAl_3$ is assumed to form in the initial step of the interaction between Ti and Al element [2.86], and this stage leads to embrittlement in the weld.

The offset LBW has an obvious effect on the interfacial IMC area scale and the strength performances of the weld. While the rise of beam offset, the area of intermetallic compound is reduced, the mechanical properties of the weld are enhanced, and the interfacial IMC phase is $TiAl_3$. With the raise of beam offset, the width of interfacial intermetallic compound is reduced, the failure of hybrid weld is easily occured at the welding area of aluminum base material [2.87].

2.2.3.3 Titanium to composite welding

As the advantages were introduced in the previous section, LBW is a proper fusion method that can be used for joining composite and titanium alloy. However, because there are great differences of the thermal behaviours between composite and titanium, a sound joint is difficult to weld for these two materials. The effects of laser travel velocity and out-of-focus on the CFRP/Ti welding were investigated in [2.87]. It was reported that the fusion joining parameters had significant influences on the strength of the weld, and from the microstructural observation in the welding area, a plenty of bubbles were formed near the interface at composite [2.88].

Recent studies systematically investigated the phenomenon and mechanism of bubble formation in offset-LBW for CFRP/titanium joining, from laser welding speed and laser defocus distance (energy intensity). [2.89] stated that laser scanning velocity significantly influence the formation of porosities, cracks near the welding area of

composite were the major defects weakening the joining strength. Due to the decomposition of composite and the resin achieved melting point, air bubbles are generated near the fusion interface.

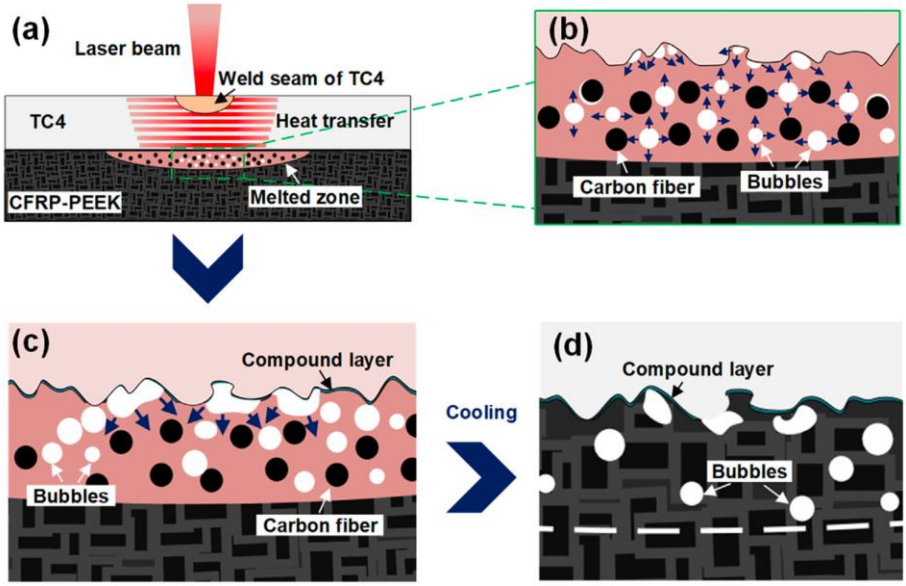

Figure 2.13. Schematic demonstration of laser welding composite to Ti6Al4V (a) Welding procedure (b) High magnification of heated area (c) Bubbles formation in joining area (d) Interface of joining area in CFRP after cooling [2.90].

In further investigated the joining mechanism for CFRP to Ti6Al4V, the schematic is presented in Fig 2.13 [2.90]. When the power beam irradiates the Ti6Al4V material, energy is transferred from the top to the joining interface, causing the resin matrix in the composite to degrade. The excessive energy accumulation of the matrix in the CFRP in the welding area leads to ablation and bubbles (Fig 2.13a). The massive heat input in the connection area results in high vaporization of the composite, leads to small scale bubbles formed near the joining area. The sizes of these small bubbles kept increasing with the energy input, as presented in Fig 2.13b. The pores formed at the joining zone contributed to the fracturing and separation of the initially surface as demonstrated in Fig 2.13c. After the temperature of sample decreased, the resin matrix is melted close to the weld area and the mixture of carbon fibers and resin is occurred in the weld near the Ti6Al4V interface, the bubbles were remained in the composite (Fig 2.13d). In the mechanical tests, because of these pores, the failure occurred at the interface between the reinforced fibres and resin matrix [2.90].

2.2.4 Research background on composite-to-metal joining

In general, composites are defined according to their characteristics, which include their low density, extreme thermo-elastic stability, high thermal conductivity, thermal shock resistance, fatigue resistance, and outstanding mechanical properties at high temperatures [2.91–2.94]. Thus, given these promising properties, composite–to-metal dissimilar joining continues to grow in popularity.

For example, aircraft manufacturers are increasingly using composite materials instead of traditional ones, such as in the Boeing 787 Dreamliner (Fig 2.14) [2.95], half of the weight of which comes from composites. The remaining weight consists of 20% aluminium, 15% titanium, 10% steel, and 5% other.

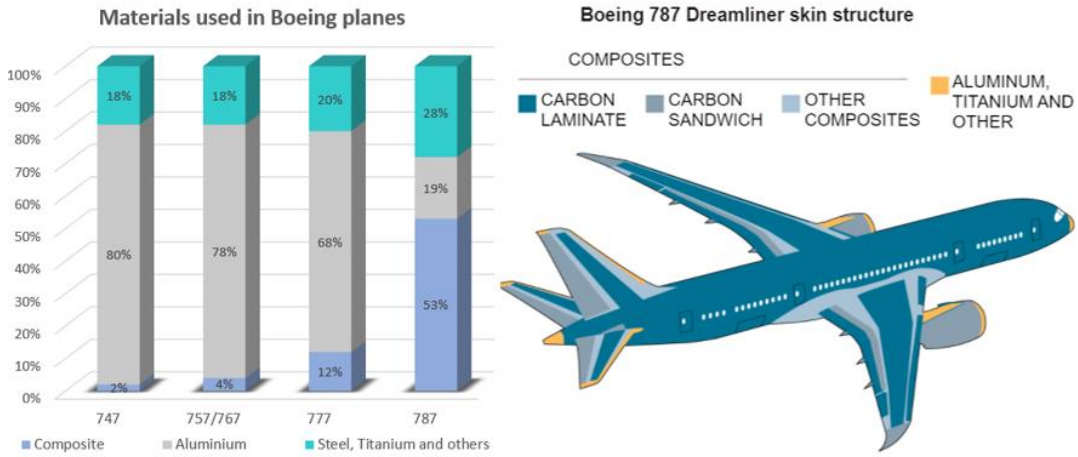

Figure 2.14 Material distribution in the Boeing 787 airframe [2.64]

Katayama et al. [2.96] carried out some of the first studies on laser joining metal-composite components, without pretreatment or laser transmission joining given that the plastic components were transparent to the laser radiation. The development of composite materials involving glass/carbon fibres and colourants led to the creation of laser conduction joining [2.97]. In this case, heat conduction ensures that heat is transmitted upwards to the joining interface [2.98].

For additional research on the fibre-reinforced polymer (FRP) and metal combination, one gentle, non-destructive joining technique that can be used for two dissimilar materials is adhesive bonding. In addition to fundamental theories relating to mechanism governance [2.104], various physical properties, such as overlap-length,

joint-end configurations, fibre-orientation, and surface preparation have been explored and their strong effect recorded [2.105]. Meanwhile, to increase the lifespan of costly hard-wearing vehicles (such as aircraft), there is currently extensive research being conducted on efficient and cost-effective repair strategies for metal and fibre-reinforced polymer structures and their bondings [2.106]. Even though the additional adhesive mass is rather small, safe load transfer requires big bonding areas compared to bolts or rivets. Another disadvantage is a spontaneous failure. By introducing ‘safety-rivets’, remedial action has been taken, thereby increasing the weight [2.103].

In composite processing industries, several issues face the design and assembly of carbon fibre-reinforced polymer (CFRP) involving the use of metal parts. According to Woizeschke [2.99], overlapping is required when joining aluminium (Al) and CFRP for typical mechanical joints (e.g. riveting or bolting [2.100]), adhesive bonding [2.101] or combined joining techniques (e.g. combined riveting and bonding [2.102]). Furthermore, fibres are interrupted by drilling for rivets and load paths subsequently decay. The fabrication (e.g. interface failures or edge defects) can cause failure. It is necessary for the structures to be reinforced in the joining area because of the locally concentrated transmission of force. Moreover, direct contact between carbon and aluminium accelerates corrosion. Hence, it would be beneficial to create a novel method for joining aluminium and CFRP structures.

2.2.5 Current joining methods for metal to composite

For the joining of thermosetting composite components with metallic components, various ideas are in use. These are adhesive bonding, mechanical fastening or both combined techniques [2.107]. As the main types of dissimilar joining for metal-to-composite, the advantages and disadvantages are as follows:

2.2.5.1 Adhesive bonding

Adhesive bonding involves the binding of two components using an appropriate adhesive. Adhesives are frequently used to join elements made of dissimilar materials in the aviation, automotive and building industries [2.108-2.111]. Joining CFRPs with aluminium alloys via adhesive bonding is certainly the most convenient method with

both clear advantages and limitations. Since adhesive bonding is an irreversible process, attempts to disassemble the joints can be expensive, which can lead to complete material damage for the joints involved. Adhesive bonding not only seals the joints but also prevents crevice and galvanic corrosion between two materials. It is possible to join almost any pair of dissimilar materials, such as metals, polymers or ceramics, with this method. Adhesive bonding is the only viable method for creating structures that join thin-walled elements of substantially dissimilar thicknesses. Adhesive bonding offers light-weighted structures compared to other assembly technologies and developments, particularly in aviation. Furthermore, stress concentration is consequently less significant when bolt holes are not necessary, which helps to avoid structure weakening [2.112, 2.113].

Moreover, adhesive bonding involves a flat, uniformly distributed and fibre friendly load introduction, while also allowing bonding between components of different thicknesses. Nonetheless, thickness is crucial in determining the overlapping length. In addition, adhesive bonding prevents galvanic corrosion and is more cost-effective for SMEs. However, the joint durability of adhesive strength and slow material degradation merit consideration. The required surface treatments and long curing time increase the time needed for production and the level of energy that is consumed. Moreover, specific attention must be given to humidity and temperature requirements [2.114]. Mechanical joint strength can be improved using sculpted metal components [2.115].

2.2.5.2 Bolting and riveting (Mechanical fasten)

Through-the-thickness reinforcement involves locking load transmission, which spreads the stress across the composite. Thanks to mechanical interlocking, higher loads can be transferred by the joint. Hence, the method is ideal for car and plane production. Here, “through-the-thickness reinforcement” is defined as the introduction of joint elements after consolidation in the cured laminate. Hole creation weakens the fusion zone, damages the fibre damage, and interrupts load transmission [2.116]. Nonetheless, it is possible to alleviate this injury through vibrational assisted drilling [2.117]. Extensive features are available for interlocking elements, such as bolts, rivets, and clinches. Another important option is small-diameter staples [2.118].

High-stress engine parts generally feature high joint strength bolts and rivets. In-plane production, composite-metal joints are often linked by titanium rivets and inserted into holes in both materials [2.119]. Bolt-joining technology is also proper because it separates the connected components by removing joint elements; thus, allowing recycling. Nonetheless, fibre damage, the yielding polymer matrix in the bolted joints and the loss of bolt clamp-up load influence joint-life strength and fatigue [2.120]. However, by embedding high strength titanium foils into the composite laminate within the fusion zone, the mechanical joint can be strengthened [2.121, 2.122]. Another alternative is a modification with double the number of plates or foam inserts [2.122], but this takes a long time to produce and is expensive for riveting and bolting composites. Hence, the use of the part determines the economic efficiency of this technique.

In summary, given the advantages and disadvantages of dissimilar joints between composites and metals in previous research, mechanical fastenings and adhesive bonding are currently the most predominantly used methods for joining composites to metals. But these joining methods still have several drawbacks, such as stress concentrations at holes, poor long-term environmental resistance, reduced strength from cut fibres, the limited availability of inspection techniques, non-uniform stress distribution and low production rates. These drawbacks prevent the adoption of more advanced multi-material joining applications and reduce the potential benefits of optimized designs.

Consequently, there is a clear need for new, flexible, cost-effective, and rapid methods for joining composites to metals, capable of meeting industry performance and manufacturing demands. Aiming to avoid the disadvantages and keep the benefits of the current application, laser riveting for dissimilar joining is developed in this paper.

2.3 Numerical simulation in laser processing

In the previous two chapters, the basic theories of laser processing and dissimilar joining methods are systematically reviewed, thereby providing the fundamental and theoretical knowledge necessary to prepare for the LMwD and LR in experimental

parts. In this thesis, laser riveting is modelled numerically to predict and calibrate the results and experimental data to further promote the experimental procedure.

Given that laser riveting is a completely novel concept in laser processing, there hardly can find the relevant simulation work. Hence, numerical modelling for laser beam profiles and laser processing, especially laser welding and additive manufacturing applications are reviewed in this section. Although such research does not directly concern laser riveting process modelling, the latest applications of another relevant modelling can be examined, thereby highlighting the main challenges facing and development of numerical simulations in laser manufacturing. Moreover, similar numerical simulations are helpful to understanding the procedures for modelling laser applications. Last but not least, these relevant laser processing models can provide high quality and efficient insights and methods.

2.3.1 Numerical modelling of the laser beam

Here, several laser beam profile models are illustrated. Although this field does not directly concern laser processing, laser beam energy distribution and beam profile are both introduced. Laser energy distribution can promote the consideration of shape, energy, and other properties in laser processing, while the keyhole welding profile can assist with understanding the focal point, beam profile and laser power density at the keyhole surface.

The principal factor that dictates temperature is laser strength and its heated element dissemination for the process modelling. In several studies, the focus is on modelling EM00 Gaussian lasing profiles [2.123–2.129] without any regard for non-Gaussian beam pumping effects [2.130]. Furthermore, pumped laser energy in solid-state lasers partially becomes the heat that subsequently serves as the laser material heat source [131, 132], thereby influencing the gain medium non-uniform temperature distribution. This distribution is determined by the gain medium configuration and cooling geometry. No useful thermal lensing effects are brought about by the pump beam non-uniform distribution or the radial heat dissipation. Hence, beam shape, quality and output constancy are all subsequently impacted [2.133, 2.134].

Thus, there are substantial differences between the laser intensity dissemination models utilized in analysis and the real Yb: YAG laser profile derived from experiments [2.135–2.137]. Furthermore, when optimal system lens focal length varies, so too do laser spot diameter and laser intensity dissemination. In laser heating process modelling, laser heat source power distribution analytical models utilize a distinct laser spot of a particular diameter. However, such models neglect the role of beam focusing distance as a technological determinant of laser intensity dissemination.

2.3.1.1 Energy distribution and Gaussian laser profile

Marcin employs the UFF100 system to examine [2.138] laser power density dissemination in the plane at right angles to the beam propagation axis (z-axis) using several measurement plane locations. Given the limitations of measuring needle resistance and the UFF100 system detector, Marcin's analysis utilizes a laser beam with a continuous power of 900 W. Measured plane position varies about the theoretical beam focal distance ($\pm\, 10\, mm$) as a result of laser head construction. In the testing planes, the beam radius exists in two perpendicular axes (w_x and w_y), which are calculated as the mean value of seven laser beam scans in the testing plane using the Prolas computer software program for the FF100 analyzer. In Table 3-1, the experimental percentage distribution of Yb: YAG laser beam power is given for several different lengths of beam focusing. In Fig. 2.15, the laser beam 3D caustic that is produced by measuring radius r (86%), is given. Here, 86% of the power distribution is observable while measuring circle radius and is created by measuring radius w_x and, in the plane x, y). This plane is defined as the dependence of the moment of the second-order power density distribution based on the PN-EN ISO 11146 standard.

Table 2-3 Percentage distribution of laser beam power for different beam focusing values

Distance from the focusing position ‘‘z’’	Power density distribution contour diagram	Power density distribution at two orthogonal axes

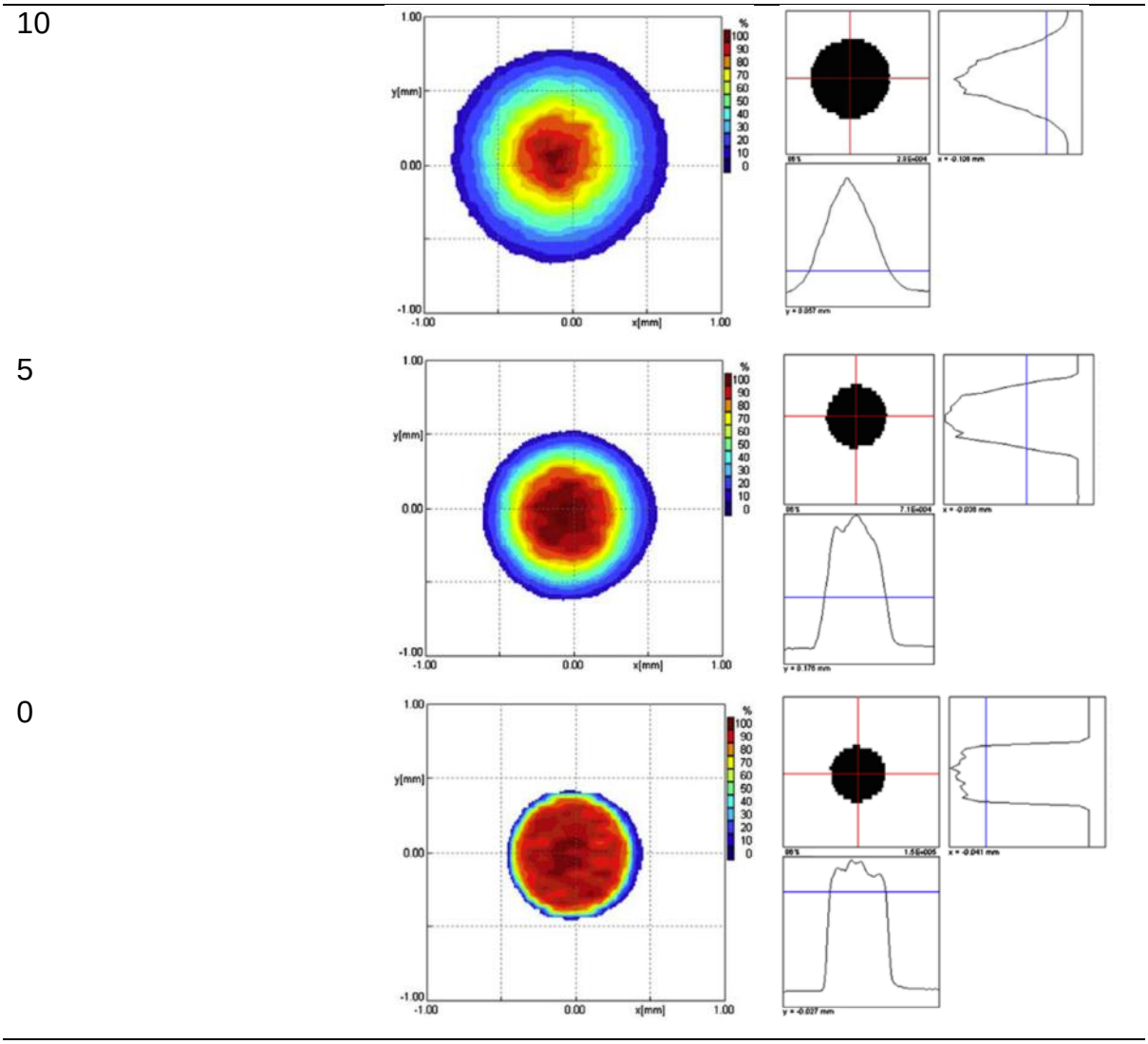

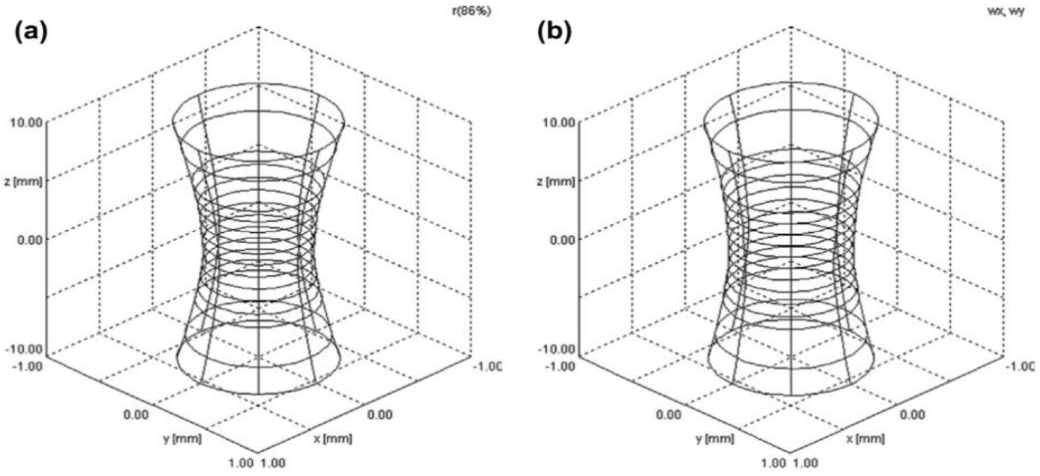

Figure 2.15 Laser beam 3D caustic derived by measuring (a) radius and (b) radiuses w_x and, based on the PN-EN ISO 11146 standard [2.138].

Hence, Table 2-3 shows that when the focusing position z = 0, countless local extremes exist in the intensity distribution which analytical laser power distribution models cannot explain.

2.3.1.2 Fibre laser beam profile in keyhole welding

The essential processing tool in deep penetration laser welding [2.139] is the focused laser beam as defined by its spot diameter and Rayleigh length. Beam profile, which is defined by the lateral power density distribution $I(x, y, z)$ along the beam propagation direction z and describes the whole tool (CW for not–polarized continuous waves), is another important but seldom examined variable. Gaussian beams retain their lateral Gauss profile along the entire focusing path z. Meanwhile, during laser beam guiding, optical step-index fibres produce a top-hat profile (the step profile which is the equidistribution of the power density). Two optical lenses then usually collimate and focus the resultant diverging top-hat profile at the fibre exit, thereby projecting the top-hat profile onto the focal plane. Then, the beam once again has a top-hat profile a priori in the focal plane while it is converted to a Gaussian profile at the optics. Thus, there is a transformation regime connecting the two.

Fig. 2.16 (a)-(b) visualizes the calculated keyhole surface (for the reference case, , $z_0 = 0\, m/min$ with a 2nd order modelled beam) from two different angles based on Kaplan's investigation [2.140]. Meanwhile, the laser beam power density distribution across the keyhole surface is positioned on the xz-plane. Here, the areas near the keyhole edge portray strongly tilted surface elements that look narrower.

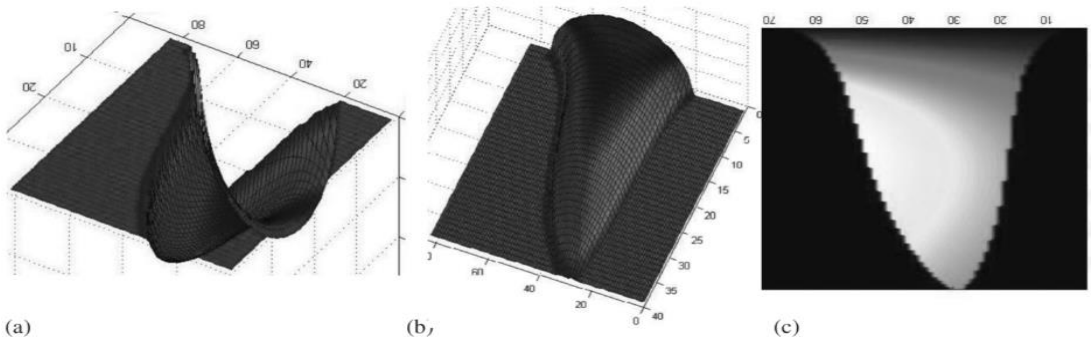

Figure 2.16 (a) Three-dimensional top view at the surface of a calculated keyhole, (b) the corresponding side view, (c) laser beam power density distribution (colour scale: from dark red 'low' to bright yellow 'high') at the keyhole surface as positioned on the xz-plane [2.140].

Moreover, the research is concluded that there is a significant difference between the realized beam profiles and the measured fibre laser beam as described through accurate second-order approximation [2.140].

2.3.2 Numerical modelling in the laser welding

In laser processing, laser welding is a particularly popular application with extensive accompanying research from several studies. Because laser welding is an important application in laser processing, its modelling is significant for laser applications as it highlights several basic rules and insights during laser processing modelling.

2.3.2.1 Modelling in laser welding

Internationally, laser welding is becoming increasingly important in micro-welding and deep welding. Like other welding processes (with fusion), local fusion and solidification produce the “welding joint” or “weld bead” through the two-piece assembly. Laser welding is based on methods for applying thermal energy to material surfaces.

Because different beam diameters can be used to apply the same energy in laser welding, indifferent spatial distributions of workpiece heat are produced, thereby creating different weld profiles. One critical parameter that determines the fusion properties and welding pattern in laser processing is beam diameter. According to Buvanashekaran et al. [2.141], the welding pattern in laser processing depends on the keyhole, conduction, and power density. Furthermore, Assuncao et al. [2.142] find that pure conduction regimes are possible in certain narrow windows based on power density and spot size. High aspect ratio weld profiles, high productivity and low distortion increase the frequency of the keyhole regime. According to Sanchez-Amaya et al. [2.143], conduction regimes allow for the production of relatively deep penetration welds with smooth beam profiles. Moreover, effort should be taken to avoid vaporization in powder bed additive manufacturing to minimize the likelihood of defects. Hence, powder fusion is preferred in conduction regimes.

With computing hardware growing increasingly efficient, numerical simulation continues to develop across the industry, including in welding and laser welding.

Moreover, the Finite Element Method (FEM) in product development continues to be increasingly used in manufacturing processes and presently forms part of the field of computational mechanics. It is possible to attribute a significant portion of such development to the industrial need to improve productivity and product quality while simultaneously enhancing cognition of the impact exerted by different process parameters. In several steel applications, such as welding, heat treatment and casting [2.145], modelled phenomena play a prominent role. The first industrial objective is concerned with designing and optimizing manufacturing processes and components. Moreover, such simulation facilitates production stage enhancement and problem resolution. Thus, several models have sought to calculate the mechanical effects of welding as residual strains and distortions. Nonetheless, manufacturers can enhance their understanding of and mastery over their processes through complete (multiphysical) simulation [2.144].

Here, two aspects of laser welding modelling are introduced. These are ray tracing and laser welding methods, with liquid and gas interface laser welding examined in detail.

2.3.2.2 Ray tracing of keyhole welding

This technique is based on a simple and frequently utilized principle [2.146–2.148]. Considering only beam geometry, the laser is discretized into “rays” with ray properties and their interaction with the vapour/liquid interface computed one after the other. According to Han et al. [2.149], there are two principal methods for calculating ray properties. These are the Direct Search Method based on the proper discriminant and the Progressive Search Method which involves surface equation and ray direction vectors. Power deposition can be subsequently calculated using the sequence of reflections properties (Fig. 2.17) provided by these two methods. While the material partially absorbs the energy (absorptivity) at each reflection, the rest is reflected elsewhere on the keyhole surface at an angle determined by the plasma refraction index [2.150]. This process terminates when the beam has been fully absorbed or the ray has left the keyhole (Fig. 2.18).

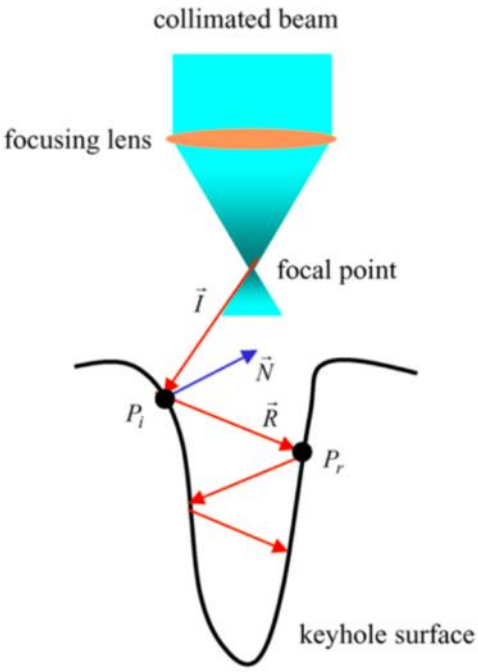

Figure 2.17 The ray tracing principal schematic based on the keyhole multiple reflection effects [2.147].

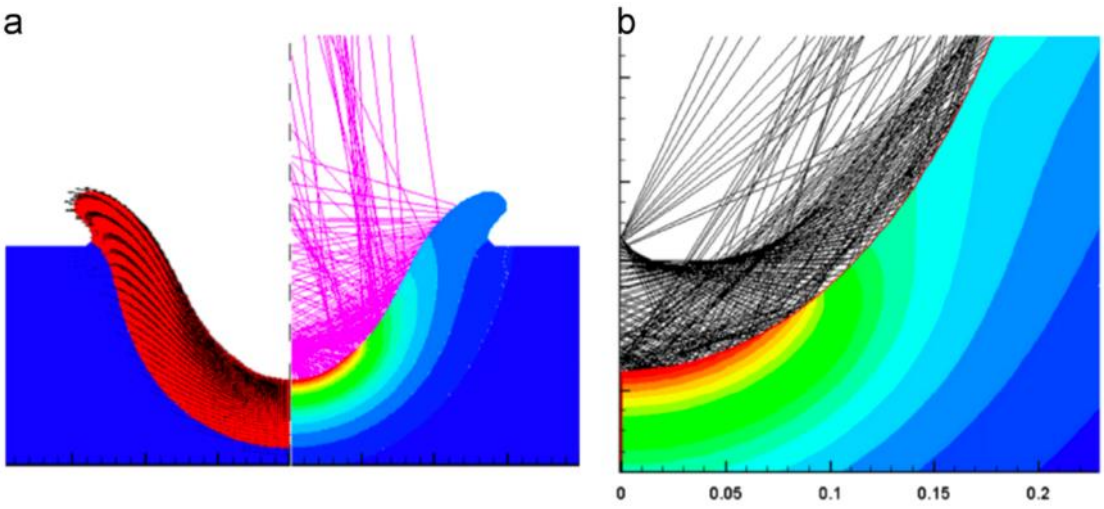

Figure 2.18 The ray tracing effect for the thermal field (a) Velocity field in liquid metal (left), reflected rays at the liquid-gas interface and thermal field (right) at t=2 ms. (b) Close-up of keyhole tip: reflected rays at the liquid-gas interface and thermal field at t = 7.5 ms [2.150].

2.3.2.3 Modelling of liquid and gas interface

In the thermal and fluid flow problems, the previous interface phenomena are added to the model as boundary conditions. Nonetheless, the liquid-gas interface can be modelled using Lagrangian methods (ALE) or Eulerian methods (VOF).

(1) Lagrangian methods (ALE)

It is possible to compute boundary node displacement physically and bulk nodes arbitrarily using the Arbitrary Lagrangian-Eulerian [2.151]. Hence, the Eulerian formula is used to calculate the solutions inside the domain while the mesh motion allows for mesh quality to be maximized.

Medal et al. [2.152] utilize ALE to simulate laser welding. Because the interface matches a system geometrical boundary, it is possible to write the sources as outlined above and apply them at the boundary.

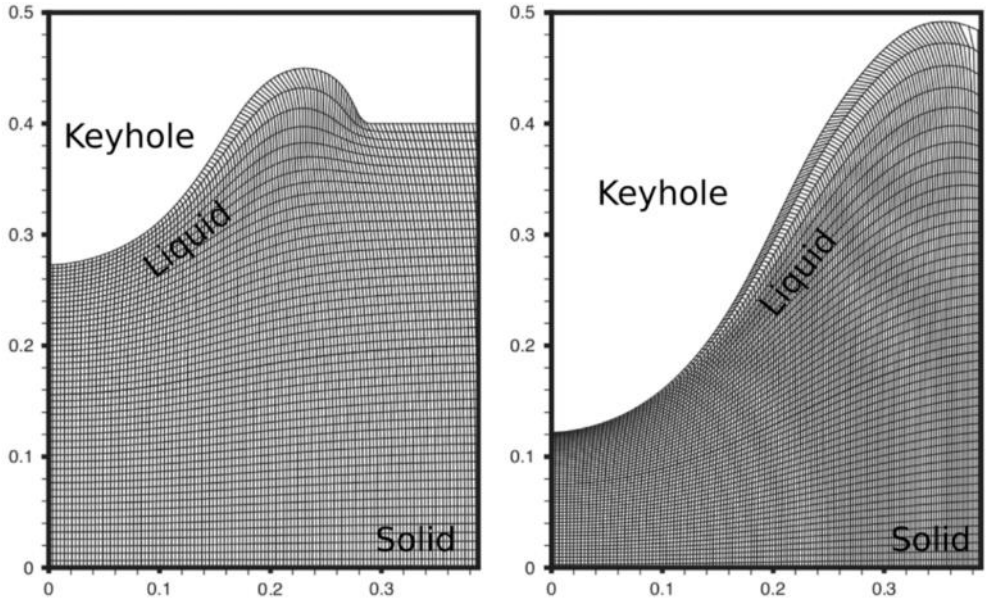

Figure 2.19 ALE mesh distortions [2.152].

In Fig 2.19, the mesh solutions following the two steps are shown. Over time, the mesh constriction can be observed at the bottom of the keyhole. In FEM, mesh quality determines the solution and interface deformation is significant. Hence, this numerical result is critical. Excessively high distortions could potentially be avoided through re-meshing, which has the benefit of being well defined at the front discontinuity. Nonetheless, it is worth noting that this technique cannot be used for “closed” frontiers (bubbles), which creates problems in laser welding simulation as porosity is a common occurrence [2.144].

(2) Eulerian methods (VOF)

The VOF method [2.153] is a free surface tracking solution more commonly linked to the finite volume method for solving partial differential equations. Here, the physical equations of the two domains (liquid and gas) must be in Eulerian formulation (fixed grid). Thus, the mesh is used for fluid flow while free boundary motion is localized and treated using the volume of fluid (VOF) method.

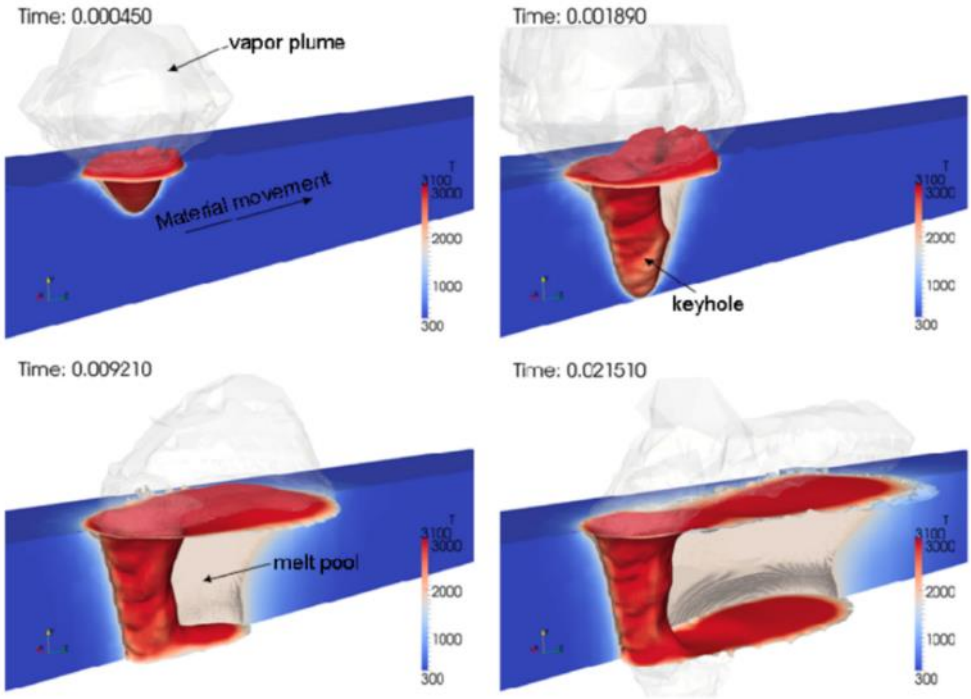

Figure 2.20 Laser welding simulation with the VOF method [2.154].

Otto et al. [2.155] have extensively employed this technique in laser welding simulation. With the finite volume discretization (Open Foam), the numerical costs of the VOF method are managed. Thus, large simulations can be carried out at a low cost (Fig 2.20).

2.3.3 Numerical modelling for the laser-wire deposition

In addition to laser beam profile and laser welding, laser additive manufacturing and metal deposition are also modelled in this thesis. Compared to laser welding modelling, these two manufacturing models focus on the material addition and melting stages in the processing, with particular attention given to phase change and thermal analysis.

2.3.3.1 FEA modelling of laser additive manufacturing

Having developed into a powerful manufacturing method, additive manufacturing allows for notable flexibility and provides new horizons that were previously impossible [2.156]. In one of the main AM techniques is direct metal is powder-based process involving the use of a laser source to melt or sinter metal powder. By creating a molten/sintered pool, the laser beam covers a powder bed. This is the first step in structural product creation [2.157].

Most available studies examine the impact of different process parameters on thermal gradients, molten pool size and their shape to characterize different DMD processes. In these studies, FEM is instrumental thanks to its ability to reduce the necessary experimental work and monitor ongoing processes.

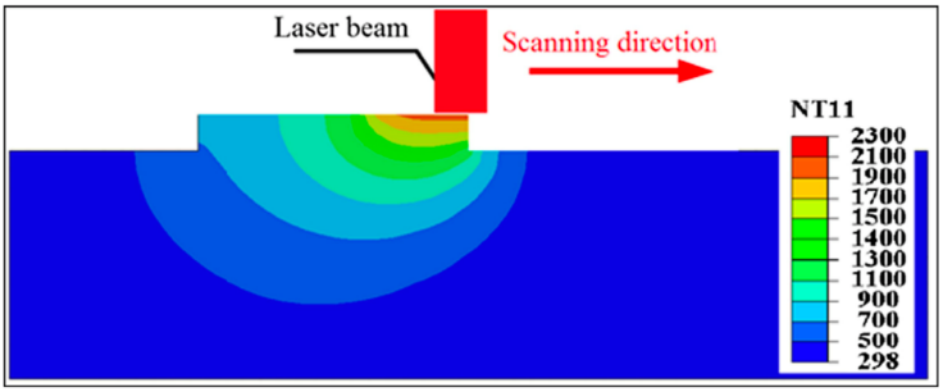

Figure 2.21 Nodal Temperature distribution in Kelvin, midway through layer deposition [2.158]

Samer builds a 3D nonlinear and sequentially coupled thermo-mechanical FE model [2.158] using the example of temperature distribution midway through first layer deposition (Fig 2.21).

More recently, in examining [2.158] the connection between scanning speed and layer deposition, Samer has two principal conclusions. Firstly, thanks to additional time available for the deposited material to absorb heat, lower laser scanning speeds increase maximum surface temperatures. With additional layer deposition, the heat accumulation from previous layers accentuates the impact. Secondly, the number of additional layers exerts a great influence on the extent to which the laser scanning speed effect impacts temperature distribution. As more layers are added, the effect

increases in its observability as the difference in deposition time for distinct velocity enhancements.

2.3.3.2 Modelling in laser metal deposition

With the laser cladding technique, alloy/coating material deposition can be achieved. Thus, strong metallurgical bonds between both materials are produced with a fine-grain pore-free microstructure and excellent mechanical properties [2.159]. Furthermore, a smaller heat-affected zone (HAZ) and lower distortions are produced by the transfer of a low thermal load to the substrate.

Extensive research has utilized 2D and 3D FEM models to calculate the steady-state and transient temperature dissemination as well as examine the impact of various factors and the way their impact varies in response to clad height and geometrical shape [2.160-2.163]. Past temperature distributions form the basis of calculating stresses and phase transformations in certain models. Moreover, select FEM models investigate cracking and base material deflection [2.162], preheating temperature and additional laser parameters [2.164]. Furthermore, with some models, the stress in single and multiple track laser cladding can be calculated [2.165, 2.167].

Currently, there are two methods that can validate the wire deposition accurately, they are volume of fluid (VOF) applied in ANSYS and the inactive elements method applied in ABAQUS respectively. They will both be introduced in the following:

(1) VOF/LS in ANSYS

In the 3D models for ANSYS, Suárez [2.167] uses residual stress models to examine clad tracks with curved geometries and the impact of multiple parameters on the maximum stresses and maximum bending angles associated with the cladded plates. Suárez calculates temperatures, strains and stresses for a single track both when there is preheating and when there is not. Furthermore, Suárez also models clad bead geometry based on experimental observations for single and overlapping tracks. By comparing sample microstructure with the melted zone and predicted HAZ (Fig 2.22), conclusive results are produced. Moreover, for the single clad tracks, the

microstructural metallographic images are compared with the theoretical temperature and phase predictions. Once again, conclusive results are produced.

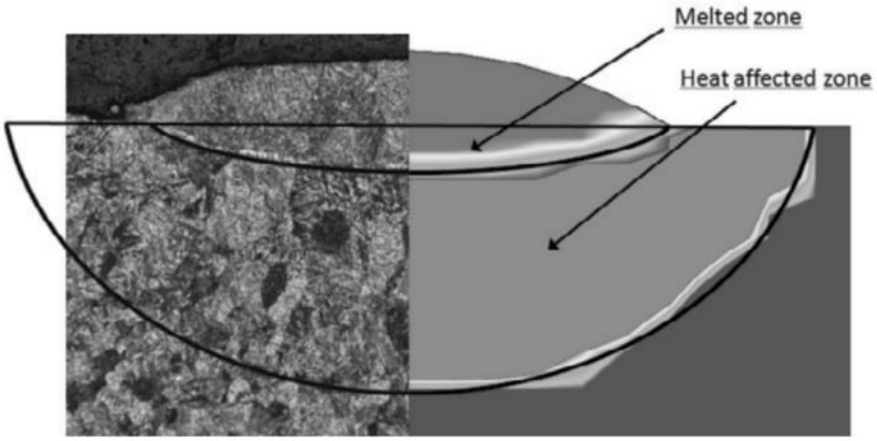

Figure 2.22 Comparing the experimental melted zone and predicted HAZ [2.166].

Unlike the previous two topics, laser additive manufacturing and metal deposition more closely resemble the specific procedures of laser riveting, especially in the wire-deposition step. Hence, it is necessary to review the numerical modelling of these two applications to prepare the laser riveting numerical modelling.

Apart from the general modelling used in laser cladding, Shaopeng Wei employs VOF and LS to simulate laser wire deposition, which are Eulerian-based interface-capturing methods (the level-set (LS) and volume of fluid methods). These models and others have been extensively employed in the simulation of multi-phase interfacial flows and free surface flows, such as the various multi-phase models [2.168]. Nonetheless, the VOF technique cannot correctly capture the flow physics at the curvature and in the direction normal to the interface as a result of the discontinuous spatial derivatives of the VOF function when close to the interface [2.169]. The LS method does not do well in terms of mass conservation because it is susceptible to numerical dissipation [2.170]. Hence, computational errors arise when solving fluid dynamics governing equations. Typical results for the liquid-gas interface simulation show poor smoothness for the discontinuous physical quantities in the VOF method and non-conservation of mass in the LS method [2.171].

Shaopeng et al. put forward a methodology that uses a coupled level-set and volume-of-fluid (CLSVOF) to measure the free surface existing between the gas phase and

the metal phase. This approach brings together the mass conservation characteristic and precise surface reconstruction abilities of the VOF and LS methods, respectively [2.172, 2.173]. Because of these properties, the thermal fluidic behaviours of the molten pool and the formation of deposition can be predicted with a high degree of accuracy. In addition, the study also set out a robust model which consists of multiple phases and accounts for a variety of factors when looking into heat transfer and free surface flow in the laser hot-wire deposition process. Such factors include the material continuum, free surface tracker, the interactions between laser materials, how materials melt and solidify, mass addition, and filter wire pre-heating. This numerical model can then be used to speculate on the geometries of the molten pool and single deposited track. The results of this process are then checked for validity by comparing them with the results derived from the laser conduction welding and laser hot-wire deposition experiments depicted in Fig 2.23.

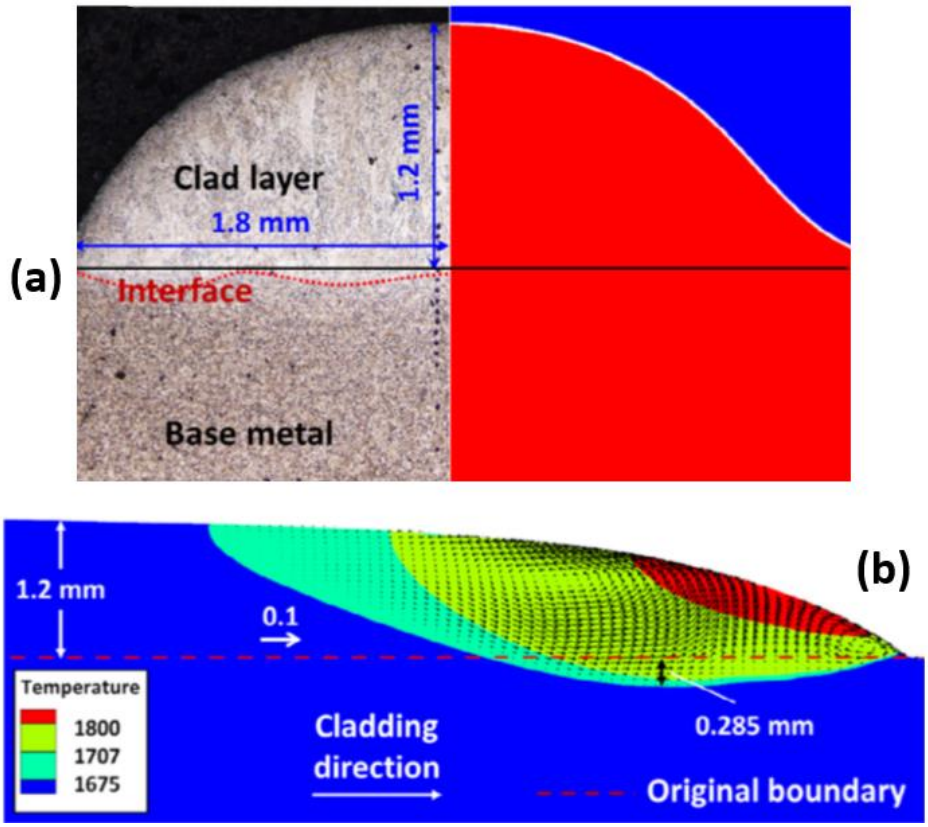

Figure 2.23 Simulation results during single-track deposition: (a) transverse cross-sectional profile of the deposited track obtained from optical microscopy and simulation; and (b) temperature distribution and fluid flow pattern along the cladding direction [2.168].

Due to specific material plastic physical properties, experimental conditions and environments are calculated in the VOF models, the results can exhibit the modelling

prediction of physical phase changes and thermal gradient near the welding area. However, limited by the strict requirements of boundary conditions, it is difficult to simulate the complicated experimental processes like multiple layers deposition in LMwcD, rivet depositing and reforming in LR experiments. Moreover, limited by the inherent calculation functions of the Ansys Fluent software, the mechanical behaviours cannot be analyzed in VOF and LS models, which still need the other numerical tools like Ansys Workbench or Abaqus to do stress analysis.

(2) Inactive elements in ABAQUS

ABAQUS is a reliable finite element analysis (FEA) software, and inactive elements are the most common method to simulate the filler welding and additive manufacturing simulation in ABAQUS, it can control the active and inactive of the single element to simulate the process of the material addition in wire deposition.

In 2016, Zhenguo et al. [2.174] developed a wire deposition modelling method through inactive elements in ABAQUS. They create and execute an LMD experiment, during which they measure temperature variation and substrate distortion using thermocouples. Moreover, they create a thermal-mechanical FEA model of the laser hot wire deposition process, Fig. 2.24 and 2.25 show the process flow and numerical results of the LMD experiment respectively.

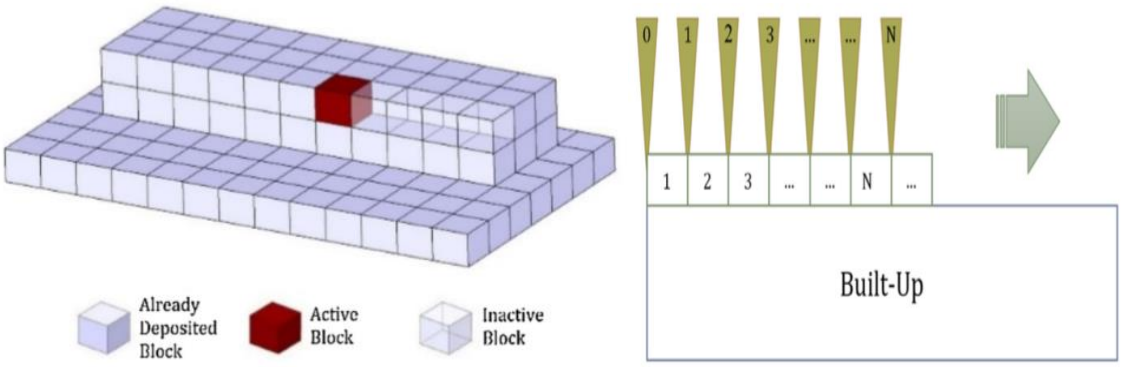

Figure 2.24 Inactive elements method in ABAQUS [2.174]

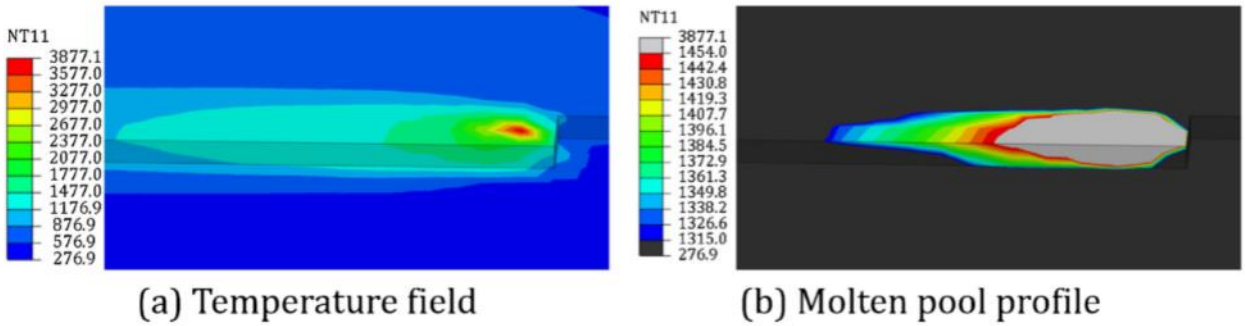

Figure 2.25 Inactive elements modelling for the profile of laser spot [2.174].

As a result, it is possible to calculate and predict the temperature, stress and strain fields and distortion. Then, the experimental results are used to evaluate simulation accuracy, which shows an acceptable agreement.

Although the previous research simulates the straight-line path LMD, the model creation, mass and heat input steps were roughly provided, just as the LMwcD is based on existing LMD experiments, thus the LMD model with inactive element method should be suited to apply into further LMwcD and LR model developments in this study.

2.4 Summary

- In AM, laser metal wire deposition is potentially the most suitable technique to be transferred to laser riveting applications. Theoretically, it can offer proper process flexibility, robustness, and process control and the deposited feature can reach a desired morphological and metallurgical performances to satisfy the joining quality.

- Currently, several joining technologies were applied for hybrid material structures, such as welding, mechanical fastening and adhesive joining, but they still have their own limitations like surface pretreatment, stress concentration and environmental requirements. The developed laser riveting applications can fill the existed gaps among current techniques in specific conditions.

- Currently, two main methods of FEA modelling are suitable for simulating the LMwD process: VOF for multiphysics simulation in ANSYS Fluent and Inactive elements for additive manufacturing in ABAQUS but considering the complex mass and heat input situation in LMwcD and LR experiments, inactive elements method in ABAQUS is the more suitable methodology as the numerical simulation approach for this research.

Chapter remarks for research

The literature review chapter has prepared the fundamental knowledge and references for the following experimental and numerical work:

- The laser system components and its materials processing mechanism were demonstrated, LMwD was selected as the fundamental methodology for rivet deposition, section 2.1 supports the principal guidance for the following LMwcD experiments in Chapters 4 and 5.
- The background of current dissimilar joining techniques and hybrid structures were introduced in 2.2, and their applications, advantages and challenges under different working conditions were explained, based on these, the technical gaps were identified and the LR concept was proposed to fill them with benefits offered.
- The literature of the current laser source with its welding and deposition modelling were reviewed, the inactive elements method was chosen as a preferable method for rivet building simulation in Chapter 8 LMwcD and Chapter 9 LR numerical model development.

Chapter 3 Experimental preparations

In this chapter, the experimental preparations of this study are illustrated. At first, the LMwD system and laser processing parameters are introduced, then the main set-up for the whole laser processing system and each specific device are introduced in 3.1. Next, material selection is explained, given their excellence in the industry and research, Ti6A4V and AA6061 alloys are selected as the experimental metals and a carbon-fibre-reinforce-polymer (CFRP) is chosen as the composite material. Moreover, the chemical composition, as well as the mechanical and thermophysical properties of these materials are introduced in 3.2. In the final part of this section, after introducing the equipment and materials, the approach of this thesis is illustrated together with considerations on laser processing parameters. For the experimental approach, the design of the experiment (DOE) is established in 3.3, and further sample preparation and evaluation methods in the following experiments are introduced in detail in 3.4 and 3.5.

3.1 Laser processing system and experimental parameters

3.1.1 LMwD processing system

The whole laser processing system is according to the standard LMwD experiments and consists of the following devices: the laser generator, delivery fibre, processing head, wire-feed device, motion unit and auxiliary. The laser processing machine is the 4-AXIS Ytterbium fibre laser system (Model: YLS-1000, IPG Photonics Corporation, USA) with 600W maximum power and the wavelength is 1.07 μm. The laser processing system is shown in Fig 3.1 (a).

For the optical setup, the laser processing head (Fig. 3.1 (b)) consists of a 200mm focus and 100mm collimator lens, and a real-time camera is mounted inside the head, the head detail was listed in Table 3-1.

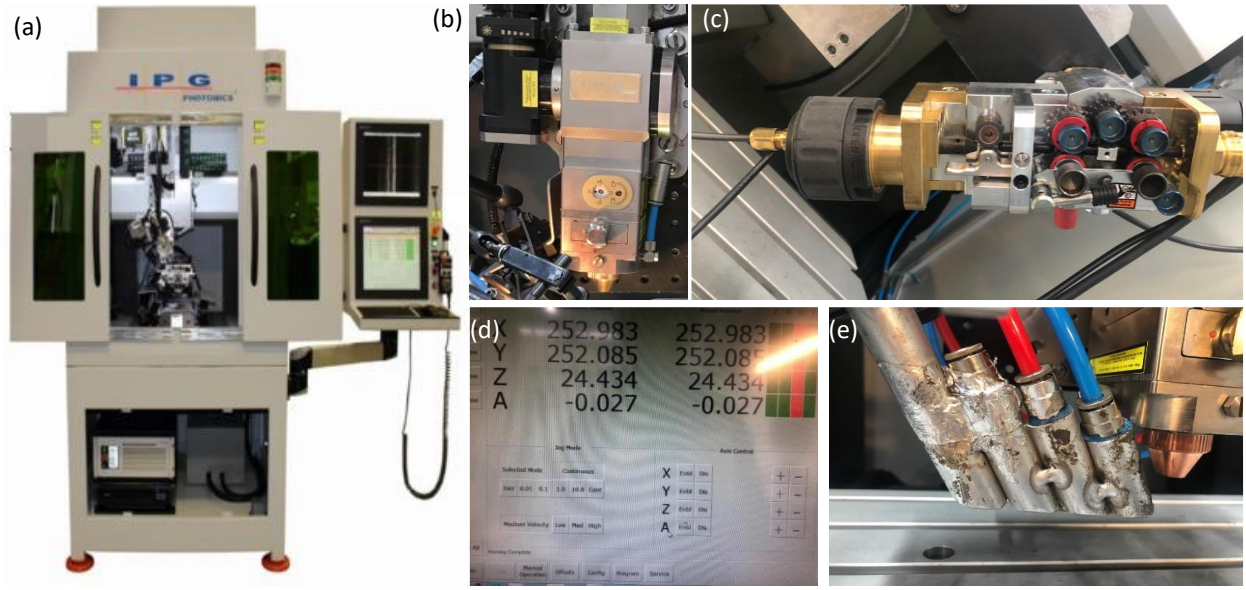

Figure 3.1 The laser processing system setup of (a) platform overview, (b) laser processing head, (c) wire feeder driven unit, (d) CNC control interface, and (e) shielding pipe.

Table 3-1 Detail description of the processing head.

Number	Item	Description
1	Focused Beam	Visible or invisible laser radiation is emitted from this orifice.
2	Lens	200 mm focus length and 100 mm collimator
3	QBH Connector	QBH style connector with optical interlock.
4	Vision System	CCD camera mounted with adjustable focus.

The wire feeding device consists of three main parts: the wire driving unit, the linear stages for wire tip position adjustment and the wire feed tube (with adjustable angle and stands off distance. The wire feeding device is shown in Fig 3-1(c).

The motion unit is made up of elements that produce the relative motion between the laser beam and the workpiece. In this work, a 3 linear axis Computer Numerical Control (CNC) system was adopted. The motion unit is shown in Fig 3.1(d) and specific motion directions are explained in Table 3-2.

Table 3-2 Detail components and functions of the motion unite.

Number	Item	Description
1	Granite Base	

2	Y-Stage	Moves the tooling table in the Y direction with respect to the laser head.
3	X-Stage	Moves laser head in the X direction with respect to the tooling table.
5	Z-Stage	Moves laser head in the vertical direction with respect to the tooling table.

In terms of auxiliary elements, there are two types of equipment in this thesis experiment: the trailing shielding device and the clamping devices. Fig 3.1(e) shows the shielding device in this experiment, the trailing shielding device produces the shielding gas for the processing surface, it protects the weld pool from contamination, while the clamping system ensures the workpiece remains fixed.

3.1.2 LMwD experimental processing parameters

The parameters influence all thermal behaviours of heating and cooling, melting and solidification in the LMwD process, those significantly affect results in geometrical, microstructural, and mechanical properties of depositions built in LMwcD and LR experiments. The main processing parameters are briefly introduced in this section and their influences on the results will be further analysed, discussed, and summarised in detail in following experimental chapters.

Laser power: the laser power directly decides the energy input, previous research state that laser power has significant effects on material deposition efficiency, and strong interactions with laser travel speed and the material input rate [4,22]. Moreover, energy input presets a direct effect on the grain size and the phase structure - higher heat accumulation results in coarser grains and microstructures [36,48]. In this research, the laser power range is controlled in 0-1000W.

Laser beam diameter /defocus distance: the laser beam diameter is determined by defocus distance from focus point, along with an increase of beam diameter or an increase of defocus distance causes generally an increase in power density. And it needs to be considered for a proper range to satisfy the melting conditions for the specific wire feeding rate in the LMwD experiment.

Laser travel speed: it determines the heat input from irradiation time and area scale, for material interaction processing, higher laser travel speed causes generally an increase in solidification and cooling rate [21,23]. In this thesis, the travel speed classified to the deposition travel speed and laser wash path scanning speed, both stand for the laser processing speed.

Wire feed speed: it determines the mass input in the deposition step in the LMwcD experiments, as known as deposition rate. Generally, increase wire feed speed with higher deposition rate will cause more energy consumption, which reduces the heat accumulation in the fusion process. In the feasibility studies of the research, the wire feed speed needs to be tested and adjusted to a proper range for a stable wire transfer condition and laser wire deposition processing.

Layer height adjustment: layer height needs to be adjusted in the layer-based additive method of LMwD, to achieve a smooth wire transfer condition and deposition, the value under or over the process window will cause the processing failures, detail of its influence will be explained in the 4.3.3.

3.2 Material properties

In this work, Ti6A4V Titanium and AA6061 Aluminium are selected as metallic materials. Meanwhile, for the composite sheet, a CFRP is selected as the experimental material. All materials were selected as a result of their proven performance in the transport sector. Each material, its benefits and its properties are outlined below:

(1) Ti6Al4V Titanium

In recent years, sheets of Ti6Al4V have been used in space laboratory chambers, air inlets and fuel tanks, while titanium capsules that contain the Iodine-125 radioisotope have been used for cancer radiotherapy [3.3, 3.4]. In general, because these sheets are only a few hundred microns thick, micro-welding technology is required to fabricate these components [3.5].

According to the advantages mentioned above, in this experiment, Ti6A4V is selected as a metal substrate and wire material. Moreover, the chemical composition, as well as the mechanical and thermo-physical properties of Ti6A4V are listed in Tables 3-3, 3-4 and 3-5.

Table 3-3 Chemical composition of the as-received Ti6Al4V Titanium (weight %).

Ti	Al	H	Fe	O	N	C	V	W	Other
Balance	6.10	0.01	0.05	0.20	0.05	0.10	4.00	0.30	0.40

Table 3-4 Mechanical properties of the as-received Ti6Al4V Titanium: Ultimate tensile strength (UTS), yield stress (YS), Young's modulus (E), elongation to fracture % (A %) and Vickers microhardness (HV).

UTS (MPa)	YS (MPa)	E (GPa)	A %	HV
950	880	114	14	349

Table 3-5 Thermo-physical properties of the as-received Ti6Al4V Titanium: Thermal conductivity (K), melting temperature (℃) and density (kg/m^3).

K(W/(m.k))	T_m(℃)	$\rho(kg/m^3)$
6.7	1650	4430

(2) AA6061 Aluminium

Recent interest has been expressed in the use of lightweight materials, especially aluminium alloys, due to a growing desire to reduce weight across the industry [3.6, 3.7]. Because of their low density and high strength among other features, aluminium alloys have long been used in structural engineering applications [3.8]. AA6061 has medium strength, high corrosion resistance, excellent ductile properties and a relatively low cost [3.9, 3.10]. Moreover, there is an outstanding property of aluminium alloys in this laser riveting experiments is that the high reflectivity interacts with the laser beam, which prevents the high heat accumulation around the hole, the detail will be discussed in Chapter 6.

According to the advantages mentioned above, AA6061 is selected as an upper sheet. Moreover, the chemical composition, as well as the mechanical and thermos-physical properties of AA6061 are listed in Tables 3-6, 3-7 and 3-8 [3.11].

Table 3-6 Chemical composition of the as-received AA6061 Aluminium (weight %).

Al	Cr	Cu	Fe	Mg	Mn	Si	Ti	Zn
Balance	0.03	0.03	0.31	0.84	0.04	0.57	0.03	0.10

Table 3-7 Mechanical properties of the as-received AA6061 Aluminium.

UTS (MPa)	YS (MPa)	E (GPa)	A %	HV
241	214	68.9	12	80

Table 3-8 Thermo-physical properties of the as-received AA6061 Aluminium.

K(W/(m.k))	$T_m(℃)$	$\rho(kg/m^3)$
200	616-654	2700

(3) CFRP Composite

Given the enhanced attention given to reducing energy consumption and pollutant emissions in recent decades, there has been a greater demand for lightweight materials used in structural applications, especially in aviation and automotive industries. CFRP composites are an ideal choice compared to traditional metallic alloys as they are strong, stiff and not too dense [3.12, 3.13]. CFRPs are frequently utilized in main load-bearing parts, such as in wings and fuselages found in civil or military aircraft, as CFPR are light yet strong. As a result of fatigue and impact damage, CFRP laminates often fail over time, with common issues including interlayer delamination, matrix cracking, fiber degumming and fractures [3.14-3.16]. The resin matrix of the as-received CFRP sheet is bisphenol-based epoxy, the orientation of the fibres is quasi-Isotropic, the melting points of carbon fibre and epoxy are 3650℃ and 160℃, the CFRP sheet density is 1152 kg/m^3 and its mechanical properties are listed in Table 3-9.

Table 3-9 mechanical properties of as-received CFRP sheets.

	Monolayer (0°±45°)	Monolayer (0°±90°)
Tensile strength (MPa)	557	503
Elongation at break (%)	3.13	2.27
Youngs modulus gloss side in compression (GPa)	32.4	
Youngs modulus gloss side in tension (GPa)	31.8	
Tensile modulus (GPa)	32.3	37.2

3.3 Sample preparation

Correct procedures must be employed to investigate the quality of the weld. If incorrect preparation techniques are used the results could be varied with erroneous conclusions drawn [3.17, 3.18]. The sample preparation procedure can be divided into the following stages:

Sectioning. A conveniently sized and representative specimen is removed from the sample once a preliminary analysis has determined a suitable cutting method, device, material, and coolant.

Mounting. Handling during the preparation and examination of samples is facilitated by enclosing the sectioned specimens in a plastic substance to provide size and shape. Thus, not only are sharp edges and coners eliminated but safety and ease of handling are also increased. The most commonly used mounting materials are phenolic and acrylic resins [3.19].

Polishing. Here, the particles are suspended in a liquid among fibres. Polishing creates mirror-like surfaces. One type of polishing, electrolytic polishing, eliminates all traces of the worked metal. At the anode, the sample is configured, and the material is removed through controlled dissolution.

Electrochemical etching. The specimens are soaked in an acid solution. During electrochemical etching, reduction and oxidation reactions occur, which typically

causes the metal to become ionized through the shedding of electrons. Elements with different electrochemical potentials are attacked at varying rates; thereby producing differential etching and chromatic contrast. Etching reactions are also influenced by irregularities in the crystal and non-homogeneity since they influence the resistance. In this case, the etching agent composition consists of 33.3% nitric acid and 11.1% hydrofluoric acid.

3.4 Experimental observations and analyses

(1) Microstructural analysis

After the sample preparation, the cross-section of samples was observed by OM and SEM for microstructural and chemical analysis, following are the detail of the analysis experimental equipment and parameter set.

Optical microscopy (OM): the analysis was took place on the light optical microscopy and photographed where photographs were taken the picture in the magnification range from 25 to 500 times, which is mainly used to observe the basic grain structure and find out the major or minor defects of the sample.

Scanning electron microscopy (SEM): the basic SEM analysis were conducted by LEO 1455VP and Zeiss Supra 35VP, which can photograph the microstructure image up to 20,000 times magnification, with a high-resolution result on a wide range of the sample location. In addition, it also can observe the sample surface from the stereo-views, therefore it is normally used for the detailed analysis of grain size, microstructure and the failure surface analysis.

SEM-EDS: Performed in conjunction with SEM of LEO 1455VP and Zeiss Supra 35VP, the energy dispersive spectroscopy (EDS) can capture elemental detail of the sample composition on the target surface. The desired elements can be qualitative analyzed by specific spot, line and area scan to obtain the composition atomic numbers and percentage.

SEM-EBSD: electron backscatter diffraction (EBSD) analysis, is used to perform quantitative microstructural analysis in the Zeiss Supra 35VP SEM. The technique can obtain microstructural detail of the structure, grain orientation, phase, or strain in the samples.

(2) Mechanical testing

The mechanical strength of depositions and rivets were measured by the micro-hardness and sample shear tests, to test the mechanical properties from the micro and macro aspects respectively.

Micro-hardness test: the Vickers hardness tests were conducted by Zwick Roell/ZHV in the following experiment, which can provide the hardness information of the specific location inside the deposition from its cross-section sample then reveal the relationship with the manufacturing process. The hardness measurements were carried out in accordance with the PN-EN ISO 6507-1:2018, the unit of hardness given by the tests is the Vickers Pyramid Number (HV), the diagonal of indentation is 10μm and load applied is 0.1kg.

Shear test: because shear strength is the most significant quality value for the rivet mechanical properties, the shear tests in chapters 6 and 7 for Ti6Al4V/AA6061 and Ti6Al4V/CFRP joints were carried out by Instron 8801, and the shear tests were carried out in accordance with the ISO 14273:2016 standard. All the rivets were located in the centre of square joining area and samples were fitted in the grip clamp with the supplementary shim. After the test, a load-displacement curve was plotted to demonstrate the shear strength of the joint.

3.5 Chapter remarks for research

According to the knowledge and guidance from the literature review in Chapter 2, this experimental preparation chapter developed the LMwcD processing system setup, the chemical composition, thermal and mechanical properties of materials (Ti6Al4V, AA6061) used in experimental Chapters 4-7 were listed in detail.

The sample preparation procedures and standards for the depositions and joints in the following experimental were demonstrated as well, and details of their microstructural and mechanical analyses were introduced and explained, which will be applied to the quality evaluations of LMwcD depositions and LR joints in the following experiments.

Chapter 4 Experimental feasibility study on the Ti6Al4V cylindrical deposition by LMwcD

In the previous three chapters, the fundamental preparation works of industrial interest in the background, the current technical supports and gaps, and the experimental processing system setup were introduced and demonstrated, which provide an overall project direction and knowledge base for the thesis. In Chapter 1, the laser riveting concept and its motivation concluded that high productivity with a sound weld quality is required in the LR applications. In Chapter 2, the literature review found that among the different additive manufacturing methods, for rivet building in this project, the laser metal wire deposition (LMwD) is the most appropriate method to fit the required conditions and goals.

However, as discussed in 2.1.6, most of the current research studied the thin wall depositions with straight-line paths, there have very few literature records about cylindrical deposition built by circular path on a minor scale. Therefore, in this chapter, to initially deposit a cylindrical rivet on the substrate for applying into the future riveting concept, as the preliminary experiment of the project, the feasibility study of laser metal wire cylindrical deposition (LMwcD) in a minor scale was conducted. In this experiment, the flow chart is shown in Fig. 4.1, 2 different deposition path strategies were designed, then the capabilities and weld qualities of their single and multi-layer deposition were evaluated from the morphological and microstructural analysis. Moreover, to further understand the LMwcD process, improve the controllability and provide the basic information for future optimization study in the next chapter, the processing factor influences, and the occurred failure modes were presented and discussed in the end.

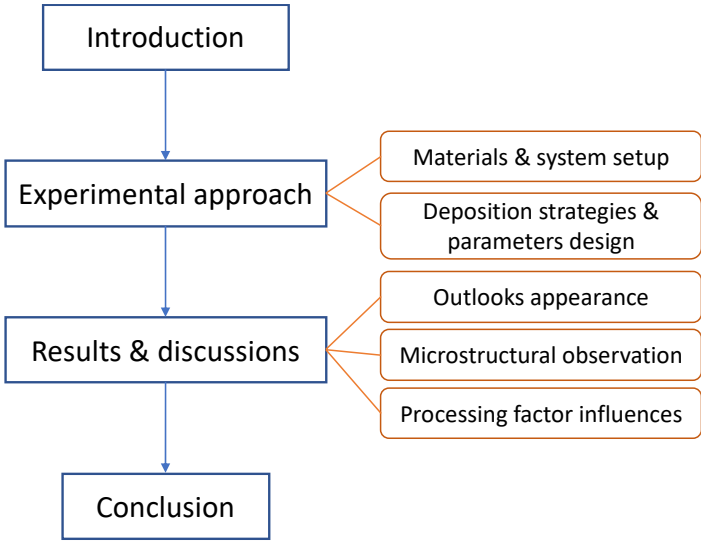

Figure 4.1 Chapter flow chart of LMwcD feasibility study.

4.1. Introduction

For LMWD approaches, specific layering is used by feeding a wire through a workpiece nozzle. Like powder injection approaches, inert gas shields the material during the molten state. Moreover, the surface area with powder-based processes is less than with LMWD, which increases the risk of atmospheric gases reacting. Hence, working in a closed chamber of inert gas is not required, thereby increasing the freedom available to wire-based applications [4.1]. Furthermore, because AM uses wire-feeding systems, the material is more efficiently used [4.2], deposited structure surface quality is improved [4.3] and the deposition rate is higher [4.4] compared to powder-feeding systems.

However, limited by the issues of properties and repeatability, in the aerospace industry, Ti6Al4V components are difficult to generate by the LPD method. It is mainly because of the high contamination risk during the LPD processing, for the Ti6Al4V material, it will significantly influence the mechanical properties of components [4.5]. Therefore, from this view, wire-based laser deposition is a proper approach to fabricate the Ti6Al4V component in AM.

However, there are still has some limitations and blank areas in the LMwD research currently, most of the manufacturing systems are equipped with the lateral wire feeder, which leads to the angle issue in the wire deposition [4.6]. For this reason, although

Demir (2018) mentioned and has built steel thin-wall structures such as cylinder and cone (8mm-35mm) [4.7] and some findings of curves path in the major diameters [4.8], there still has very limited research on the minor scale for the curve track deposition for currently.

Therefore, this chapter aims to investigate the capability of the laser wire deposition applied with different circular track strategies in the minor-scale (1-3mm radius), both in the first layer and multi-layers deposition. Two path strategies are designed, and their performing experiments are conducted, then geometrical appearance and microstructure of results are presented and compared. Moreover, failure modes are analyzed through parametric control and processing observation during the experimental procedures.

4.2. Experimental approach

4.2.1 Materials

The materials of wire and substrate both are Ti-6Al-4V titanium alloy, the micro-scale wire diameter is 0.8mm, and the dimension of the substrate is $252mm \times 101mm \times 14mm$. Before the test, the substrate is polished and cleaned in the preparation procedure. The as-received titanium properties were introduced in 3.3.

4.2.2 Laser-wire deposition system

In the LMwcD experiment, the whole laser processing system is shown in the 4.2 consists of the following devices: the laser source, delivery fibre, processing head, wire-feed device, motion unit and auxiliary. The laser processing machine is the 4-AXIS Ytterbium fibre laser system (Model: YLS-1000, IPG Photonics Corporation, USA), the energy source is a single-mode continuous wave (CW) laser with 600W maximum power, focus distance is 200mm and the working distance is at 220mm, thus the defocused laser spot was applied in this experiment, the laser head was set with 5° angle difference with vertical axis to avoid reflective damage.

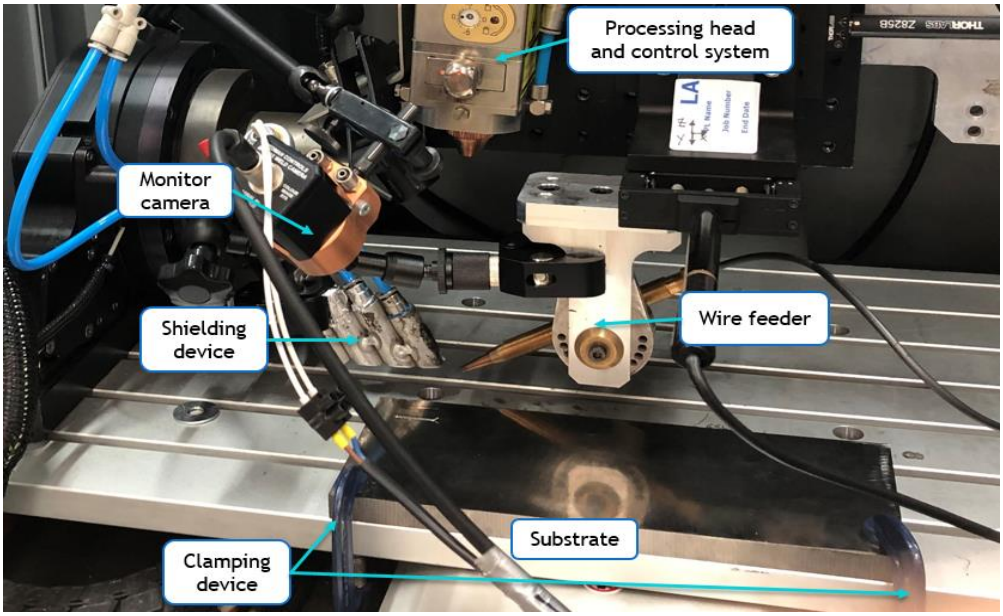

Figure 4.2 Overview of the laser metal wire deposition processing system

As introduced in the 3.1. in this experiment, faction of each component is explained below: (1) Wire feeding device consists of three main parts: the wire feed driving unit, the linear stages for wire tip position adjustment and the wire feed tube with adjustable angle and stands off distance. (2) The motion unit is made up of elements that produce the relative motion between the laser beam and the workpiece. In this work, a 3 linear axis Computer Numerical Control (CNC) system was adopted, so technically, it can process the predefined linear or curved 2D route on the substrate. (3) In terms of auxiliary elements, there are two devices in this experiment: the trailing shielding device and the clamping system. The trailing shielding device delivers the shielding gas for the processing surface, it protects the weld pool from contamination and oxidation for titanium material, while the clamping system ensures the workpiece is fixed, avoiding the influence of distortion. The schematic of the LWD process in this work shown in Fig. 4.3. And all fixed parameters of this system are listed in Table 4-1. For the microstructural observation, the cross-section and higher magnification images were taken with an optical microscope (OM, Leica DMR).

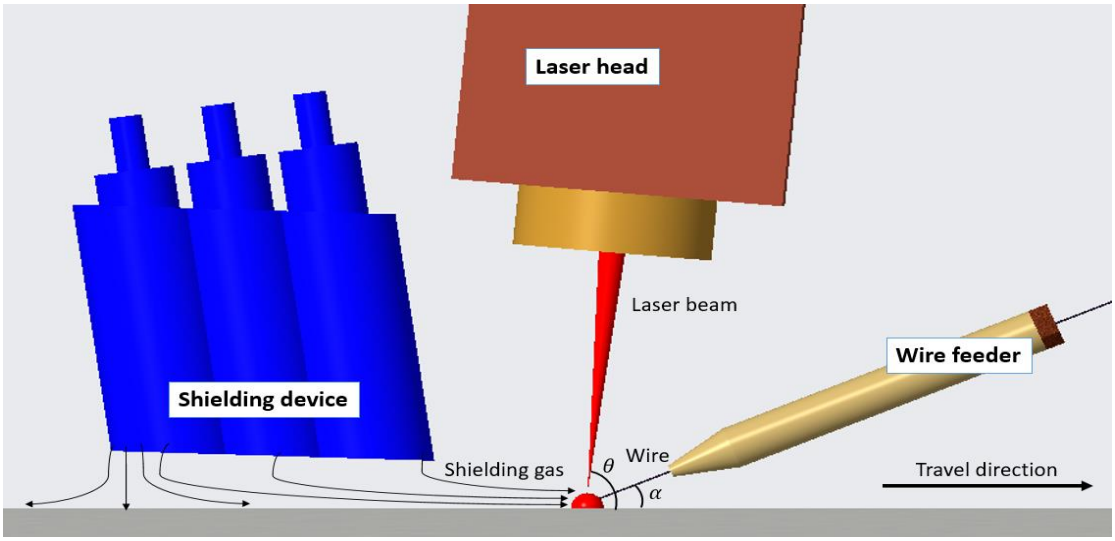

Figure 4.3 The schematic of LWD processing.

Table 4-1 Fixed parameters of the LWD system.

Fixed parameters	Level
Spot diameter, $ds\ (mm)$	1.4
Wire diameter, $dw\ (mm)$	0.8
Laser incident angle, $\theta(°)$	85
Wire feeding angle, $\alpha(°)$	30
Wire feeding direction	Front
Shielding gas	Argon
Shielding gas flow rate	25L/min

4.2.3 Experimental path strategies and processing parameters design

In this work, two different shapes have been initially designed, which are the cylindrical one and the mushroom-like one. In both cases, because of the limited deposition rate and the thickness limitation of the upper sheet for LR application, one single layer of material is not sufficient to build a cylinder with enough height. Thus, each cylinder was manufactured by depositing a certain number of layers onto the substrate. Two different path strategies were adopted for depositing the material in each layer: the 3-arcs and full circular path strategies.

(1) 3-arc path

In this design, shown in Fig 4.4 (a) below, the processing path is made up of 3 arcs, defined by the radius R and the distance D. The process starts at point A, at which the laser beam is switched on, and the wire starts feeding. During the process the wire is fed into the weld pool, ensuring a smooth deposition driven by surface tension. The wire is fed until location D, at where it is retracted, and the laser beam is kept switching on. The reason why the wire is retracted before completing the overall circle is the wire can easily get stuck in the solid substrate when it is fed at the rear edge of the weld pool. In fact, from point A to C, the wire is fed at the leading edge of the weld pool.

The main advantage of the 3 arcs strategy, compared to the latter full circular one, is the flexibility. The geometric configuration of the path can be shaped to build different shapes of cylinders, particular reform the mushroom-like cap in the last layers deposition, according to the applications and interlock requirements.

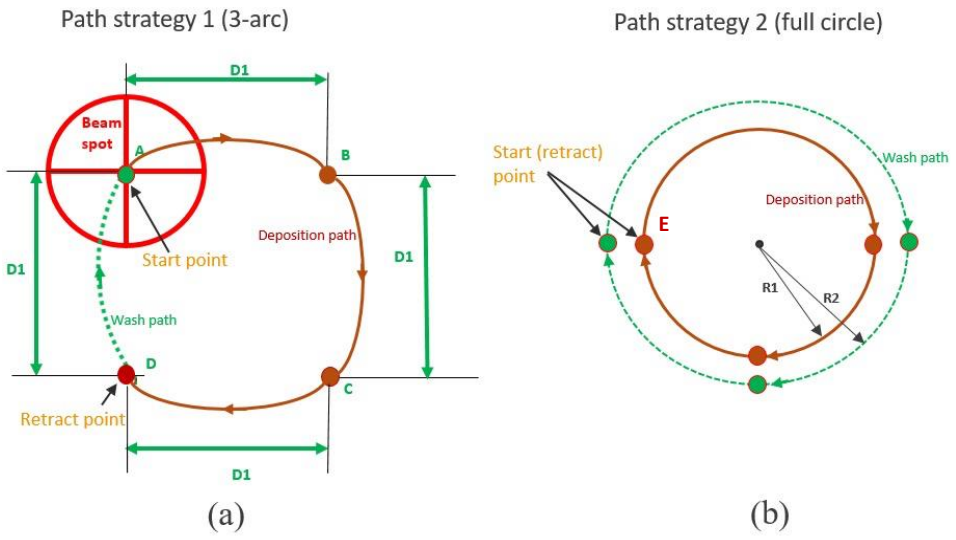

Figure 4.4 (a) Sketch of the 3-arc route, where arc AC is the deposition path and arc DA is the wash path. (b) Sketch of the full circular path, the internal loop is deposition path, and outer dashed loop is the wash path.

(2) Full circle path

As shown in the Fig 4.4 (b), during the full circular path, the processing route is a full circle with radius R. The processing path is continuous, instead of being discretized like experienced with the 3 arcs procedure. The process starts at location E, at which the wire is fed at the beginning and retracted at the end.

The advantages of the circular path compared to the 3-arc consists of eliminating discontinuities at the arc extremities and the fact that the wire deposition is conducted for the overall path. According to the results observed in 4.3, The drawbacks of the 3-arc design path are laid bare, and a new processing path plan is designed – the full circle path.

For both strategies, after the deposition of each layer, an extra laser pass is conducted without feeding wire in. This pass is called the wash pass and is implemented onto the previously deposited layer while that is still in a high temperature range (>1000℃). The benefit of the wash pass is improving the geometrical quality of the layer by controlling the weld pool dynamics before the material starts solidifying. In addition, in the wash path of the multi-layer depositions, regarding the energy accumulation in the process, in the later layers deposition the power is gradually reduced and the laser scan speed almost doubles, thus the overheating is avoided.

After starting process parameters have been defined on single-layer deposition, some combinations of process parameters have been adjusted to attempt the build of multi-layers cylinders, which are listed in Table 4-2.

Table 4-2. Selected processing parameters.

Parameters	First layer	4-layer	5-10 layers	Unit
Power		600		W
Travel speed		45		mm/min
Wire feed speed	285	375	285	mm/min
Wire retract speed	3300	2850	3300	mm/min
Path strategy	2	1	2	
Wire retract point	E	D	E	
Path radius	0.75, 1, 1.5	2	0.75-1.25	mm
Wash path speed		85		mm/min
Wash path power		510		W
Layer cooling time	N.A.	0.4	4	S
Layer height		1	0.75	mm

4.3. Results and discussion

4.3.1 Geometrical appearance

The preliminary results achieved for the full circle and 3-arc strategies are reported in this section. For both strategies, the process conditions were conducted on single-layer deposition first and then transferred to the manufacture of the multi-layers cylinder.

4.3.1.1 Path strategy 1 (3-arc)

Single-layer deposition

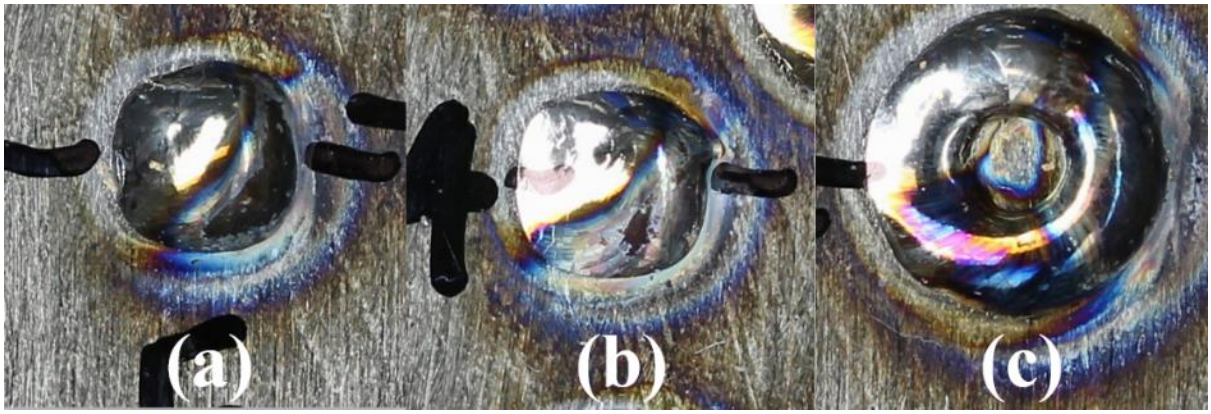

Figure 4.5 The single circle layer deposition applied in path strategy 1: (a) Path radius= 0.75mm (b) Path radius=1mm (c) Path radius=1.5mm.

Different values of path radius were tested, and their configurations are shown in Fig 4.5. From the top views, the three depositions for circles with different radius all achieve a similar semi-sphere geometry, thereby satisfying the most basic requirement for the multiple layer building of the cylinder. However, the defects are also obvious. For Fig. 4.5(a) and (b), a sharp tip is formed after processing because of the lack of material input in the fourth path of the 3-arc route, which causes the melting liquid flows to travel to the vacancies and form at an angle in the centre of the deposition. For Fig 4.5(c), because the semi-spheres radius is increasing, in the wash path, the free melting metal cannot fill the vacancies and therefore a slight gap is present in the fourth path route. In sum, the geometries of the depositions are asymmetric, and the wash pass can help in improving the geometry by spreading the added wire material more homogeneously.

4-layer cylinder deposition

The processing procedures are recorded by a camera as shown in Fig. 4.6. In Fig 4.6(2), the liquid bridge is formed between the wire and melting pool in the deposition shows agreement with [4.9], which also suggests boiling of the wire in front formation in the laser wire deposition processing. Meanwhile, in Fig 4.6(3), because of the closed deposition path and temporally intensive energy input, the melting pool covers whole final layer, and the light surface can be easily observed in Fig 4.6(4) regarding the high temperature inside. From the results shown in Fig. 4.7. An angle of inclination between the central cylinder axis and the vertical axis is clear. Given the discussion on single circle layer results, the lack of material input in the fourth path of the 3-arc route caused the similar angle issue. When the multiple layers were deposited during processing, slight cavity formed, and the angle problem becomes visible once the deposition has completed its path strategy.

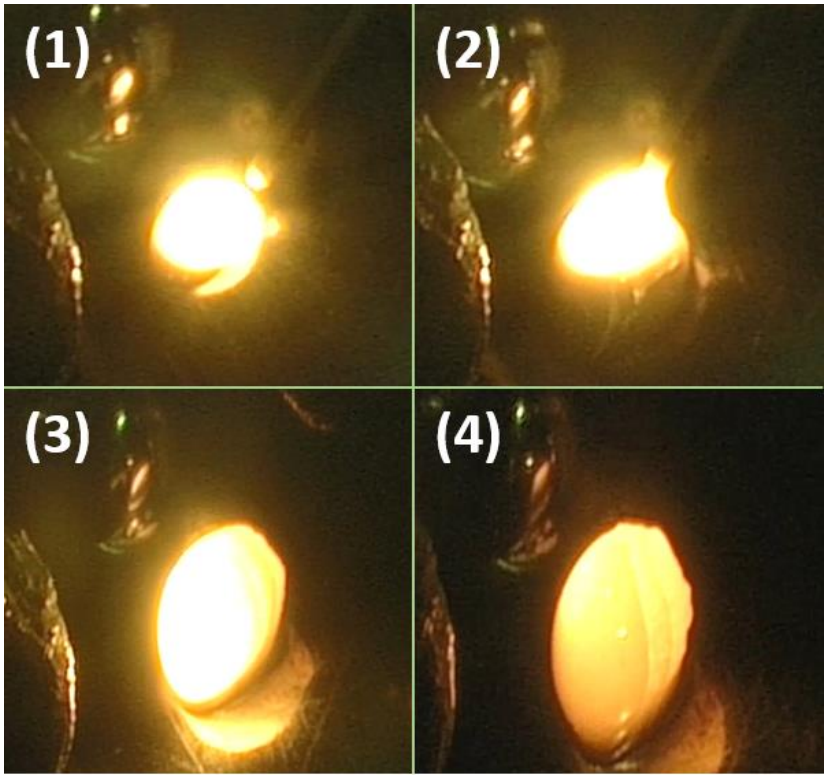

Figure 4.6 Cylinder building processes in 3-arc strategy: (1) Feed wire reaches the weld pool, (2) Continuous wire-feeding in the second layer, (3) Melt pool free form and the (4) Cooling process.

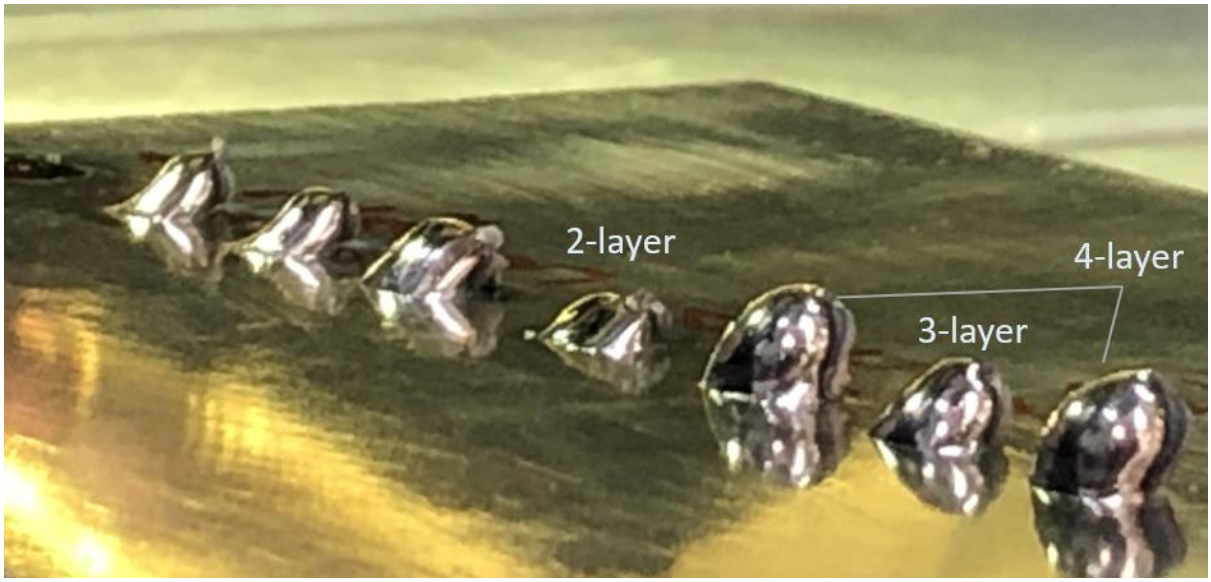

Figure 4.7 Outlooks of the different layer depositions built by the 3-arc path.

Given the single and multiple layer deposition results of the 3-arc, the most significant issue is the lack of material input in the final path processing, which leads to defects, such as the vacancies and inclination angles shown in the single and multiple layer deposition respectively.

4.3.1.2 Path strategy 2 (full circular)

In path strategy 2, a full circular path is designed to solve these problems, the wash path extends from the one forth path to an additional circle path, thereby providing adequate heat to the deposition and flattening it. Similar trials are then carried out, with the results on single layer and multiple layers deposition as follows:

Single-layer deposition

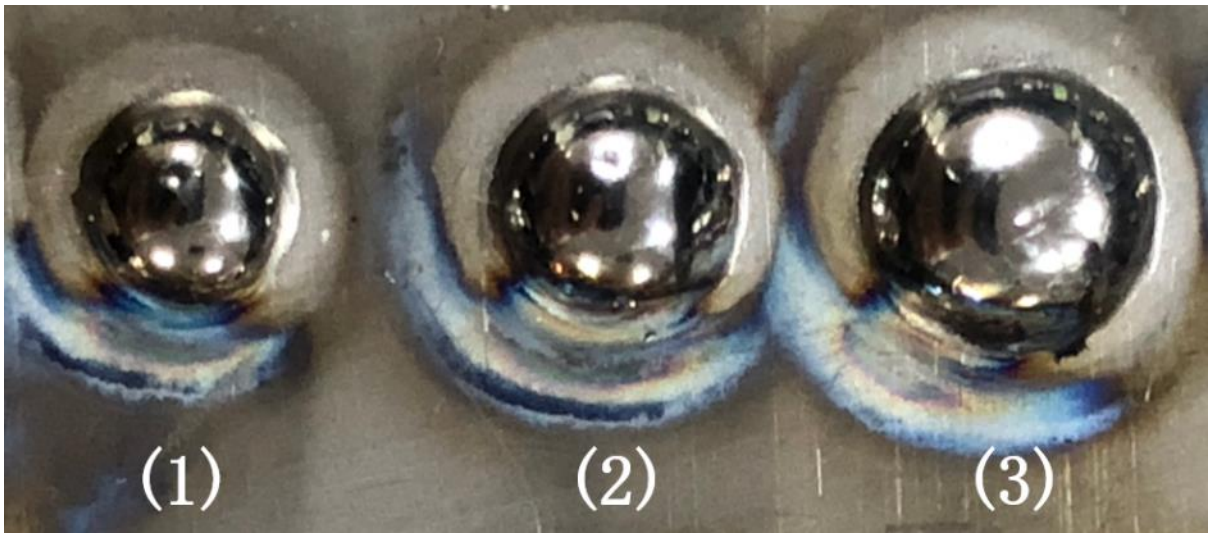

Figure 4.8 Top view of Single circle deposition in path strategy 2. Path radius is set to (1) R=0.75mm, (2) R=1mm, (3) R=1.5mm.

Table 4-4. Geometric dimensions of the single layer samples (full circle)

Samples number	Height (mm)	Diameter (mm)
(1)	0.80	3.5
(2)	0.75	4.4
(3)	0.75	5.5

The geometric shapes and dimensions of single layer depositions for different radius are shown in Fig 4.8 and Table 4-4 respectively. Because the material input track follows the laser scanning in the deposition procedure so that a whole circle is formed, the single layer geometry has a flat semi-sphere shape. The circular strategy promoted a more symmetric geometry when compared with the specimens achieved with the 3 arcs procedure.

Multiple layers deposition

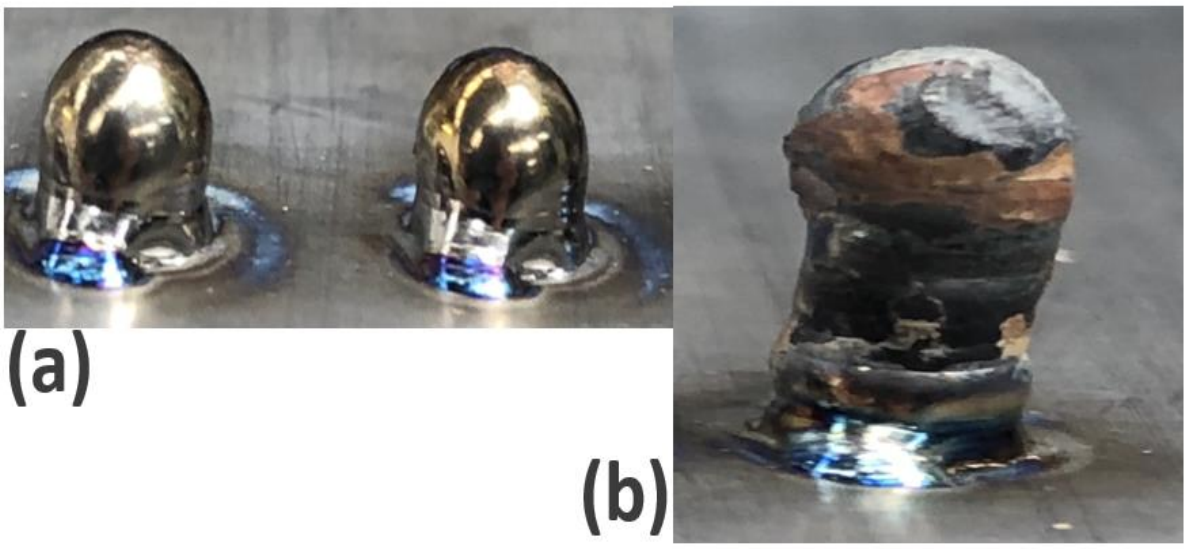

Figure 4.9 Multi-layer depositions applied in path strategy 2: (a) 5-layer cylinder and (b) 10-layer cone cylinder.

The multi-layer cylinders are shown in Fig. 4.9. In experiment (a), a radius of 0.75mm is applied to the full circular path route for a 5-layer cylinder building with a height adjustment of 0.75mm and a cooling gap time of 5s. Thanks to the stable processing in each layer of the deposition stage, the cylinder presents relatively smooth top and lateral surfaces. Meanwhile, as previously mentioned, because of the improved full circular strategy, the problem of the inclination angle in the multiple layer deposition experiments has also been improved. For the further trial in (b), a 10-layer cylindrical deposition was built with full circular path, but after the fifth layer, the path diameter was increased 0.25mm for each deposition cycle, to deposit an assumed mushroom-like crown. Consequently, a slightly larger hat formed at the cylinder top, which corresponds with the aim of the cylinder, seeing as such a shape can interlock the two sheets properly in further joining experiments. Therefore, compared with the results for path strategy 1, the proper geometric features produced make the full circular path the ideal route for depositing the cylinder. Furthermore, path strategy 2 is applied in the next joining experiments for composite to metal.

4.3.2 Microstructure

4.3.2.1 Path strategy 1 (3-arcs)

Fig. 4.10 below is the Ti6Al4V phase diagram, it demonstrates the influence of vanadium composition in various temperature gradients [4.10]. T_{Diss} is the temperature of the dissolution start point for the α grains, and transfer to β grains, according to [4.11], it approximate is $708℃$. M_s stands for the martensite start temperature.

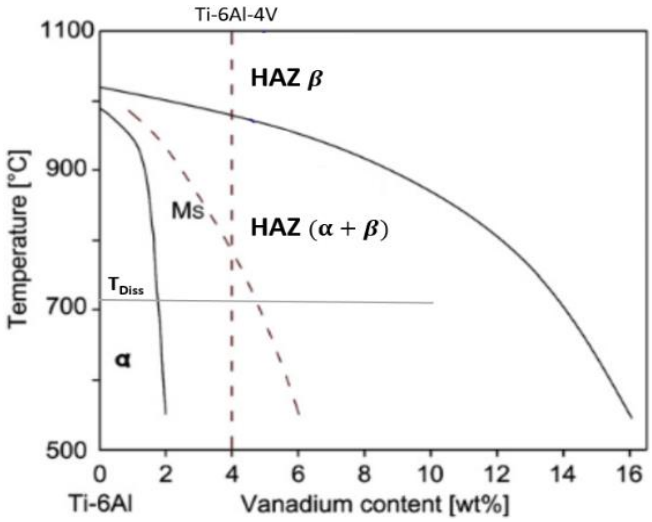

Figure 4.10 Pseudo-binary phase diagram of the microstructural zone at Ti6Al4V [4.11].

Similar to the single bead investigation in the [4.8], the microstructure zones of circle layer deposition show in Fig. 4.11, depending on the temperatures heat history underwent and the types of the growth of the grains, it is divided into three areas: base material (BM), heat affected zone (HAZ), fusion zone (FZ) and added material (AM).

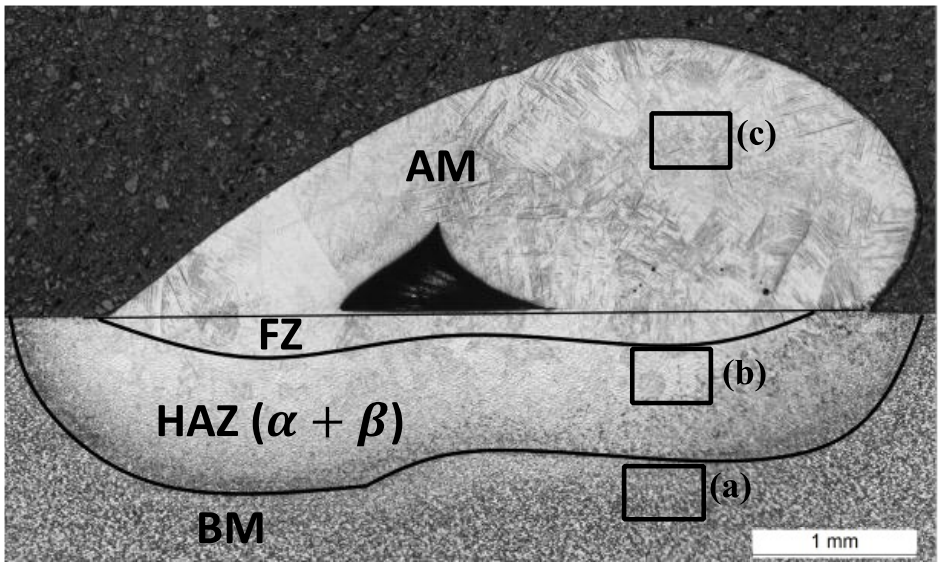

Figure 4.11 Single layer micrograph at the path strategy 1 applied radius=1mm.

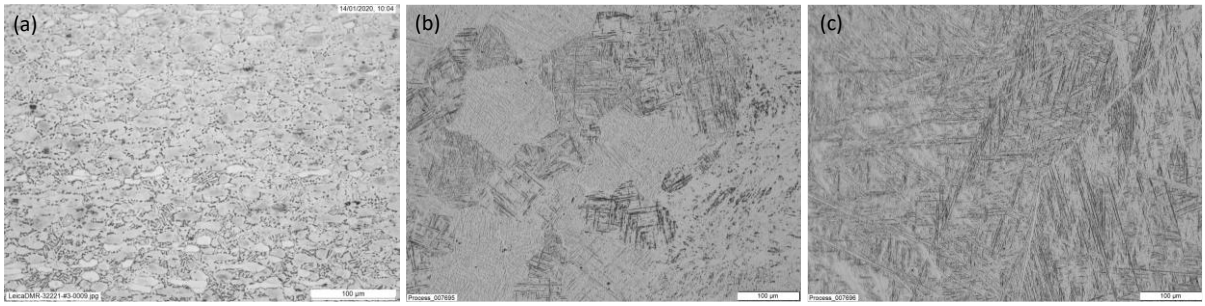

Figure 4.12 Microstructure of (a) base material (b) heat affects zone (c) fusion zone and added.

In Fig. 4.11, The bottom is the BM area, which has no significant thermal heat going through here, so it presents the microstructure of the as-received Ti6Al4V material, which mainly consists of globular α grains (Fig. 4.12(a)). In the HAZ, according to the [4.11], after the temperature achieved the T_{Diss} and stay in a certain time, the transformation of grains is started, the α grains in size are decreased or dissolved to β grains. Meanwhile, in Fig 4.12(b), α-lamellar become finer, basket-weave and colony structure appear in orderly from far to near the fusion zone. Fig 4.12(c) shows the microstructure part of added material, as well in the FZ, all the zone is melted, and grains are completely transferred to the β columnar grain.

From the overview of the microstructure map in Fig. 4.13. Because of the lack of material input in the fourth deposition path, after the wash path, an irregular cone-shape cavity was formed with around a 600μm radius at the base. Moreover, in the transition area between the added material and substrate, a small number of pores are observed as the main defects.

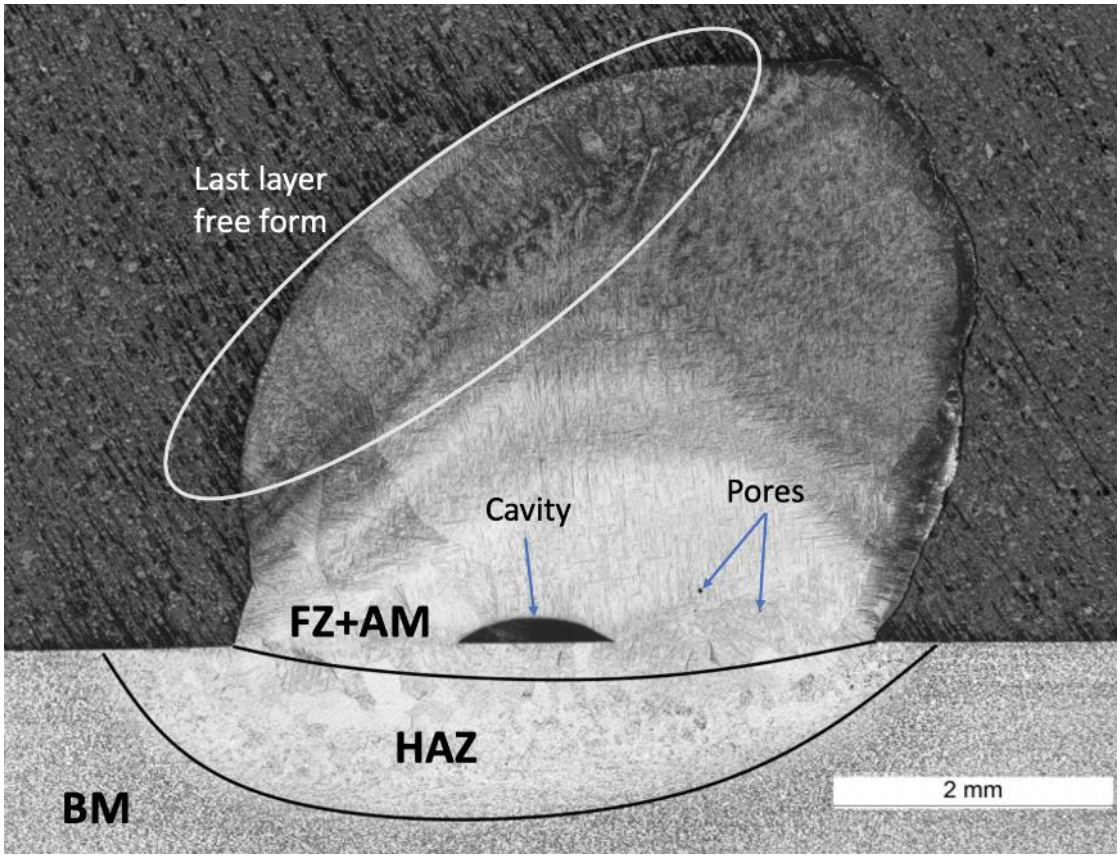

Figure 4.13 Macrograph of 4-layer cylinder deposition applied path strategy 1.

The cross-section microstructure of the 4-layer cylinder is shown in Fig. 4.12. The grain growth in the FZ and HAZ is similar to the single-layer deposition mentioned above. The cavity and pores inside are the main defect form, however, compared with the single deposition in Fig 4.11, because of the reheat by the four repeat depositions heat affected, the size of the cavity in the middle part was shrunk, and the pore number was reduced. In addition, it is noteworthy that there is a dark-coloured free form area is shown in Fig. 4.13, which normally occurs in the last layer in the LMwcD process, due to the cooling rate and the heat thermal historical difference, the deposited region went through the β-phase up to 4 times, but the final layer only cooled from the T_β one time, which leads to this significant uniform [4.12]. In this case, because of the deposition angle issue in this path strategy, the slant molten pool appearance is observed as well.

4.3.2.2 Path strategy 2 (full circular)

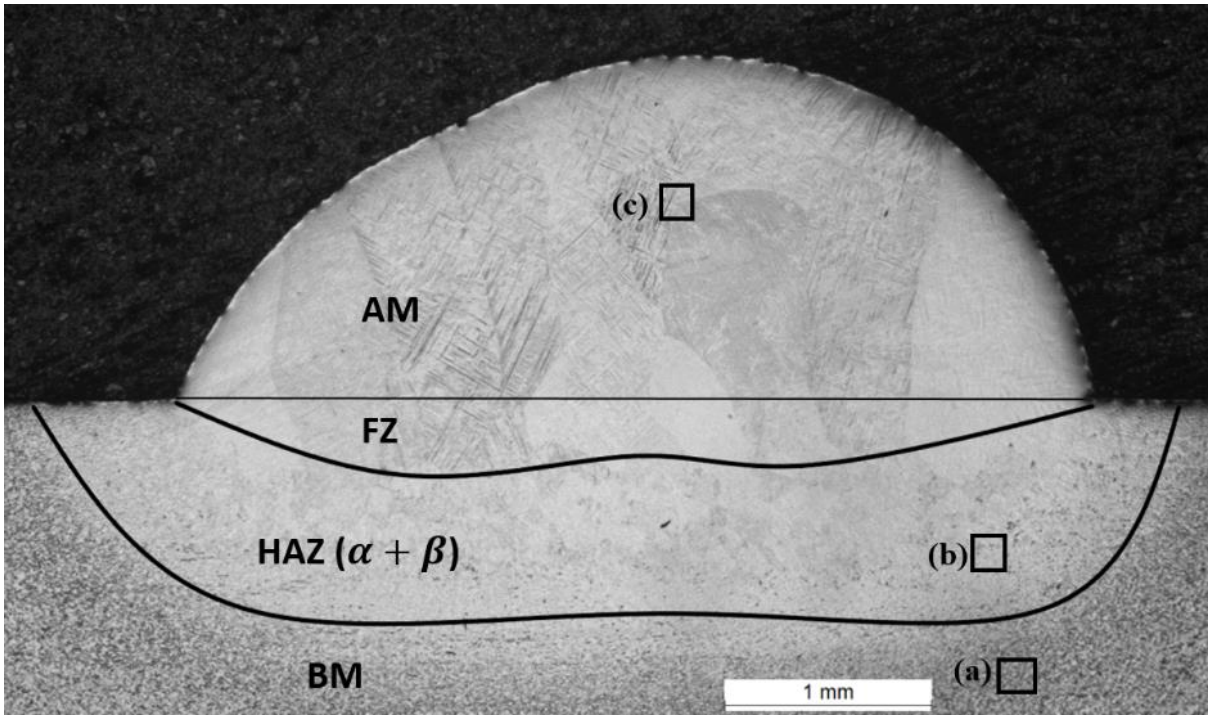

Figure 4.14 Micrograph of the single layer at the path strategy 2 applied radius=1mm.

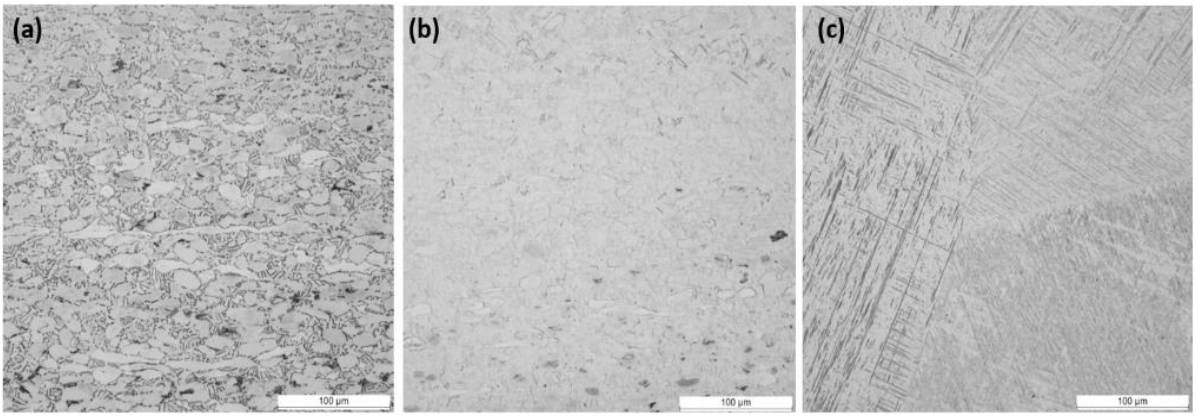

Figure 4.15 Micrograph of (a) base material (b) heat affected zone (c) fusion zone and added material.

Fig. 4.14, 4.15 and 4.16 show the microstructure zones of the single and multiple layers deposition respectively built by full circular path strategy. Similar to both single and multi-layer depositions for the different thermal historical areas, which are based material (BM) with the α grains, heat affected zone (HAZ) with β grains transferred from partly, and the fusion and added material zone where most of α grains are mostly dissolved to β grains, the microstructure details show in Fig 4.15. For the defect observation compared to the results of path strategy 1, the full-circular path strategy

filled the mass input in the final arc pass, which eliminates the defects previously mentioned in 3.2.1.

Due to the same reason of uniform material distribution, without the mass input influence in the full-circle strategy, the deposition angle issue has been fixed. The α grains, globular β grains in substrate HAZ, columnar β grains in added materials, and the equiaxed β grains in the final layer can be observed in Fig 4.16, the microstructure in this cylinder deposition also shows a high agreement with the straight-line path LMwD of Ti6Al4V in previous studies [4.13, 4.14], however, because the special thermal historical went through in this circle path, the β grains were reheated in every single layer, it affects the grain growth during the processing, so a reduced number and increased single β columnar grain size were formed in AM area. Moreover, similar to the single layer deposition, the defects (cavities and pores) are eliminated.

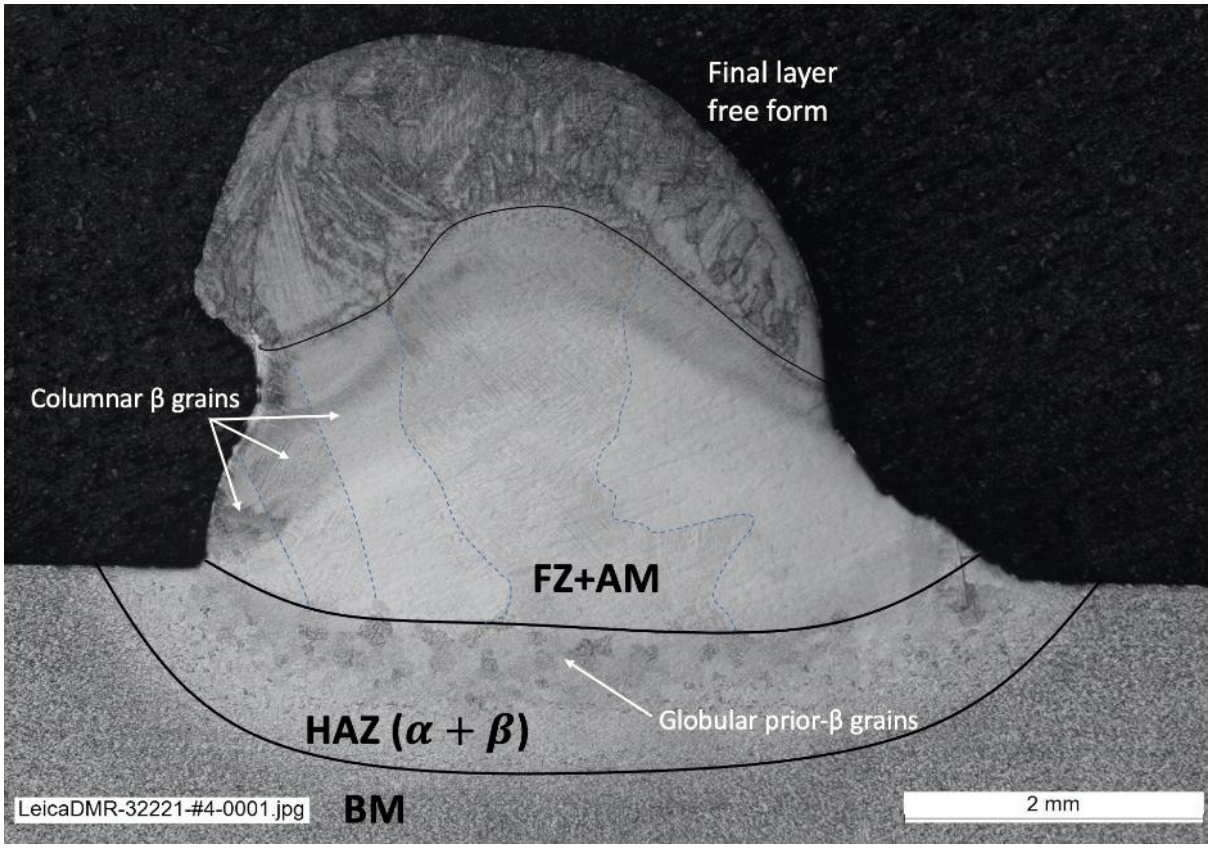

Figure 4.16 Macrostructure map of 5-layer cylinder deposition applied path strategy 2.

4.3.3 Processing factor influences

In multi-layer deposition experiments conducted in this chapter, several factors influence processing quality, morphological and microstructural performances of the

depositions. Testified by numerous try-and-narrow trails for the appreciate parameters development, the factors of the height adjustment, shielding gas flow and wire feed/retract speed were found that significantly affect processing. The influences of these three factors are demonstrated below.

(1) Height adjustment

The effect of height increment in multiple layer depositions, applied as a straight-line path, has been discussed in [4.15], the experimental results of which demonstrate strong agreement. Three groups of different height increments are tested, which are 0.75mm, 1mm and 2mm. It is found that there is no significant change in cylinder geometry as the height increment increases. Normally, the connection between the deposition and wire is the stable liquid bridge, but when the height increment is excessive large, the connection between the wire and deposition turns into a droplet. Consequently, deposition formation is negatively affected. The connections of the height increments 2mm and 0.75mm are shown in Fig 4.17.

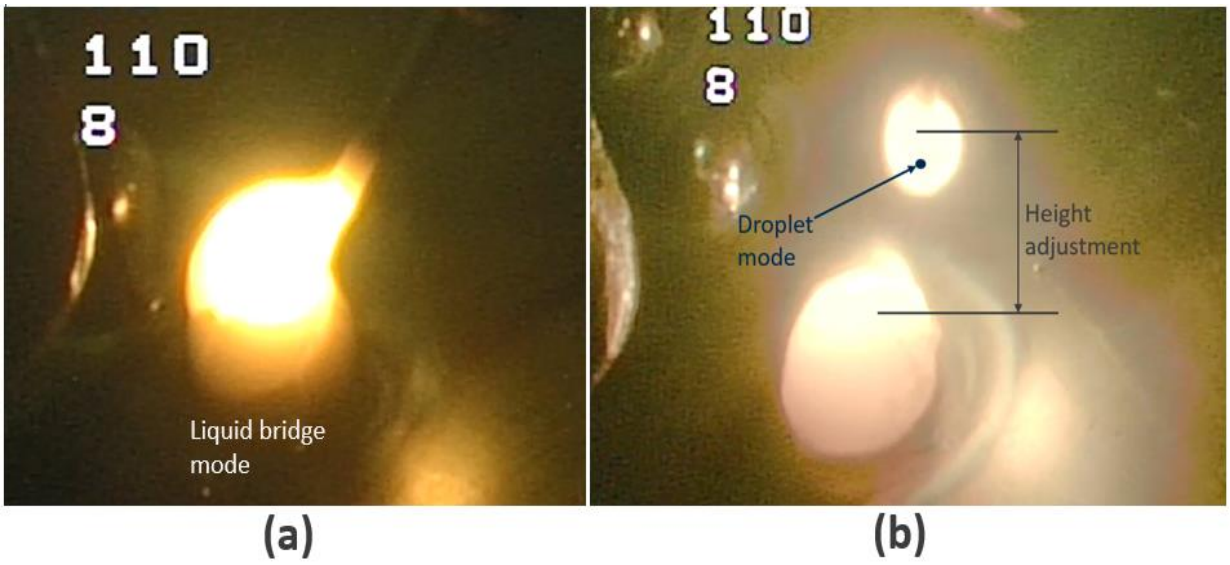

Figure 4.17 Connections between different height increments in processing: (a) Liquid bridge (height increment with 0.75mm), (b) Droplet (height increment with 2mm).

(2) Shielding gas flow

As introduced in 2.1.3, the shield gas is mainly used to control the plasma and protect the melt pool in the laser welding processing. However, because the conduction mode is used in processing, instead of the keyhole mode, its only function in this experiment

is to protect the processing surface from contamination. In the single layer deposition, the gas tube pushes forward the substrate so that the gas flow can cover the whole area. However, in the multiple layer deposition, as deposition height increases, the gas flow is distributed in the air and the deposition is uncovered. Another problem is that, if the gas nozzle is not in the correct position, the gas will blow the melting pool during processing, as shown in Fig 4.18. Therefore, having the shielding gas in a proper position is an important factor that ensures processing stability.

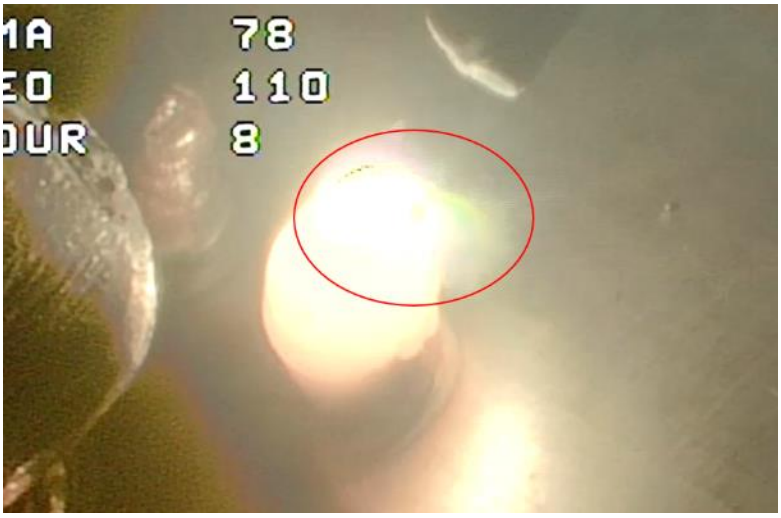

Figure 4.18 Influence of improper shielding gas position, which produces a small flame in the wash path.

(3) Wire feed and retract speeds

Both wire feed and retract speeds are significant parameters in laser processing, as they have a close relationship with processing and geometrical shape. The wire feed speed directly controls the mass input in the deposition. However, as discussed in [4.3], if the feed speed becomes too low or too high, the wire transfer takes on a droplet form or displays stubbing conditions. Meanwhile, retract speeds affect the procedure after the deposition path at the retraction point. During processing, sufficient speed is needed to retract the wire from the melting pool, otherwise, it will be stuck with the deposition and interrupt the whole experiment, as shown in Fig 4.19.

The processing factors investigated in this chapter were concerned about their effects on the experimental processing, which determines the controllability of the experiment. The more detailed influences of the specific control processing parameters (power,

speed, and height adjustment) on the deposition results will be further explored in the next parametric study chapter.

Figure 4.19 Failed retraction during processing with the wire stuck in the deposition.

4.3.4 Discussion between two path strategies

In path strategy 1, although the wash path can mitigate the effect of a lack of material, flatten the circle and improve the condition of wire retraction, the obvious angle and cavity issues still appeared in the multi-layer depositions. Meanwhile, in the full circular path strategy, a 5-layer cylinder was built, and which shows proper geometrical shape and intact section view compared to the multi-layer deposition built by the 3-arc strategy. The wash path reducing the power or increasing the speed of the laser scanning is reasonable and can achieve the close effect while saving on energy and time.

In multiple layer deposition, like the laser wire layer, there are two laser transfer modes: the liquid bridge and the droplet. Excessive wire height will break the liquid bridge and cause a droplet to form instead. Shielding gas is a significant factor in multiple layer deposition. When the layers are deposited, the quality of the deposition surface is ensured. If the angle or position of the shielding gas is incorrect, the shape of the cylinder head is negatively affected. The values for the wire feed and retract speed are important parameters in deposition processing that significantly influence the geometrical shape and experimental stability.

4.4. Summary of findings

In the preliminary stage, single-layer and multiple layers deposition experiments were conducted using the 3-arc path and full circular path strategies respectively. Both results proved the feasibility of the cylinder building based on the laser wire deposition method in micro-scale (circle radius from $500\mu m$ to $1.5mm$).

Although the multiple layers deposition was successfully implemented in the two path strategies, the results still demonstrated flaws in the single layer deposition and an angle issue while cylinder building for the 3-arc path. However, after being fixed up with the mass inputting at the final arc, the full circular route can successfully achieve better geometry and microstructure both in the single layer deposition and multiple layers deposition. Compared with the previous research in straight-line deposition, the full-circle deposition shows a high agreement with former results in the microstructure map.

The variation of processing parameters not only influences cylinder geometry but could also lead to unsuccessful building procedures in multiple layer deposition processing, especially for the parameters of height adjustment, shielding gas position, feeding and retract speed. When the height adjustment exceeds 1mm, the wire transfer mode is broken to the droplet, which causes unstable processing. The incorrect gas position will lead to the issue of surface contamination. As for the wire feed/retract speed, both of them decide the final procedure in the deposition path, because of the mass input relationship, the wire feed speed influence the volume of the deposited cylinder, the improper level of feed/retract speed leads to the wire sticking in the melt pool at retracting point.

Chapter remarks for research

Based on the previous literature of straight-line and thin wall LMD deposition, the cylindrical deposition methods were developed in this chapter, the experiment proved that the cylindrical deposition in minor scales can be achieved by ALM with the circular track. And the sound welding and deposition qualities indicate its feasibility to apply into the LR concept as the rivet deposition method in the following joining experiments.

The investigations of path strategies comparison and parameters influences in the deposition identified the key factors that affect the processing and results, which provides the general guidance and directions in following LMwcD studies for the parametric design and optimization.

Chapter 5 Understanding and parametric study on Ti6Al4V LMwcD experimental processing

In the last chapter, the feasibility study of laser metal wire cylinder deposition (LMwcD) has been conducted, it shows that both 3-arc and full circle path strategies can successfully build up a deposition cylinder on small scale (1-3mm), moreover, the full circle path has achieved a proper result, which systematically analyzed in geometrical and microstructural aspects. Therefore, in this parameter analysis section, the full circle path strategy will be used as a basic initial group in the investigation.

After the feasibility study, several parameters of cylinder building were investigated in 4.3.3, but as discussed in chapter 2.2.1, for the current joining techniques, the productivity is another vital factor to an industrial application. Besides, in the preliminary test of full circular strategy, to build up an 8-layer cylinder deposition, it costed almost 120s for the whole processing, which is much more than it in the traditional mechanical riveting. Therefore, processing time reduction is the main goal in this parametric improvement chapter, to improve the deposition productivity for the further laser riveting applications.

5.1 introduction

As the motivation explained in the last paragraph, followed by the feasibility results concluded in the last chapter, the full-circular LMwcD was applied as the basic approach. In this chapter, aims to increase productivity during the processing, several actions have been taken step by step. The chapter flow chart is shown in Fig 5.1 below, first of all, the basic relationship between the travel speed and wire feeding speed is investigated to find out the appreciated and highly efficient travel/wire ratio in 5.2. Next, based on the preliminary results in 5.2 and the initial normal (full-circular strategy) deposition method in chapter 4, five new cylinder deposition methods are designed and developed in 5.3. Then their result comparisons were presented in 5.4, which mainly focuses on the productivity, geometrical appearances and the microstructural differences, all the results of processing and observation detail were

analyzed and discussed in 5.5. Finally, for the whole project, further experimental trials on the titanium and initial dissimilar joining results will be introduced in 5.5.3.

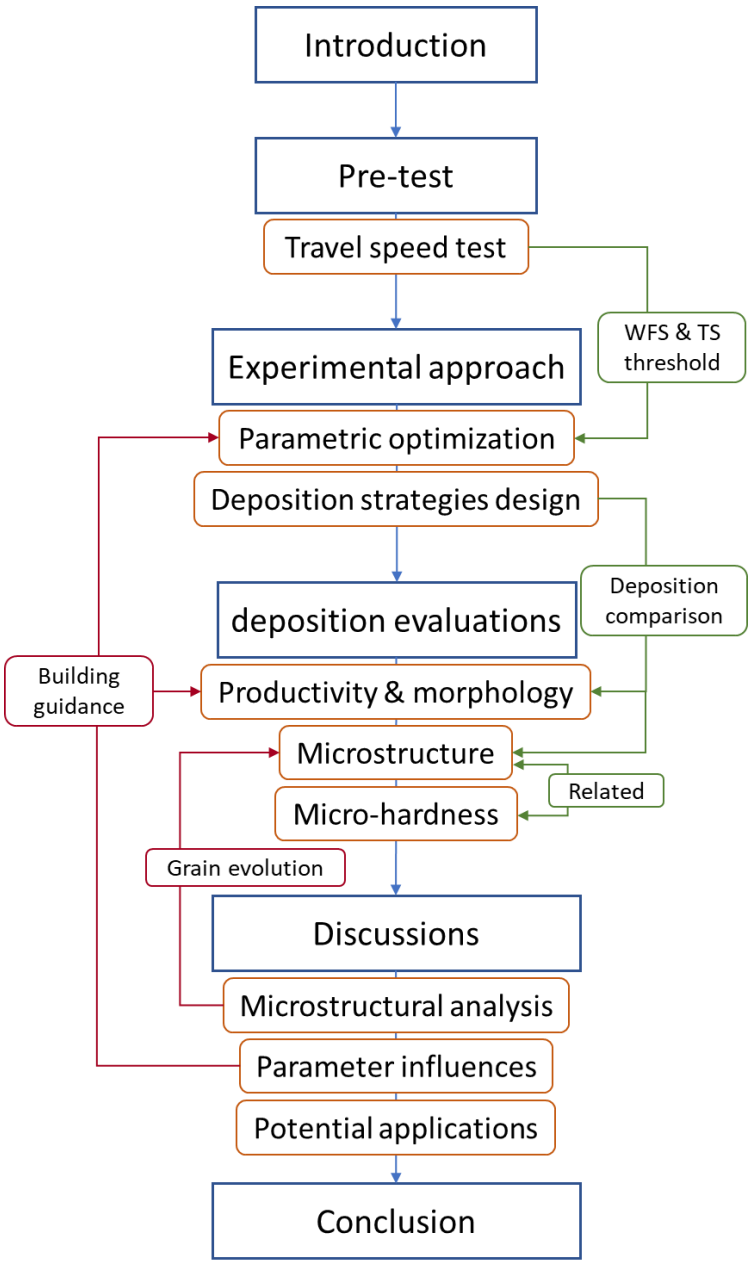

Figure 5.1 Chapter flow chart of LMwcD parametric study.

5.2 Initial travel speed test

In the processing procedure of LMwD, wire feeding speed (WFS) and laser travel speed (TS) are two significant parameters to the deposition geometrical appearance, and previous research also discovered the three different wire-transfer models applied various WFS and TS: (a) droplet (b) smooth (c) stubbing conditions [5.1]. Besides, from the aspect of stable processing, keeping the WFS/TS ratio constant ensures that

both the amount of material per unit of length and the heat input are kept constant [5.2, 5.3]. Therefore, the values of WFS/TS named k, in this case, will be tested and a most suitable one will be determined, both of processing time and stable procedure aspects are considered in this case.

From the last section in 4.3, the LMwcD applied by full-circle path strategy shows a stable processing and a proper geometrical appearance, and its results satisfied the requirements of the cylinder building part of the project, so the WFS and TS are picked from table 4-2 and set the k value to the 5. Then, aim to find the fastest deposition method parameters, the relationship between power and travel s, in this case, will be investigated. Keep the k value as a constant, vary the values of TS from 0.17mm/s to 2.17mm/s and power from 300W to system maximum value (600W), and observe the results of processing status under different conditions, the results are shown in Fig 5.2 below.

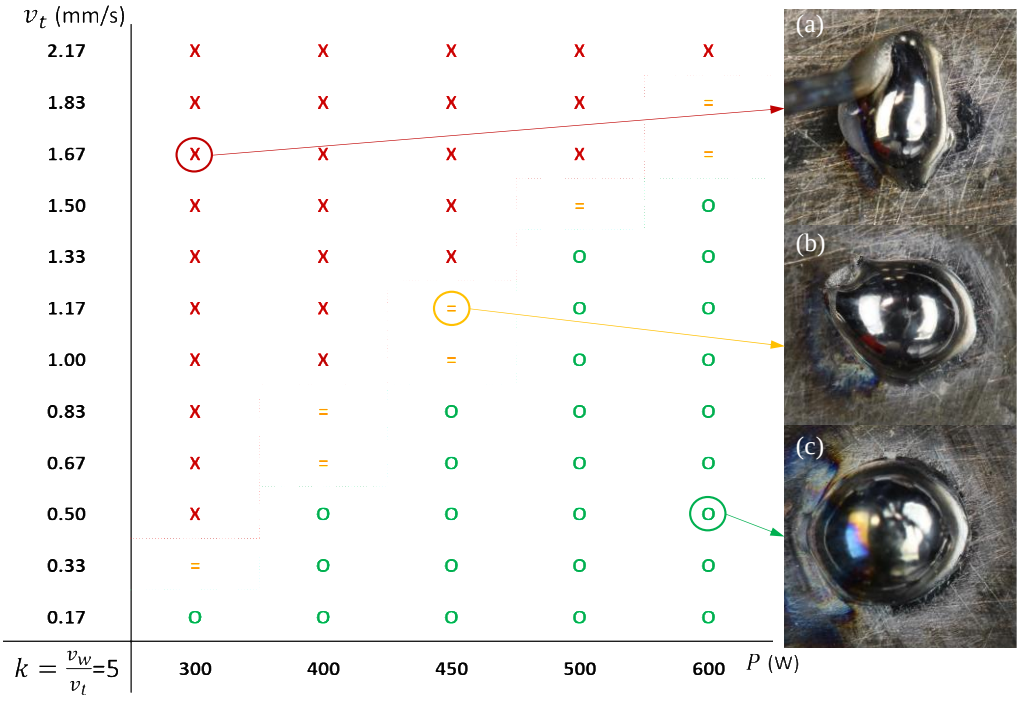

Figure 5.2 Processing modes applied with different value sets of power and travel speed: (a) failure deposition, (b) unstable processing and (c) stable processing.

In the results presented above, the single cladding of LMwcD experiment applied in different conditions with a wide range of travel speed (0.17 - 2.17mm/s) and power (300W - 600W) are tested, there are three modes shown in the table, the red block is failure deposition, the green block is successful deposition, and yellow one is unstable.

In the failure deposition parameter conditions shown with red marks, because the power is too low or the travel speed is too high, the energy input per area is not enough to melt the base substrate and deposit the wire on it, to generate the proper bonding between the added material and base surface (Fig. 5-2(a)).

For the yellow mark conditions (Fig. 5.2(b)), the energy input is higher than which in the red block, the base is started to melt, and the wire can be just deposited on it, but the wire travel motion is still slightly fast to build a proper deposition, and the processing wire transfer status is similar to the droplet model in [5.1].

As shown in Fig. 5.2(c), the green circles mean the deposition can stable processing in the experiment, the energy input and wire feed/travel speed are balanced, a proper deposition can be built on the substrate, which corresponds to the liquid bridge wire-transfer model, so, these parameter conditions are suitable to apply in the LMwcD. Therefore, based on the stable processing status, the productivity is another key factor in this parameter study, the highest power (600W) and the fastest travel speed (90mm/min) are selected for the high-speed deposition in the next new deposition design part.

5.3 Deposition methodologies design

Based on the results of the feasibility study shown in the last chapter, as the further optimization and supplementary experiments, the parametric study used the same Ti6Al4V alloys and processing system setup introduced in 4.2.

5.3.1 Design of experiments (DOE)

The design of experiments (DOE) is a systematic approach that utilizes statistical tools to analyze engineering correlations based on different factors and response variables present in a system. Response variables are measured using the purposeful and programmed variations imposed on the process parameters. DOE can successfully maximize the amount of useful information in a study while minimizing the amount of data that must be collected. The fundamental principles of DOE are:

Randomization. Tests are performed in random order; thereby ensuring the reliability and validity of statistical estimations.

Replication. The same experimental conditions are repeated so that the variability associated with the process and inherent random variations can be estimated, in this study, all experiments with each parameter set was repeated at least 3 times to ensure the reliability and controllability of the process.

Blocking. The effect of potential or known risk factors is removed to increase precision.

The factorial experimental design involves the simultaneous variation of several factors which impact response variables so that the effects of variables can be investigated. Moreover, such a decision also involves estimating response variable sensitivity about each factor or several combined factors which interact with one another.

5.3.2 LMwcD parametric study

The factorial experimental design involves the simultaneous variation of several factors which impact response variables so that the effects of variables can be investigated. Moreover, such a decision also involves estimating response variable sensitivity about each factor or several combined factors which interact with one another.

In this section, because of the proper geometrical and microstructural conditions presented in 4.3, the full-circular strategy was used as the normal cylinder deposition method (NM), meantime as the initial control group in this parametric study, based on it, several parameters will be adjusted to develop new deposition methods with higher efficiency. In previous tests, the following parameters have directly or indirectly affected the processing time:

- Travel speed: In this cylindrical deposition processing, there are two travel speed values are involved, one is the deposition path travel speed, and another is wash path speed, both of them are significant to the total processing time, and because the processing of wash path without wire feeding, its speed value will set double to the deposition path speed.
- Wash path: besides the wash path speed can affect the processing time, the wash path number is also a variable factor, though the previous tests, removing some wash path in the later part of the deposition, will slightly affect the deposition results, which can reduce total processing time.
- Cooling time: cooling time in each layer is another key value to the total time, this period not only influences the deposition solidification and shape formation but also the cooling rate is vital to the microstructural phase change in the different areas of deposition.
- Power: in this case, the energy input and cooling time work together to affect the processing efficiency, the higher power input can reduce the cooling time, but it still needs to adjust to a suitable range to keep a stable deposition.

Finally, in this parametric improvement study, after the optimized consideration of parameters mentioned above, four new cylinder deposition methods are designed, they are High Speed (HS) deposition 1, HS deposition 2, Continuous spiral (CS) deposition and high-speed spiral (HSS) deposition, their specific parameter values show in Table 5-1 below.

Table 5-1 Specific processing parameters of new methods.

	NM	**HS1**	**HS2**	**CS**	**HSS**
Travel Speed (mm/s)	0.75	1.5			1.5 - 3
Circle route radius (mm)	0.5				
Wash speed (mm/s)	1.5	3		N.A.	
WFS (mm/s)	4.1	7.5			
Layer Cooling time (s)	8	2		N.A.	
8 layers wash path number	8		3	N.A.	

Five methods will be investigated in this study, at first, the full-circle strategy was used as the normal method (NM) applied with the additive layer method (ALM), then, through adjusting the processing parameters, the following four deposition methods are designed. In high-speed deposition 1 and 2, the travel speed of deposition and wash path are increased to 90 mm/min and 180mm/min, meantime the cooling time of each layer is reduced as well.

Based on the HS2 method, a continuous spiral (CS) method was also designed, the process starts from the substrate and continues depositing the wire without a break until the final layer reaches a certain height. Finally, the deposition speed is doubled to complete the final design of the HSS deposition. The schematics of ALM and CS are shown in Fig 5.3 (a) and (b) respectively, theoretically, the CS approach saves the time from cool steps and the wash path compared with ALM. Experiments of new deposition methods will be conducted, and their results show in 5.4.

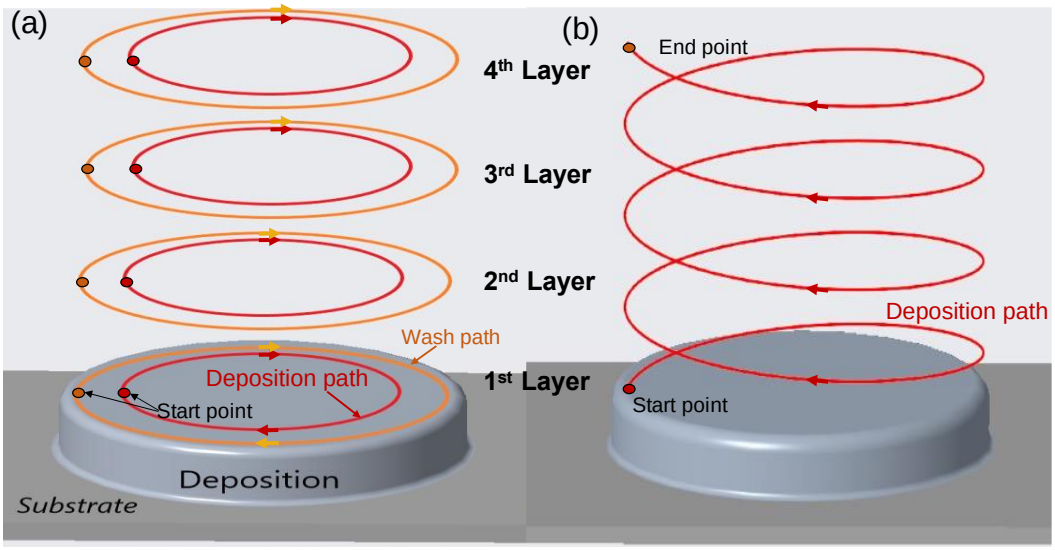

Figure 5.3 Process schematics of (a) ALM and (b) CS deposition strategies.

Experiments of five new deposition methods were conducted, the comparison results are presented from morphological, microstructural aspects. The OM, SEM and EBSD analyses were employed for microstructural observation, EDS was employed for chemical composition tests and the Vickers micro-hardness was measured on the cross-section to evaluate the local strength of depositions, detail of evaluations have been introduced in 3.6. Each deposition strategy was repeated at least 3 times to ensure the replicability of the method, and a random one was selected from similar depositions for the same strategy.

5.4 Comparison results

From macro to micro views, the as-built depositions were evaluated and analyzed from four general indicators: (1) Processing time: efficiency improvement as the main aim of the parametric optimization, the reduced processing time can increase the productivity for the industrial application. (2) Geometrical dimensions: the produced deposition shape and depositions decide their applicable conditions, as well as the morphological influences of processing strategies, were revealed in 5.4.1. (3) Microstructure: the cross-section overviews were observed to analyze the microstructure differences among varied thermal histories of design deposition strategies. (4) Microhardness: the local strengths of depositions were measured and their relationships with the microstructure appearances and processing underwent were discussed and concluded. The detailed comparison results of multilayer depositions applied with 5 designed LMwcD methods were presented in the following sections:

5.4.1 Productivity and geometrical dimensions

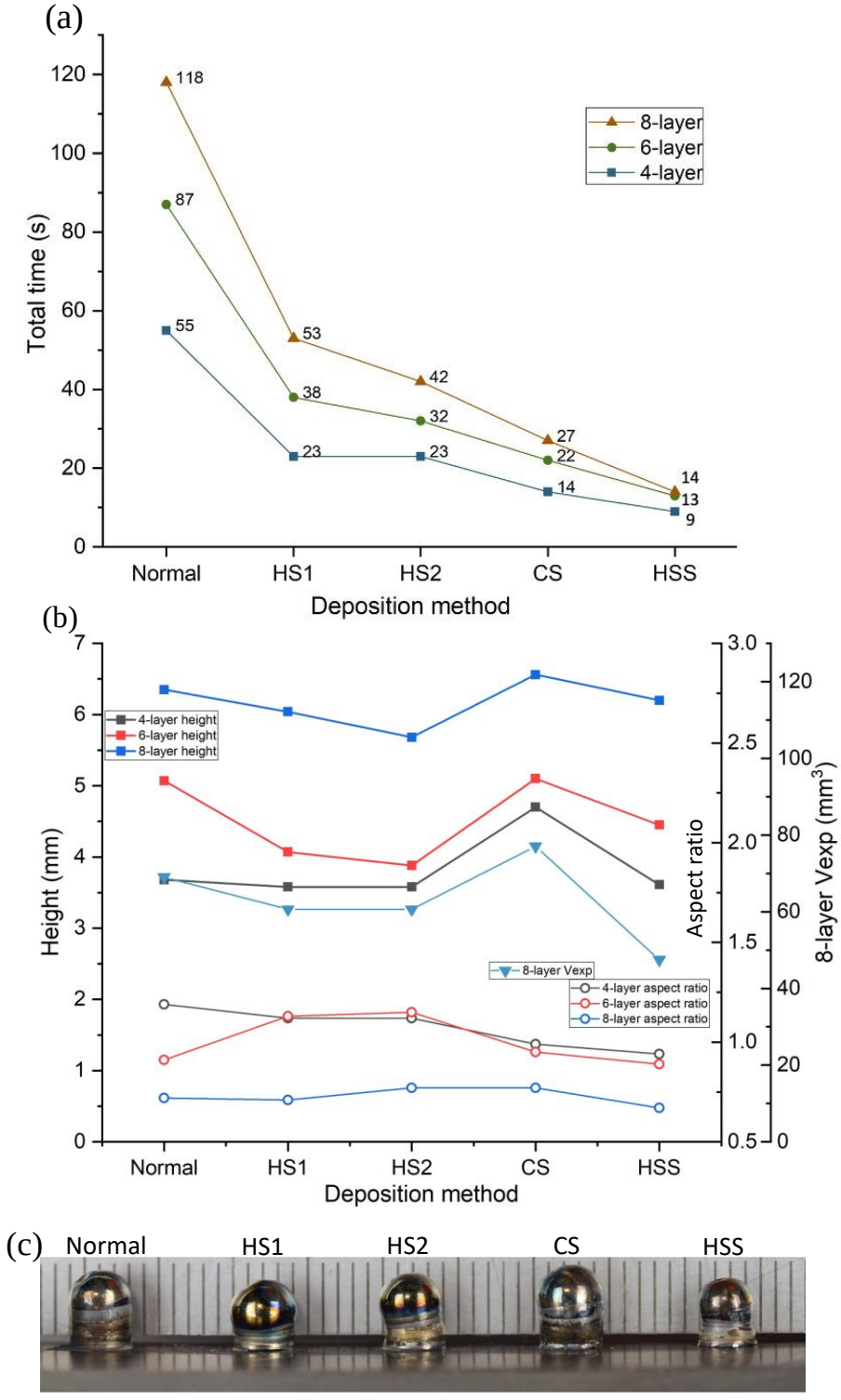

Figure 5.4 Results comparison of 5 cylindrical LMwcD methods in (a) Total processing time, (b) geometrical dimensions for multilayers deposition (c) outlook of 6-layer cylindrical depositions.

The productivity and geometrical dimension are the two significant considerations in industrial demand. In this comparison study, 3 different multilayer depositions (4, 6, 8 layers) were built, the total processing time of 5 cylindrical deposition methods are shown in Fig 5.4(a), which clearly presents the processing time is gradually reduced from initial normal to the final HSS deposition method. Compared to the initial normal deposition method, after increasing the travel speed and compressed the cooling time, the processing time of HS2 deposition is reduced around 58%, 63%, and 64% respectively in 4, 6, 8-layer depositions (productivities increase to 239%, 271%, and 281%). For the final HSS deposition method, after removing the washing and cooling step, and changing the deposit strategy to a continuous spiral track, a significant reduction of processing time for three types of multilayer deposition are observed around 84%, 85%, and 88% (productivities soar to 611%, 669%, and 843%).

Since the wire feed speed is increased simultaneously during the deposition procedure, there is a little range effect impacted on the overview of geometrical dimensions regarding the sharp drop of total processing time in Fig 5.4(b). The height of HS2 depositions is slightly lower than the normal depositions due to the expected deposited material being reduced, for instance of 8-layer depositions, the V_{exp} of HS2(1) is $60.64\ mm^2$ which is of the normal method is $69.06\ mm^2$. The aspect ratio measured from the ratio value of deposition diameter width to height in this study, it in HS2 deposition is lower than the normal method as well, energy input in a former deposition is reduced as a result of increased travel and wash speed, [5.4] reported the similar effect of energy input on general dimension for LMwD. As for the HSS deposition, it is measured a similar height and slight lower aspect ratio compared with the initial normal method, but its $V_{exp} = 47.48\ mm^2$ is much less than NM deposition, it can be explained by [5.2] that the dilution of cladding positively correlated with the energy input, it means in additive layer manufacturing (ALM) such as Normal, HS1, and HS2 deposition methods, with repeating and increasing of the heat input, the thermal cycles in NM strategy remelts the deposited material, and caused father dilution inside the deposition and/between the substrate. Because of the longer deposition time in spiral strategy and higher wire feed speed, the CS deposition method has the highest expected deposited volume and height but is limited by the high-power input and height adjustment set (same value of the HSS), the aspect ratio

is little higher than HSS method. In addition, another point should be emphasized that the specific geometrical dimensions (height, aspect ratio, area of HAZ, and deposition contact angle) are not only affected by deposition strategy, but also highly depends on each single processing parameter (power, travel speed, wire feed speed, and height adjustment), and they combinedly influence the building dimensions of the LMwD [5.4-5.6].

The example samples of 6-layer deposition are shown in Fig 5.4(c), their corresponding dimension features have described above. All of them demonstrate the feasibility without the angle issue mentioned in the previous study, but there shows a wrinkled area opposite to the shielding pipe, and the shielding gas influence will be discussed in detail in 5.4.2.

5.4.2 Microstructure overview

The deposition and wash track strategies significantly affect the heat input and cooling rate in the deposition processing, the different designed deposition methods lead to the various extends of phase change and grain evolution in the materials. In this microstructural analysis, NM, HS and HSS these three typical methods were selected and recorded, and their 6-layer deposition was sectioned and observed by OM. Fig 5.5 is the video shot at the end of the final layer deposition track, as discussed in the last section, it can be identified that a larger and lighter molten pool was formed in the (a) NM deposition method thanks to higher heat input and accumulation, and it also presented a clearer temperature gradient from top to bottom regarding the slower ALM steps. However, in the HS and HSS experiments (Fig 5.5(b) and (c)), compared to the NM deposition, because of lower energy input and faster process, the molten pools were slightly smaller and darker, and were showing a clearer boundary between the melting and solidified materials. The process influenceing the microstructural appearances will be present in following sections, and these processes also show a high agreement with the processing FEA modelling results presented in chapter 8.

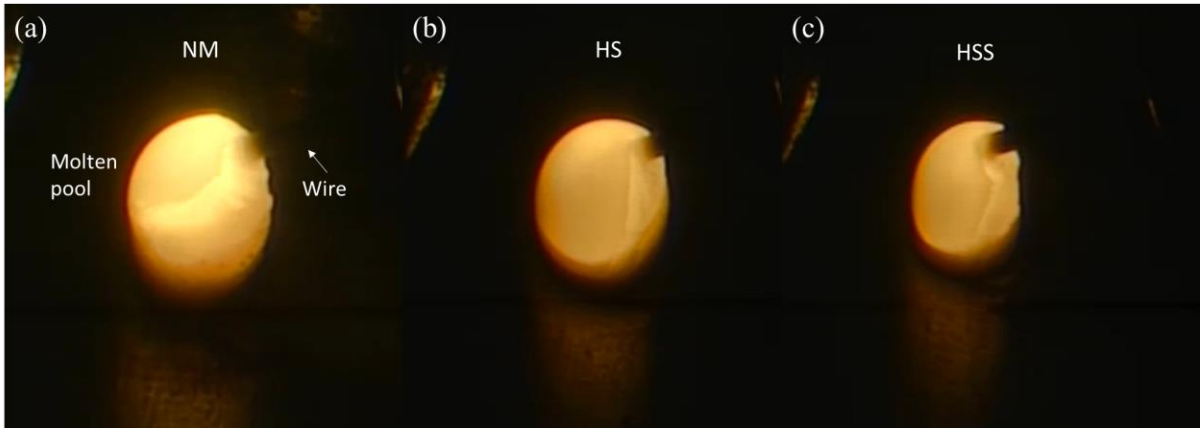

Figure 5.5 The processing record to monitor the molten pool appearances of (a) normal, (b) HS and (c) HSS methods at the end of the final layer deposition track.

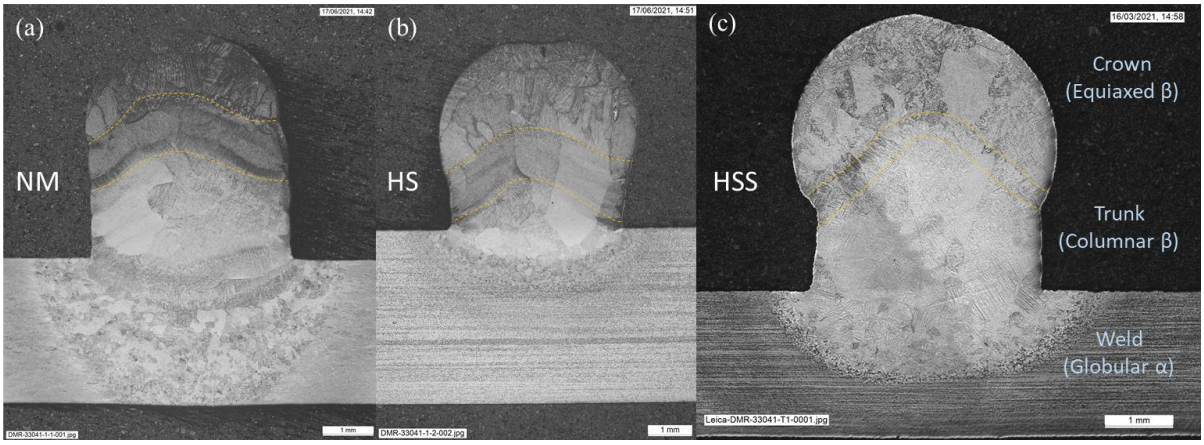

Figure 5.6 The microstructural cross-section overviews of 6-layer deposition manufactured by (a) normal, (b) HS and (c) HSS deposition methods.

The corresponding cross-section overviews of three different methods are presented in Fig 5.6. the normal deposition shows the same microstructure with feasibility results in Fig 5.6(a), and the cross-section overviews of HS and HSS were presented in Fig 5.6(b) and (c) respectively. Both of them obtained the intact section without the significant defects of pore and crack which normally occurred in the welding area. In addition, because these three deposition methods were all designed from the general LAM concept, their macrostructure section overviews consisted of similar structures, the equiaxed β, columnar β and globular prior β grains were observed in order from top to the weld areas.

But there still has some detailed differences were observed, first point is the heat input directly presented on the HAZ sizes of the three depositions, the HAZ of NM method

has penetrated the substrate which is unexpected in the industrial application because of the subsequential residual stress. Besides, one difference is because the NM deposition went through the highest temperature at the top area, the equiaxed β grain size was finer than the other two depositions, however, the largest equiaxed β grain size was observed in HSS deposition due to the lower heat input and high cooling rate. For another point, the segregation band shows a strong relationship with the layer cooling steps, the HS deposition shows a wider area of segregation bands since the faster thermal cycles and subsequential cooling gaps, on contrary, only one narrow band is generated in the HSS deposition regarding the continuous deposition process, it also causes a higher heat accumulation and faster cooling rate inside, which increased the β grain size and reduced its number. The detail about grain evolution will be further discussed in 5.5.1.

5.4.3 Micro-hardness

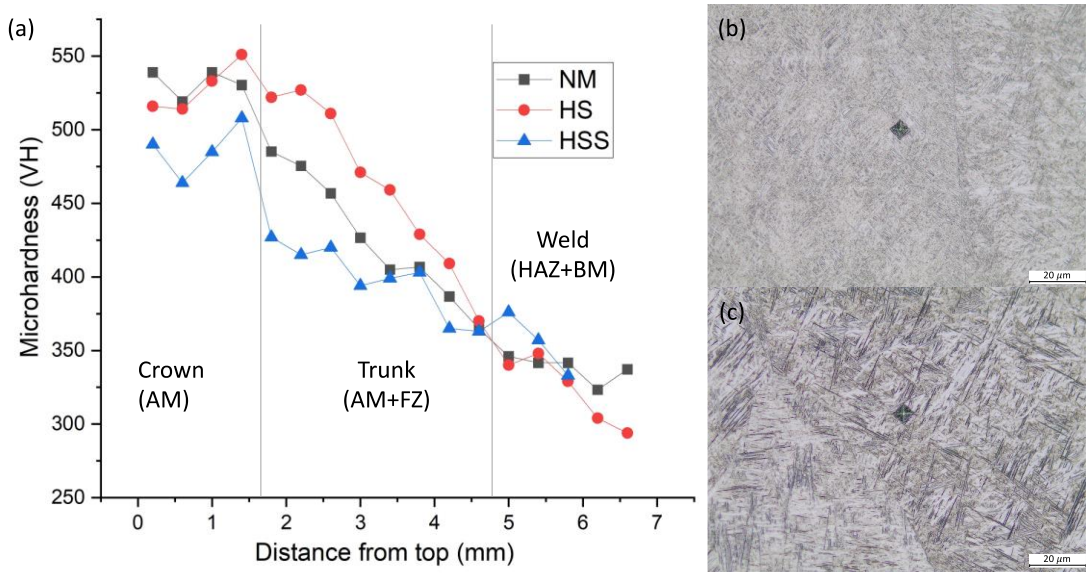

Figure 5.7 (a) Comparison micro-hardness results of NM, HS and HSS depositions, and the indentation locations on the top area of (b) NM and (c) HSS deposition.

To evaluate the mechanical properties on the deposition of different building strategies, and the strengths of different structures, further Vickers microhardness tests were conducted on the selected original NM, HS and HSS depositions, the indentations were tested vertically from top to the weld area, and the result was shown in Fig 5.7. In the NM method, the highest hardness (539VH) was measured in the final layer at the top area, where the material deposited in the last track with the equiaxed

β and colony α were formed followed a slower cooling ratio. The segregation bands underwent repeated thermal cycles attained higher hardness and followed trunk area with the columnar β and secondary α martensite structure measured a lower hardness with around 450VH.

The previous study concluded that hardened by solid solution, dislocation, and boundary hardening, which also increased the hardness compared to the BM [5.8]. Compared to the results with HS and HSS depositions, there is a clear trend that HSS deposition has the softer overall strength since rapid cooling condition followed by the faster processing, the finer Ti α-β structure with a smaller grain size was measured a lower microhardness. Therefore, the higher energy input with a slower cooling rate promotes the primary grains growth inside the structure, the solid solution and grain boundaries was improved which enhances the deposition strength in this LMwcD experiment.

According to the micro-hardness results of three typical LMwcD methods presented, it can be concluded that the NM and HS can obtain stronger mechanical properties in trunk and head zones, it is suitable to be applied into discrete cavities repair or nonstandard cylindrical building for enhanced structure integrity and strength. As for the HSS, it is a preferred deposition method to build up the joint in following laser riveting concept regarding its optimized processing time with higher productivity and reduced overall energy input with less residual stress generation and distortion. But for specific application, the load bearing conditions and failure locations are required and analysed to provide the detail for design and development of deposition strategy demanded.

5.5 Discussion

Based on the overall results presented in 5.4, further details of the microstructure and experimental processing in the depositions were discussed and analyzed in this section. First, for the grain transformations, the contributing factors of primary α grains phase change in Ti6Al4V deposition were analyzed, as well as the microstructure differences at top and weld areas applied with different strategies were observed.

Afterwards, the experimental processing parametric study was conducted, the layer height adjustment, travel speed and laser power were investigated, their influences on the geometrical dimensions of 6-layer HSS deposition were measured and discussed, the study also is the extension of 4.3.3. Finally, the potential applications of LMwcD techniques were introduced respectively from the materials, dissimilar joining, and component repair fields.

5.5.1 Microstructural analysis

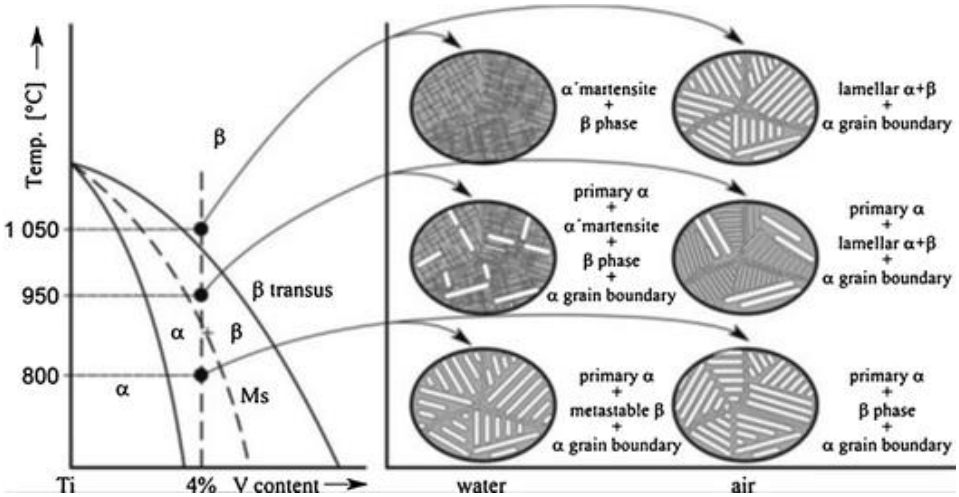

Figure 5.8 Ti6Al4V phase change and grain identification in varied cooling rate environments [9].

The general α to β transformation in Ti6Al4V under different cooling conditions was demonstrated in Fig 5.8 above, the α grain boundary normally formed in a high temperature and/or a lower cooling rate, along with the decreasing of processing peak temperature, the lamellar α+β grains can be observed below the β transus temperature, the general trend of grain evolution is shown in Fig 5.8 [5.9].

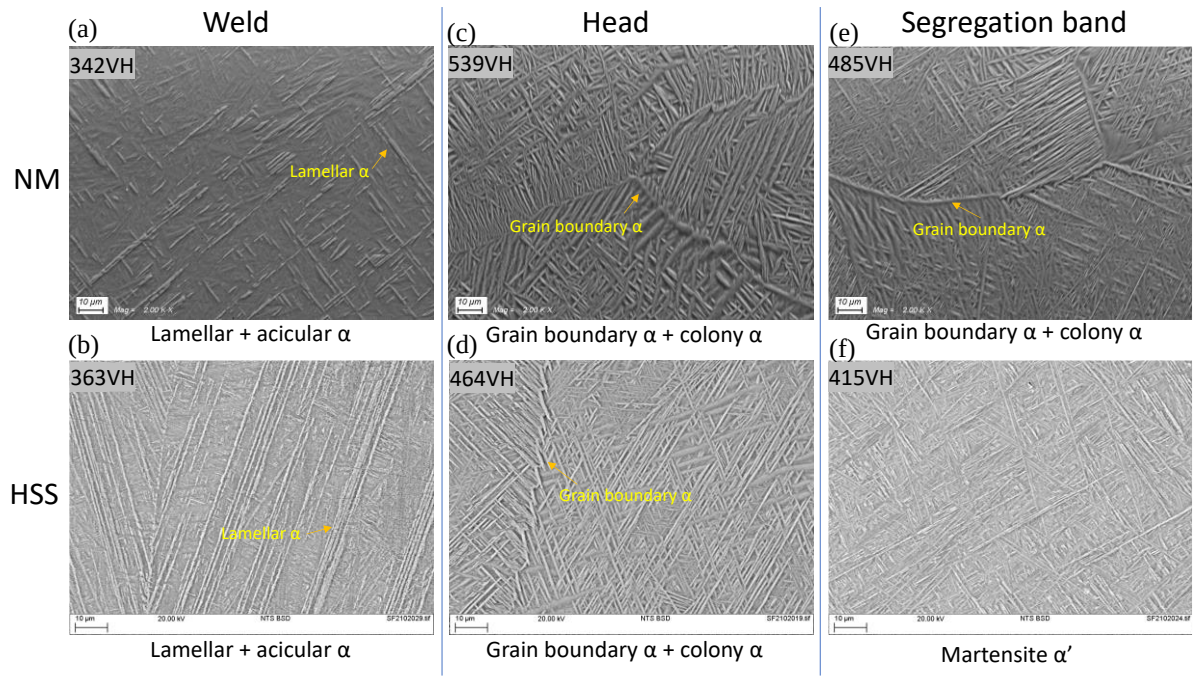

Figure 5.9 High magnification observation for NM deposition in (a) weld, (c) head and (e) segregation band areas, and similar location for HSS deposition in (b) weld, (d) head and (f) segregation band areas.

As the two typical methods of ALM and CS strategies, the high magnification SEM images of microstructural comparison between NM and HSS 6-layer deposition were presented in Fig 5.9. Near the welding area of depositions (Fig 5.9(a) and (b)), because the location under the melting pool and the temperature went through comparative lower than the melting temperature, the lamellar α (bright thin grains) and acicular α (dark area) appeared in both depositions, which shows the high agreement with [5.10]. In the deposited materials at the head areas of the depositions, because a high temperature went through the deposition process, the primary α dominantly formed instead of the lamellar grains (Fig 5.9(c) and (d)) in both depositions. Due to a higher temperature and slower cooling rate, the large primary grain boundary α surrounded by colony α were observed, which also was reported in the [5.11], However, discontinued grain boundary α and basket-weave microstructure was formed in HSS deposition mainly because of a higher cooling rate in the process. The difference caused by similar reasons also can be found in the segregation band areas in Fig 5.9 (e) and (f), a denser equiaxed β grain and wider segregation band were generated in the NM deposition, so the primary grain boundary α can be easily observed in the segregation area, but as shown results in 5.3.2, the only basket-weave

structure was generated in the HSS deposition regarding a high cooling rate of the deposition strategy.

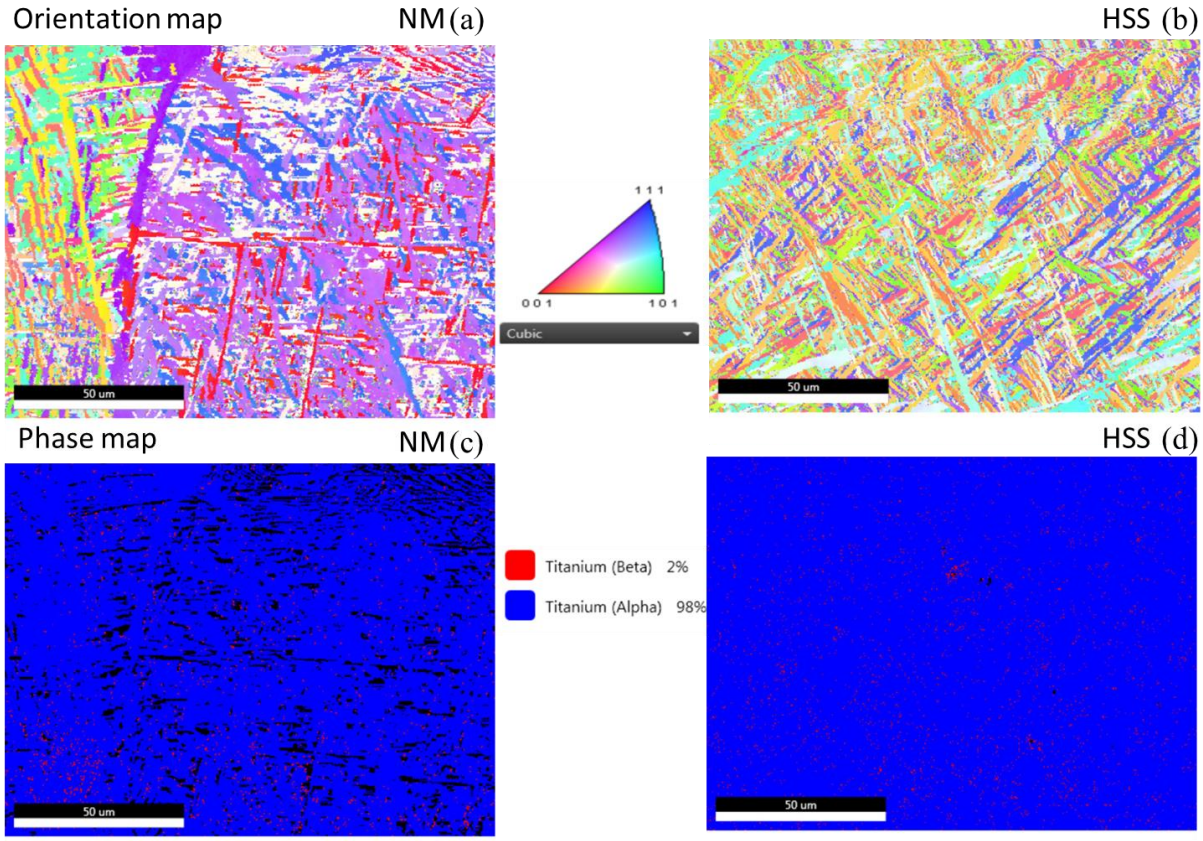

Figure 5.10 EBSD analysis of grain orientation maps at the crown area of (a) NM and (b) HSS depositions and the same location phase maps of (a) NM and (b) HSS depositions.

Further EBSD mapping at crown areas was conducted on the NM and HSS depositions to analyse the grain orientations and the phase contents. The sample is the middle cross-section of the deposition, in the orientation maps in Fig 5.10(a) of NM deposition, a grain boundary was observed, and the grain growth is the normal direction from the bottom to the top but the transverse direction in HSS corresponds to the spiral deposition path direction, the most reasonable explanation is in the NM deposition, not only the slower deposition caused a lower cooling speed, but the wash step also remelted the material and changed the cooling and grain growth direction. In addition, the phase maps (Fig 5.10 (c) and (d)) demonstrated expected results which shows the α grains were dominantly generated in both NM and HSS deposition, which confirmed the arguments in 5.3.2.

5.5.2 Processing parameter influences

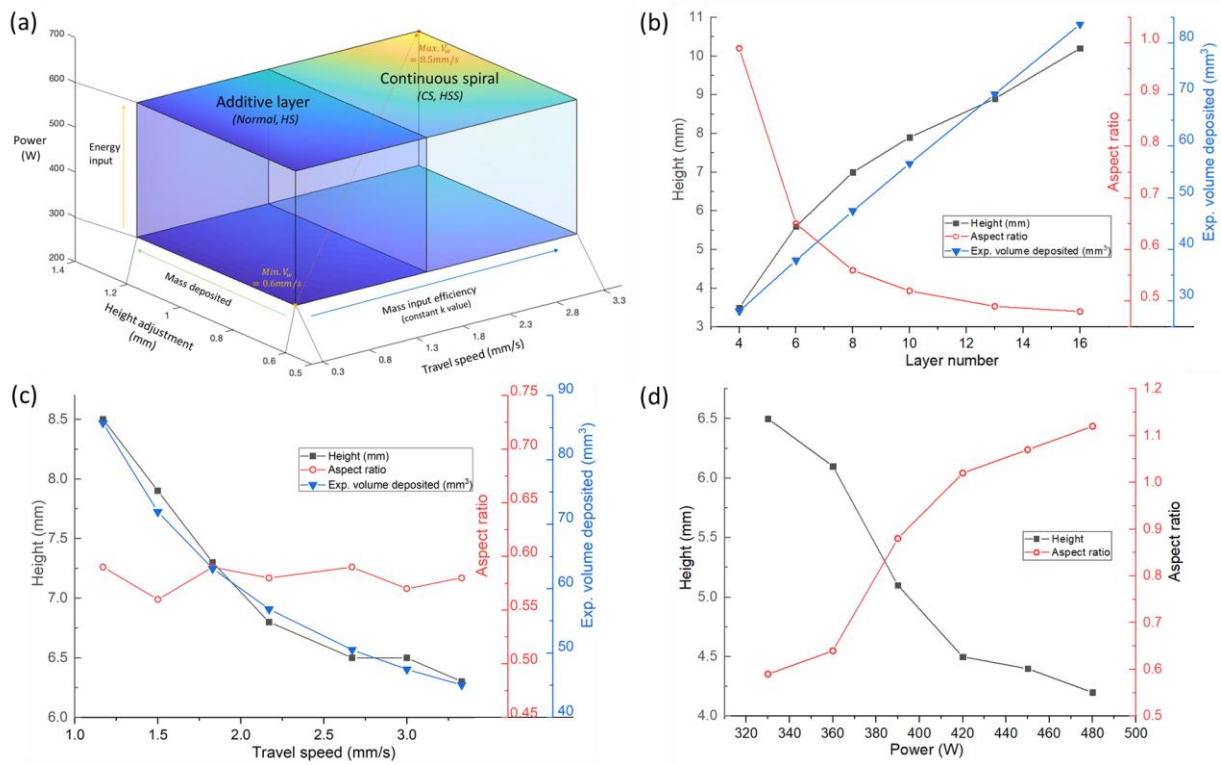

Figure 5.11 Processing parameter influences of LMwD for cylinder building, (a) processing window for HS and HSS deposition, and geometrical features of CS deposition in different parameter trials: (b) layer numbers, (c) varied travel speed in 4-8 layers processing (8-layer deposition, power=330W, WFS=7.5mm/s), and (d) varied power in 4-8 layers processing (8-layer deposition, travel speed=3mm/s, k=2.5).

The detail of power and speed relation for single layer deposition is discussed in the last section, based on it, a wide range of parameter experiments were conducted for the multiple layer depositions of ALM (Normal and HS) and continuous spiral (CS and HSS) methods, the range of specific parameters have been identified by numerous try and narrow tests. Fig 5.11(a) demonstrates the processing window of multi-layer depositions built by two route strategies, showing the processing ranges of power (300-600W), travel speed (0.3-3.3mm/s) and height adjustment (0.6-1.2mm) for layer gap. It is clearly indicated that, for the ALM methods, which has nearly half narrower in travel speed range than the which of CS methods, due to the limitation of deposition strategy, in the ALM processing, like the similar thin-wall deposition in LMwD techniques, after the cooling time, the wire and previously added layer need to remelt again in each newer-layer deposition process, it partly consumes the energy input and the higher time threshold is needed, which limited the maximum travel speed in the

layer processing. However, in the CS deposition processing, with the increase of layer deposited and energy accumulated continuously, [5.12] stated that in a higher temperature melt pool, there is a reduction of the viscosity of a liquid, which means the fluidity is increased when the temperature climbs, so the higher WFS and travel speed are more easily allowed to apply in the CS deposition processing, [5.13] also provided an obvious positive correlation between the energy input with both WFS and deposition rate. Based on this, reasonable speculation is that in the ALM method, the deposition rate can be directly improved by increasing the energy accumulation during the process, such as increasing the power and washing path time and reducing the layer cooling time.

The expected deposited material volume and solidification behaviour are combinedly influenced by power, travel speed, wire feed speed and height adjustment, during the deposition processing, power controls heat input, wire feed speed controls mass input, and travel speed controls both since it decides the total processing time. To achieve a stable CS deposition process, the adjustment is needed timely for height movement to keep the liquid bridge status, which is highly related to the solidification behaviour and volume deposited in the processing, hence the height adjustment is negatively correlated with travel speed and power, meanwhile has a positive correlation with wire feed speed. In addition, the investigation of WFS of the first welding layer is explained in the previous section, for the full range of wire feed speed did not show in the processing window due to its maximum value being changed by different layers and affected by total heat input, but current processing system applied cannot flexibly change the wire feed speed during the process, so it is difficult to measure the superior limit value of wire feed speed in the upper layer. However, the experience of parameter tests reveals that for the cylinder deposition, to achieve stable processing, the deposition ratio k should keep in a proper range of 2-5, as for the relationship of WFS with other parameters, a positive correlation is shown with all of the power, travel speed and height adjustment, therefore, the minimum WFS value measured 0.6mm/s and maximum is 8.5mm/s in this parameter study.

Further trials for higher multi-layer HSS deposition have been conducted, the geometrical dimensions are shown in Fig 5.11(b), the newly added deposition parameters set same as the 8-layer deposition (power=330W, travel speed=3mm/s,

WFS=7.5mm/s) and keep them in constants. For calculated material volume deposited, it shows a linear relationship with increasing layer number, although the height of deposition has a positive growth with layers, the slope decreases, and the situation happened as well in the decrease of aspect ratio, the assumption is that in higher layer deposition, because the power was not adjusted (reduced) properly and timely, the energy accumulation is increased along with the processing time increases, therefore, the solidification behaviour is inhibited, and it leads to the further dilution inside the deposited material, and the newly deposited layer spread down under the surface tension. So, in the process of building up a higher layer deposition, in order to obtain a proper and exact uniform cylinder feature, the balance of height adjustment, travel speed and power should be considered and adjusted precisely in the processing of each layer.

The further parameter studies of power and travel speed for the 8-layer CS deposition are conducted, because the basic start layers (1-3 layer) need a stable process to provide a proper welding quality with the substrate, so only the parameters of upper layers (4-8) are varied in the investigation. Fig 5.11(c) demonstrates the deposition geometrical features under varied travel speeds, it shows that with increasing travel speed (i.e., the total processing time is reduced), the expected deposited volume and deposition height is decreased subsequentially, but there had no marked change for cylinder aspect ratio, which is mainly because the wire deposited volume and processing time reduced simultaneously, the overview size of the whole deposition is minimized.

For the power influence, Fig 5.11(d) reveals an obvious drop of deposition height and rise of aspect ratio with increasing power input, this result shows a strong agreement with the previous research. [5.14] reported that it is the most significant factor to influence the thickness of the wall in the WAAM process, and he explained the area of melt pool is increased with energy input rise, more wire is deposited to keep the arc gap, hence which increases the bead thickness. [5.15] also observed the same relationship of multi-layer deposition in plasma transferred arc (PTA) wire deposition, the high power will lead to a fall of height and rise of width for the overview dimensions.

5.6 Conclusions

Aim to improve the productivity, HS (with ALM) and HSS (with CS) deposition methods were designed and developed in the parametric study, and proper cross-section surfaces were observed in CS depositions without the major defect (porosity and crack).

- Compared with the initial normal deposition method, the optimized HSS compresses the total time from 118 to 14s to build up a similar height feature of 8-layer deposition, the productivities of the ALM method can be improved around 6-8 times in 4-8 layers deposition.
- The processing parameters and deposition strategies influence the microstructure appearance in the multiple-layer deposition, the basket-weave was appeared in the HSS and HS since a rapid cooling in the process, on the contrary, the α colony grains were formed in the head area of NM deposition regarding the ALM process with higher heat input and followed with the slower cooling condition.
- The micro-hardness results present a clear relationship between the microstructure formation and local strength, instead of the basket wave structure observed in HSS deposition, larger grains like a primary colony and grain boundary α formed in NM deposition can provide a comparative higher microhardness because of the boundary hardening. Therefore, it can conclude that the local micro-hardness is positively correlated with the heat input and negatively correlated with the cooling rate.

Under the effect of the heat accumulation and solidification behaviours in the process, the building dimensions are not only influenced by key process parameters (power, WFS, and travel speed) but also affected by deposition strategies. As a result, energy input has a negative correlation with the deposition height, but positive with mass input.

Chapter remarks for research

Based on the initial depositions developed in the feasibility study, this chapter systematically investigated and optimized the LMwcD method. For the potential application and industrial purpose, a higher deposition rate and productivity were researched by the HSS method designed and will be selected as the rivet building method in following LR experiments.

From the academic aspect, the processing parameter relationships with the detailed microstructure formations and micro-hardness of deposition were demonstrated and concluded in this chapter. As the same material and method employed, this work provides the basic understanding and logic for methodological design and improvement in its LR applications in chapters 6 and 7.

Chapter 6 Experimental study of metals joining by laser riveting of Ti6Al4V to AA6061

The research of LMwcD has been systematically investigated in previous experiments. Chapter 4 successfully built up the multi-layer depositions applied with full-circular ALM, which proved the experimental feasibility of the LMwcD for the single rivet building on the substrate. Afterwards, a parametric study was conducted in Chapter 5, it optimized the productivity up to 8 times by HSS-LMwcD, and the analyses comprehensively revealed relationships among the processing parameters, thermal behaviours, microstructural and mechanical performances in the LMwcD. In sum, the LMwcD work provided the fundamental theories and guidance for depositing the rivet as the sound joint in the LR concept.

The first dissimilar joining experiment in this thesis is for titanium to aluminium. This chapter systematically investigated the Ti6Al4V/AA6061 LR joining technique, the chapter flow chart was shown in Fig 6.1 below. Because of the processing and material differences involved between the additive manufacturing and dissimilar materials joining experiments, LMwcD cannot directly transfer to the LR concept, a new LMwcD method was designed and developed in the 6.2 preliminary test, which can be applied as rivet building in the LR concept. After the rivet deposition, a post-wash process and its parametric studies were designed in the 6.3 methodology section, to find out the relationship between the processing parameters and joint properties. The LR joints were evaluated from microstructural analyses and mechanical tests, the results were detailed presented and discussed in 6.4.

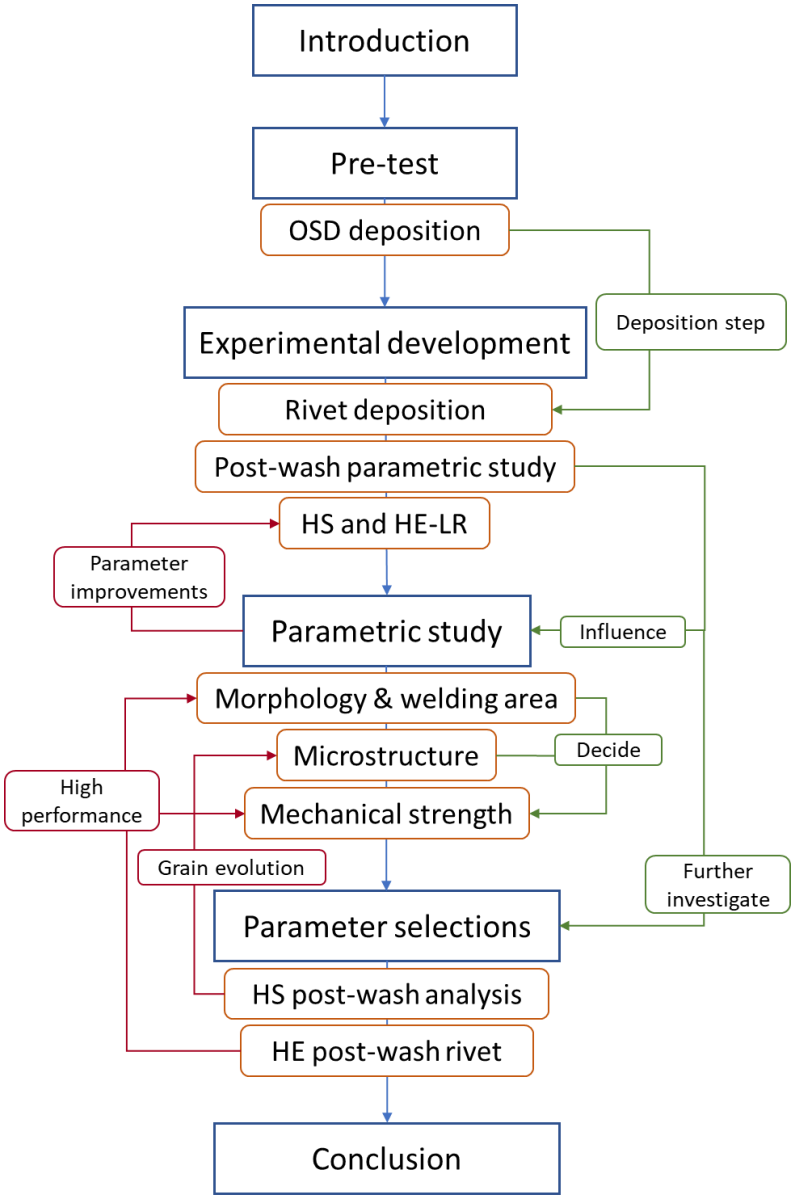

Figure 6.1 Chapter flow chart of Ti6Al4V/AA6061 LR experiment.

6.1 Introduction

Light-weight structures received increasing attention in recent years, both in the automotive and aerospace sectors where mass reduction is a fatal factor to control the industrial issues of resource depletion as well as pollutions [6.1]. Therefore, the weight reduction of body frame is a high-demand technique for transport manufacturers, as one of the feasible solutions, an advanced dissimilar joining technique is a preferable alternative selection compared to the traditional mechanical fasten in the aerospace industry [6.2]. Moreover, with the updating development of

multi-material structures, an increasing demand is requested for a proper and suitable technique for dissimilar joining [6.3].

It is a practical approach to achieve the solution of lightweight, to use titanium and aluminium alloys multi-material parts manufactured instead of the large intact titanium structure for lightweight and low-cost design [6.4, 6.5]. Fusion welding joints produced by laser brazing [6.6] and welding [6.7] are investigated for aluminium to titanium joining in recent research, but the limited efficiency is an existing challenge for current welding techniques [6.8]. Therefore, the novel approaches are designed and systematically studied, to archive the lightweight by joining the Ti/Al alloy sheets, for instance, self-piercing riveting (SPR) [6.9], friction stir welding [6.10], clinching [6.11] and adhesive bonding [6.12]. In related dissimilar joined components, a growing percentage of titanium alloy has consisted in hybrid structures, and Ti alloy rivets are employed in the aerospace sector [6.13, 6.14]. Currently, in the aerospace industry, manufacturers tend to replace rivet materials from aluminium with titanium [6.15]. But with the increasing quantity of rivets are used in the components, the mass of the whole structure is increased as well, and the diameter of the single rivet directly influences the mechanical strength of fastened joint, normally a larger rivet diameter can provide a higher strength [6.16]. Therefore, for dissimilar joining, although the drawback of adhesive and welding is their low processing efficiency, mechanically fasten also has its potential issue is that the structure weight is increased with large amount rivets used, furthermore, the joint penetrates all through the sheet and substrate, the stress concentration area is created inside the component, which is unexpected for the load-bearing structure.

The recent laser deposition research also investigated the laser metal wire deposited on the substrates with dissimilar materials, but all these studies focus on the straight-line and thin wall deposition on a major scale so far, the fabrication and result in analyses from the fusion aspect. However, there still has no related LMwD research is designed or developed on the joining application similar to mechanical fastening. The initial general concept is through the hole of the upper metal sheet, built up a pin by LMwD on the substrate, then two metal sheets can be interlocked by the deposited pin. If the feasibility can be proved, it will obtain the benefits of both high efficiencies and keeping intact substrate compared with current mechanical fasten and adhesive

bonding. Furthermore, LMwD application of multi-materials structure can make full use of the advantages of both low-cost manufacturers from AM and lightweight structure from dissimilar joining.

In this chapter, a new offset spiral deposition (OSD) method is designed and developed which can provide a higher wire feed speed (WFS), and proper welding and depositing condition through the cross-section microstructure analysis. Based on this, the OSD is applied into the dissimilar joining concept to develop a novel technology named laser riveting (LR), the Ti6al4V and AA6061 are joined, and two sheets are interlocked via an insert AMed rivet. The rivet was post-washed by different kinds of laser scanning to get an improved welding condition and crown geometrical feature, the relationships of the processing parameters, microstructural and mechanical qualities of joints were evaluated in the parametric study.

6.2 Offset spiral deposition

6.2.1 OSD motivation and methodology

Before the LMwcD is applied to the dissimilar metal joining, a new spiral deposition method named offset spiral deposition (OSD) has been designed and developed. Normally, in the previous LMwcD method, the wire transfer between wire and deposition should keep in the liquid bridge mode which provides a more stable and controllable process. However, newer designed OSD method aims to process the spiral cylinder deposition from a certain height offset (≥1mm) from the substrate, the droplet wire transfer mode will be utilized in OSD, due to the following two considerations:

(1) Break the WFS and TS limitations in the initially deposited layers, hence achieving a higher deposit rate and productivity. As discussed in 5.4.2, because of the functional flexibility of the current device, the WFS is fixed from start to end, so its value highly relates to the processing parameters of the initial layers. According to the parameter studies, it increased along with the rise of energy input and accumulation, and it still requires a proper welding condition and reduced TS by contrary, but in this scenario, the corresponding range of k factor and layer height adjustment finally result in the

subsequential limitation of WFS. In the previous HSS deposition method, due to the processing limitation in the first welding layer, the allowed maximum value for WFS is 8.5 mm/s, but in the OSD, the WFS can easily run above 20mm/s.

(2) Break the physical height limitation between the wire tip and substrate, providing higher flexibility for the application. In the normal LMwD setup (Fig 4.3), the feeding angle is recommended to range from $30°$ to $45°$ [6.17, 6.18], therefore, if the LMwcD is applied into the applications involved with the objective of an upper layer such as hole repairing and laser riveting. In these applications, the maximum height value of the hole cannot exceed the radius of the hole, otherwise, it will obstruct the wire tip touching the centre point at the substrate, which strictly limits the dimensions of the small-scale hole applications. However, OSD deposits material from a higher operation plane, which can considerably avoid the limitation of hole size and height and break the relationship between them, thus can support application in a wider dimension range.

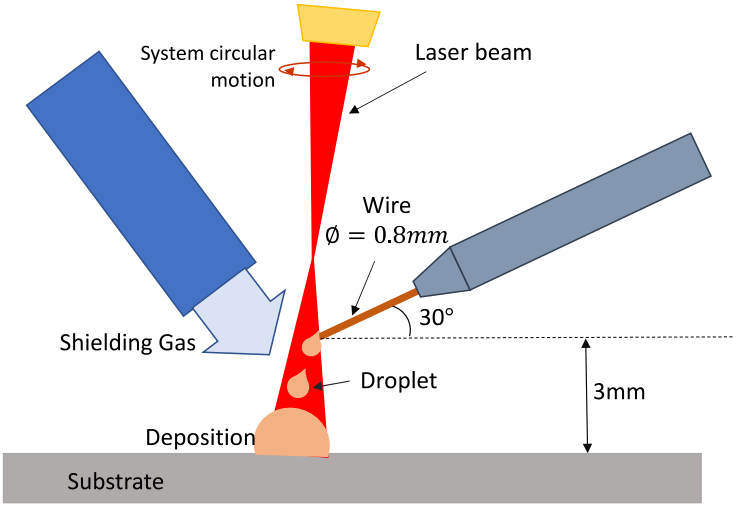

Figure 6.2 schematic drawing of the offset spiral deposition.

Fig 6.2 schematically demonstrates the OSD method, compared with LMwD, the height offset is 3mm which means the operation plan is 3mm above the substrate for all of the processing positions (wire tip, shielding and laser spot), the wire feeding angle set to $30°$. Laser mode is continuous wave (CW) mode and power is 600W, and WFS and system TS are set to 300 mm/s and 21mm/s respectively. Another different point in OSD is that compared with LMwD, the laser will be released in advance before the wire feeding, to get a better wetting condition on the substrate.

6.2.2 OSD results

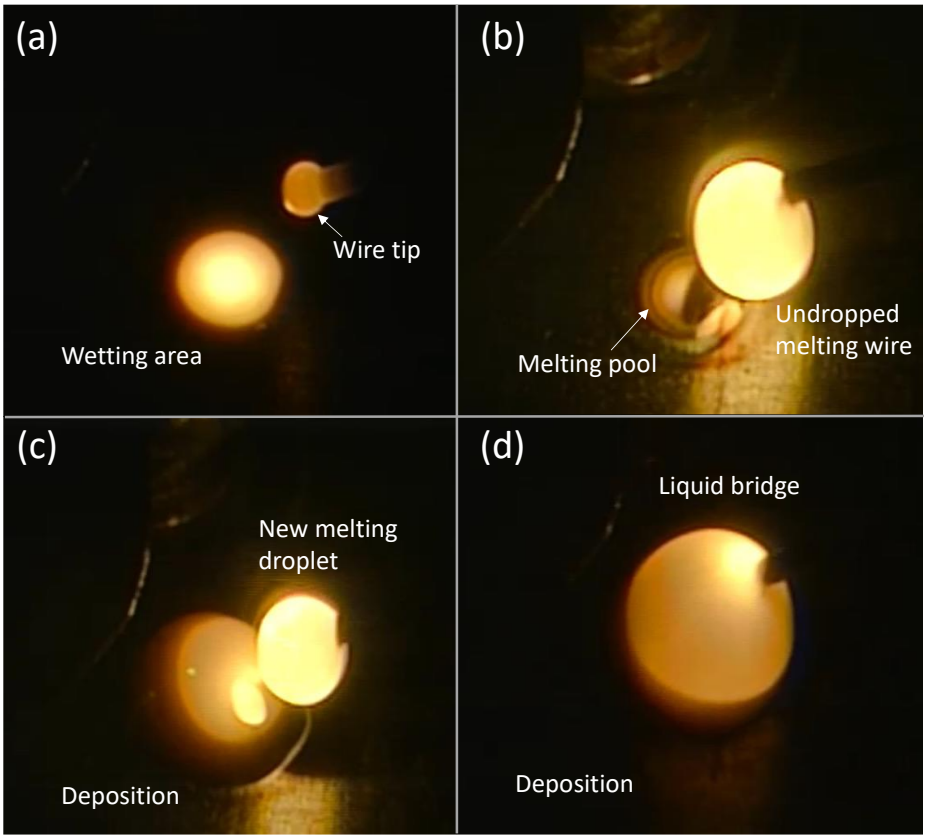

Figure 6.3 Process recording of OSD for cylinder building: (a) Surface wetting of substrate, (b) Melting droplet on the feeding wire tip, (c) Droplet feeding between the deposition and wire, (d) liquid bridge depositing.

The OSD method for cylinder building up is shown in Fig 6.3, the process is divided into 4 steps:

(a) Surface wetting. Different from the normal LMwD, the laser will be released and melt the substrate surface 1 second before feeding wire, which wetting the substrate and prepare a proper wetting condition for the upcoming welding from the melted droplet, and this step will be continued in the next step and end at when the first droplet deposited on the substrate.

(b) Droplet forming. When the wire feeding start, the feeding wire is melted and emerged to a droplet at the wire tip in the laser-scanned area. Because of the surface tension force, the melting material will not drop immediately, but the feeding wire will

continue to increase the mass and volume of the droplet, the procedure normally over 1 or 2 seconds up to the WFS input.

(c) Droplet depositing. When the mass reaches the limitation, the melted titanium droplet will drop from the tip, which is combinedly influenced by the drop adhesion and cohesion boundaries of gravity force, and combinedly with surface tension force and liquid viscosity [6.19]. The dropped material will be properly welded on the surface wetting area thus building up an initial deposition feature. Afterwards, the forming and falling of droplet depositing will repeat, but the procedure time is reduced along with the increased height of the deposited feature.

(d) Liquid bridge feeding. With the increase of building height by continuing droplet depositing, when the height reached a certain value, and the distance between the wire tip and melt pool decrease to the maximum limit of height adjustment, after the last droplet merged into the deposition, the wire-deposition connection of droplet mode will transfer to the liquid mode, then the process continues following the CS deposition method until completion.

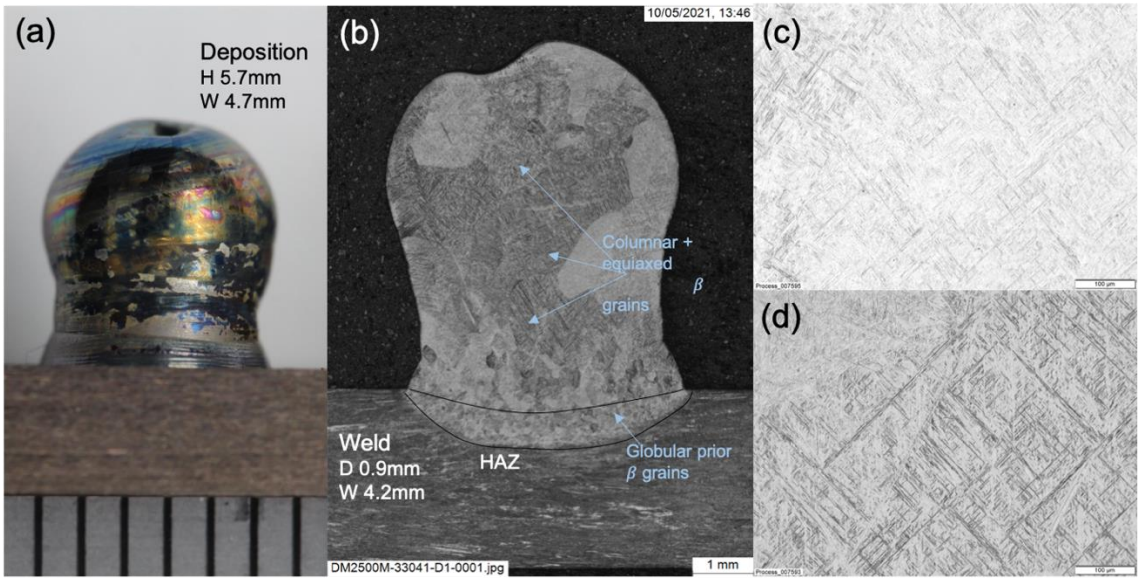

Figure 6.4 Observation results of OSD for cylinder deposition sample: (a) outlook appearance, (b) overview cross-section microstructure and higher magnification (× 100) on (c) head area and (d) middle area.

The outlook and geometrical shape of the OSD samples are close to the other cylinder features built by LMwcD methods in Fig 6.4(a), the height of the building feature is

5.7mm and width is 4.7mm, the aspect ratio is 0.82, and for the dilution and HAZ area, the depth is 0.9mm and width is 4.2mm, which is slightly smaller than the LMwcD for the same mass deposited. The cross-section microstructure overview is shown in Fig 6.4(b), and the intact surface is observed without any defect in welding line and deposition such as pore, cavity, and crack, which ensures the basic strength capability. In addition, processed by the heat treatment, α dissolved to form the β prior globular in HAZ and dilution area, which shows the agreement with 4.3.2 and 5.3.2. Although the columnar and equiaxed β grains also are shown in the middle and top areas respectively in the added material area, the segregation band was not observed in the upper layer, and a clear trend of β gain growth transformation from globular to middle columnar and final equiaxed in the vertical direction from weld to crown zone. Fig 6-4(c) and (d) show the specific basket-weave microstructure in the crown and trunk area of deposition respectively, and the acicular α is observed in the added material.

6.2.3 Discussion and conclusion

In the traditional LMwD method, the wire feeding is started with laser motion simultaneously, and the wire directly melts and welds on the substrate. But the condition is under a limited range of k-factor (normally 1-5) in the previous study, but if the k-factor increase to 6 or above, it will lead to an unstable stubbing and depositing failure in the process. In the OSD processing, because of the wetting procedure before the wire feeding, the substrate is sufficiently melted, and the offset height provides a higher fault tolerance between the WFS and TS. Therefore, compared to the LMwD, the OSD can easily offer a much higher deposit efficiency, for example, it takes 87s to achieve 8-layer expected volume deposited ($69\ mm^2$) in the normal LMwcD in 5.3.1, but applied in OSD method, for same deposited volume, it only needs 3s (1s wetting time and 2s wire feeding) for deposition and even compared with the fastest HSS deposition in 5.3.1, it also can provide 3 times WFS in the process.

From the microstructure results, the cross-section map shows a sound welding condition between the substrate and added material, which means in the wetting and droplet deposition processing, the first molten droplet is properly welded with the wetting area on the surface, moreover, continue feeding the material built up an intact cylinder deposition feature. For the deposition texture, it should be noted that due to

the special deposition strategy, the heat accumulation and thermal gradient uniform decreased in the process, the texture evolved to the equiaxed β grain dominantly, which is desirable to obtain for an improved isotropic mechanical performance in the titanium components [6.20]. Therefore, from the morphology results, the mechanical properties of rivet manufactured by the OSD method is guaranteed and improved for further laser riveting application compared with previous methods.

6.3 Laser riveting experimental setup and methodology

In this LR experimental preparation section, a similar LMwcD processing system was employed regarding the similar deposition step for the rivet building, the system components and specimens used were introduced in 6.3.1. The laser riveting consists of two steps: rivet deposition and post-wash processing, the basic processing procedures of the whole laser riveting were demonstrated in 6.3.2.1, then the parametric study of the post-wash process and optimized experiments were designed in 6.3.2.2 and 6.3.2.3 respectively, to further explore the post-processing influences on the technique.

6.3.1 Experimental system setup

In this study, same with the previous experiments, in order to properly melt the wire and deposit the desired rivet, the LMwcD equipment were employed, Fig. 6.5(a) shows the LR system setup which consists of (1) the wire feeder tube with its driven and control unit (ABICOR BINZEL, Master-Feeder-System MFS-V3), (2) IPG laser source and processing head and which mounted on (3) the 3-axis motion system to realise the OSD track for the riveting process, (4) the shielding device regarding the protection for titanium material fusion process.

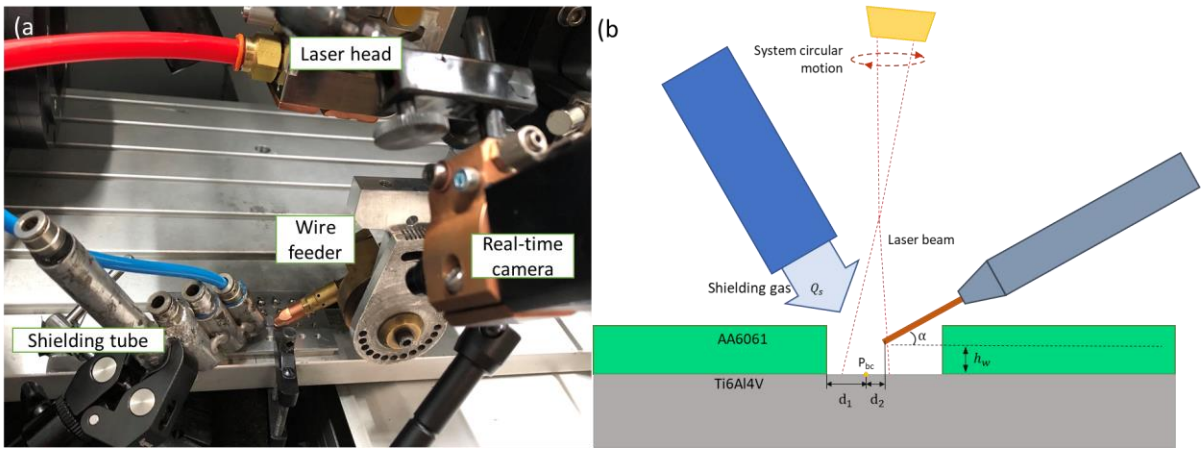

Figure 6.5 LR experimental setup for AA6061 to Ti6Al4V joining (a) processing system components, (b) diagram of the LR deposition start position.

In this dissimilar metals joining experiment, 4mm thickness Ti6Al4V (grade 5) was used as the substrate, the same material 0.8mm TC4 (grade 5) filler wire was applied to achieve a better rivet welding condition, and 2mm thickness AA6061 was used as the target joined upper sheet, shielding gas was argon with 25L/min flow rate, to prevent the melting pool from the oxidation and contamination issues.

6.3.2 Experimental processing design of laser riveting

6.3.2.1 Deposition and wash step

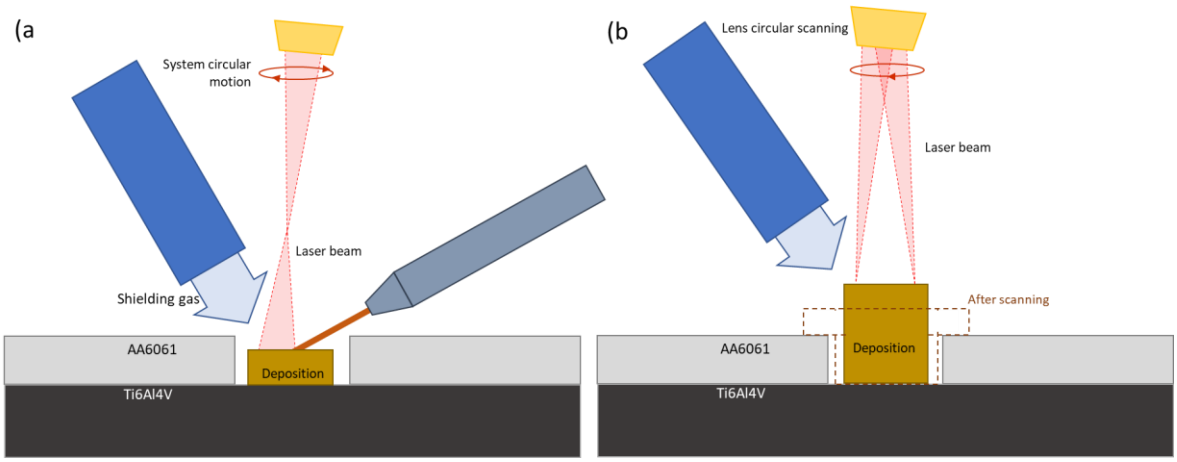

Figure 6.6 Diagram of the LR processing: (a) rivet deposition and (b) laser post-wash.

As explained in 6.2, the angle issue restricted the wire feeding of the HSS deposition in the hole, so the ODS method was developed and applied in the LR joining in this chapter. In the initial deposition step, the start deposition was demonstrated in Fig. 6-5(b), the wire offset height h_w was set to 1mm, and the feeding angle is 30°. Because

the circular deposition starts from the left point, to properly deposit the initial material fill the left area, the laser is defocused at the working plane with the 2mm beam diameter, and the beam centre position P_{bc} is in the middle of the left area which at d_1=0.5mm and the wire tip has slightly touched the beam at d_2=0.4mm.

Fig. 6.6 demonstrates the manufacturing procedures of laser riveting, which is divided into two steps. In the deposition step, a few seconds of laser scanning on the substrate to prepare for a following better welding condition with deposited wire. Then the wire keeps fixed feeding in the first couple of seconds to build up the base additive layer and continue executing the spiral deposition.

After the deposition step, a laser scanning with circular motion named post-wash procedure was implemented on the top of deposition for certain seconds to improve the welding condition and geometrical shape of the rivet and depending on the post-wash parameters, the behaviour of the rivets was present differently. Before the start of the post-wash process, the rivet position was flip horizontal to further better melt and lead the melting material to fill the hole, thus reducing the effect of the wetting issue in the deposition step.

6.3.2.2 Parametric study of post-wash

Although the OSD method applied into the LR joining concept can successfully build a riveting feature, its performance still can be improved by the post-processing procedures. A parametric study was carried out to further discover the relationship between the post-wash parameters and rivet qualities.

In this study, three parameters were designed as control variables which are processing strategy, beam diameter, scan speed and processing time. The beam diameter and the scan speed were varied, and the influence of different processing times from 4 to 16 also was tested, samples were produced and labelled through varied processing parameters are listed in table 6-1, and the considerations of each factor were explained in below.

Table 6-1 Rivets post-washed in a parametric study.

Sample	Group	Start time	Beam diameter (mm)	Wash speed (mm/s)	Time (s)
1	**1**	In deposition process (~1700℃)	2	10	4
2					8
3					12
4					16
5	**2**	After process (~80℃)	2	10	4
6					8
7					12
8					16
9	**3**	After process (~80℃)	2	1000	4
10					8
11					12
12					16
13	**4**	After process (~80℃)	0.3	1000	4
14					8
15					12
16					16

Post-wash start-time(temperature): two different post-wash strategies were designed, one is the laser is kept scanning and post-wash starts immediately after the deposition step, the post-wash starts at the melting temperature (~$1600 - 1800$℃) of deposition, and continue finishing the post-wash step, which keeps the deposition above the melting temperature then cooling down to room temperature. Another after process strategy is laser start scanning after 150s, the post-wash starts at a low temperature (~$30 - 100$℃) after cooling down, then remelts the deposition for certain seconds then cool down to the ambient temperature.

Wash speed and **beam diameter:** because the scanning moved in a circular path and the beam spot cannot cover the whole deposition, the speed and corresponding beam diameter might influence the melting and solidification dynamic behaviours in

the process, 10m/s and 1000mm/s two laser travel speed, 2mm focus and 0.3 defocus beam diameter were tested respectively in this experiment to find out the trend of results.

Processing time: there is a heat accumulation expected in the wash path with the increasing time, which leads to the trend of rivet reforming from crown to the welding area, and its threshold and extend still need to be clarified and identified.

6.3.2.3 High-speed and high-energy experiments

Based on the initial results from the parametric study in 6.4.1 and 6.4.3, according to the difference presented with the varied parameters in the experiment. Further experiments with higher laser power and beam scan speed were carried out, to explore the microstructural and mechanical effects from these two key factors, the processing time was set from 4 to 12, to observe the development of the progress, the samples were produced by high-speed (HS) and high-energy (HE) parameters were listed in table 6-2.

Table 6-2 Rivets produced by HS, and HE-LR experiments.

Method	Sample number	Scan speed (mm/s)	Power (W)	Processing time (s)
HS	17	2000	450	8
	18			12
	19			16
HE	20	1000	800	4
	21			6
	22			8
	23			12

In both HS and HE experiments, the beam diameter was fixed at 0.3mm and started the scanning after 150s cooling time. In the HS post-wash experiment, the scan speed

doubled to the 2000mm/s which expects to reveal the grain growth with the further relationship between the post-wash step and phase change phenomena at the rivet crown area. For the HE, the laser power was increased to the 800W, which aims to test the rivet performance after the high energy post-wash, it can provide the benefit of higher efficiency through reducing the processing time, however, there still has the concern that the AA6061 upper sheet might be melted by the extremely high energy input in the process.

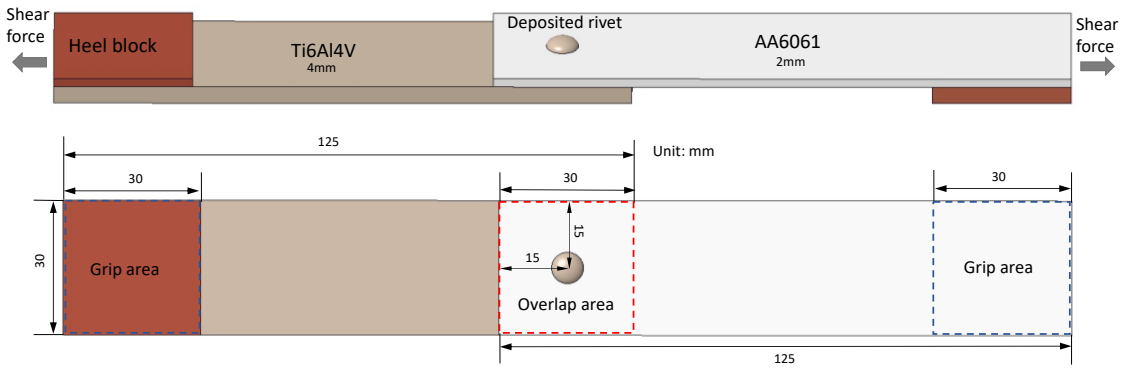

Figure 6.7 Sketch of shear test on Ti6Al4V/AA6061 LR joint.

All the samples were evaluated from their geometrical measurements, microstructural results of the sample cross-sections were analysed by the OM and SEM, and mechanical strength was measured by shear tests and micro-hardness tests. The detail of sample preparation was introduced in 3.4 and the shear test samples, the loading sketch and specimen dimensions are shown in Fig. 6.7, the load velocity is set to 10mm/min.

6.4 Results and discussion

In the results and discussion section, first of all, the outlooks and cross-section overviews of LR joints are presented in 6.4.1. In the parametric study, the processing parameter influences on the welding area dimensions, and microstructure formation in the rivets were observed and analyzed in the 6.4.1 and 6.4.2 respectively. The shear strength and micro-hardness of rivets were measured in 6.4.3, and the correlations of rivet mechanical performances with previous recorded welding conditions (6.4.1) and microstructure formations (6.4.2) are revealed and discussed. Further designed HS experiment (6.4.4) exhibited microstructure appearances of the equiaxed α grains evolution under the extreme high post-wash speed, and HE experiment (6.4.5)

reforms an outstanding welding condition in a short processing time and further unexpected welds in an excessive processing time with aluminium material. The detail of LR experimental results and their discussion was in following:

6.4.1 Geometrical dimension and cross-section overview

6.4.1.1 Rivet outlooks and cross-section overviews

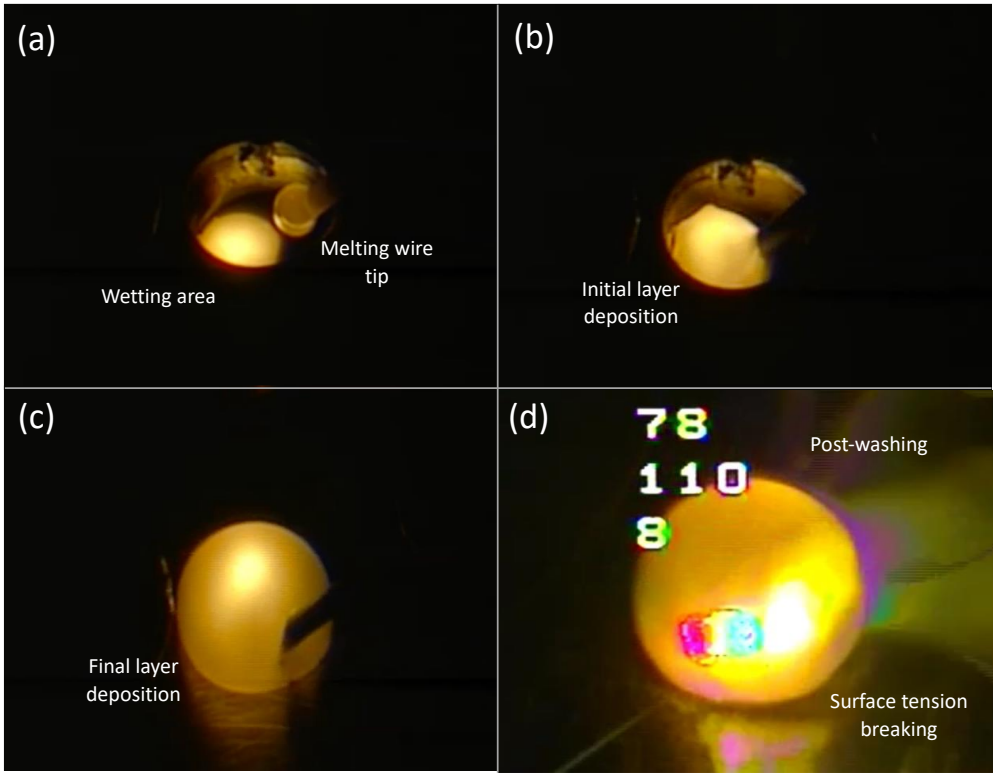

Figure 6.8 Process recording of LR joining: (a) substrate surface pre-wetting, no deposit (b) initial root deposition of the rivet, 1mm deposition height (c) rivet building at final circle layer, 6mm deposition height (d) post-wash process on the top of the rivet, 5mm final deposition height.

Figure 6.8 illustrates the processing of LR deposition and post-wash. The pre-designed OSD deposition was applied into this joining processing, a defocused laser was released onto the left side of the substrate in the hole and 2s wetting time allows laser continued melting the surface to create a proper interaction condition for wire deposition (Fig. 6.8(a)), the wetting step improved the initial wire welding quality and increased the wire deposition rate regarding the high energy input in the LMwcD as discussed in 5.5.2. Once the feeding wire was deposited onto the substrate and the first layer was established, the HSS strategy was executed by the CNC system to build

up a 6-layer deposition in the hole (Fig. 6.8(b) and (c)) gradually. To improve the welding area and the crown feature, a laser post-wash procedure was then implemented on the top of the deposited rivet, with a certain duration (4 to 12s) shown in Fig. 6.8(d). The rivets applied with varied post-wash parameters were presented, and their outlooks and overview results were shown below.

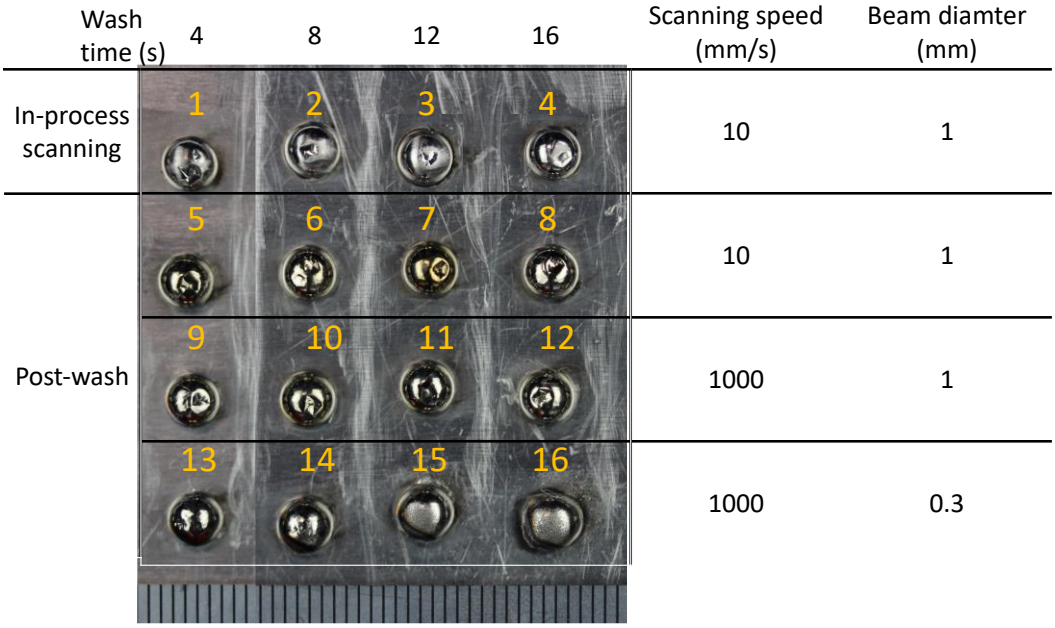

Figure 6.9 The outlooks of post-washed rivets in the parametric study from the top view.

The LR concept was applied to the Ti6Al4V and AA6061 joining, after the deposition step, an initial rivet was successfully built up and two sheets were interlocked by the joint. To further improve the joining quality of the rivet, a parametric study was designed and conducted, the outlooks of post-washed rivets against varied scanning strategy, speed, spot diameter and time were shown in Fig 6.9. Similar to the original rivet, the smooth and shiny rivet caps were formed thanks to the proper shielding condition in the process, and there is no clear appearance difference were observed in samples 1-14. But a rough surface can be seen on the rivet cap, and flatter shapes were measured in samples 15 and 16 with a high-power input and scan speed.

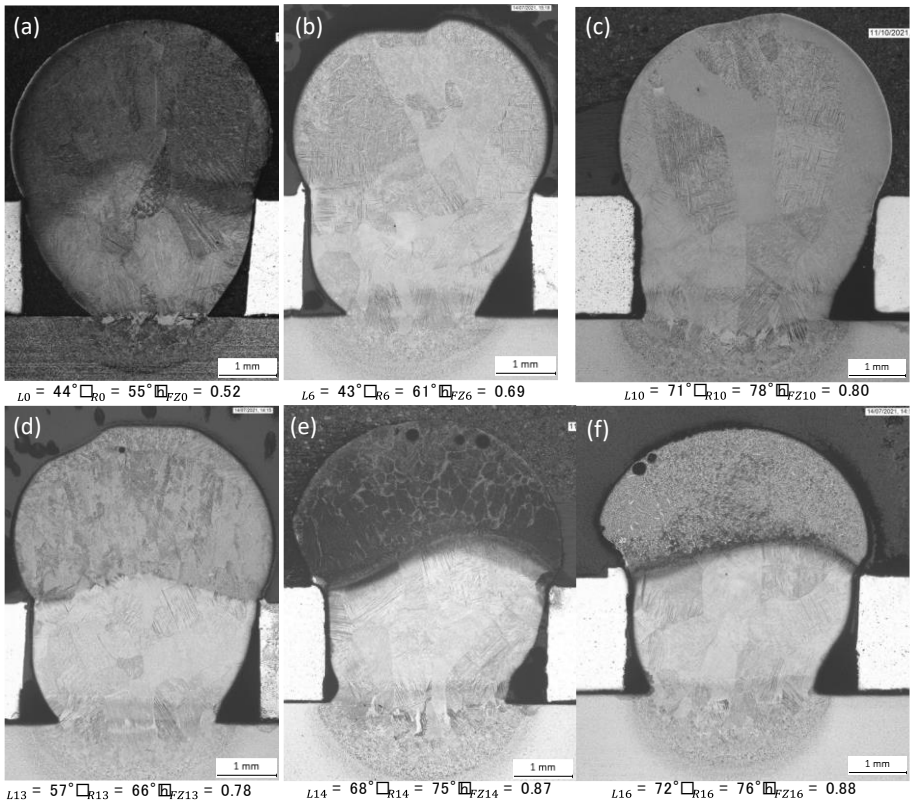

Figure 6.10 The cross-section overviews of (a) original rivet, sample number- (b) 6, (c) 10, (d) 13, (e) 14 and (f) 16.

In this experiment, multiple trials were conducted for each same parameter set to avoid the operation error, and a random rivet of each set was selected to evaluate, the rivet was sectioned along the central line with 0.1mm measurement error in this study. In order to demonstrate the influences for parameters, the cross-section overviews of the original rivet, 8s fixed-time processed samples with different factors (number 2, 6, 14) and 0.3mm fixed beam spot with various scanning times (number 13, 14, 16) were presented in Figure 6.10.

From the cross-section views of rivets, more information inside the hole and deposition was found under the OM photograph, compared to the initial rivet built up in the deposition step, there are two most obvious differences that can be identified in the post-washed rivet, one is the crown area structure due to the varied parameters applied in laser processing at the top of deposition, and another is the welding area at the root of rivet regarding the high energy input and accumulation caused the remelting of rivet in the post-wash processing. Further detail about the observed difference is presented and discussed in this and the following sections.

6.4.1.2 Geometrical dimensions of the welding area

Due to the heat input and accumulation in the post-wash process, the originally deposited rivet was completely remelted during the post-wash process, as shown in Fig. 6-11(b), the fusion zone (interface identified at the roots of columnar β grains) was enlarged in post-washed rivet, which proves that the deposited material was fully melted and diluted into the new molten pool formed in the substrate, and the enlarged HAZ area also can indirectly confirm the remelting and enlarging of fusion zone at the weld area, besides, this phenomenon also is consistent with the corresponding developed LR numerical simulation results in Chapter 9.

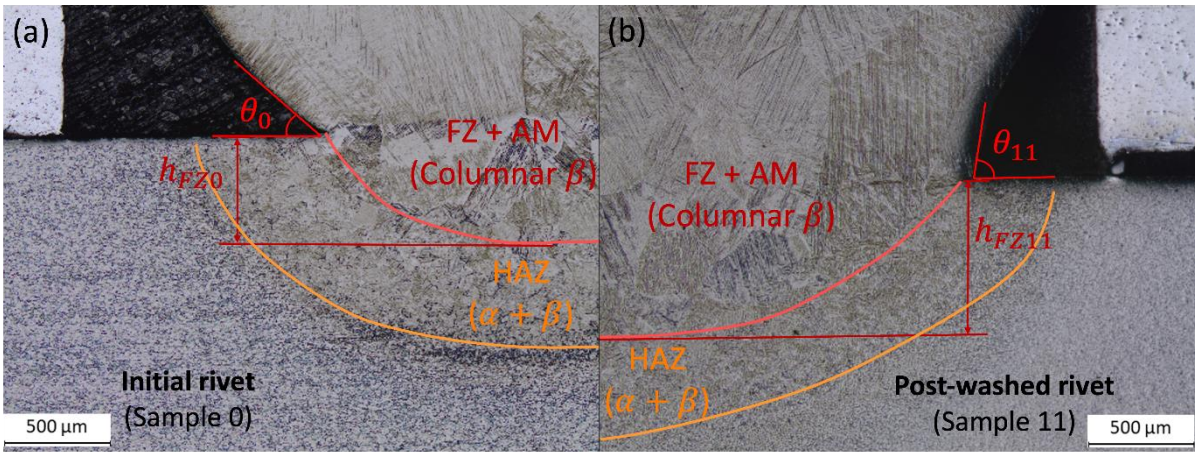

Figure 6.11 Welding area comparison between (a) original rivet and (b) post-washed rivet – sample 11.

The example comparison at the welding areas between the original and post-washed rivets (sample 11) are shown in Fig. 6.11(a) and (b) with clear differences marked. The combined effects of high-speed scanning melting the rivet deposit, and gravity condensing the molten material resulted in the molten liquid flowing downwards. This enlarged the welding area and reformed the geometrical shape of the rivet, resulting in a tighter fit onto the trunk (AA6061 upper sheet). Near the weld area, larger HAZ and FZ areas were observed in Fig. 6.11(b), and the measured FZ depth was increased from $h_{FZ0} = 0.52\text{mm}$ in original rivet to $h_{FZ11} = 0.80\text{mm}$ measured in the post-washed rivet. Besides, the weld diameter was increased from $\mathrm{D_{w0}} = 1.97\text{mm}$ in the original rivet to $\mathrm{D_{w11}} = 2.89\text{mm}$ in the post-washed rivet, the corresponding welding area was expanded from 3.05 mm^2 to 6.56 mm^2 by the post-washing process. Therefore, after the post-wash process, the larger fusion zone and reformed rivet

shape improved the welding area, which led to enhanced shear and pulling strengths of the rivet [6.21, 6.22]. From this parametric study, the average welding diameter was measured with a 50.8% increase. In addition, compared to the original rivet in Fig 11 (a), the re-melting process consolidated voids and gaps between the deposit and upper sheet were shown in Fig 11 (b), and the reformed deposition shape raised the deposition wetting angle θ.

After the post-wash, compared with the original rivet, the wetting angle at deposition weld was increased from $\theta_0 = 44°$ to $\theta_{11} = 81°$ in the post-washed rivet, which improves the load-bearing condition [6.23, 6.24]. The wetting angles are noted in the Fig 6.10, a clear increase of angle values in both sides can be seen from the original rivet to the post-washed rivet. The increased wetting angles optimize the shear strength regarding the microstructural zones and force analysis. For instance, shown in the weld comparison (Fig 6.12), along with extended lines of rivet roots, the horizontal load is transferred in the boundary area between HAZ_{β} and FZ zones, which weakens the joining strength [6.23]. On the contrary, the shear load is almost vertically transferred into the $HAZ_{\alpha+\beta}$ and base material in the sample 11 as presented in Fig 6.11(b), the denser microstructure hances the joining strength and local mechanical performances of the joint [6.25].

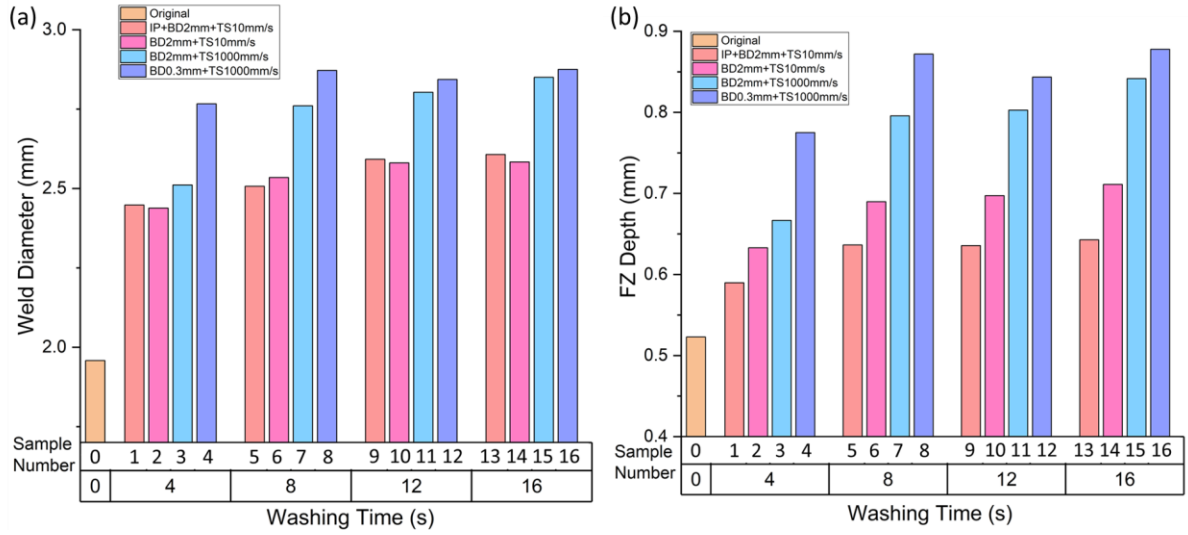

Figure 6.12 Welding geometrical dimensions for different post-wash rivets in a parametric study of (a) weld diameter and (b) fusion depth.

The weld area dimensions of rivets produced in the parametric study were plotted in Fig 6.12, which illustrates the relationships between the geometrical size of the

welding area and the processing parameters. All welding areas of post-washed rivets were enlarged along with the increase of scanning time, but limited by the scanning speed and the defocus of the laser beam, there is almost no further expansion of group 1 and 2 rivets, and post-washed rivets after 12s, these two methods show a very similar weld diameter, but the post-wash method generated a deeper FZ depth thanks to the flipped laser angle and adjusted start position, more energy was input in the deposition. Due to the faster laser scanning speed improving the melting and solidification status of the deposition, groups 3 and 4 presented a much larger FZ area since the energy continue reforming the welding condition after longer scanning. Furthermore, combined with the effect of beam scanning at focus position concentrated the energy and raise the heat input, the dynamic driven force and high heat accumulation inside the group 4 depositions not only broke the surface tension of the rivet crown but also further remelted the welding area compared to the group 3. Nevertheless, it is important to note that the sample 14-16 present the very close FZ sizes, it is mainly because the surface tension was broken under a certain period post-scanning (8s in this case), the melting material was touching the upper aluminium resulted in a mass heat transfer from the deposition which limited the fusion zone expanding.

6.4.2 Microstructure analysis

6.4.2.1 Welding area

Besides the morphological differences discussed, further microstructural changes also were observed at the rivet welds manufactured in a parametric study. Fig 6.13 presents the detailed differences of the grain structure in rivet subjected to the different post-wash strategies with same 8s scanning time. Under the slow speed scanning with 10 mm/s, the globular β grains were directly transformed to the columnar β grains around the top interface of the HAZ_{β} area. In the higher magnification SEM observation in Fig 6.13, sample 2 and 6 shows a similar structure with the welding area in HSS deposition in Fig 5.10, but with a thicker lamellar α regarding the higher energy input.

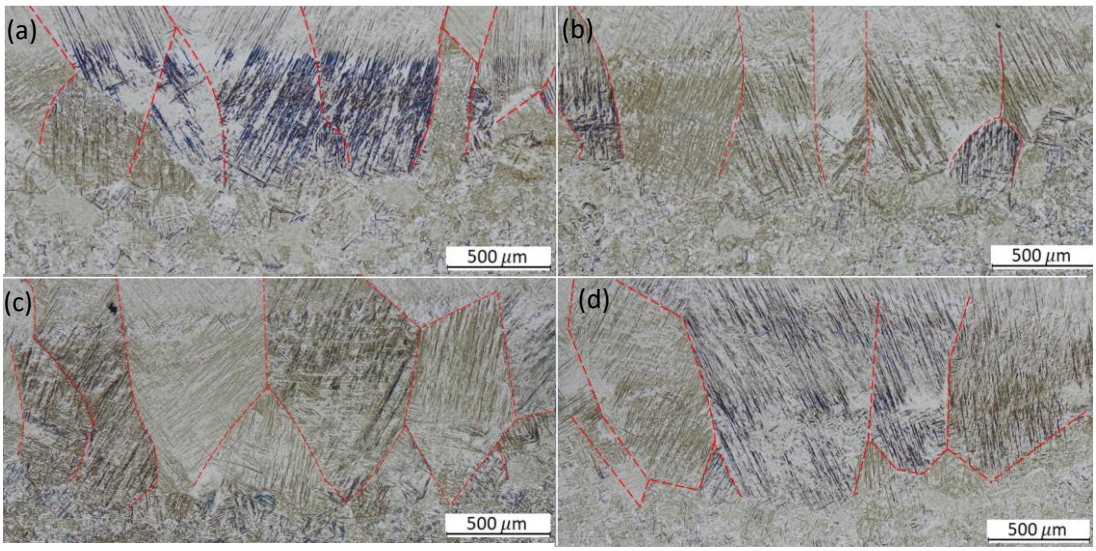

Figure 6.13 OM observation (25X) of the FZ interface at weld areas of rivet sample (a) 2, (b) 6, (c) 10 and (d) 14.

Compared to le 2 and 6, sample 10 and 14 with 1000mm/s laser scan speed present the grain size and structural differences near the fusion zone. The thinner grain roots of columnar grains were measured, with the equiaxed β were formed below the columnar grains due to the high energy input, the denser grain boundaries might hence the joining strength [6.26]. Fig 6.14 (d), (e) and (f) show the detail inside the equiaxed β, the lamellar α gathered around the grain boundaries and it can be observed that the thicker lamellar grain is measured along with a longer scanning time of higher heat accumulation.

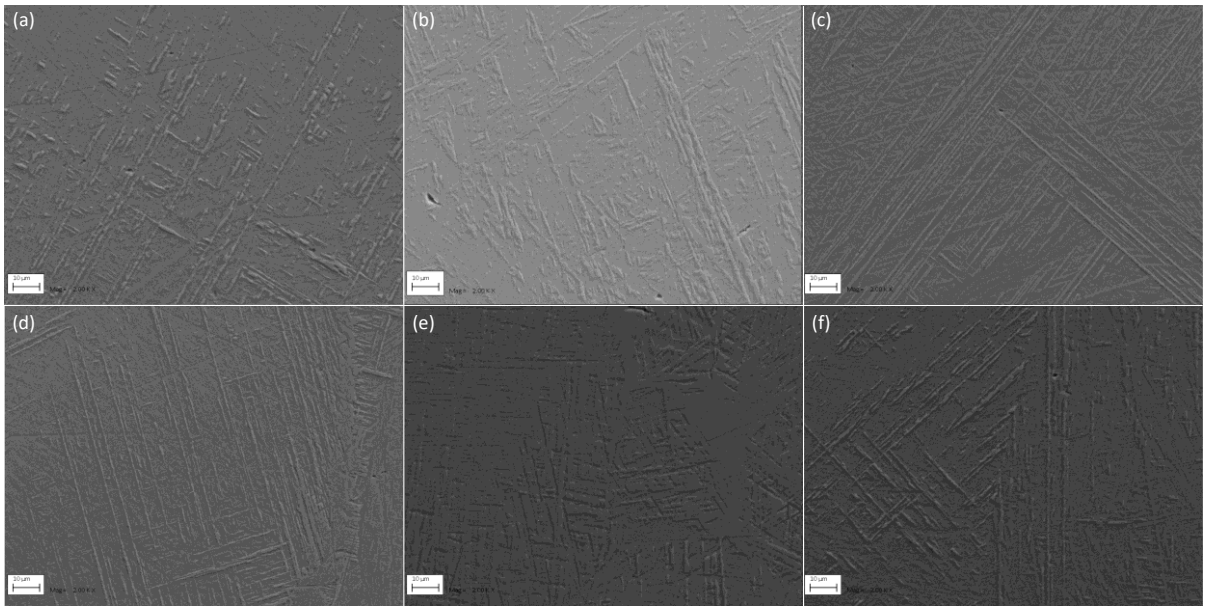

Figure 6.14 SEM observation (2000X) of microstructure at weld areas of rivet sample (a) 2, (b) 6, (c) 10, (d) 14, (e) 15 and (f) 16.

6.4.2.2 Rivet crown

The original and group 1, 2, and 3 rivets present similar cross-section overviews with OSD features in 6.2, the $HAZ_{(\alpha+\beta)}$, globular, columnar β were formed in turn from bottom to the top of rivets. From the overviews in Fig 6.10 a very soft segregation band were observed in the original, sample 6 and 10 rivets, but which is obvious in the group 4 rivets. Because the rivet is fully remelted in the post-wash process as explained in the previous welding section, the segregation band does not stand for the remelted and originally deposited material but identifies the interface of cooling rates went through between the crown and trunk area, which also decides the microstructural appearance formed in the crown area. In the post-wash processes of sample groups 1-3, due to a wider 1mm beam spot with a relative lower emery intensity, the regular Widmanstätten structure observed in the crown area is consistent with the previous LMwcD-HSS and OSD cylinder.

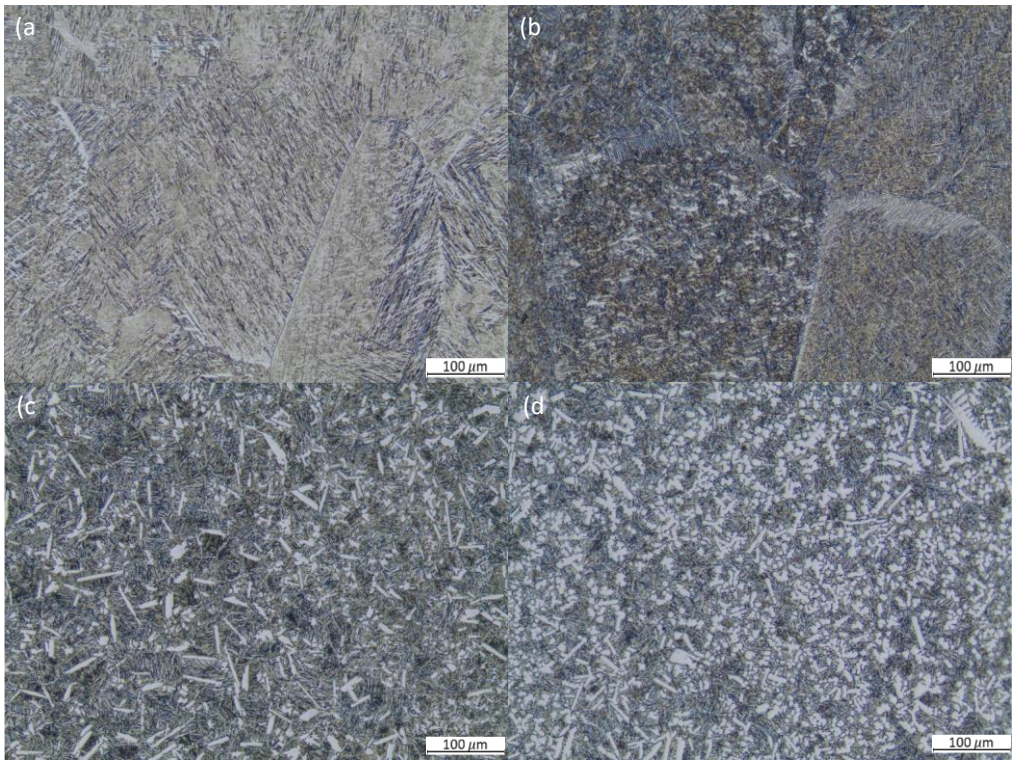

Figure 6.15 OM observation (25X) of crown areas of rivet sample (a) 13, (b) 14, (c) 15 and (d) 16.

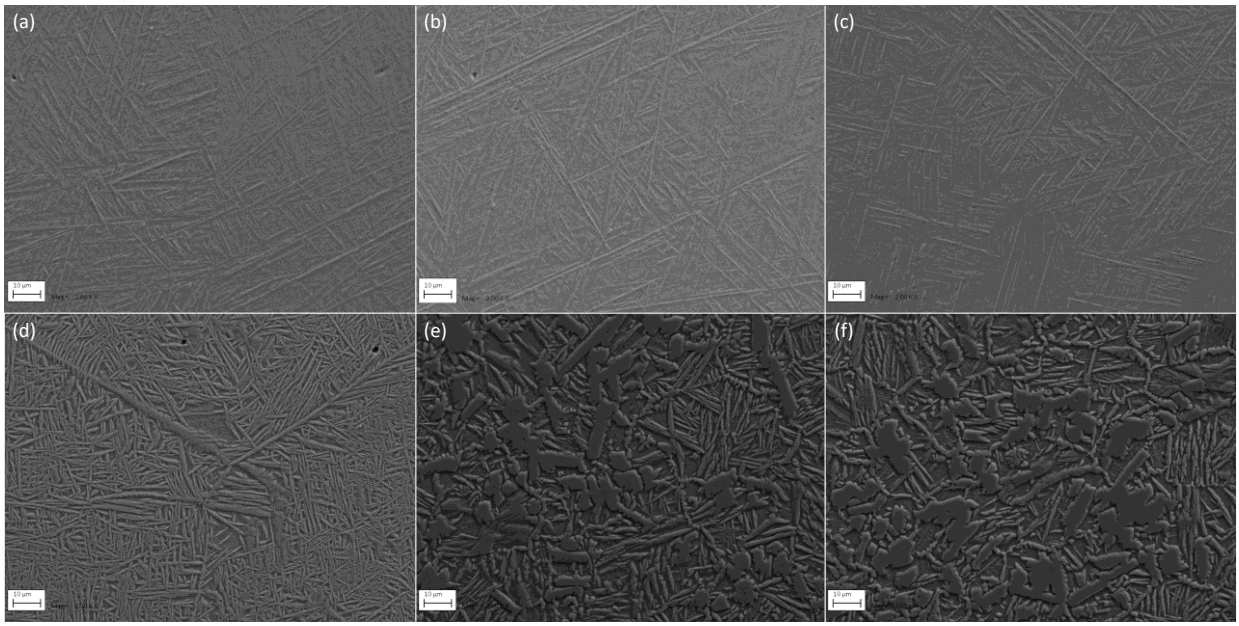

Figure 6-16 SEM images (2000X) of microstructure at crown areas of rivet sample (a) 2, (b) 6, (c) 10, (d) 14, (e) 15 and (f) 16.

The laser post-wash processing of group 4 was worked with 0.3mm at the focus position, the comparatively high energy was released on the rivet crown, combined with the dynamic driven force by high scanning speed, the surface tension of the remelted deposition was broken, thus the heat interaction and transfer with the aluminium upper sheet resulted in the huge differences of the cooling rate at the crown area and trunk area. In the 4s scanned sample 13, the colony α grains was transformed from basket-weave structure since the high heat input, but it is worth noting that, as shown in Fig 6.15 and Fig 6.16, an obvious phase change occurred in the crown area of the post-washed rivet after longer period scanning in sample 15 with 12s and 16 with 16s, where plenty of dense primary-α like grains was formed instead of the colony α grains. This is very rarely recorded in reports on LMwD research.

One possible assumption is that the re-melting status of the material had been maintained in the post-scanning process, then followed by a slow air cooling from a high temperature (above 2000℃) to the ambient one. This special thermal history caused the formation of the primary-α in the re-melted crown. Another possible scenario is that a small part of the aluminium surface was cut by a high-velocity laser beam in the post-scanning, the particles were splashed into the melt pool, and this increased the aluminium fraction in the material which enhanced the stabilization of

the α phase [6.27]. Further metallurgic and chemical analysis and testification had been conducted on the HS-LR samples on these aspects.

6.4.3 Mechanical properties

6.4.3.1 Shear test

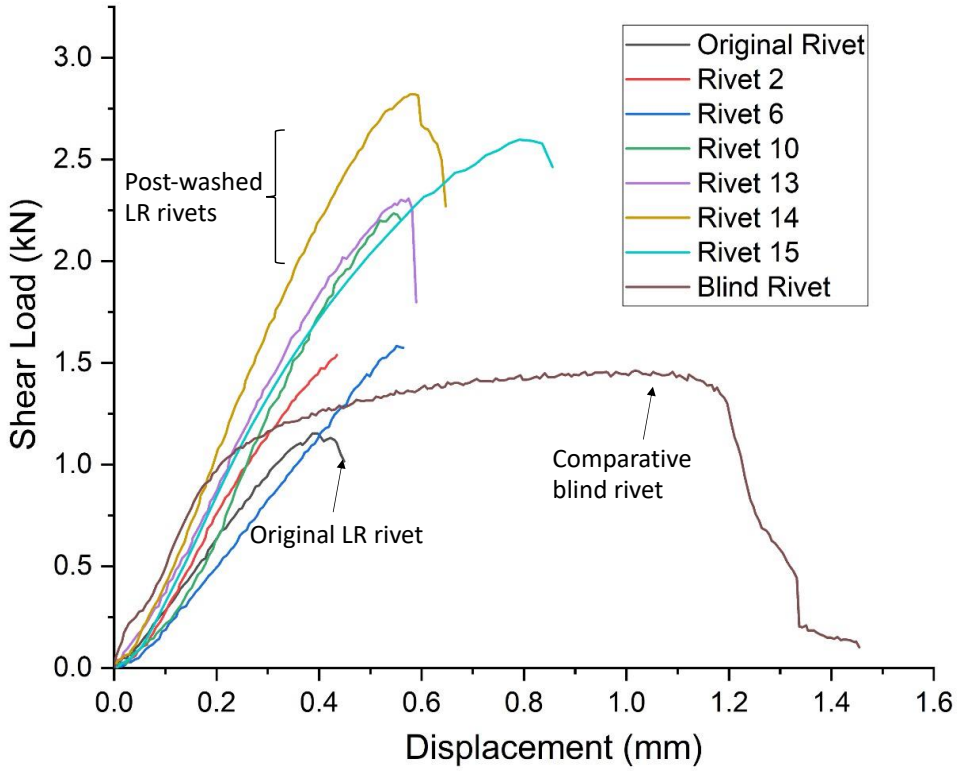

Figure 6.17 Shear tests of 4mm diameter unwashed, post-washed LRs and mechanical blind rivet.

Because currently there is no commercial used titanium rivet for the hybrid joining aim, instead of it, as one of the commonly used mechanical rivets in aerospace applications, a 4mm 6 series blind rivet made of aluminium alloy body and carbon steel mandrel, was selected for comparison [6.24]. The shear tests of unwashed, post-washed LR rivets and the blind rivet joints were carried out. The corresponding load-displacement curves are plotted in Fig 6.17.

All of the rivets failed near the welding and connection area on the substrate surface where the shear force was primarily loaded. Because of the superior ductility of forged aluminium, the blind rivet showed the largest elongation (1.02mm) compared to the

titanium LRs. However, for the peak shear strength, due to the higher strength of Ti6Al4V alloy, the unwashed rivet still reached 1.28kN, close to that of the blind rivet at 1.46kN. And thanks to a sounder welding connection enhanced, the post-washed rivets improve the overall performance, as the example of sample 14, its load-displacement curve not only presents a reasonably good ductility with 0.6mm maximum displacement but also showed the highest peak shear load of 2.82kN, an increase of 120.3% and 93.2% compared to the unwashed LR and the blind rivet, respectively. The benefit of post-wash was clearly demonstrated.

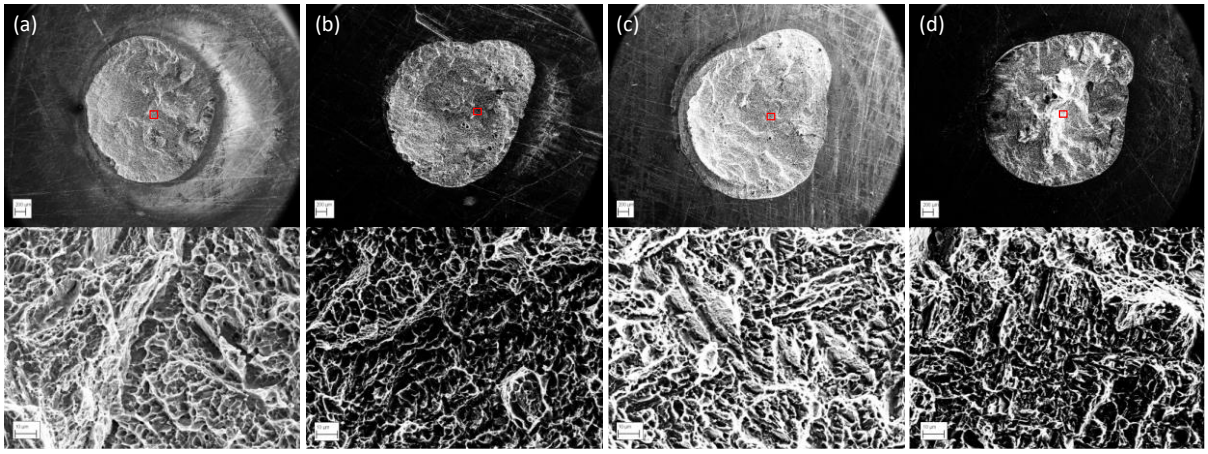

Figure 6.18 fracture surface of (a) original rivet, (b) sample 6, (c) sample 10 and (d) sample 14.

The comparison results from Figure 6-17 also illustrates the strength difference of rivets manufactured in the parametric study, the results hardly descript the exact relationship between each post-wash parameter with the shear strength, but they still show a similar trend with the welding area, especially with the FZ depth plotted in Fig 6.12. The fracture surfaces were photographed in Fig 6.18, all of the rivet failure at the bottom interface of the FZ area, and the fracture depth increased from the original to sample 14 rivets, which proved the relationship between the joining strength with the FZ depth from the morphological aspect. For further detail presented in the Fig 6.15, due to the shear force transversely tested on the rivet, all the fracture surfaces present the brittle mode in the fracture surface, therefore the microstructural refine and improvement in FZ also promotes crack initiation and fracture damage in this case [6.28].

Although the welding area and load bearing conditions have been improved by laser post-wash in shear test results, from the macrostructure overviews shown in the Fig

6.11, the clearance hole is not completely filled by remelted rivet. Under the wetting, liquid viscosity and surface tension force conditions, the gap between Al sheet and rivet was not fully filled by remelted material, it needs to be noticed that which will harm the fatigue strength of the joint, and this geometrical impact should be minimized or eliminated in future optimization research of this technology.

6.4.3.2 Micro-hardness

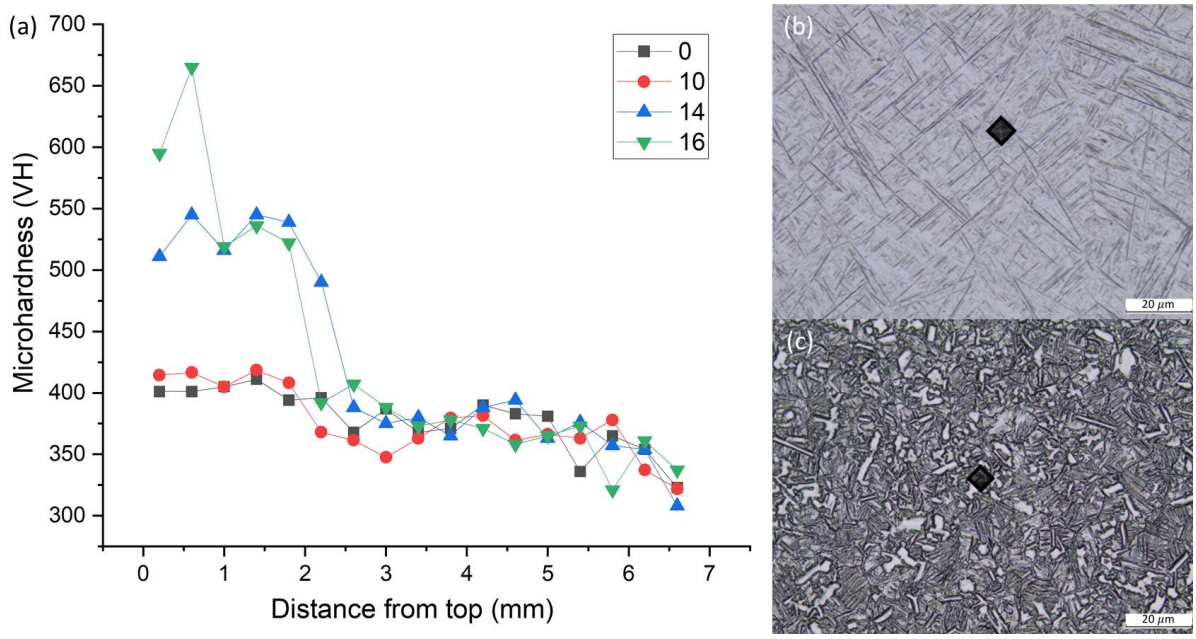

Figure 6.19 Micro-hardness comparison between original and different post-washed rivets.

The grain phase differences between the rivets without and with the post-wash are also reflected in the micro-hardness curves in Fig 6.19, which illustrates that the group 4 post-wash process enhances the hardness at the crown area. The original rivet, sample 10 and show similar results with HSS-LMwcD deposition since the same basket-weave structure formed, and sample 13 is consistent with NM-LMwcD deposition regarding the same colony α grains in the crown area. But in the group 4 rivets with longer scanning time, due to the difference presented on the microstructure with the previous rivets, the crown area of sample 16 was measured with the highest hardness with an average of 630 HV0.1 increased 56% compared to the average of 402 HV0.1 in the unwashed rivet. In the laser wire deposition for the Ti6Al4V, grain boundaries, and dislocation distribution of the α and β phase structures, appeared in the microstructure dominantly influence the hardness [6.25], therefore higher value in

group 4 post-washed crown area is mainly because the large crowded primary α grains formed applied by high speed and focused laser scanning.

The micro-hardness of the original and post-washed rivets do not show a significant difference because due to similar microstructures. As such they should have a similar stress-strain curve at the welded location. However, the post-washed rivet has a larger welding area (Fig 6.12), thus in the load-deformation curve, the maximum shear load of the post-washed rivet is higher than that of the original rivet, in accordance with their welding areas.

6.4.4 HS post-wash rivets

After the rivets were evaluated in the parametric study, the primary α grains appeared in the group 4 rivets with an increased laser scan speed and a long time. Therefore, in this section, the scanning speed was twice as it set in group 4 with 2000 mm/s to reveal the further detail of surface-breaking behaviour and newly formed α grains.

(1) Cross-section overviews

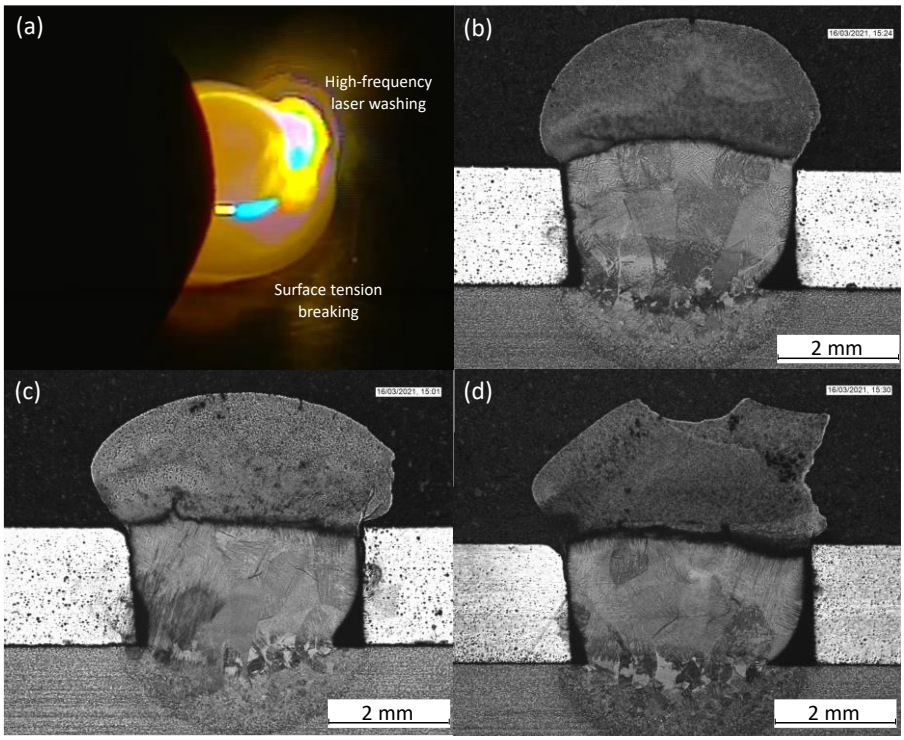

Figure 6.20 (a) Process record and cross-section overviews of HS post-washed LRs scanned with (a) 8s, (b)12s and (c) 16s.

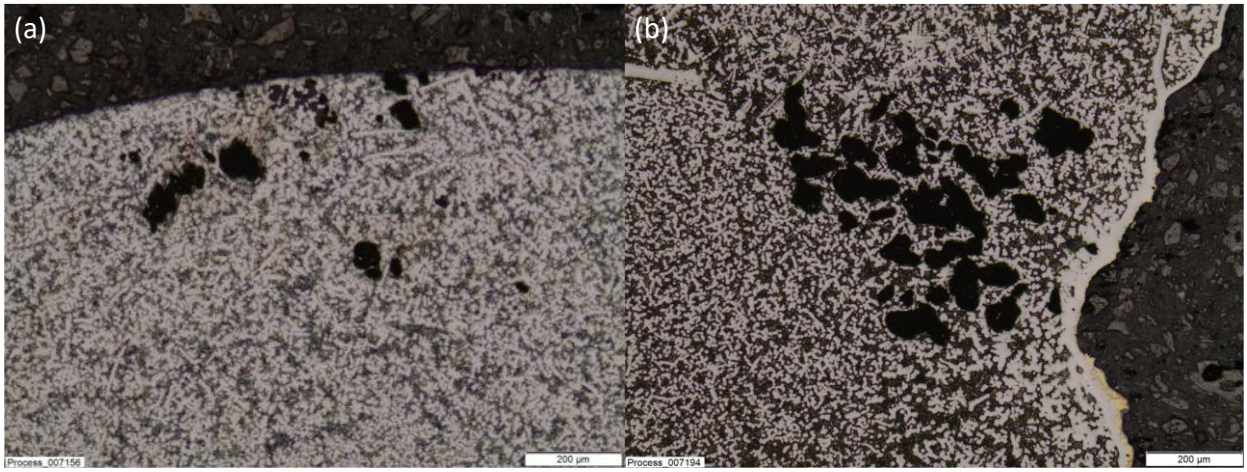

Figure 6.21 Major defects observed in (a) sample 15 and (b) sample 16.

Compared to the group 4 process, a larger melting crown shown in Fig 6.20 (a) process record demonstrates that the surface tension was further broke because of the higher scan speed with a stronger dynamic force inside. Besides, the equiaxed α grains were generated earlier as well as with a larger number in the HS post-washed rivet. Due to the breaking of surface tension, the segregation band appearing, welding area expansion, and limitation also were observed in the HS post-washed rivets, but the crown shape was reformed flatter under the higher scan speed, which expects to provide a better interlock. However, the 0.3mm laser beam spot with a high scan velocity leads to an intense material interaction, the pores were formed in the group 4 rivets in Fig 6.10 when the speed is 1000 mm/s, after the speed increased to 2000mm/s, although the laser motion monitored in Fig 6.20(a) was more uniformly distributed in the processing, the major cracks and pores still are found at the edge of the cap (Fig 6.21), and the crown material was impacted and seriously damaged during a longer time processing after 16s (Fig 6.20(d)), and the defects are most likely formed along the edges of the primary grains due to the residual stress in the cooling step.

(2) Microstructural analysis

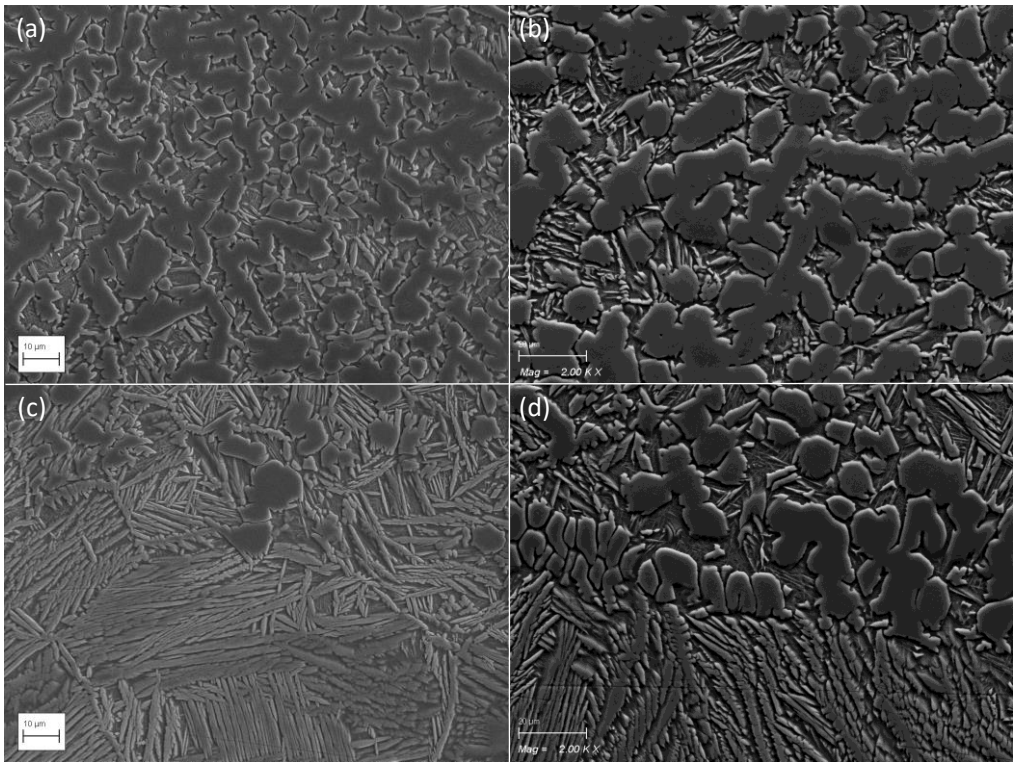

Figure 6.22 High magnification microstructure observation (2000X) at crown areas of the sample (a) 17, (b) 19, and segregation bands of (c) sample 17 and (b) 19.

The higher magnification comparison photographs between samples 17 and 19 on crown and segregation areas were shown in Figures 6.22. It presents a clear trend that the density and grain size of α the structure was increased along with the prolongation of scanning time. As explained in the previous section, the high density of equiaxed α grains were very rarely appeared in the existed normal LMwcD, but the similar not exact same situations were recorded in a few literatures mainly about casting and post-heat treatment for titanium material [6.29, 6.30]. Therefore, the primary grain structure most likely formed in this special heat treatment under the high temperature (>1605℃) environment with an extremely high dynamic driven force condition.

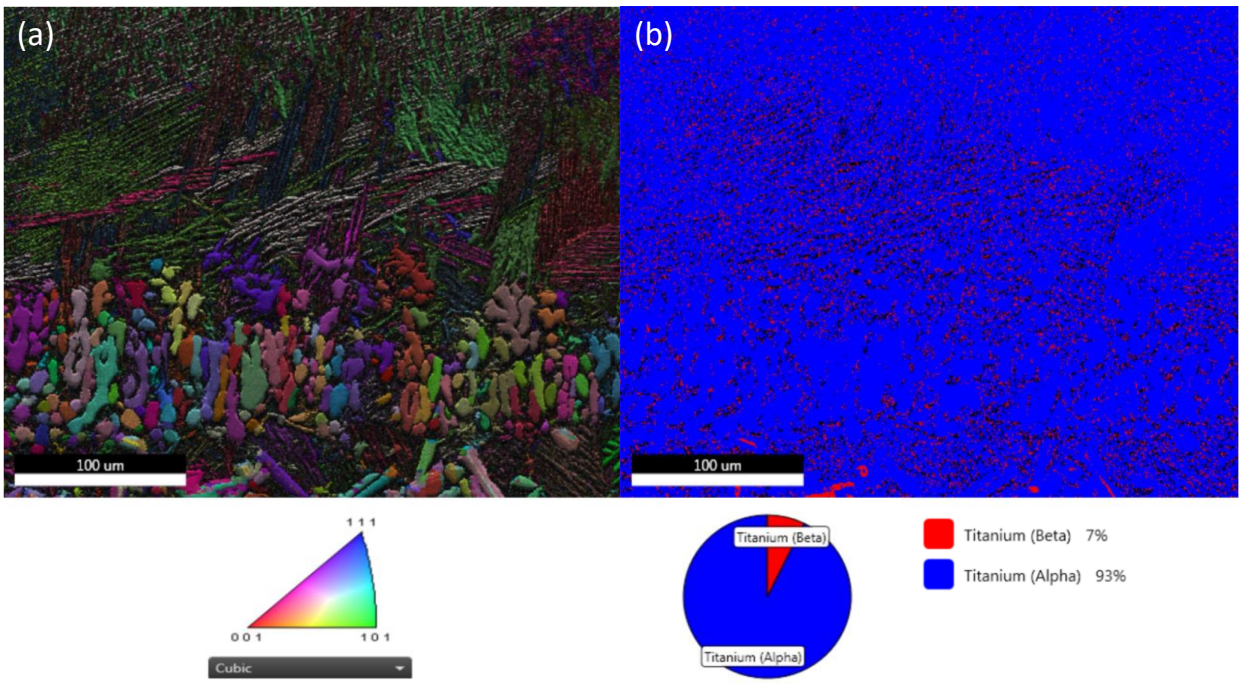

Figure 6.23 EBSD analysis of (a) grain orientation and (b) phase maps at segregation band area of the sample 19 rivet.

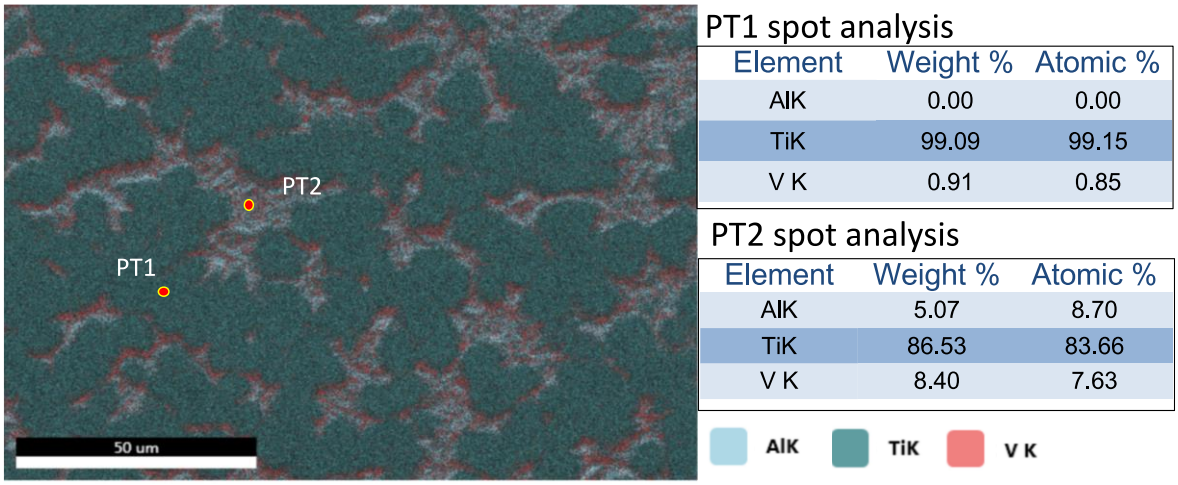

Figure 6.24 EDS chemical map scan and spot analysis on the crown area.

The previous parameter study demonstrated that the equiaxed primary α grains first appeared in sample 15, with 12s laser scanning at the focus position and the initial assumption is that it was transformed from the colony α grains in sample 14 with 8s scanning. In the HS-LR deposition, the segregation bands shown in Fig 6.22 can clearly reveal the evolution from α the colony in the trunk area to equiaxed α grains in the crown area, and the grain structure is denser with a closer distance to the top edge. Further EBSD analysis was conducted on the segregation band of sample 19, the phase map (Fig 6.23(a)) confirmed the assumption that the new appeared large

grains are primary α, moreover, the orientation map (Fig 6.23(b)) exhibits that almost all the basket-weave and equiaxed α grains near the segregation band, present the transversal instead of the longitudinal growth directions observed in the previous LMwcD depositions (Fig 5.11), this phenomenon proved that deposition touched the hole edges of upper Al sheet resulted in the transversal orientations of heat transfer and cooling rates inside the deposition in the process.

In addition, The EDS analysis on the sample 19 crown area (Fig 6.24) further testified the microstructure and element contents from the chemical aspect, the primary α grain mainly consists of pure titanium element (99% titanium) according to the PT1 spot analysis and the PT2 spot analysis shows that the Al and V content as the β stabilization weight was the rise, the normal basket-weave was fill inside the gaps among the large primary grains.

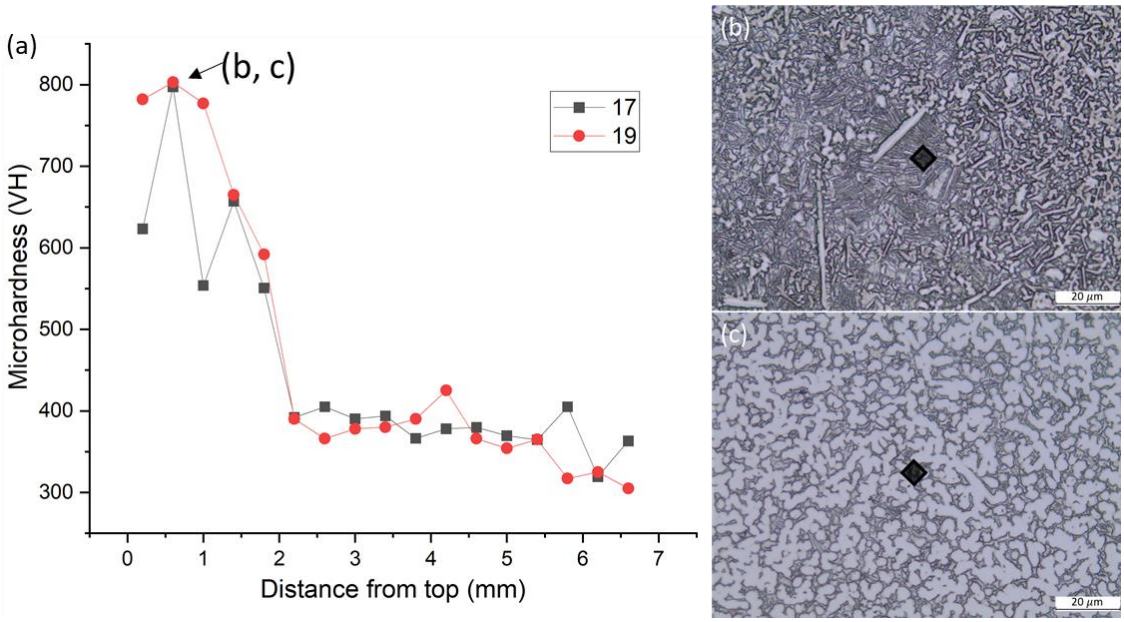

Figure 6.25 Micro-hardness curves comparison between samples 17 and 19, and the indentation test locations of (b) sample 17 and (b) 19.

As discussed in the microstructural analysis above, due to the crowded α grains formed in the HS-LR rivets, a much higher microhardness was measured at the crown area (Fig 6.25), the highest value in sample 19 reached 803VH, which is 20.8% and 95.4% higher than which in sample 16 and original rivet. Therefore, the denser and larger primary α grains formed in HS rivets provide a higher strength for the local

microhardness, however, as for the potential risk, the defects are easily formed in this brittle structure which harms the joint quality especially at the pulling condition.

6.4.5 HE post-wash rivets

According to the shear test results in 6.4.3, it concluded that the failure is most likely occurred at the boundary between the FZ and HAZ, the shear strength is positively associated with the FZ area and depth, and the heat input in the process directly decide the re-melting behaviour and subsequential FZ between the diluted deposition material and the substrate. Therefore, in this high-energy (HE) LR experiment, the power was around twice as it set in the parametric study with 800W to reveal the further detail of remelting and surface breaking behaviour for the LR joints with varied times.

(1) Overviews and microstructural observations

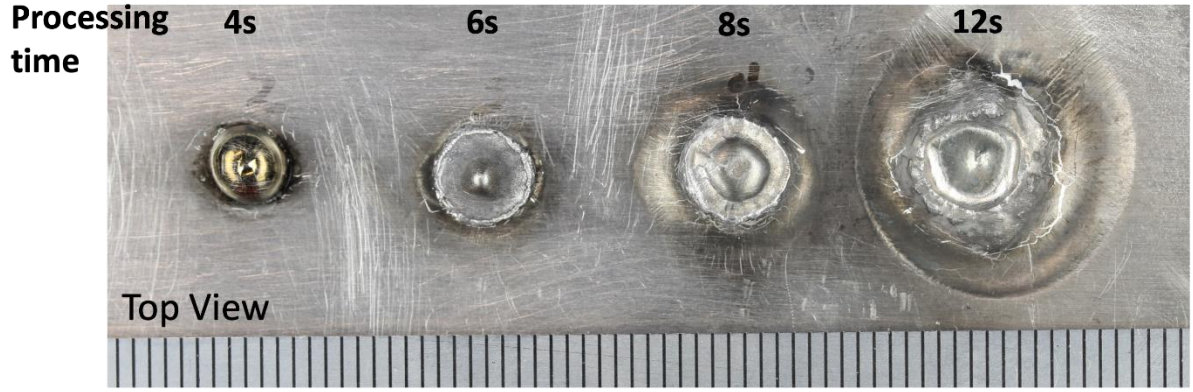

Figure 6.26 Outlooks of HE rivets applied with varied scanning times: sample 20 (4s), 21 (6s), 22 (8s), and 23 (12s).

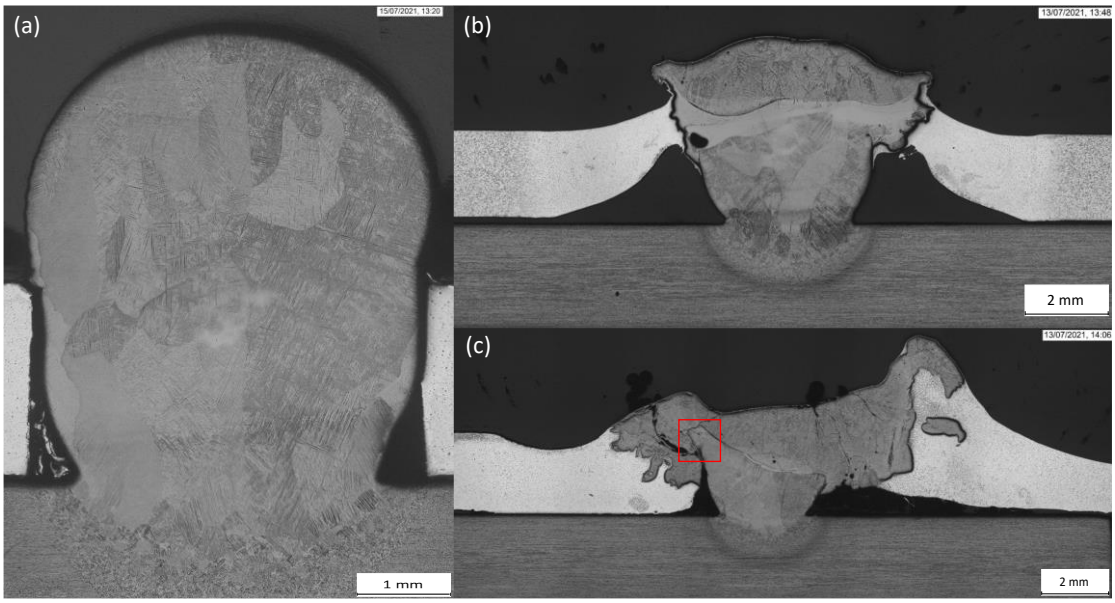

Figure 6.27 Cross-section overviews of sample (a) 20, (b) 22 and (c) 23.

From the rivet outlooks presented in Fig 6.26, sample 20 shows the same appearance as the normal rivet in the parametric studies, and its cross-section microstructure overview presents the same equiaxed and columnar β structure in the crown and trunk area. And because of the raised high-power input, the melting pool formed in a short time and penetrated the substrate, consequently, larger welding diameter and FZ depth were measured with 3.35mm and 0.99mm, the dimensions illustrate the mass heat accumulation in the deposition, the high temperature further reduced fluid viscosity in the melting material and diluted in the substrate which further expands the whole FZ area and improves the wetting angle.

But after 4s scanning, the heat input broke the thermal balance at the hole edge of the Al sheet, the deposition starts welding with the upper sheet near the crown area where the wash-path was implemented. As shown in Fig. 6.27, there is a trend that more Al material welded and mixed into the deposition along with the increase of scanning time, and major depression was formed around the deposition due to the material mixture after 8s scanning. In addition, it needs to be noticed that a considerable distortion was generated and measured at the edge of the substrate and sheet which mainly caused by the mass heat went through and followed residual stress, therefore, the longtime should be controlled to avoid the residual issue in HE method, in this case, is 6s and the specific value depends on the situation.

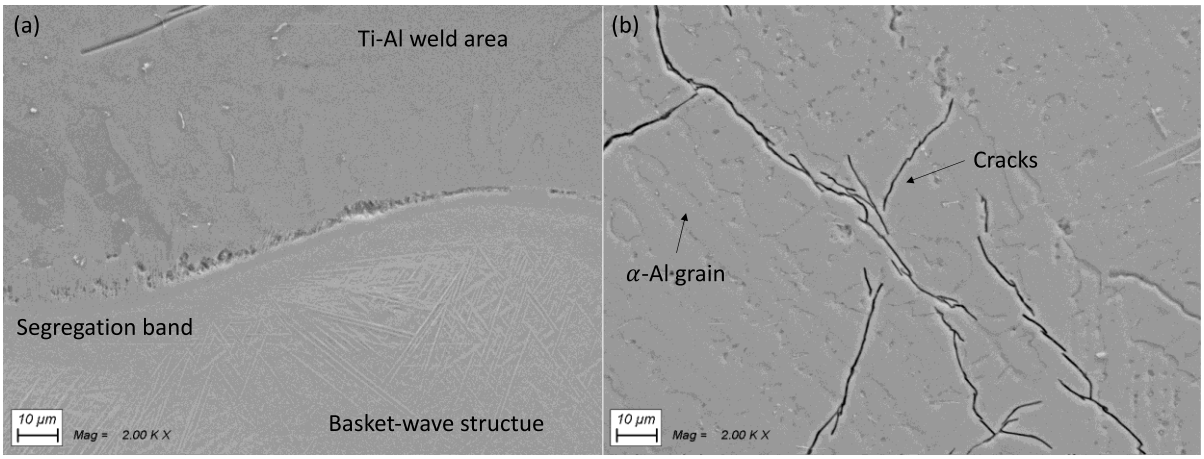

Figure 6.28 High magnification microstructure observation (2000X) at (a) segregation band and (b) crown mixture areas.

Line scan

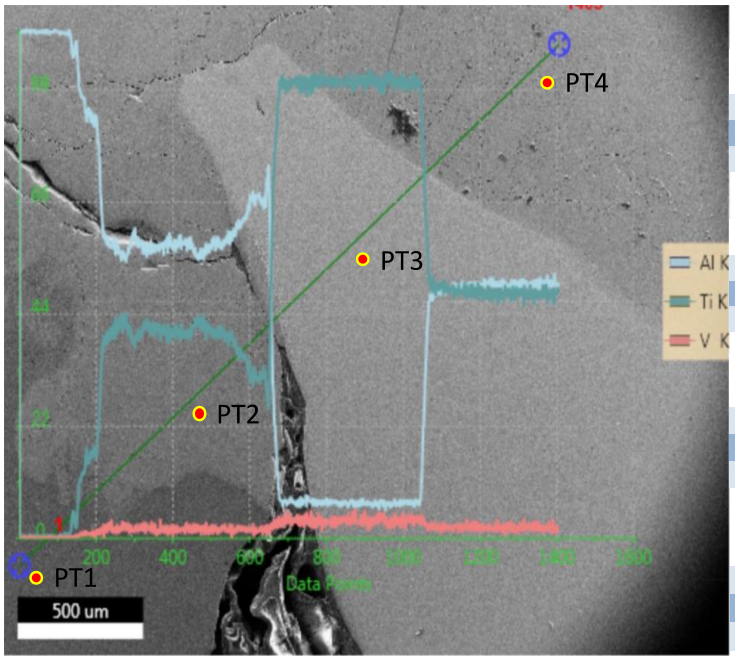

Spot analysis

PT1

Element	Weight %	Atomic %
AlK	99.71	99.84
TiK	0.20	0.11
V K	0.09	0.05

PT2

Element	Weight %	Atomic %
AlK	56.81	70.06
TiK	41.70	28.97
V K	1.48	0.97

PT3

Element	Weight %	Atomic %
AlK	5.90	10.04
TiK	89.48	85.79
V K	4.62	4.17

PT4

Element	Weight %	Atomic %
AlK	49.05	63.17
TiK	48.02	34.83
V K	2.93	2.00

Figure 6.29 EDS line scan chemical analysis at welding area between deposition and upper sheet.

A segregation band were formed between the crown mixture and deposition trunk, and from the detailed SEM photograph in Fig 6.28, the deposition still maintains the basket-weave titanium structure. However, the Al sheet partly diluted into the deposition leads to the microstructural changes, the elongated α-Al grains were observed at the crown area, and the cracks were formed in this area regarding the similar Ti-Al IMC structure. In Fig. 6.29, further EDS line scan analysis measured the element content variation from the AA6061 sheet to IMC layer, deposition, and mixture area, the curves

demonstrate the Al element content was firstly decreased and then increased, Ti shows an opposite trend, and the detail content values in different areas were listed in the spot analysis results.

(2) Shear test and fracture mode

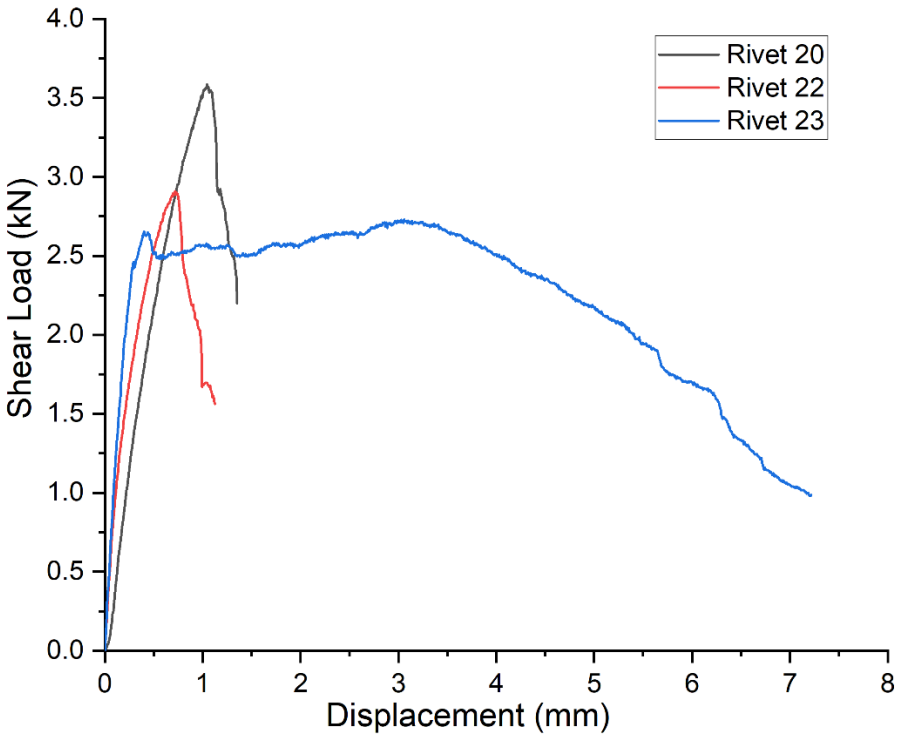

Figure 6.30 Comparison shear test results of samples 20, 22 and 23.

For the mechanical properties, the shear tests were conducted on the HE rivets, and their load-displacement curves were plotted in Fig 6.30. Sample 20 measured the highest maximum shear load with 3.59KN, which is 180.4% higher than the initial rivet and 145.9% higher than commercial blind rivet, Fig 6.31(a) shows the fracture surface where near the interface between the FZ and HAZ area, thus this highest value is mainly thanks to the improved contact angle and largest FZ area was formed at the joint weld among all the rivets in this experiment. A lower maximum shear load was measured in sample 22, although a similar FZ area was formed, according to Fig 6.27(b), the welding process changed the load applied angle and structure bearing condition, as well as the along with the increase of heat input, the IMC between Ti/Al start formed at the interface, which reduces shear strength of the joint.

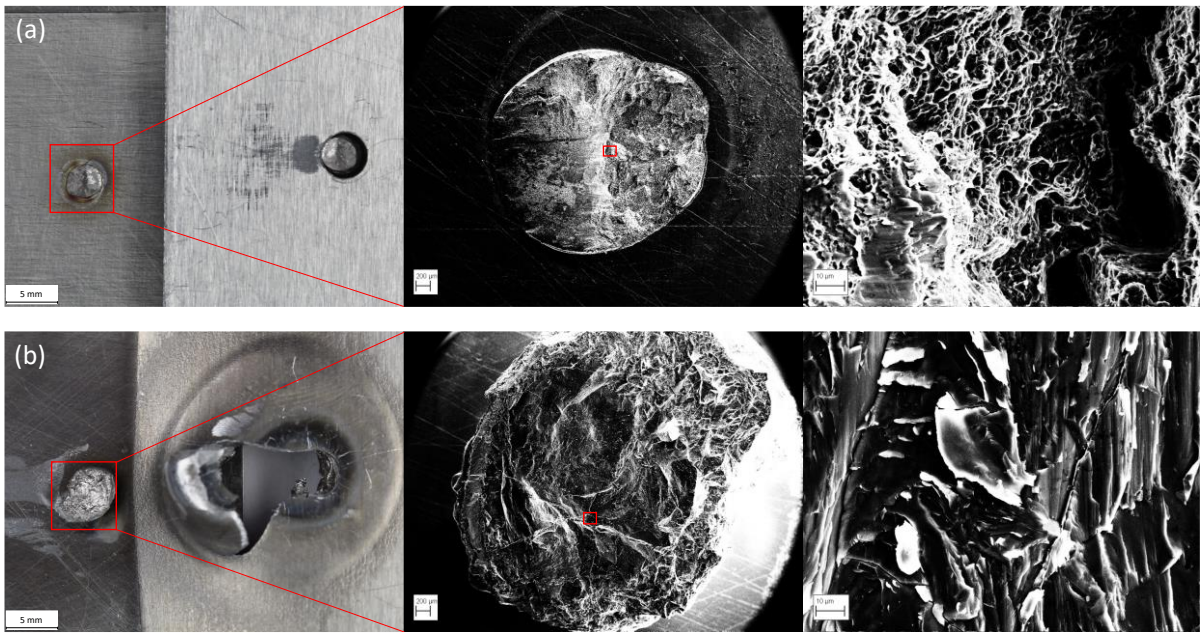

Figure 6.31 Fracture surface observations of the sample (a) 20 and (b) 23.

Compared to sample 22, sample 23 presents a closed 2.65KN maximum shear load but with a long elongation in the test, since instead of the brittle fracture mode occurred in samples 1-22, the ductile fracture mode occurred at the crown mixture part where can be observed in Fig 6.31 (b), the image also presents the Al-Ti weld fracture surface, the failure initiation most likely from the original cracks observed in Fig 6.28(b).

6.5 Conclusions

OSD deposition was designed and developed to avoid the issues of feeding angle and edge obstacle in the LR trials, moreover, it can further improve the productivity compared to the HSS deposition. The OSD method was applied to the dissimilar joining concept, the Ti6Al4V and AA6061 sheets were innovatively and successfully joined by laser riveting, and the rivet is post-processed by a high-velocity laser scanning. Post-wash procedure fully remelted the original rivet, the geometrical dimensions of both the crown and welding area were improved, which provides higher strength compared to the original rivet.

- Parameter study on post-wash processing revealed that the welding area is positively correlated with the heat input and scanning time (negatively with

focus distance), but limited by the surface tension of melting material, the welding area maintains the same level after a certain period of scanning. Plenty of primary alpha phase was formed in the crown area since the special thermal history with a high scanning speed (>1000mm/s), which dramatically increases the micro-hardness of the rivet.

- The shear test demonstrates the LR rivets failure normally brittle fractures at the boundary between the HAZ and FZ area, therefore the deposition FZ area and depth directly decide the shear strength of the joint and which is positively associated with a heat input of the process. As a result, the originally deposited rivet has almost achieved the maximum shear force with the comparative blind rivet, but sample 20 (4s HE post-washed) measured the highest maximum shear load with 3.59KN, which is 180.5% higher than the initial rivet thanks to the high energy input improves the welding condition and wetting angle.

Chapter remarks for research

Based on the LMwcD research for rivet deposition, Ti6Al4V and AA6061 sheets were successfully joined by the LR method in this chapter, with OSD employed for rivet building and post-wash implemented for quality improvement. The initial shear strength testified the positive feasibility of the LR concept for the hybrid metal structures, and it will be trialled as the preliminary test in composite joining next chapter.

The parametric study shows the factor influences on the morphological, microstructural, and mechanical properties of the rivet, the specific HS-LR revealed the equiaxed α grains formation, and HE-LR significantly enhanced the shear strength of the joint, the analyses results provide the LR basic information, which will be referred in following CFRP processing improvement.

Laser riveting as a novel concept has unique benefits compared to the current conventional metals joining method, the basic deposition process, and its feasibility study is introduced and investigated in this paper, but it still needs further

comprehensive and optimization research to achieve a mature industrial standard in future work.

Chapter 7 Experimental study of Ti6Al4V to CFRP joining by laser riveting

The joints between titanium to aluminium were successfully manufactured by the LR method in the last chapter. The rivet properties were systematically evaluated and investigated by the parametric study which revealed that generally increasing the heat input improves the welding condition thus enhancing the joining performance. After the process optimization, the HE rivets can provide almost 246% strength of the commercial blind rivet, the results proved the feasibility and reliability of the LR method for metals joining.

The metal to composite joining by LR technique was explored in this chapter, however, not like the high reflective and low weldability of aluminium properties, the toughest challenge in this experiment is that the CFRP would be significantly degraded in the fusion process. Therefore, first of all, the degradation modes and heat transfer influence in the laser processing with CFRP were introduced and identified in the 7.1 preliminary tests. Based on the results of initial trials, in the 7.2 experimental setups, the protection tools were selected and employed, LMwcD and post-processing riveting methods were designed to avoid the high heat input and damage of CFRP. The produced rivets were observed and tested by microstructural and chemical analyses and the mechanical properties were measured as well, their results were discussed and analyzed in 7.3, the chapter flow chart is shown in Fig 7.1.

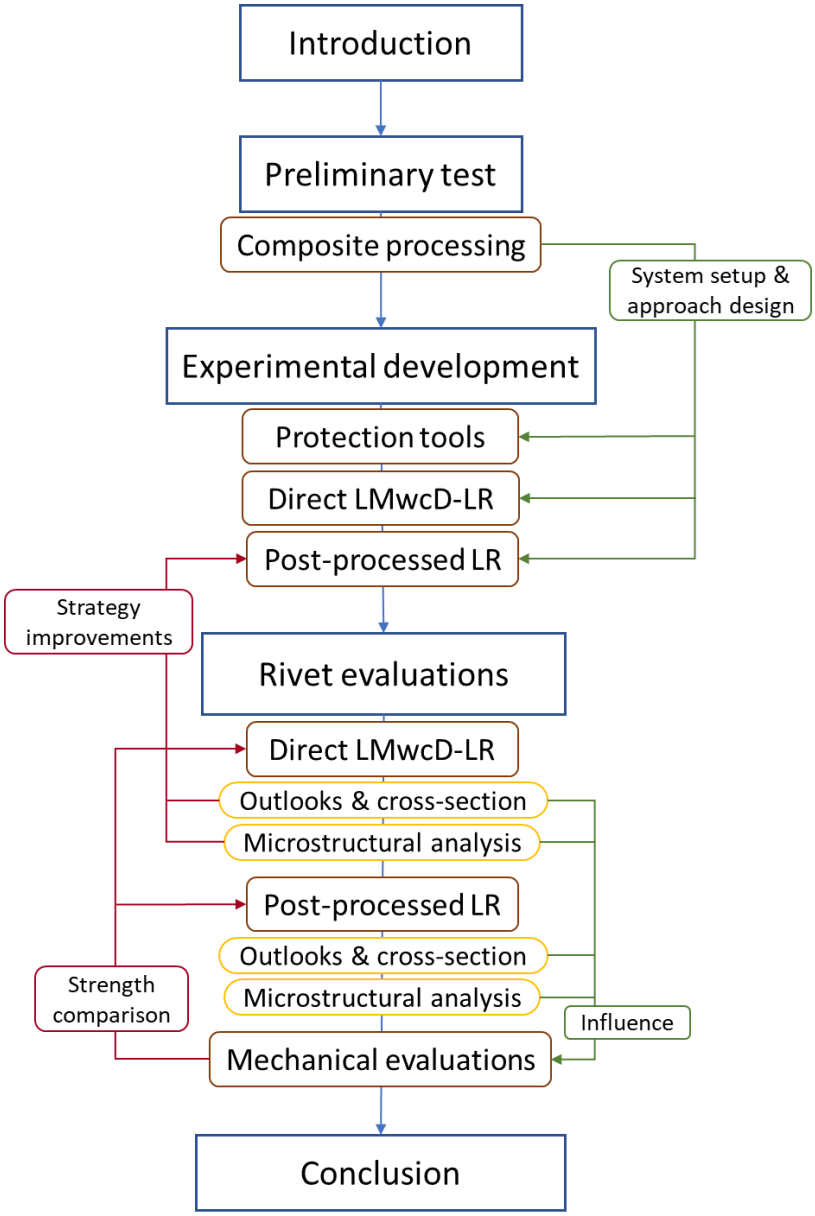

Figure 7.1 Chapter flow chart of the Ti6Al4V/CFRP joining experiment.

7.1 introduction

In industry, composite is a kind of high promising material used in high-temperature structures because of its outstanding thermal and mechanical properties, such as high strength with lower weight, low thermal expansion, excellent ablation, and high-temperature shock resistance [7.1, 7.2]. Therefore, composite is not only widely used in advanced productions of wind turbines and sports equipment, but also highly demanded in applications of the aerospace sector [7.3], and there is an increase of proportion is used in airplane body frame thanks to its high-performance. With the update of the techniques and applications in the aerospace sector, further

corresponded requirements are proposed like lightweight structure and joining of the dissimilar materials [7.4]. For that reason, as one of the possible options to achieve the goal of light-weight structure, hybrid joining techniques received increasing attention from both industrial and academic research [7.5, 7.6]. However, for the CFRP joining application with other metals such as copper and titanium, the high-temperature condition is principally required in the process [7.7-7.9]. As a high-performance metal material, titanium is widely used in the aerospace industry because of its excellent corrosion resistance and mechanical properties, and it is the only metal material that can avoid the issue of corrosion defects when joined with CFRP components [7.10, 7.11].

In the composite manufacturing procedures, there has still some obstacles that need to be overcome for the joining CFRP to other metal materials in the design and assembly process. [7.12] stated that, in the conventional mechanical fasten [7.13], adhesive [7.14] and combined joining methods [7.15] for Al to CFRP. Currently, most of the CFRP and Ti6Al4V joining techniques still take the traditional riveting as a basic reference. In addition, limited research of the alternative joining techniques for the CFRP to Ti6Al4V is presented [7.16-7.18]. For the hybrid joined components in the aerospace industry, adhesive bonding is one of the options to replace the riveting [7.19]. Nevertheless, there still have issues existing the adhesive bonding of CFRP and Ti6Al4V joint, such as the requirement of a standard and duplicable surface pretreatment, limitation of high-temperature and humidity conditions [7.17]. Moreover, the composite joints produced by adhesive or brazing normally have a low tolerance with high-temperature environments [7.20]. For example, the metal materials processed by brazing usually have a lower fusing temperature and instability in a high-temperature processing condition. On another hand, the fusion joining procedure generally needs a certain duration, processing pressure and temperature, however, the mechanical strength will be influenced because the composite will experience degradation and damage in these processing conditions [7.21, 7.22].

So far, numerous types of research are conducted for the joining CFRP to metals in recent years. As related to multi-material manufacturing, [7.23] investigated the 3D additive manufactured structures of dissimilar materials between polymer and 304 steel by laser-based powder bed fusion (PBF) and fused filament fabrication (FFF).

[7.24] studied Al and CFRP joining methods of the mechanical rivet, adhesive and bonded for by conventional methods, and developed the CFRP and Aluminium joint by hybrid joining technique of adhesive bond-electromagnetic rivet, which achieved a sound joint, but a potential downside is a rivet still penetrated through the sheets as common mechanical fasten. In addition, lap welding was employed to join the CFRP and Ti6Al4V are introduced by [7.25], the research conducted the laser processing into the joining and gave the initial guideline for the lap welding for CFRP/Ti6Al4V, the method also was applied and investigated in the Al/CFRP joints as recently reported by [7.26].

In this chapter, due to the huge difference in melting and degradation temperature between Ti6Al4V and CFRP, several preliminary trials are conducted to test the effect of laser processing on the composite and Ti6Al4V substrate. Based on the preliminary results, two improved LR method are employed for joining CFRP to Ti6Al4V, but the degradation of CFRP still cause the contamination issue during the process, the cross-section microstructure is observed, and contamination is demonstrated and analyzed in 7.3.2. Furthermore, to avoid heat damage in the LR process, a new joining method is designed and named post-scan LR, which melts the pre-built deposition on top, to form a proper crown to interlock the composite sheet. For this method, varied washing times are implemented, the LR joints manufactured by different methods are evaluated by microstructure analysis and tensile shear strength tests.

7.2 Laser processing on CFRP preliminary tests

In this composite to metal joining experiments, 2.5mm thickness Ti6Al4V was used as the substrate, the CFRP was applied as the target joined upper sheet, its properties detail is fully introduced in Section 3.3. the pre-drilled matched hole is 5mm diameters, and the deposited filler material is 0.8mm diameter Ti6Al4V wire.

In the CFRP material, the degradation points of epoxy resin (160℃) is 10 times lower than the melting point of Ti6Al4V alloy (1605℃), so it will significantly damage the CFRP material if the laser wire process is directly implemented on it. Therefore, the preliminary experiments are conducted to test the thermal performance of CFRP under the simplified laser processing conditions. The results were observed and

discussed below, these tests also can provide initial guidance and direction for the further DOE of laser riveting applied in composite joining.

(1) Direct scanning and offset scanning

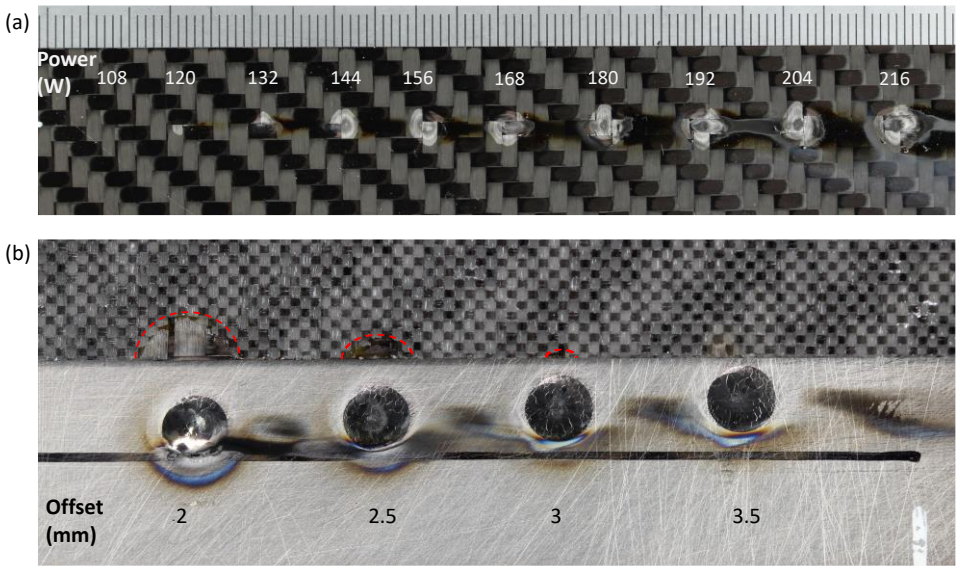

Figure 7.2 Basic laser scanning interaction of CFRP: (a) direct 1s static scanning by varied power range from 108W to 216W, (b) circle scanning on the Ti6Al4V substrate with different distance from CFRP sheet (offsets are 2mm, 2.5mm, 3mm and 3.5mm).

The 1s scanning of fixed laser test was taken on the CFRP top surface with varied power, the top view of the scanned CFRP sheet is shown in Figure 7.2 (a). From Fig 7.2 above, no change occurs under the 108W power input, since the material was heated under the degradation point of epoxy, the surface was not influenced by the laser irradiation. However, when the laser power is input over the 120W, the CFRP surface starts to degrade regarding the surface temperature above the epoxy degradation temperature (160℃) and the damaged area is enlarged along with the increase of input power. In addition, it is observed that even the carbon fibre was damaged in the upper melting pool of higher power set (above W), which is mainly because after the epoxy was vaporized, the energy accumulation is concentrated on the rest of the carbon fibres, the temperature soared and led to the degradation. Moreover, it needs to be noted that the shielding gas takes away the heat from the melting pool, but it also hurt the CFRP material, so a degradation trail appears along the direction of gas flow.

Except the direct scan damage, the effect of an offset laser circular scanning was investigated, the path radius is 0.5mm, travel speed is 42mm/min, power is 600W and the beam spot is 1.5mm, the distance between CFRP upper sheet and centre of the circle was adjusted from 2mm to 3.5mm, their degradations caused by heat transfer from titanium substrate were observed in Fig. 7.2 (b). It shows that in a near offset (<2.5m), although, without physical conduction with the melting pool at the substrate, the heat transfer still caused a serious degradation at the bottom surface of the CFRP sheet. In addition, it demonstrates a strong positive correlation between the offset distance and the affected area, when the distance increases to 3mm, the degradation is minimized or even eliminated over the 3.5mm.

(2) Initial laser riveting test

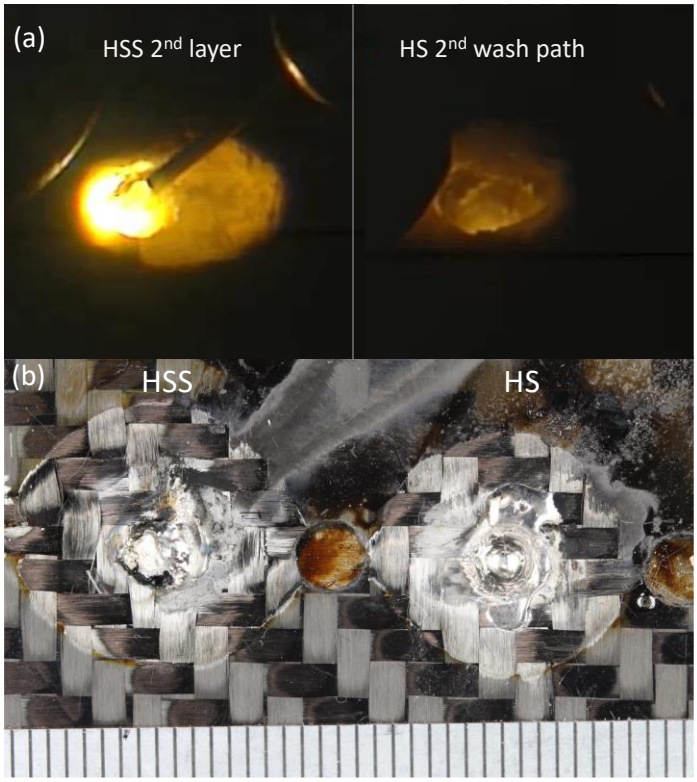

Figure 7.3 Laser riveting on the Ti6Al4V/CFRP joining (a) the HS and HSS method processing records, (b) top views of the HS and HSS rivet joints and CFRP damaged area.

The 2 layers HS and HSS LR methods were designed from the considerations of less heat input and higher productivity respectively, and they were directly employed to join the CFRP sheet and Ti6Al4V substrate. The processing records and top view of joints are shown in Fig. 7.3. In the 2nd layer deposition process of direct laser riveting, it is worth noting that not like the high reflective and melting temperature properties of

aluminium materials in dissimilar metals joining experiments in Chapter 6, the outer reduced laser distribution still resulted in a much larger area was damaged in the CFRP sheet, recorded in Fig. 7.3(a).

Besides, the large, combined degradation caused by laser radiation on the top surface and heat transfer from the substrate is observed in Fig. 7.3(b). As for the inside wire deposition, unlike the low weldability performance between aluminium and titanium, in this composite joining, the filler materials were directly mixed into the epoxy and fibres, the deposition mixture was formed with a lower height caused the wire deposition transferred to the droplet mode. The top view of joints also presents the mixture boundaries, when the melted titanium wire contacted the composite, the epoxy was destroyed due to the low thermal resistance, the rest small portion of fibres was mixed into deposition.

These direct trials also presented two major processing risks inside the deposition regarding CFRP degradation in the LR joining: (1) Oxidation: a rough added materials growth and appearance were recorded in the video at the initial layers welding and deposition, which shows a similar condition with the poor shielding titanium deposition, the phenomenon mainly because the gas (CO_2 and carbide) was produced from CFRP degradation, the massive gas interfered the shielding condition and caused oxidation issue in the titanium processing, the situation was improved in the later process. (2) Contamination mixture: the epoxy degraded but the carbon fibre left due to its higher melting point around 3000℃, mixed with the deposition and weakens its strength regarding their huge difference of properties and poor weldability.

In sum, according to the preliminary tests above, the direct LR damage on the CFRP sheet mainly occurred regarding the following three aspects:

- The outer laser radiation on the top surface.
- Bottom surface degradation is caused by the heat transfer from the melting pool on the titanium substrate.
- The melted liquid wire material contacts with the hole edge, which degraded the epoxy and mixed with the deposition.

7.3 Experimental setup and methodology

Because of the same technique conducted, the similar LR processing system introduced in 6.3 was employed in this Ti6Al4V/CFRP joining experiment, aiming to reduce the processing damage on CFRP as illustrated in the pre-test, the additional assistant parts were considered and manufactured in 7.3.1. For the rivet deposition methodology, based on the conclusion from chapter 5, two direct LMwcD methods was proposed at first in 7.3.2, then the post-processing LR methods were designed in 7.3.3 to further prevent the heat transfer and accumulation conditions in the process.

7.3.1 Experimental system setup

In this study, the LMwcD system was employed for the CFRP-LR experiments, same as the previous experimental setup (Fig. 7.4(a)), the system consists of the essential equipment with IPG laser source and processing head, Binzel wire feeder, shielding gas pipe, and system motion unit. In this experiment, the general idea applies the LR concept that uses the titanium wire deposition to build up a mushroom-like rivet to interlock the Ti6Al4V substrate and CFRP upper sheet. However, the preliminary tests revealed reactions of CFRP sheet in the laser deposition process, the connection areas such as top surface near the hole, a bottom surface and hole edge were significantly degraded, melted by laser scanning and heat transfer, and mixed with the inside deposition.

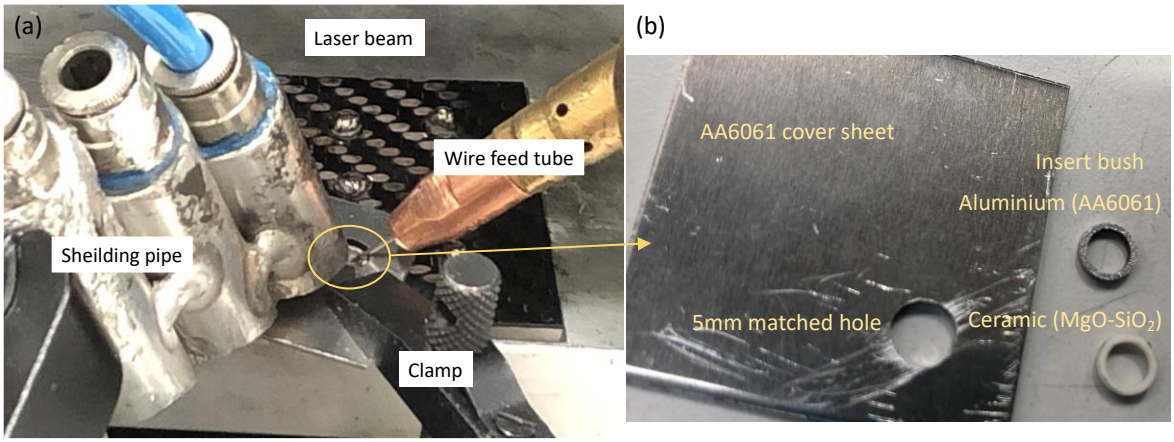

Figure 7.4 Experimental setup for the CFRP-LR study, (a) LR processing system setup, (b) designed and selected tools for CFRP protection: cover sheet and insert bush.

To avoid the damage concluded in 7.2, a 1mm thickness cover sheet and an insert bush (0.5mm wall thickness) were designed and used in the following LR experiments (shown in Fig 7.4(b)), the material of AA6061 is selected for cover sheet thanks to its high reflective with laser. It can provide the protection function, which is also used as one of the insert bush materials. Except for the aluminium, ceramic was selected as another material for the bush regarding its high melting point and excellent performance of thermal insulation.

7.3.2 HS and HSS LR trials

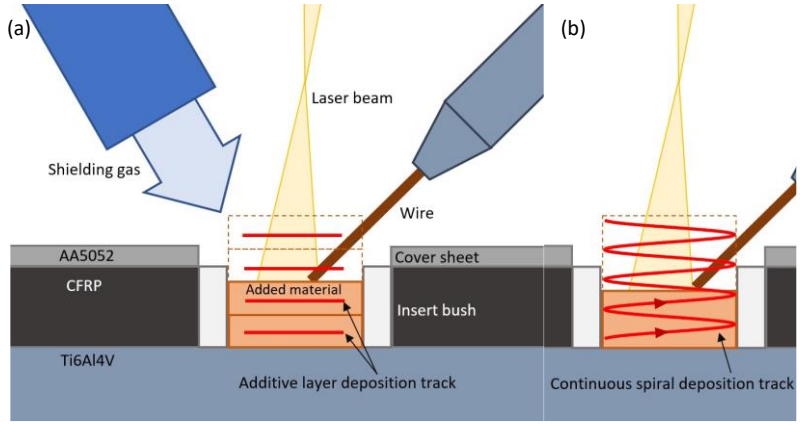

Figure 7.5 Designed CFRP-LR methods in the deposition strategies study: (a) ALM deposition method, (b) CS deposition method.

In the initial tests of the LR for Ti6Al4V to composite joining, along with the experience on the previous Ti6Al4V/AA6061 experiments, HSS and HS two strategies were re-designed and applied to deposit the rivet inside the hole shown in Fig 7.5, regarding the following considerations from the results in Chapter 5:

- The HSS is the fastest deposition strategy to build up the cylinder feature, which provides the highest productivity, meanwhile, faster processing also reduces the total energy input which improves the distortion and residual stress issues.
- Compared to the HSS method, HS separates the whole deposition processing into 4 repeated cycles, thanks to this deposition strategy, it can reduce the heat influence on the composite sheet to some extent to extend the cooling time between the deposition steps, which can theoretically minimize the degradation in the epoxy.

HS and HSS both can successfully build up the rivet features in the Ti/Al LR trials, and the processing parameters were adjusted to the appreciate ranges shown in Table 7-1 below. In the Ti/Composite LR joining experiments this chapter, insert aluminium and ceramic bushes were respectively applied with two deposition strategies. And two deposition strategies were tested on composite joining with aluminium and ceramic materials inserted bushes in this chapter.

7.3.3 Post-processing LR experiments

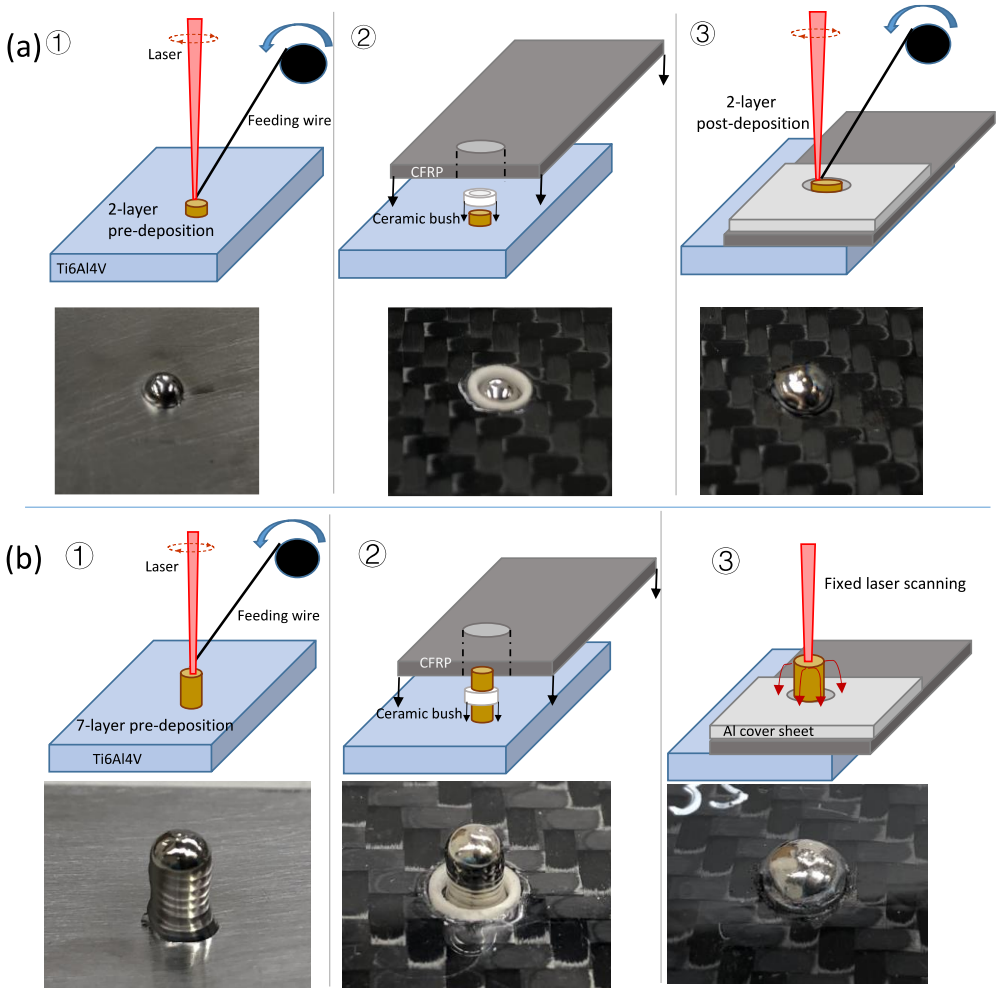

Figure 7.6 Schematic of the improved LR post-processing concepts and processing procedures: (a) post-deposition LR and (b) post-scanning LR.

After the evaluated the two continuous deposition methods (HS and HSS) in 7.4.1, to further reduce the heat input in the processing, minimize the degradation that occurred in the CFRP, two new separate rivet deposition methods were designed and tested,

named post-deposition (PD) and post-scanning (PS) method. Through the processing monitoring and result in analyses from the HS and HSS joining, most of the heat damages on CFRP were generated and transferred from the rivet deposition procedure, so the general idea of new designed PD and PS methods is that building up a multilayers cylindrical deposition first on the titanium substrate without composite joined, then cover the CFRP sheet and inserted bush on the cylinder pre-deposition through their holes, finally depositing or melting the top area of deposition for reforming or building a proper crown by the post-processing art to interlock the CFRP upper sheet. PD and PS methods were similarly divided into three steps (Fig. 7.6):

Pre-deposition: at the beginning of the joining process, to avoid the heat transfer from the titanium substrate at the bottom of the CFRP sheet, 2- and 7-layers pre-deposition were built up by LMwcD, on the substrate without CFRP involved in the PD and PS methods.

Assembly: the CFRP sheet with matched hole and bush will be inserted on the pre-deposition.

Post-processing: then in the PS joining method, the 7 layers of pre-deposition will be remelted by fixed beam scanning and reforming a rivet cap to interlock the CFRP sheet and titanium substrate. In the PD method, the LR is applied to continue depositing the wire onto the riveting feature in the hole and finish the joining with 2 more layers.

Table 7-1 Experimental parameter of direct deposition and post-processing LR methods.

	HS	HSS	PD	PS
Power (W)	600			
Beam spot diameter (mm)	1			
Deposition travel Speed (mm/s)	1.5	2	2.2	
Deposition route radius (mm)	0.5		0.4	
Wire feed speed (mm/s)	7.5	8	8.5	
Wash speed (mm/s)	N.A.		Fixed	
Wash duration (s)	N.A.		3	
Shielding gas	Argon			
Shielding flow rate (L/min)	30			

All the processing parameters of the PD and PS methods are listed in table 7-1. The samples of direct deposition and post-processed methods were evaluated by morphological, chemical and section microstructural analyses, the strength was measured by a shear test, the loading sketch and specimen dimensions are shown in Fig. 7.7, the load velocity is set to 10mm/min, the analysis and test detail were introduced in chapter 3.

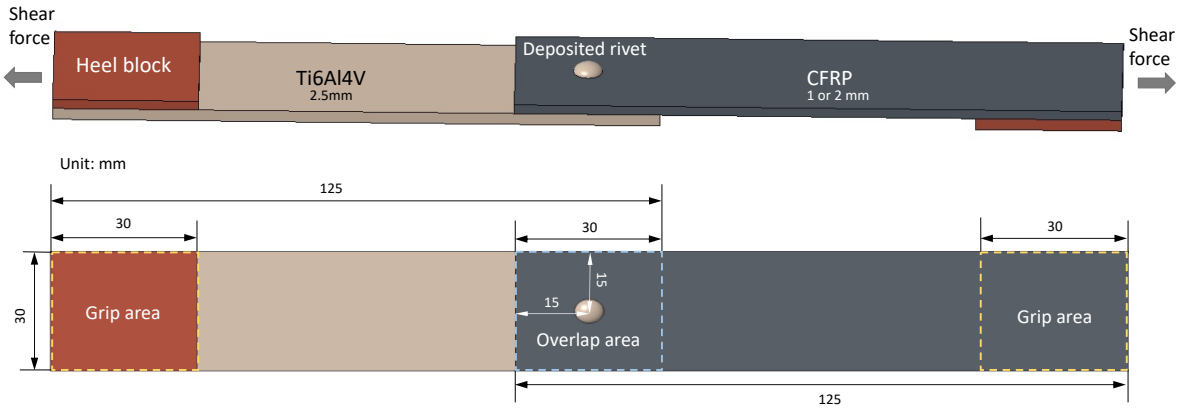

Figure 7.7 sketch demonstration of the shear tests for Ti6Al4V/CFRP LR joints.

7.4 Results and Discussion

The experimental results of LR dissimilar joining for Ti6Al4V were presented and discussed in this section, the produced rivets were observed and analyzed from the geometrics, cross-section macrostructures, microstructural and chemical tests, those evaluate the joining performance from global to local views, the results of direct LMwcD and post-processed rivets were shown and analysed in 7.4.1 and 7.4.2 respectively. Last but not least, as a joining technique, the mechanical examinations of rivets applied different deposition strategies were conducted, and their strengths and further relationships with processing methods and parameters were analysed and discussed in 7.4.3.

7.4.1 Direct LMwcD-LR experiment

(1) Outlooks and microstructure

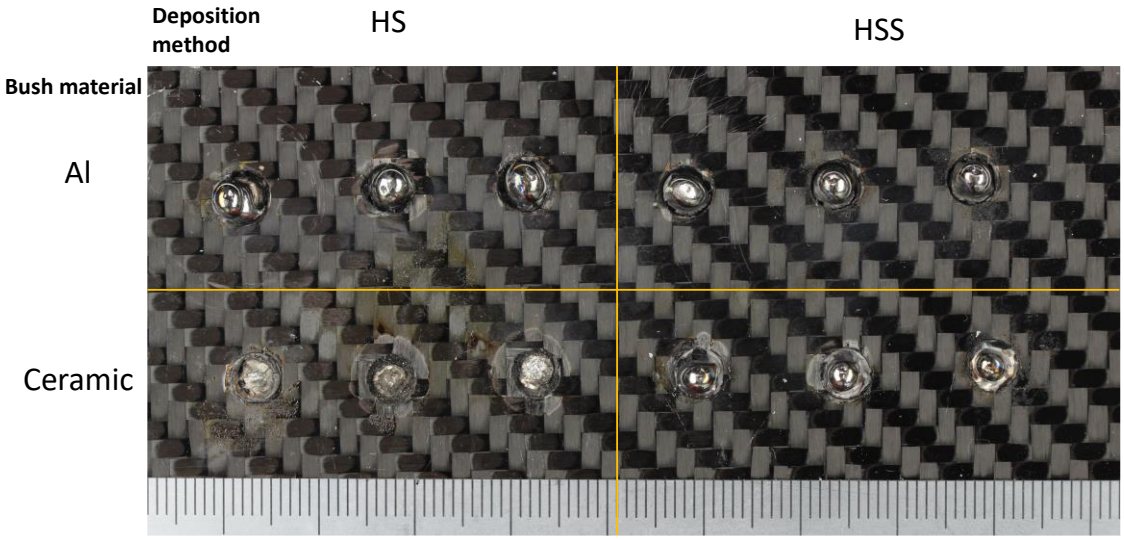

Figure 7.8 Top view outlooks of rivets manufactured by direct HS and HSS deposition methods applied into Ti6Al4V/CFRP joining.

After the processing parameters were adjusted to the proper ranges, the joining experiments were repeated 3 times for each kind of rivet to avoid the operation error influenced on the results. Fig. 7.8 shows the rivet outlooks manufactured by direct LMwcD methods with different insert bushes. From the overall appearances, compared to the results of the pre-test in Fig. 7.3, it can be clearly seen that the degradation bands were narrowed after the cover sheet and insert bush were applied in the experiments. From the top views of the rivets, both HS and HSS depositions with Al bush and HSS deposition with ceramic bush rivets were successfully built up with smooth rivet caps, which presents a similar appearance to the metal LR results in chapter 5, thus the results proved the initial feasibility of the LR concept in Ti/composite joining.

However, the rivets of HS deposition with ceramic bush were broken after the process, the sectioned microstructure shows the fracture was occurred in the middle of the deposition. As discussed in LMwcD parametric study in Chapter 5, the heat accumulation in the deposition built by the ALM method is much higher than which built by CS methods. In this case, higher energy input and accumulation resulted in that the heat-affected zones that appeared in the CFRP sheet being larger than other

joints, which means the composite was severer degraded in the process. Therefore, one preliminary scenario is that the degradation of epoxy interferes with the shielding gas and the broken carbon fibres contaminated the deposition in the process, and the detail of this phenomenon and further analyses were presented and discussed in the following sections.

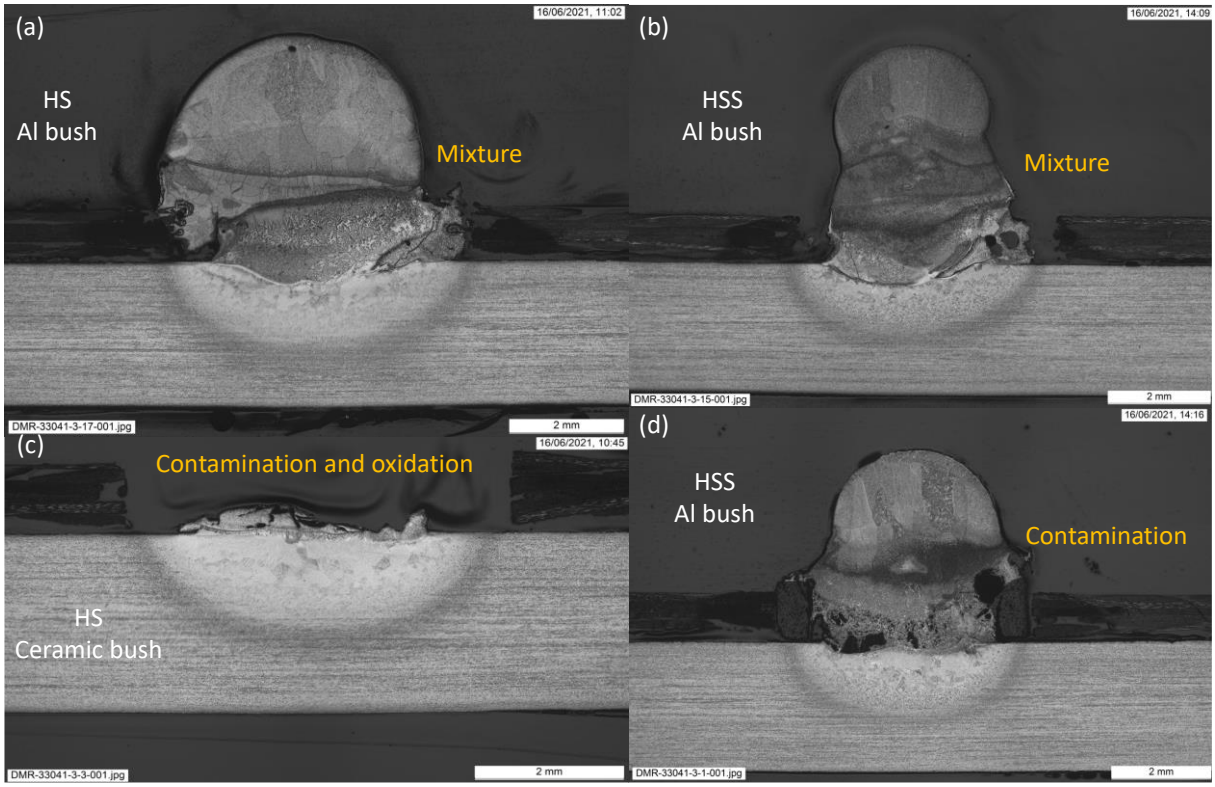

Figure 7.9 Cross-section microstructure overviews of (a) HS and (b) HSS deposition methods with AA6061 bushes; (c) HS and (d) HSS deposition method with ceramic bushes.

One of each kind of rivets was selected and sectioned along the middle line, and their cross-section microstructure overviews are shown in Fig 7.9 above. Similar features were observed between two LMwcD rivet joints applied with the Al bushes, the rivets were successfully built and only a few minor defects (pores and cavities) were found inside the deposition, which means the rivets have the basic strength compared to the contaminated deposition produced with ceramic bush, and due to the deposition strategy difference, the HS rivet (Fig 7.9a) with the higher heat input and accumulation, presents a correspond higher aspect geometrical dimensions, and larger HAZ area than the HSS rivet (Fig 7.9b). However, because of the comparatively lower melting temperature, the Al insert bushes were melted and mixed into the wire deposition immediately at the beginning of the deposition process, the mixture texture can be identified in the trunk part of the rivet near the welding area, but it results in a backward

that the rivet crown cannot be formed in a mushroom-like cap to interlock two sheets, thus it hardly can provide a satisfied pulling strength for the joint.

Instead of deposition broken in HS ceramic rivet (Fig 7.9c), a rivet was built up inside the ceramic bush applied with a lower heat input HSS deposition method. But the substrate and cover sheet heat transfer still caused the degradation in CFRP. As general reasons explained in the section 7.2, the cross-section overview (Fig 7.9d) presents obvious and massive defects formed in the middle zone of deposition caused by the same contamination and oxidation issues, which significantly weakens the joint strength. But compared to the deposited rivets with Al bushes, the ceramic prevented the melting mixture occurred in the deposition thanks to its high thermal resistance capability, and the rivet thus can form a proper cap to interlock the substrate and upper sheet to provide a certain pulling strength for the joint.

(2) Chemical and contamination analyses

In this initial experiment, the SEM and EDS tests were conducted on the sectioned samples, the further chemical and microstructural analyses were carried out, to obtain detailed information on the contamination area of the rivet with ceramic bush, and the mixture area of the rivet with Al bush.

Figures 7.10 and 7.11 present the EDS chemical analysis results of HSS-LR rivets applied with Al and ceramic insert bushes respectively. In Fig 7.10, the point and line scan chemical analyses on the deposited rivet with Al bush demonstrate that a competitive increase of aluminium content with 10.88% at the middle rivet area since the Al bush was melted in the deposition, but due to the small volume of the bush material, the phenomenon is most obvious in the mixture area, then the fraction is gradually decreased along with the increase of the deposition height. The higher Al weight% also caused the microstructural difference, which enhanced the stabilization of the α phase in the material, and the primary grains were observed in Fig 7-12b microstructure map.

HSS-LR with AA6061 bush

Point analysis at mixture area

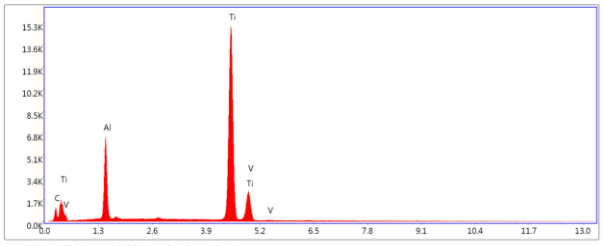

Lsec: 26.3 58 Cnts 8.680 keV Det: Octane Pro A

Element	Weight %	Atomic %	Net Int.	Error %	Kratio	Z	A	F
C K	2.37	8.21	170.37	5.86	0.0149	0.8533	0.7335	1.0000
Al K	10.88	16.73	1855.69	3.26	0.0647	0.7149	0.8301	1.0029
Ti K	84.96	73.60	7009.09	1.55	0.5675	0.6585	1.0133	1.0011
V K	1.79	1.46	124.64	10.96	0.0117	0.6483	1.0053	1.0022

Line scan

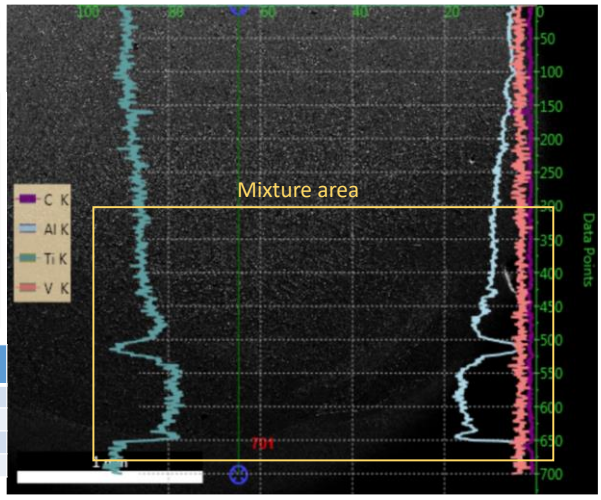

Figure 7.10 EDS chemical analysis for the HSS-LR rivet applied with Al bush.

HSS-LR with Ceramic bush

Point analysis at contamination area

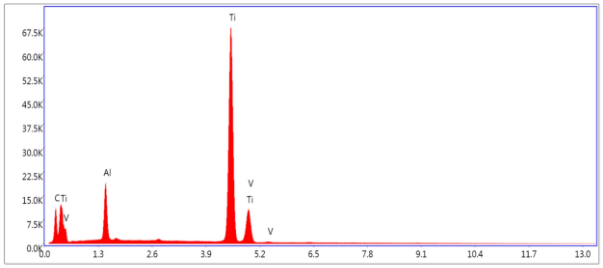

Lsec: 90.9 10.315K Cnts 0.270 keV Det: Octane Pro A

Element	Weight %	Atomic %	Net Int.	Error %	Kratio	Z	A	F
C K	7.01	22.16	723.64	3.41	0.0472	0.8462	0.7969	1.0000
Al K	6.84	9.63	1549.30	3.01	0.0404	0.7104	0.8289	1.0031
Ti K	83.47	66.20	9173.47	1.44	0.5553	0.6546	1.0150	1.0012
V K	2.69	2.00	248.60	4.03	0.0175	0.6445	1.0066	1.0021

Line scan

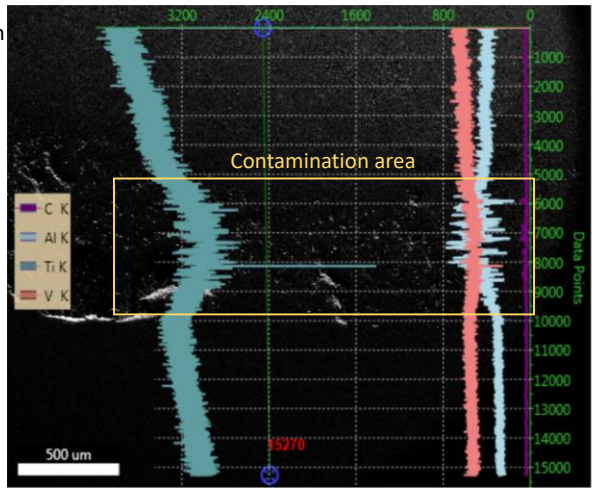

Figure 7.11 EDS chemical analysis for the HSS-LR rivet applied with ceramic bush.

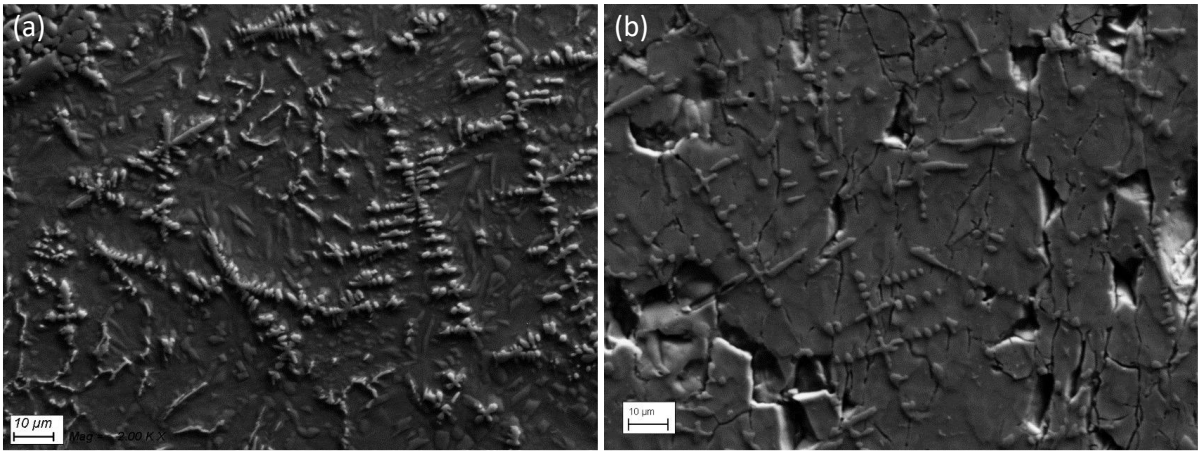

Figure 7.12 High magnification microstructural analysis on (a) contamination and oxidation area of HSS-LR rivet applied with ceramic bush and (b) mixture area of HSS-LR rivet applied with Al bush.

In Figure 7.11, at the trunk part of the ceramic bush rivet, the line scan chart demonstrates the weight of main element titanium of the Ti6Al4V deposition was decreased in the contamination and oxidation occurred area, the decreased value mainly caused by the defects formed in the areas. Besides, the content fluctuation of the carbon element was detected in the line scan, and its remarkable high weight value was measured in the point analysis, which confirmed the assumption that the carbon fibres were broken and contaminated the deposition in the fusion process. Although the carbon contamination hardly is observed under the microscopy (Fig 7.12a), the primary grains formation occurred which is caused by the carbon elements and/or oxidation.

A slight increase of aluminium was measured in the contaminated area as well, and it might lead to the formation of α grain, and which was observed in the 2000x high magnification SEM photo (Fig 7.12b), the dendrites is similar to the grain shape in the steel material, thus it likely formed under the combined effect of carbon content. And the defects such as cracks and cavities can be clearly seen in the microstructural observation, which indicates the strength weakened and fracture occurred in the deposition.

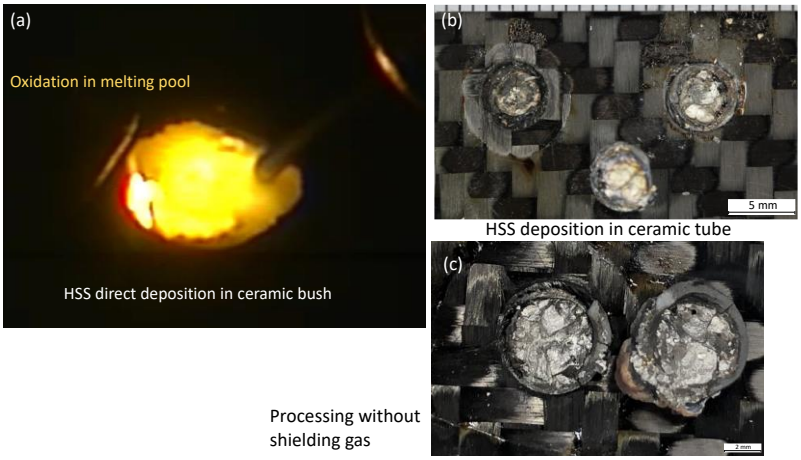

Figure 7.13 HS-LR joining with ceramic bush: (a) experimental processing record, (b) top views of fracture surfaces and (c) comparison experimental without shielding gas.

Further trials for the HSS-LR failure rivet were investigated, the processing record (Fig 7.13a) shows that the depositing material grows with a rough melting pool appearance, the behaviour is consistent with the oxidation issue that occurred in the LMwD process. A comparative HSS-LR test was carried out without shielding in process, the comparison top views (Fig 7.13b and c) present a similar fracture surface both from

the substrate and deposited rivet sides. Therefore, this supplementary evidence was provided and proved the contamination and oxidation were combinedly resulted in the broken of the rivet and caused the processing failure in the experiments.

7.4.2 Post-processing LR experiment

(1) Outlooks and cross-section overview

After the direct LMwcD trails, the post-processing LR methods were designed and developed, to avoid the CFRP degradation issue, and with ceramic bush to prevent the problem of materials was mixed into the melting deposition. Figure 7.14 shows the rivet outlooks deposited by post-processing LR methods, from this overall top view, it shows that the area of CFRP degradation bands surrounding the deposition was clearly reduced, since the joining process was divided into pre-deposition and post-processing steps. The pre-deposition input the heat and built up the cylindrical feature in advance, consequently only a part of total energy was absorbed into the CFRP in the followed the post-joining process. There still has some appearance differences between PD (Fig 7.14a) and PS (Fig 7.14b) deposition, the cap appearance of the PS rivet is smooth and shine, but the PD rivets show a rough crown surface against the shielding pipe direction, it is mainly because the post-deposition in PD took a longer processing time with 6s than the 3s post-scanning in PS, the long-period laser processing may lead to the oxidation on the top surface regarding the damage of epoxy nearby.

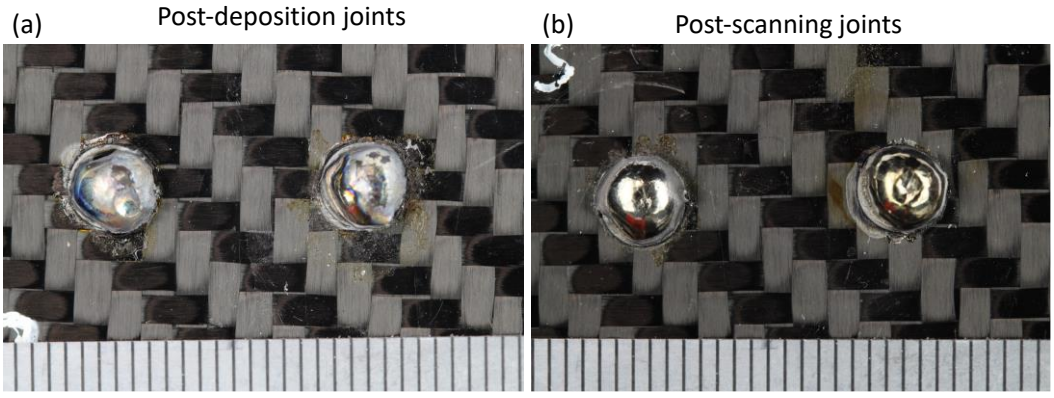

Figure 7.14 Top view outlooks of (a) PD and (b) PS LR joints.

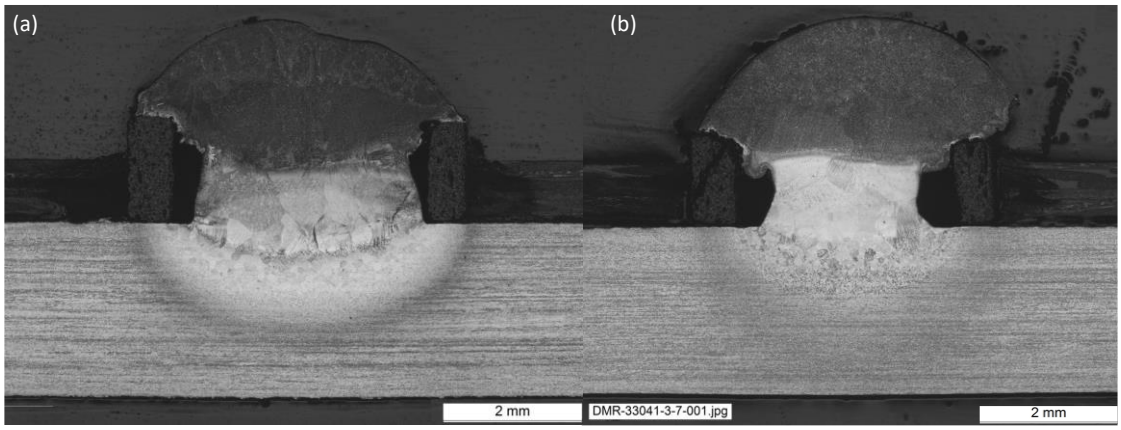

Figure 7.15 Cross-section microstructure overviews of (a) PD and (b) PS LR joints.

The cross-section overviews of post-processed rivets as shown in Fig. 7.15, the geometrical heights of rivets are lower than the direct LMwcDed rivets with shorter deposition steps. Due to the optimized joining methodologies, the contamination and oxidation issues were avoided, both of PD (Fig 7.15a) and PS (Fig 7.15b) rivets present an intact deposited trunk and a mushroom shape crown, which can provide the basic shear and pulling strength for the joints. Besides, thanks to the higher heat input and the post-deposition step, the PD rivets obtained a wider welding and deposition diameter, which expects to provide a stronger shear strength according to the previous LR investigation. However, it needs to be noticed that a larger HAZ in CFRP was observed in PD, which influences the strength of the CFRP sheet near the hole, and further detailed impacts will be discussed in 7.4.3. In addition, compared to the PS, the PD method has lower flexibility regarding its processing method, same to the issue explained in 6.1, the wire feeding angle and hole edge limitations only allow the pre-deposition process is applied in the thinner material upper sheet (<2mm).

(2) Chemical and microstructural analyses

PD-LR with Ceramic bush

Line scan

Point analysis at crown area

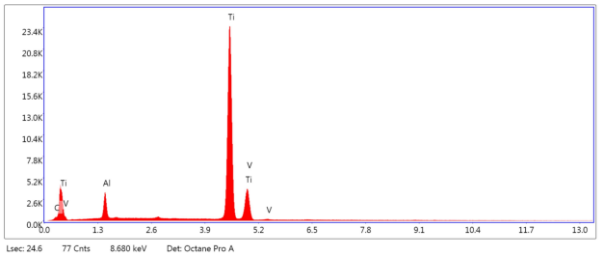

Element	Weight %	Atomic %	Net Int.	Error %	Kratio	Z	A	F
C K	0.29	1.13	36.62	13.89	0.0021	0.8640	0.8206	1.0000
Al K	3.67	6.30	946.62	4.01	0.0215	0.7206	0.8102	1.0032
Ti K	92.25	89.13	11794.33	1.51	0.6215	0.6633	1.0148	1.0010
V K	3.79	3.44	407.49	4.58	0.0249	0.6532	1.0056	1.0016

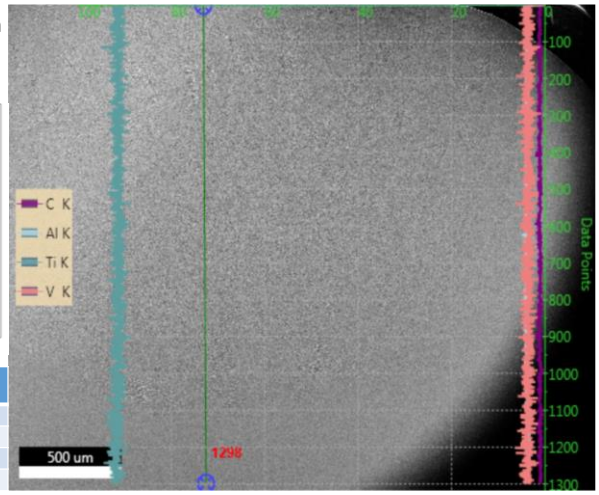

Figure 7.16 EDS chemical analysis for the PD-LR rivet applied with ceramic bush.

PS-LR with Ceramic bush

Line scan

Point analysis at crown area

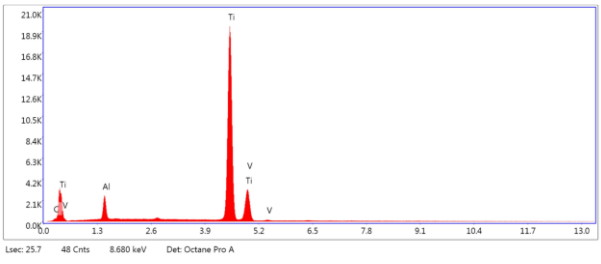

Element	Weight %	Atomic %	Net Int.	Error %	Kratio	Z	A	F
C K	0.07	0.27	6.81	66.40	0.0005	0.8577	0.8309	1.0000
Al K	3.30	5.71	652.11	4.10	0.0191	0.7135	0.8110	1.0032
Ti K	92.97	90.66	9110.61	1.53	0.6204	0.6568	1.0150	1.0009
V K	3.66	3.35	301.67	5.17	0.0238	0.6469	1.0059	1.0015

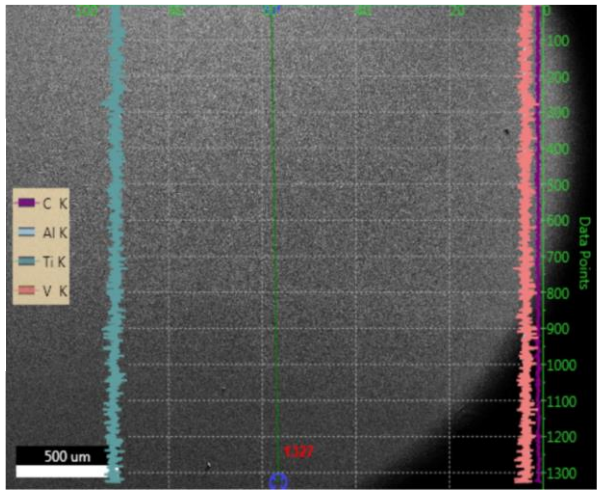

Figure 7.17 EDS chemical analysis for the PS-LR rivet applied with ceramic bush.

Further SEM microstructural and EDS chemical analyses were tested on the post-processed rivets. Fig 7.16 and 7.17 chemical composition tests demonstrate that in both of PD and PS-LR rivets, there is no obvious fluctuation of violet carbon curve appeared in the elements line scanning, furthermore, the measured value of carbon content in point analysis is extremely low compared to the results of HSS-LR rivets and the whole chemical composition is similar to which in the previous LMwcD and metal LR EDS analyses. But still, a few carbon atomics were detected in the point analysis of the PD rivet at the crown area, which explains the slight oxidation and contamination caused by the rough surface on the cap. In the PS rivet, the point analysis with comparative low carbon content indicates that the interferences from contamination and oxidation were almost eliminated in the deposition, and the damage

of CFRP was minimized and hardly impacted on the rivet deposition in the process.

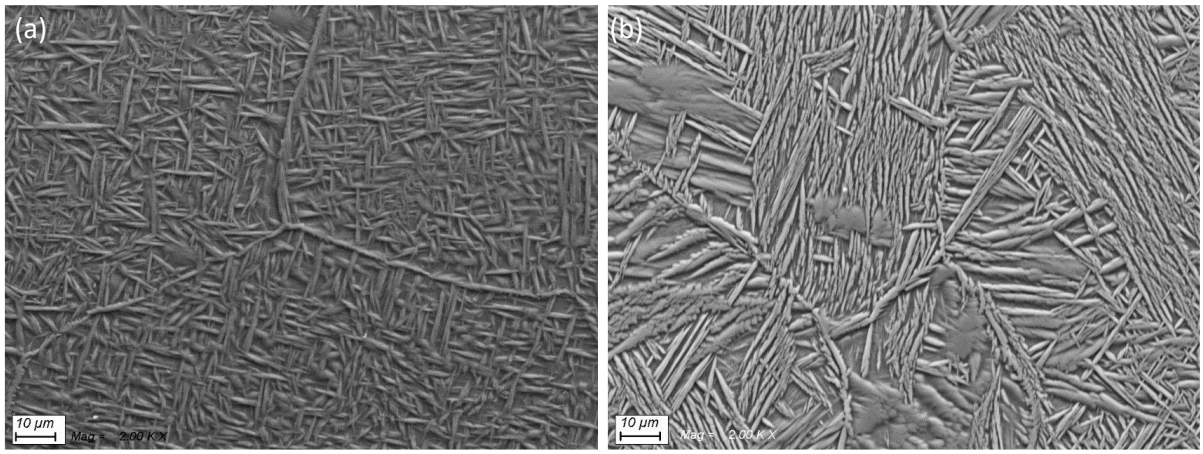

Figure 7.18 High magnification microstructural analysis at (a) crown area of PS-LR rivet and (b) crown area of PD-LR rivet.

In the high magnification SEM microstructural observation, the primary grain boundary α was formed at the crown area in both of PD and PS-LR rivets, but due to the differences in the manufacture strategies and laser scanning time in the post-processing step, the basket-weave structure was observed in the PS rivet (Fig 7.18a), instead of it, the colony α structure transformed in the PD rivet regarding a longer processing time followed higher energy input (Fig 7.18b). Moreover, the grain evolution in this experiment shows a high agreement with the previous parametric study on the post-wash step of metal LR.

7.4.3 Mechanical properties

In the mechanical evaluations for the rivets, the shear tests, fracture surface analysis and micro-hardness tests were carried out for the HSS-LR and post-processing-LR joints, because the Al bush has the mixing issue leads to a poor interlock for the joint, only the ceramic applied as the insert bush material for the rivet samples.

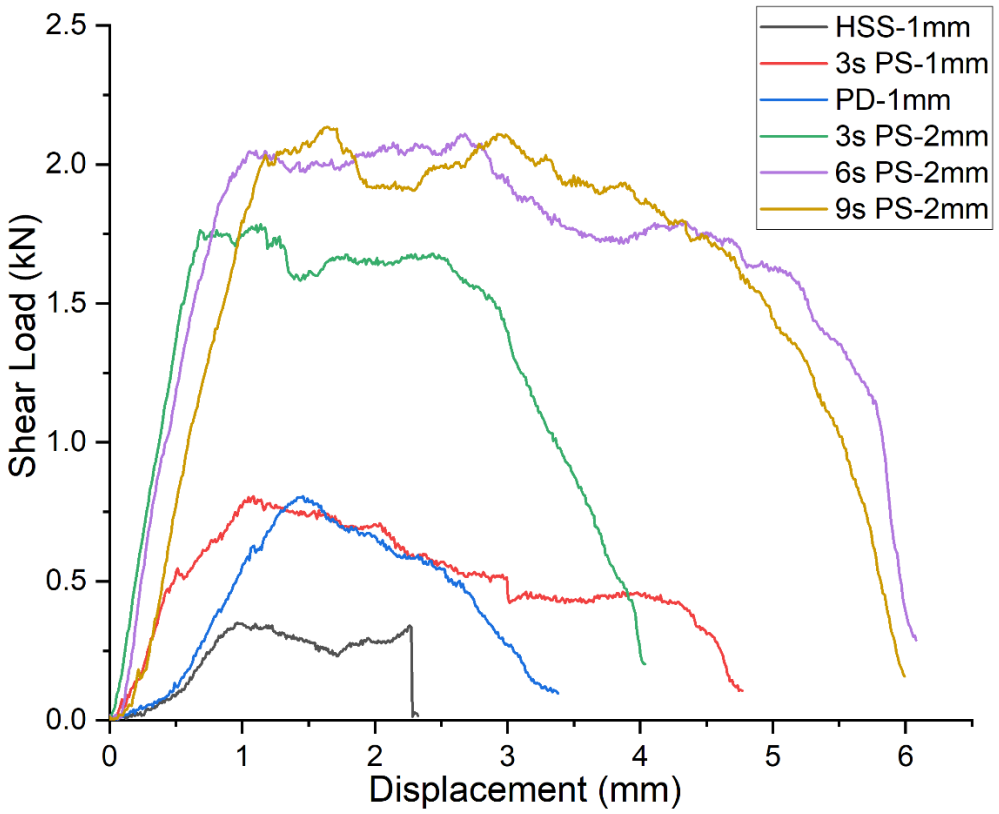

Figure 7.19 Shear test comparison results of HSS and PS rivets joined with 1 and 2mm CFRP upper sheets.

Figure 7.19 demonstrates the comparison shear test results, the load-displacement curves clearly present the three different groups for HSS-LR, post-processing-LR with 1mm and 2mm CFRP samples. Due to the contamination and oxidation problems occurred in the initial-layers deposition processing, a large number of defects (cracks and cavities) were formed inside the deposition. These defects embrittle and reduce the rivet strength, the HSS-LR rivet was sheared apart at the middle of the rivet trunk part at the contaminated area shown in the side view of joint (Fig. 7.20a), and the curve measured the lowest shear load with 0.34kN. In addition, the microstructural SEM photograph on its fracture surface is shown in Fig 7.21, compared to the normal LR joints in chapter 6, a rougher and more brittle appearance with dense pores, and the embedded carbon fibres were observed in the higher magnification image, which proved further detail evidence for the contamination issue.

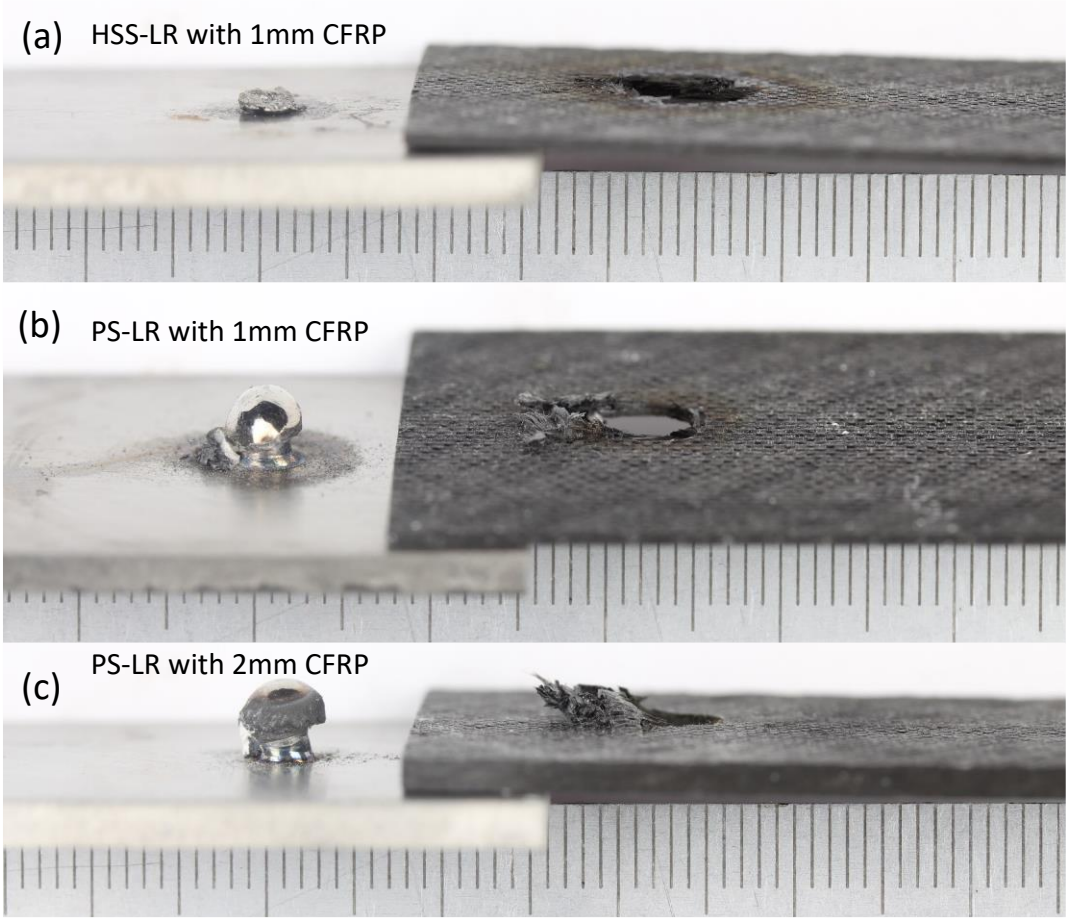

Figure 7.20 Side views of joint failure occurred in rivets applied (a) HSS-LR and PS-LR joining with (b) 1mm and (c) 2mm thickness CFRP sheets.

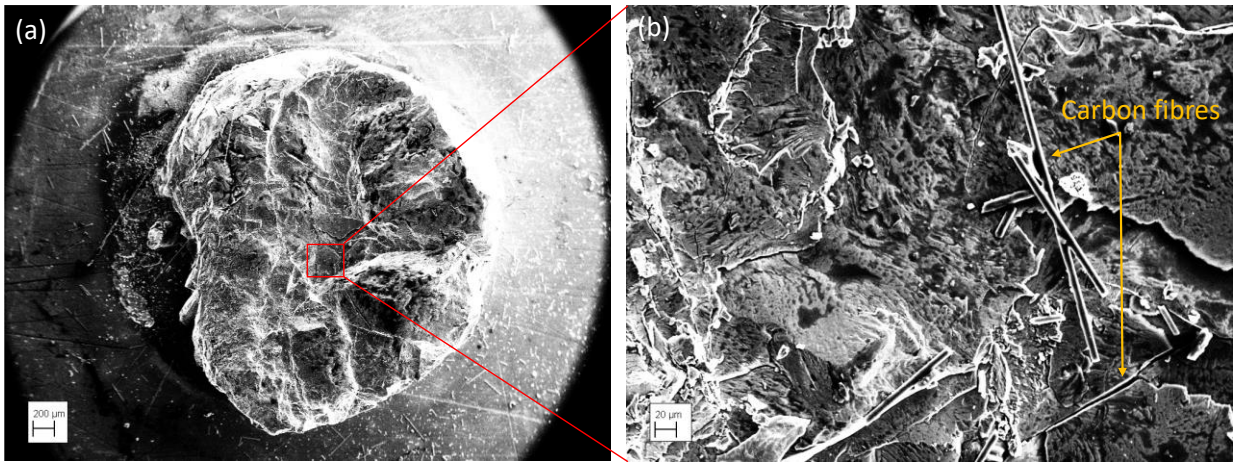

Figure 7.21 SEM microstructural observation on HSS-LR fracture surface in (a) 50x and (b) 500x magnification.

Except the HSS-LR sample failed inside the deposition, all other post-processed rivet failures occurred at the CFRP upper sheets, example side views are presented in Fig 7.20a and Fig 7.20b with 1mm and 2mm thickness CFRP respectively. In the 1mm

CFRP shear tests, the PD and PS rivets measured close maximum shear loads with 0.81kN which is 238% as higher as the value of the HSS rivet. However, because the failure at the hole edge of CFRP, the missed load-bearing condition at the initial few millimetres in the PD curve indicates the CFRP near the rivet hardly can provide the strength regarding the degradation of the surround composite material. From this aspect, the PS is more statable applied as the actual LR application for titanium to composite joining.

In addition, the structure integrity of CFRP upper sheet directly decides the joining strength since the failure occurred at the CFRP edge, the 3s PS rivet joined with a 2mm CFRP sheet shows an 121% higher shear load with 1.79kN compared to the 1mm upper sheet. Moreover, the influence of scanning period on PS rivet strength was investigated in this study, according to the shear test results shown in Fig 7.19, because the longer scanning time increases the heat input on the rivet cap, the crown formed a flatter geometrical shape provides a tighter interlock for the joint, so along with a longer scanning time, the maximum shear strength of 3s PS rivet is slightly improved to 6s PS rivet with 2.11kN, but limited by the surface tension force in the melting titanium liquid, the geometrical shape of melting pool would not be changed after a certain period, a longer 9S PS still presents a similar maximum shear load (2.14kN) with 6s PS rivet. Nevertheless, it needs to be noticed that the initial missed load-bearing status was found in the 9s PS rivet curve, mainly because after a longer laser beam scanning, the degradation in CFRP occurred near the deposition regarding a higher heat accumulation. Therefore, the scanning time should be controlled in a suitable range which long enough to form a flatter crown shape but be limited and stopped before the threshold of CFRP degradation started.

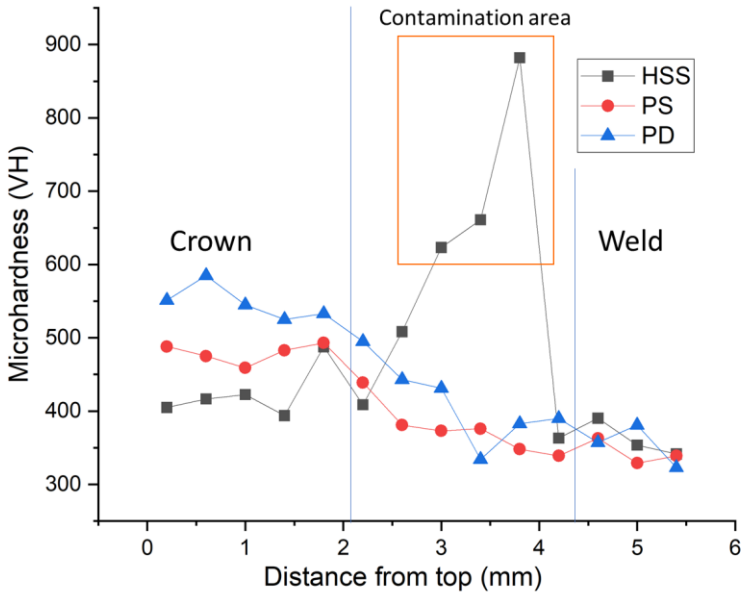

Figure 7.22 Micro-hardness comparison results between HSS-LR and post-processed rivets.

Further microhardness tests were conducted for the HSS and post-processing samples, the results were presented in Fig 7.22. The microstructure directly affects the microhardness behaviour, the micro-hardness curve of HSS rivet shows the ordinary values on top with equiaxed β structures and the HAZ areas, but the hardness values were dramatically increased in the contamination and oxidation area, one assumption is the mixed carbon fibres or particles hardened the material and the observed dendrity microstructure (Fig 7.12b) provides a higher strength. In addition, the PS and PD curves show a high agreement with previous LR studies, higher values were measured both in the PD deposition and HAZ areas than PS rivets, since a larger number of primary and colony α grains and narrower β grains formed respectively under a higher heat input process.

7.5 Summary of findings

The exploration trials for LR applications were carried out in this chapter, the CFRP interaction with the LMwcD were tested in the preliminary trials, the further LR experiments were designed and developed, and their joints were evaluated from microstructural, chemical, and mechanical aspects, and the results found:

- The LMwcD was directly applied into the LR concept for Ti6Al4V/CFRP joining, the insert bush and cover sheet effectively prevent the CFRP degraded from laser scanning and deposition mixture.
- The Al material bush was mixed into the titanium deposition regarding its low melting point, thus the rivet hardly provides the pulling strength for joint. The ceramic bush can avoid the mixing problem, but it caused the oxidation and contamination issues due to the CFRP sheet degraded by heat transfer from the substrate, the EDS analysis also detected an obvious carbon fluctuation in the contamination area.
- Because the heat input and accumulation were controlled and reduced, the post-processed rivets eliminated the contamination issue in the process, the cross-section presents a similar structure with previous LMwcD from both microstructural and chemical observation.
- Shear tests and fracture surface analyses demonstrate the internal fracture that occurred at the contamination area in the HSS-LR rivet, which resulted in the lowest shear strength in the experiments. On the contrary, built by the post-processing deposition strategies, PD and PS rivets failed at the CFRP edge which significantly increased the shear strength of joining structure. However, a certain extend scanning time range for the PS-LR method needs to be optimized for a proper interlocked rivet cap to avoid further damage to the CFRP.

Chapter remarks for research

After the dissimilar metals joining, further LR metal-composite joining was carried out in this chapter. The serious degradation in CFRP and contamination inside the Ti6Al4V in LMwcD tests were identified by microstructural analyses since massive heat input in the process and the huge thermal property differences between materials.

The contamination issue was eliminated by the post-processed LR methods through reducing the heat accumulation, the deposition failure mode was improved to the CFRP break which enhances the mechanical performance of the rivet. As the exploration study of LR joining application, although the post-processed CFRP rivet can provide a certain strength presented in the shear tests, it still needs further

systematic studies to further the interlock and strength improvement in future work to achieve a more applicable and sounder joint.

Chapter 8 Numerical study of Ti6Al4V LMwcD processing

In order to assist thermal and mechanical prediction in the LMwcD processing detailed in this thesis, three numerical models were developed: First, one is used to simulate straight-line wire deposition processing, to calibrate the basic wire-deposition simulation development method, and, based on this model, then two models of NM-LMwcD feasibility experiment in Chapter 4 and HSS-LMwcD in Chapter 5 are developed, which mainly predicts and monitors the heat transfer and residual stress in each individual step in the complicated depositions. To verify the accuracy, all models will calibrate with the thermal history data collected from the corresponding experiments. Therefore, after the LMwcD experiments were completed in chapters 4 and 5, primary numerical models were developed to calibrate the previous experimental results, assist with the experimental investigation of multiple layers of deposition, and predict how the process works under different conditions.

In this chapter, straight-line, NM, and HSS-LMwcD numerical processing models were developed. First, the general methodologies of the whole model were introduced in 8.1, especially the parts related to heat transfer that occurs during the processing and the inactive element method in Abaqus, which functions to simulate the materials deposition procedure. Afterwards, in 8.2, the numerical model generations were explained in detail and the thermophysical properties of materials on heat flux setting was sequentially demonstrated. Then, after the data from the results of the simulation were collected, comparisons between the experimental and numerical results were discussed. Finally, depending on the results shown in 8.3, the quality, merits and drawbacks of this model will be discussed and concluded in 8.4.

8.1 Methodology

Before proceeding to build the model, the FEA modelling method and some basic mathematical problems need to be defined and clarified as they support the modelling processing through correct technical guidance.

8.1.1 FEA mathematical representation

(1) Heat transfer modelling

To properly simulate the process of heat transfer during welding, transient thermal analysis is needed, which can be provided by running a model of the heat flow which is properly used on a 2D or 3D arrangement to create a temperature field that can then be used in thermal stress analysis [8.1]. The total effective heat input (J/s) for an arc welding process can be calculated using the following equation:

$$Q = \eta V I$$

Where η is the process efficiency, V is the welding voltage, and I is the welding current. The thermal efficiency for gas metal arc welding processes is 0.8, as recommended in the R6 procedure.

A model for the heat input during welding can be constructed in one of three ways: a static heat source with prescribed temperature, a static heat source with volumetric flux, and a moving heat source with volumetric flux, listed in order of increasing complexity and accuracy.

Of these approaches, utilising a static heat source with prescribed temperature is the most straightforward and models heat input by viewing the weld (for the model) as being set at a fixed temperature above Tm (material melting temperature) for a period Δt (measured in seconds). The difficult part of this method is choosing an appropriate hold time; too long results in the weld being exposed to too much heat and would also lead to a greater level of plastic deformity, which could negatively impact the estimation of residual stress [8.2].

By way of comparison, a static heat source with volumetric flux sets welding arc energy input (heat flux), rather than temperature and welding efficiency. By applying the computed length of the weld pool, the flux lasting time t can be approximated.

Moreover, this method is applied across the whole weldment, the cross-section of the weld in a 2D model or the whole weld in a 3D model at the same time.

Finally, a moving heat source with volumetric flux can only be used in a three-dimensional welding simulation. In this approach, the heat source can move along a predetermined path. This movement most accurately reflects how welding occurs. The heat source is allowed to travel along a predefined path which represents the most realistic form of the welding process. With regard to ABAQUS, a programmed user-subroutine is applied to create a moving heat source to simulate the welding process, in which the welding voltage, efficiency, current, heat flux, speed, and the heat source's dimensions must be defined

(2) Equivalent heat conduction for convection in the melting pool

This section summarises transient conductive heat transfer's finite element formulation. For more details see the reference section below. It should be noted that heat transfer by means of mass transport in the melt pool is not directly simulated in the present study [8.3]. To address this, the effects of heat transfer are incorporated into the simulation using a distributed heat input model. By enforcing energy balance in a Lagrangian reference frame x for a domain of volume V (see Fig 8.1), the following partial differential equation is produced:

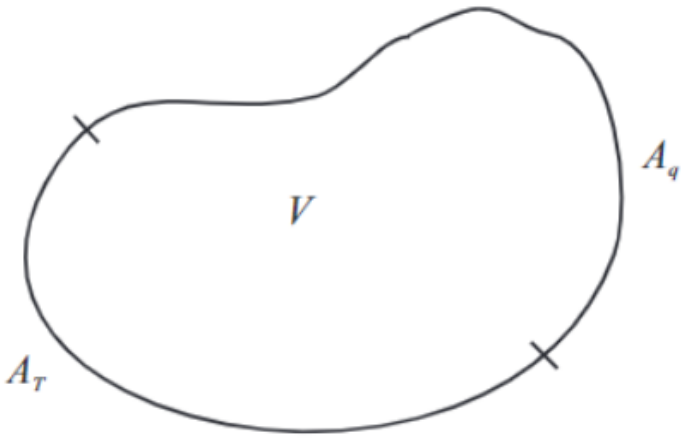

Figure 8.1 A body showing volume, the prescribed temperature on the surface, and prescribed surface flux on its surface [8.4].

$$Q(x,t) - \frac{dH}{dt}(x,t) - \nabla \cdot q(x,t) = 0 \quad \text{in the entire volume } V \tag{1}$$

Where x is spatial coordinate and t is time. T is the temperature, q is the heat flux vector, Q is the heat source, and H is the enthalpy.

The initial temperature field is given by

$$T(x,t_0) = T_0(x) \quad \text{in the entire volume } V \tag{2}$$

Where, T_0 is the prescribed initial temperature. The boundary conditions below are applied on the surface,

$$T(x,t) = T^p(x,t) \quad \text{on the surface } A_T \tag{3}$$

$$q^s(x,t) = q^p(x,t) \quad \text{on the surface } A_q \tag{4}$$

Where $T^p(x,t)$ and $q^p(x,t)$ denote the temperature-dependent surface flux and prescribed temperature, respectively. Surface convection and radiation are defined as follows:

$$q^p(x,t) = h(T - T_\infty) + \sigma\varepsilon(T^4 - T_\infty^4) \tag{5}$$

Where, h is the convection coefficient, and T_∞ is the room temperature. ε is the emissivity and σ is the Stefan–Boltzmann constant.

The energy flux q is expressed as a function of temperature T using the nonlinear isotropic Fourier heat flux constitutive relation:

$$q = -k(T)\nabla T \tag{6}$$

Where, k is the thermal conductivity. The rate of the enthalpy can also be rewritten as

$$\frac{dH}{dt} = \frac{dH}{dT}\frac{dT}{dt} = \rho C_p \frac{dT}{dt} \tag{7}$$

Where ρ is the density of the flowing body, Cp is the specific heat.

Substitution of Eqs. (6) and (7) into Eq. (1) results into the following:

$$Q(x,t) - \rho C_p \frac{dT}{dt} + \nabla \cdot [k(T)\nabla T] = 0 \tag{8}$$

Using an implicit formulation, the temporal derivatives at time n t are approximated by the backward finite difference:

$$\frac{d^n T}{d^n t} \simeq \frac{T_n - T_{n-1}}{t_n - t_{n-1}} \tag{9}$$

Where, T_n and T_{n-1} are the temperatures at times t_n and t_{n-1}, respectively.

Using the Galerkin finite element discretization and the New-ton–Raphson solution scheme, Eqs. (8) and (4) result into the following element residual R and Jacobian $dR/d^n T$:

$$R = \int_{V_{element}} \left\{ B^T k B^n T - N^T Q + N^T N \rho C_P \frac{T_n - T_{n-1}}{t_n - t_{n-1}} \right\} dV + \int_{A_{q_{element}}} N^T q^p dA \tag{10}$$

$$\frac{dR}{d^nT} = \int_{V_{element}} \left[B^T k B - B^T \frac{\partial k}{\partial T} B^n T N - N^T \frac{\partial Q}{\partial T} N \right. \tag{11}$$

$$\left. + N^T N \rho C_P \frac{1}{t_n - t_{n-1}} \right] dV$$

$$+ \int_{V_{element}} \left[N^T N \rho \frac{\partial C_P}{\partial T} N \frac{T_n - T_{n-1}}{t_n - t_{n-1}} \right] dV$$

$$+ \int_{A_{q_{element}}} N^T \frac{\partial q}{\partial T} N dA$$

Where, T is the element temperature nodal vector, N and B are the operators that compute the temperature and temperature gradient as follows:

$$T = NT \tag{12}$$

$$\nabla T = BT \tag{13}$$

(3) Mass addition

Detailed below is the calculation for metal feed volume from the wire deposition process. In the laser wire deposition process, the filler wire steadily flows into the molten pool. The wire deposition can result in material utilisation efficiency of $\sim 100\%$ [8.5]. The wire deposition rate in kilograms per second (kg/s) can be expressed as

$$\dot{m} = \rho v_f \times \pi r^2 = \rho v_s \times A \tag{14}$$

Where D is the diameter of the filler wire, A is the cross-sectional area of the added layer formation, and v_f and v_s represent the wire feed rate and laser scanning speed, respectively.

8.1.2 Inactive element method

In this experimental model, to simulate the mass addition deposition procedure, the inactive element method is applied in the ABAQUS.

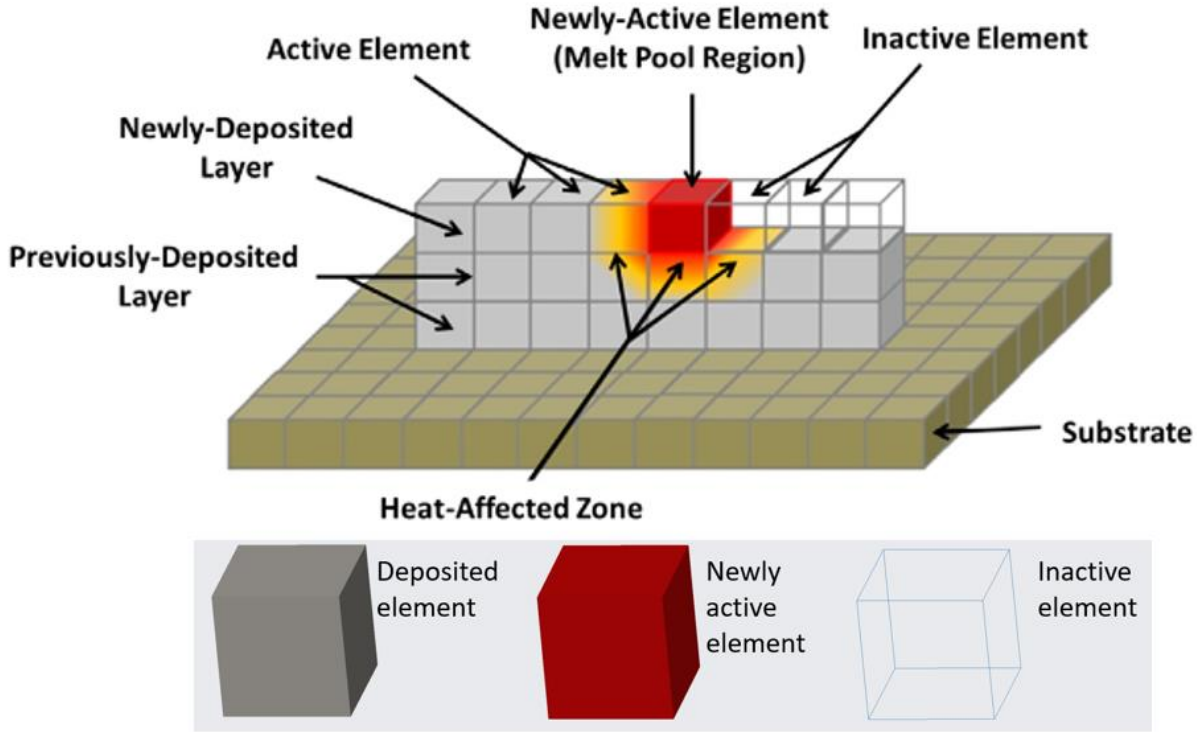

Figure 8.2 Inactive element method.

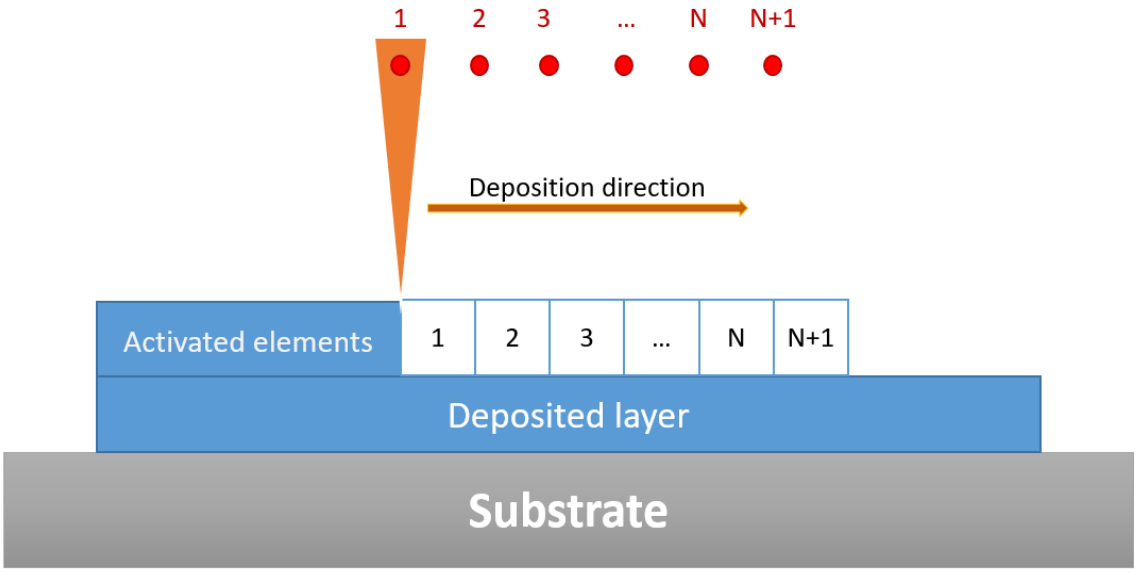

Figure 8.3 Simulation processing steps in inactive element method.

The simulation of mass addition (also named as “massification”) can be achieved by a number of fixed geometry situations, each geometry relating to a specific time, every

new time-step has additional mass inserted into the mesh. Then, the neighbouring mesh is linked, and the environmental values are inputted, and the boundary conditions are simultaneously set (see Fig 8.2). The number of new elements introduced over a time interval is then a function of the wire feed rate. It should be noted that to produce a proper simulation of input heat flux and local liquid flow mechanics, each set consists of small elements [8.6].

In the present research, the blocks are categorized into three categories: the red block activates when the laser beam is scanned onto it, whilst the inactive blocks will activate sequentially as the laser moves. As shown in Fig 8.3, the small blocks are the discrete parts of the current layer, the built-up is the substrate or the completed layer, and the handstand triangles represent the laser beam. Initially, there is no block or laser on the built-up plate. During the first step, block 1 is introduced and activated instantaneously, before the laser beam moves at a speed of from position 0 to position 1. In step two, block 2 is introduced and activated, before the laser beam moves from position 1 to position 2.

In relation to the inactive element method, the elements which represent the metal deposition regions are taken out of the analysis, meaning that only nodal degrees of freedom that correspond to active elements are accounted for. Numerical implementation involves calculating the elemental residual (equation (10)) and Jacobian (equation (11)) for only the active elements and only solving for the active nodal degrees of freedom.

8.2 Simulation of LMwcD

As discussed in 2.3, in this chapter, the ABAQUS as a reliable and suitable FEA software, is employed in this thesis. The flow chart in Fig 8.4 illustrates the basic processing steps of numerical modelling in this case.

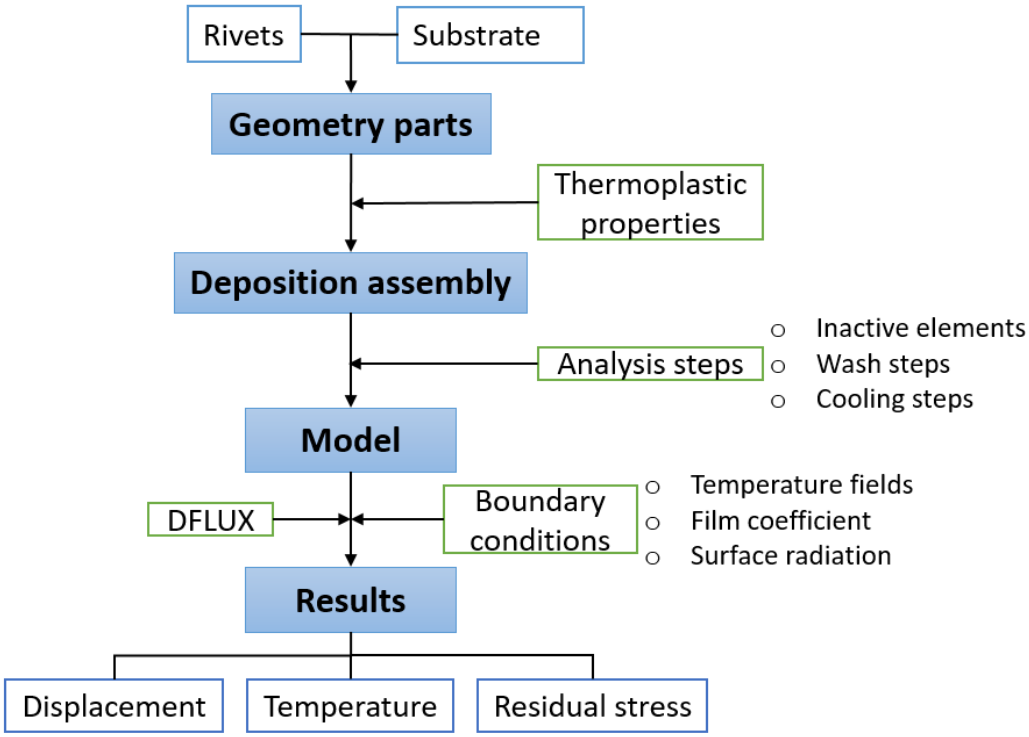

Figure 8.4. ABAQUS flow chart for the deposition modelling process.

8.2.1 Simulation modules in ABAQUS/CAE

ABAQUS/CAE is a simulation software used to develop an FE model which allows simulations to be made in nine modules:

(1) The PART module creates the geometry and regions for relevant sections. In addition, the sketch can be further partitioned to separate material regions that have distinct properties whilst also refining the mesh.

(2) The PROPERTY module takes the component which is going to be modelled and allows the user to define its material property/properties. In the instance that there are several parts that possess different properties, each individual part must be referred to as a section property.

(3) The ASSEMBLY module helps to position the parts in a manner that represents an actual configuration.

(4) The STEP module determines both the analysis time steps and output requests. It advises the simulation history, meaning that the results are dependent on the order of

events. The output can be preselected to incorporate appropriate variables for the analysis in question as well as the output results times.

(5) The INTERACTION module determines and oversees the mechanical and thermal interactions between regions of a model and its surroundings. A typical example of a thermal interaction in the process of welding is surface heat loss.

(6) The LOAD module administers loads and boundary conditions (BCs) to regions or defined sets. It then assigns them to STEPs in the analysis history. Note that loads and boundary conditions can be applied as either thermal or mechanical conditions.

(7) MESH breaks up the assembly into regions that possess different element types and densities. This step represents or approximates a geometry by incorporating nodes and elements.

(8) The JOB module functions to allow for an analysis to be introduced as a job. An input that is submitted to the job for analysis holds all relevant information for the model in question, such as element numbers, part geometry element type, BCs, material properties, etc. Once submitted, the job can then be monitored and managed.

(9) The VISUALISATION module looks into the modelling results. Such results can be plotted using a specific contour or path. X-Y plots can also then be generated to compare the result's revolution over time.

8.2.2 Experiments set-up

In the part of LMwcD experiments in this thesis, normal and high-speed continuous spiral deposition methods have been developed in chapter 4 and 5 respectively, to assist develop and validate the models in the simulation part, 3 standard experiments are designed to collect the real-time data, which are basic straight-line deposition, normal 4-layer normal deposition, and 6-layer high-speed continuous spiral (HSS) deposition.

All the substrates and deposited wire in three experiments have the same material use Ti4Al6V and the dimension of the substrate are designed to $150mm \times 25mm \times 3mm$, in this deposition processing, the deposited wire diameter is $0.8mm$. In order to complete stable processing in the experiments, and be simulated smoother in the modelling, the processing parameters will be set to appreciate value level, all the processing parameter of the validation experiment shows table 8-1 below. For the thermal-history data collection preparation, TC-08 Thermocouple Data Logger (Pico Technology) is set with K-type thermal couples, which can measure the temperature value of the target area between 0 – 400℃.

Table 8-1. processing parameters of validation experiments.

	Straight-line deposition	NM-LMwcD	HSS-LMwcD
Max. Power (W)		600	
Beam diameter (mm)		2	
Deposition trave speed (mm/min)	90	45	90
Wash path speed (mm/min)	N.A.	90	N.A.
Wire feed speed (mm/min)	432	246	432
Wire feed angle (°)		30	
Gas flow (L/min)		20	
Cool down time (s)		120	

(1) Basic straight-line deposition

Before the LMwcD experiments and their modelling are investigated, the first validation experiment of basic straight-line deposition is conducted, this experiment aims to build up the fundamental deposition numerical model with simple travel movement. Sketch and dimensions of the straight-line experiment are shown in Fig 8.5 below, the deposition path length is 30mm and the deposition processing starts

from left ends to the right with 90mm/min deposition speed, two thermal couples are located in 10mm distance from the start and endpoint, this enables to expect two various thermal history curves with different peaks regarding the processing time increase, which also can provide certain reliability on the whole temperature field of this model.

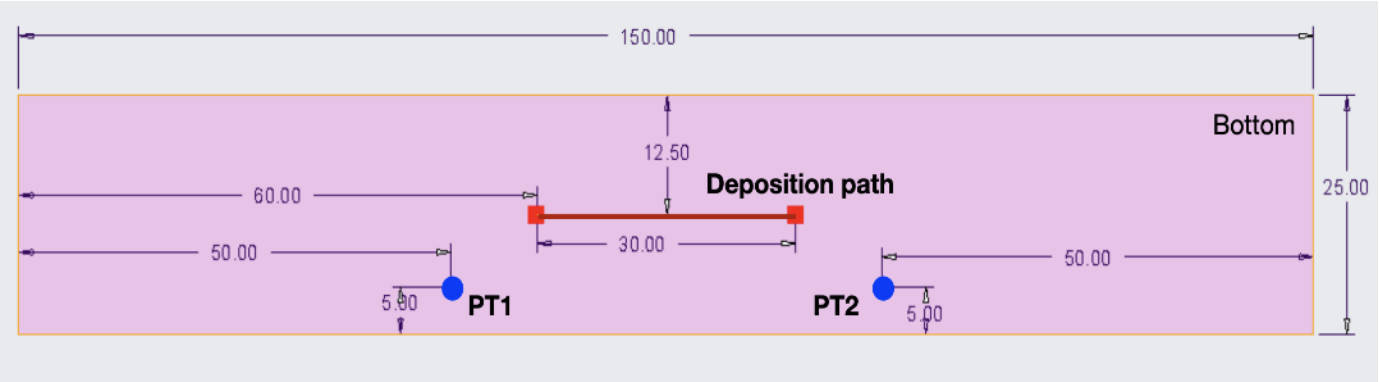

Figure 8.5 Sketch and dimensions of the straight-line experiment.

(2) NM-LMwcD

In the first basic straight-line deposition experiment, LMwD modelling has been built systemically, this thesis's experiments (both LMwcD and dissimilar joining parts) will be developed gradually based on the previous fundamental model. In this chapter, normal LMwcD and HSS laser-wire deposition experiments are designed and conducted, Fig 8.6 shows the thermal couple's positions and the sketch dimensions, the cylinder deposition will process in the middle point of the substrate. In order to validate the bottom temperature field of the substrate, test points are located in positions with different distances from the central (deposition) point.

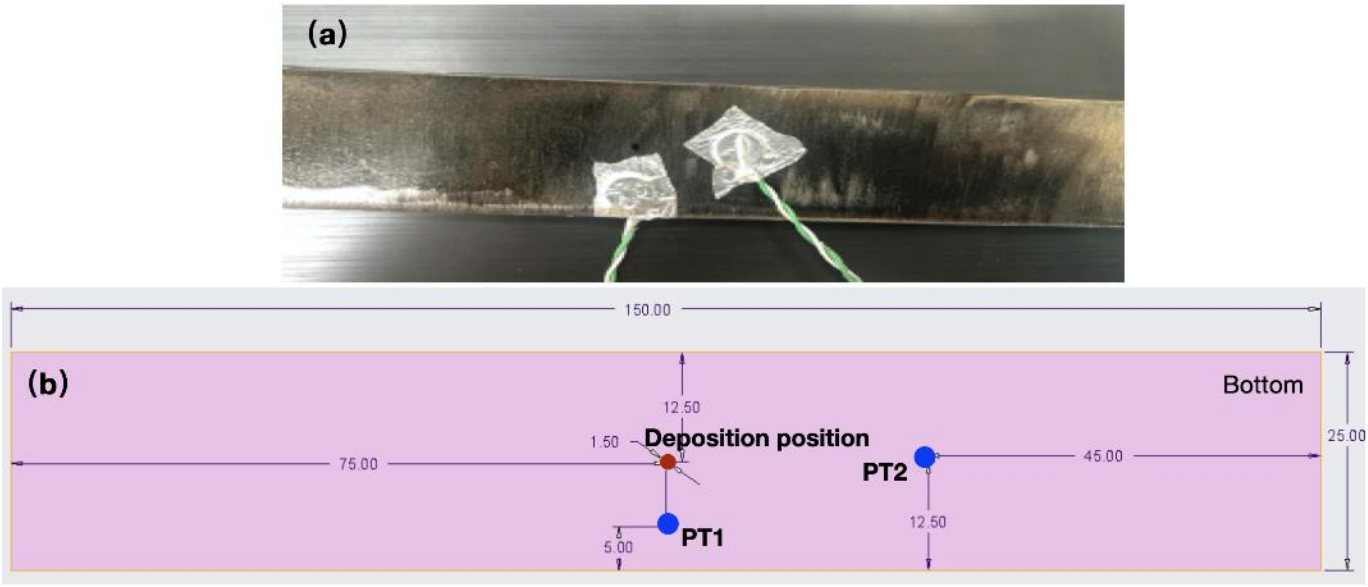

Figure 8.6 Normal LMwcD experiment: (a) thermal couples and substrate (b) Sketch and locations.

(3) HSS-LMwcD

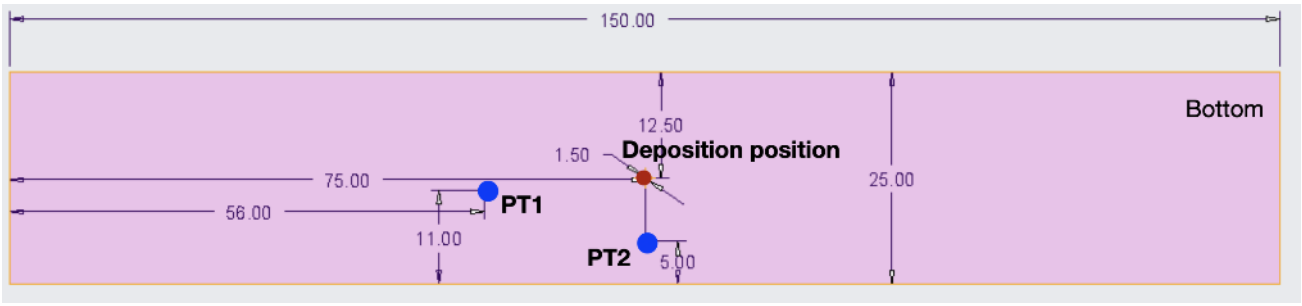

Figure 8.7 Sketch and dimensions of 6-layer HSS deposition experiment.

After the normal deposition method, a 6-layer HSS deposition experiment is conducted in the third experiment, which is also the final LMwcD method designed according to chapter 5. Similar to the normal deposition experiment above, the deposition path is in the centre of the substrate and two thermal couples are set to the substrate and differently far away from the processing position, Fig 8.7 above shows the thermal couple's positions and the sketch dimensions.

8.2.3 Generation of FEA model

Three FEA progress models are developed in this chapter without the heat energy setup, the basic settings of modelling geometry, material properties and mesh design are introduced in the following:

8.2.3.1 Deposition geometry creation

In the part modular, the geometrical features are created based on the experiment expectation/demand or result outcome. In the additive manufacturing simulation, the whole model structure is divided into two main components: substrate and adding material, the detail of the parts creation in the three models are introduced below.

(1) Basic straight-line deposition

In the first basic straight-line deposition model, overlook the adding material and the substrate shown in Fig 8.8 To simplify the model behaviour from the experiment processing, the adding material part is designed to a long half-cylinder shape in the part modular, the cross-section sketch refers to the real result from the experiment outcome, and the substrate refers to the exact dimension of the used object.

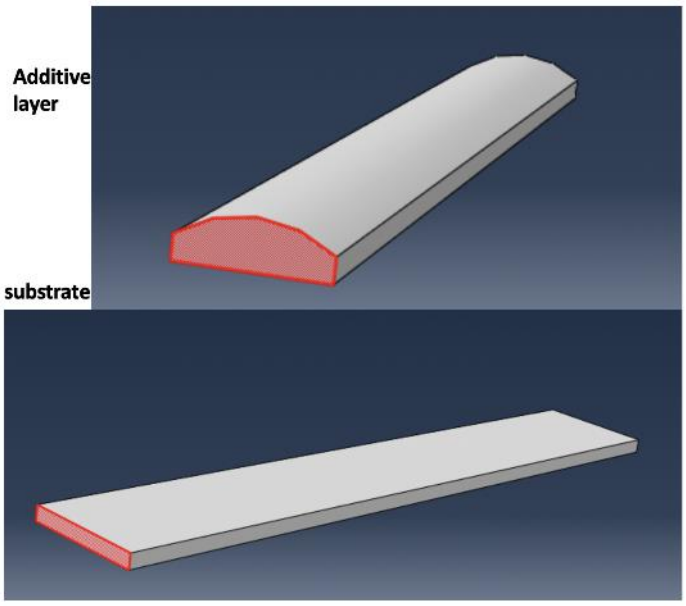

Figure 8.8 Parts creation of substrate and adding material in the straight-line numerical model.

In this model, for the adding material's part dimension, cross-section height is $1mm$, and width is $3mm$. For the substrate, the dimension is $50mm \times 50mm \times 10mm$, and all the three models in this chapter share the same dimension of this substrate.

(2) Normal deposition

Fig. 8.9(a) shows an image of a deposited rivet of the Normal deposition experiment. This image demonstrates the weld profile. Additionally, an axisymmetric 2D model of the rivet was produced. The geometry of the rivet is calculated so as to reproduce the deposition profile as accurately as possible and simplified geometry is used to minimise any potential issues when sketching.

Fig. 8.9(b) shows the geometry of the rivet zone with created partitions, based on the different procedures in the experiment: deposition step, wash path step, cool down step, and three sets of depositions with three separate layers. Additionally, three pins in the deposition central parts and a substrate were created.

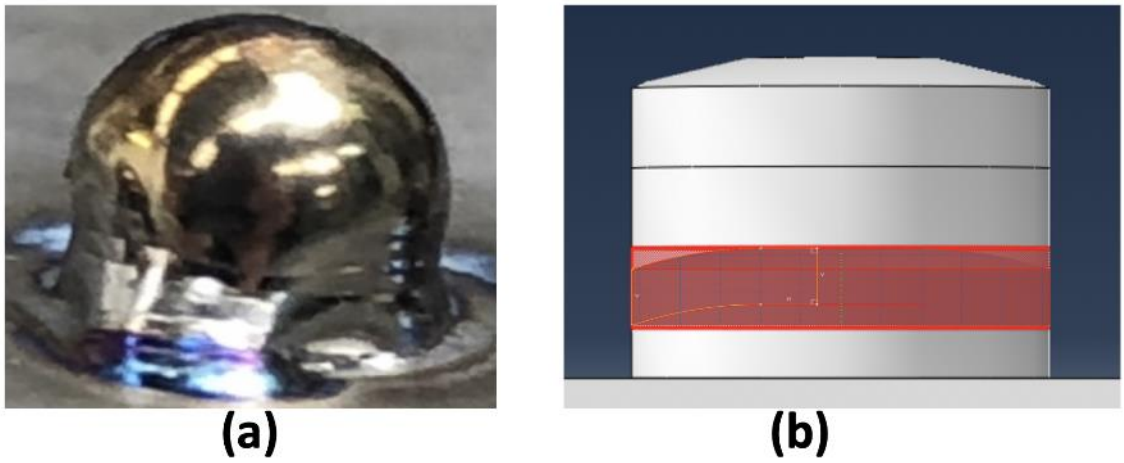

Figure 8.9 (a) the experimental geometry shape of the Normal LMwcD rivet whilst (b) details a simplified geometry shape and middle layer sketch for rivets parts in ABAQUS.

Here, according to the result record, the radius of each layer rivet is $2mm$ and the thickness is $0.8mm$ (which is the same as the height adjustment in the experiment).

(3) HSS deposition

In the third numerical model, the overall shape of the deposited rivet is similar to the previous model, which is a similar-cylinder body with several layers and a pin inside. However, because of the difference between the two LMwcD methods, the layer divided in the rivet is a similar quarter circular-cone with various thicknesses, which instead of the half-cylinder in the previous model, Fig 8.10 shows the rivet part creation in the HSS deposition model. In the HSS deposition model, wash path and cooling

time are removed, quarter layers with different heights are added in turn during the deposition procedure, in which way to simulate the spiral deposition processing.

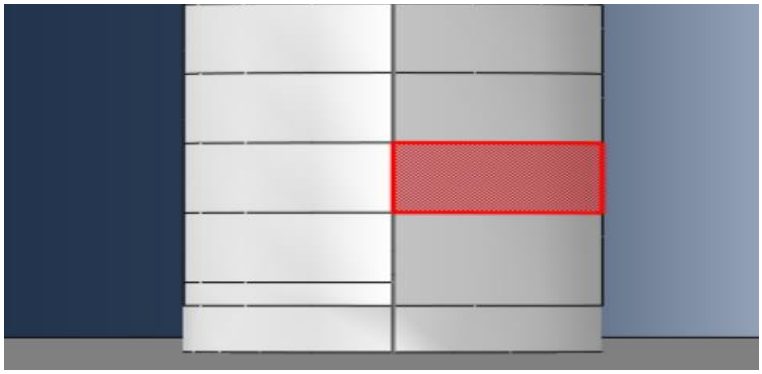

Fig 8.10 Rivet part creation in the HSS deposition model, highlight area is an example of a single quarter layer.

8.2.3.2 Materials thermophysical properties

In this LMwcD numerical study, as all experimental material is Ti6Al4V, three models share the same material properties, the material property data used was gathered from existing experimental measurement and literature surveys [8.7-8.10]. The thermal and mechanical properties, including density, conductivity, elasticity, thermal expansion coefficient, plasticity and specific heat were determined using values that were either fixed or temperature dependent. Both the substrate and deposition are the Ti6Al4V, and the material thermophysical property data used are listed in Tables 8-2 and 8-3, and Fig 8-12.

Table 8-2 Thermal conductivities and densities of Ti6Al4V depend on temperature.

Thermal conductivity $W/m/℃$	**Density** kg/m^3	**Temperature** ℃
7.07	4480	20
9.44	4430	200
14.5	4380	600
19.79	4330	1000
27.5	4250	1500
28.5	4200	1800
67.5	3890	1928
71.5	3650	2300
73	3500	2500

77	3250	3000

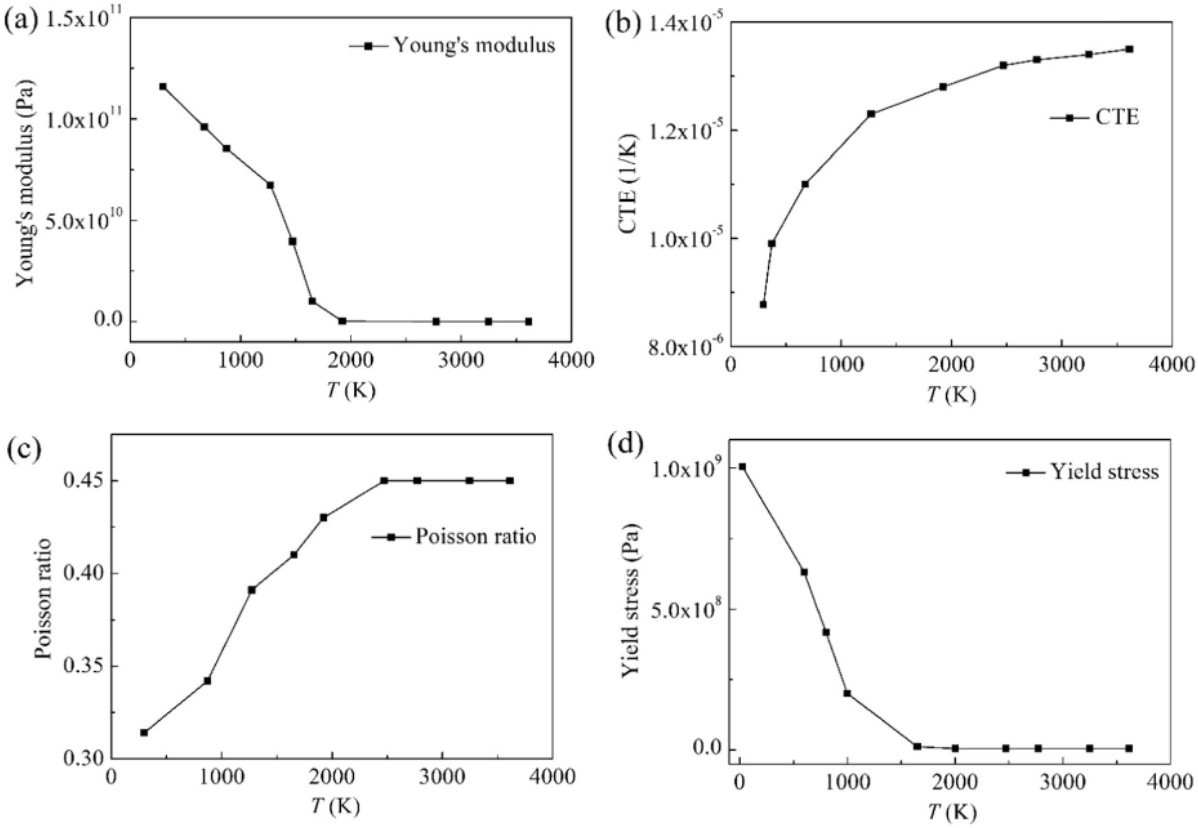

Figure 8.11 Mechanical properties for Ti6Al4V: (a) Young's modulus, (b) coefficient of thermal expansion, (c) Poisson ratio and (d) yield stress [8.9, 8.10].

8.2.3.3 Element type and mesh design

The meshing for this thesis was applied in the assembly module for the deposited material and part module for the substrate respectively. This allows for the mesh size to be easily managed separately.

A general mesh view is shown below in Fig 8.12 In order to optimize the balance of calculation usage and accuracy of the model, seeds distribution will be adjusted from coarse to fine size, which depends on the distance from the deposition (heat input) position, the seed size in the central. For instance, in the mash map of straight-line deposition model mash map below, the overall seed sizes are divided into three parts, the seed size of far areas near the edge part is 4mm, then the near parts between the

central and edge, which seed size is 2mm, in the central areas of substrate and the deposition (rivet) zone, the seed size of them are 1mm, all the three models applied the similar distribution strategy to divide the assembly mesh. The detail of element generation in mesh modular in three models are listed in the following:

- Straight-line model: The geometry mesh was constructed on the deposition assembly with a total of 300 elements, and 6318 elements on the substrate part.
- Normal deposition model: The geometry mesh was constructed on the rivet assembly with a total of 12507 elements, and 30703 elements on the substrate part.
- HSCS deposition model: The geometry mesh was constructed on the rivet assembly with a total of 21983 elements, and 36289 elements on the substrate part.

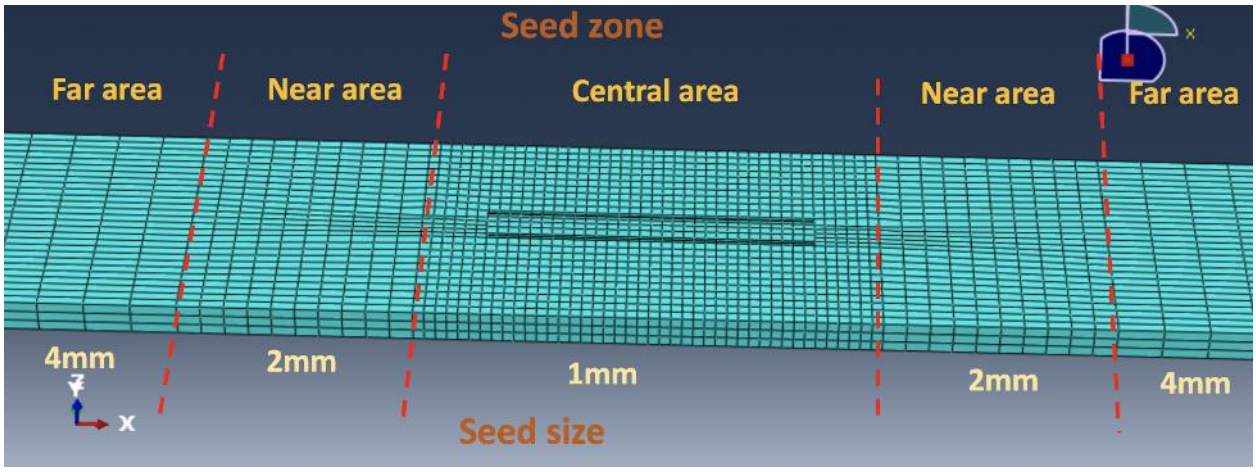

Figure 8.12 Mesh modules in the Straight-line deposition model

In this study, all three models aim to the thermal stress analysis, so the same mesh strategy is applied to them. Mesh shapes of both the deposition part and the substrate are set to Hex, and the technique used is a sweep method. What is more, there are several selections for element types such as linear, quadratic, hybrid and reduced integration. With regard to the analysis type in the mesh module, the Couple Temperature-Displacement (C3D8T) is chosen, and the setting interfaces are shown in Fig 8.13

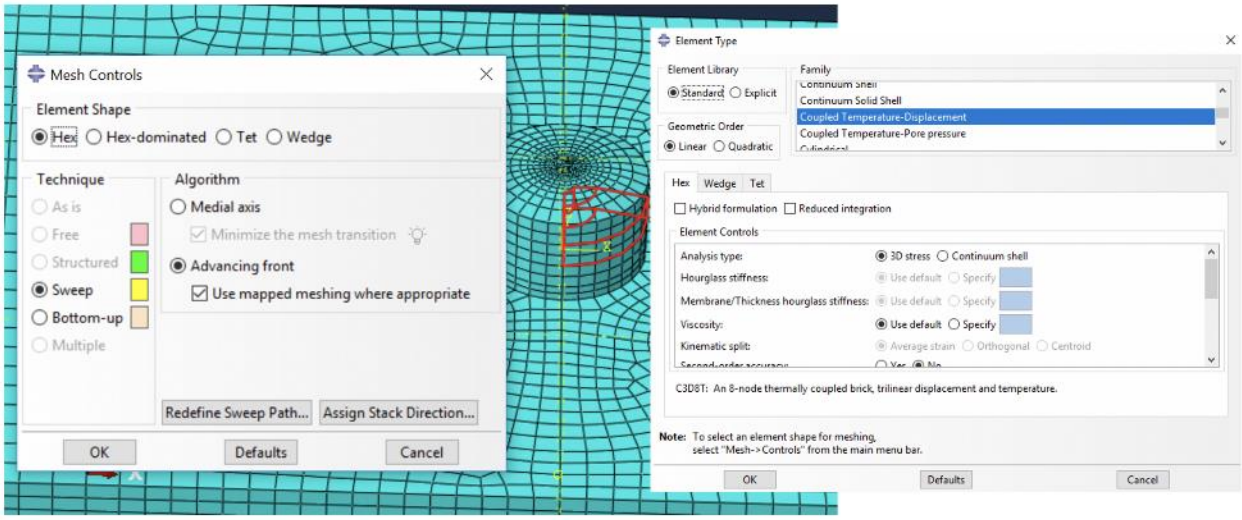

Figure 8.13 Element and mesh setting in Normal deposition model.

8.2.4 Heat flux modelling

8.2.4.1 Heat flux load

During the laser deposition process, the physical phenomena associated with the melt pool are incredibly complex and largely dictated by mass and heat transfer. Several research projects are being conducted on heat flux modelling in the laser processing area. Such studies tend to focus on 3D body heat flux as a means to simulate the melt pool profile. In Zhidong‘s study, the different 3D heat sources (cylindrical, semi-spherical, semi-ellipsoidal shape) used to simulate laser powder bed fusion were compared, and new equations for their varied thermal conductivity and laser absorptivity were proposed [8.11]

Since Rosenthal [8.12] first suggested punctual and linear heat sources in his pioneering research, a number of other more realistic sources have been put forward. In instances where the distribution along the thickness is not as important as it is with thin plates, the surface Gaussian heat source model offers a promising proposal for bed-on-plate cases when conductive laser welding needs to be simulated [8.13]. On that basis, in the present research, because the laser processing is carried out using a conduction mode instead of a keyhole mode, the keyhole profile in the model does not need to be simulated. Therefore, in this study, surface heat flux can be considered as the most suitable energy source to simulate the laser interaction.

The laser beam heat source power is described using the Gaussian distribution model distribution presented in Fig 8.14 The mathematical form can be written as:

$$q(r) = \frac{3\eta_1 Q_1}{\pi r_0^2}\left(-\frac{3r^2}{r_0^2}\right) \qquad (15)$$

Where the laser beam power is $600W$ and $480W$ for the deposition and wash path respectively, and the laser spot radius r_0 is $1mm$. In the heat transfer simulation, because the absorptivity of laser power is influenced by various factors (target's roughness, temperature, incident angle, etc.), in this case, the absorptivity of laser power $\eta = 0.2$ depends on the specific model is taken.

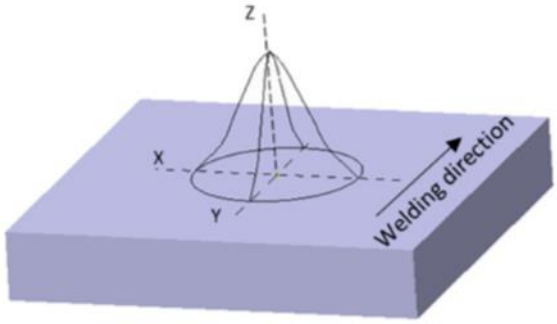

Figure 8.14 Gaussian distribution model [8.14].

There are two kinds of thermal load that are active during the deposition and wash path period and the setting surface on each layer of rivet (Fig 8.15). All of the user-defined DFLUX subroutine content is programmed with the Fortran language, to precisely simulate the laser source moving in the process.

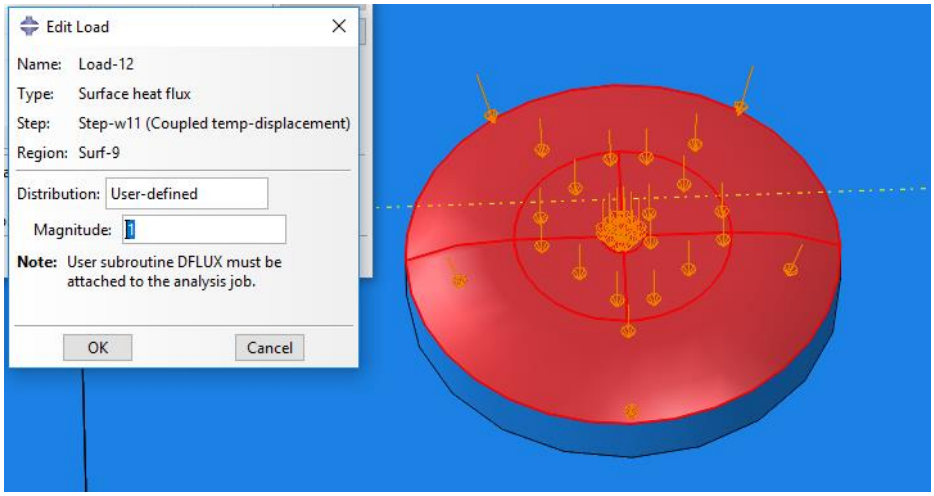

Figure 8.15 Thermal load setting for first layer wash path in Normal deposition model.

8.2.4.2 Boundary conditions

Three different boundary conditions and model interactions have been set: mechanical and thermal boundary conditions, model surface film coefficient, and model radiation coefficient.

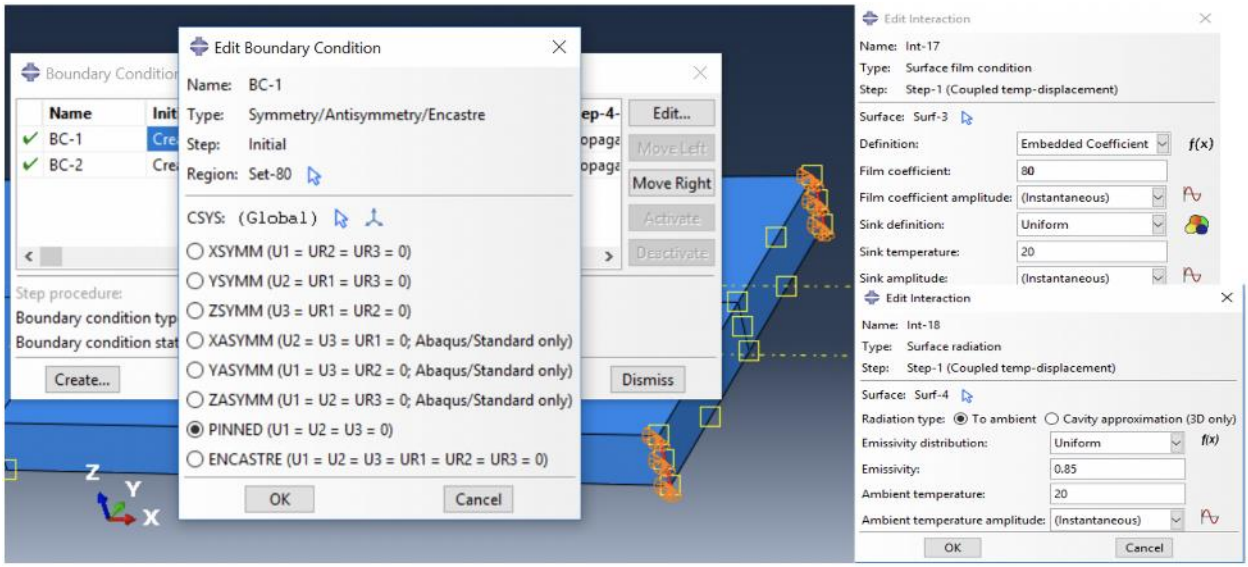

Figure 8.16 Boundary and interaction setting interfaces in Normal deposition model.

As shown above in Fig 8-17, to make a high agreement with the experimental condition, the mechanical boundary is pinned to the four corners and the room temperature is 20. According to the previous research [8.15, 8.16], in the surface film and radiation coefficient setting interfaces, the film coefficient and emissivity at ambient temperature are set to 25 and 0.8, respectively. However, during the processing, because of the temperature change in the material, the surface film coefficient was adjusted to the higher value level corresponding to the condition.

8.2.4.3 Processing procedure steps and parameters

In the step modular, each motion procedure in the processing is divided and defined by a time period specification, and for the FEA calculation, the number, minimum/maximum value, temperature boundaries of each step are set in this modular as well.

(1) Straight-line deposition

Classically, the whole processing will focus on the two kinds of procedure in numerical modelling: loading and unloading, which need to be considered specifically depending on the calculation condition and capability. Similar to the normal thermal-stress modelling in ABAQUS, the whole processing procedures of laser metal wire deposition (LMwD) modelling is divided into deposition (loading) and cooling (unloading) steps.

Since as the fundamental model, the straight-line deposition follows the basic setup in deposition and cooling procedures. The long half-cylinder deposition is partitioned into 30 small parts, and every one of them will be activated in turn in each deposition step according to inactivated element method. Therefore, in the deposition procedure, the laser travel speed is 90mm/min, the total processing time is the 20s, thus the time of each step should be set to 0.667s. For the cooling procedure, steps are created, total cooling time is 130s, duration of each step is set to 30s. Fig 8.17 below shows the set-up interface of the step manager in the straight-line model.

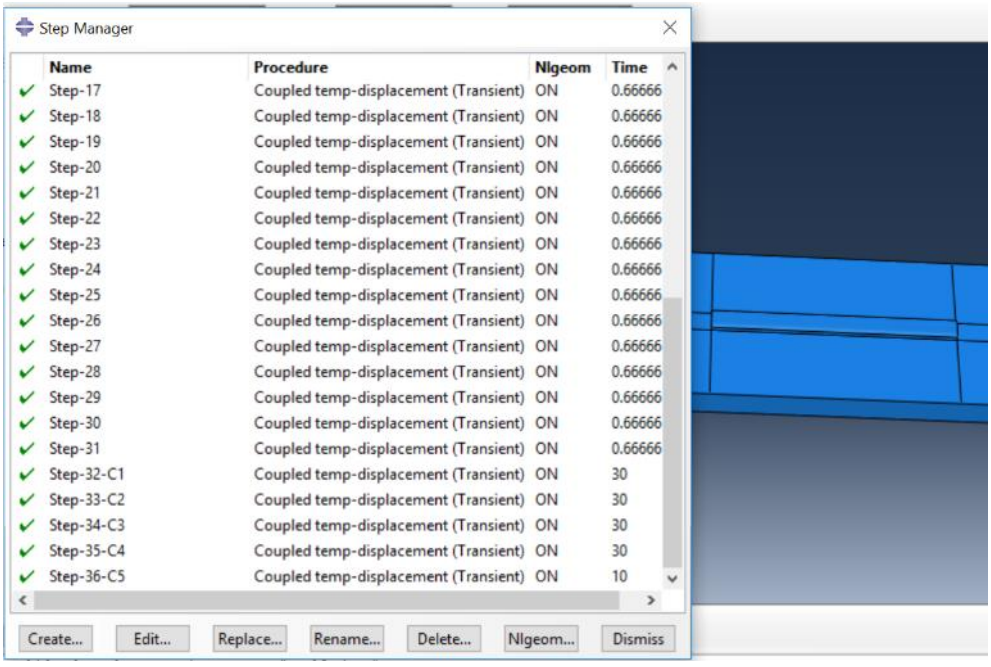

Figure 8.17 the step set-up of deposition procedure in the straight-line model.

(2) Normal and HSS deposition

In the Normal deposition modelling, the rivet has three layers deposited in total. For each layer, the processing time is divided into three parts according to the experimental procedure: deposition period, wash path period, and cooling time. For

example, for the first layer in the deposition, the deposition path is 9s and the inactive elements method is employed in this period. Afterwards, it will into wash-path immediately before finally the 5s cools down, then the next layer is then processed.

Instead of the wash path and cooling steps, the deposition path did the continued spiral motion in the HSS deposition model. Moreover, as mentioned in the part modular, each layer consists of 4 divided deposition quarter-cylinder, and two deposition steps correspond to a quarter layer. Therefore, in this 6-layer HSCS deposition model, there are 48 deposition steps, and each cooling step was set to 20s, 54 steps in total are set in this model.

8.3 Results and discussion

Temperature history results were recorded and collected from the thermal couples in experiments, and they were compared with those from the developed numerical modellings in this result section. First of all, the microstructural, thermal and mechanical relationships in the model were introduced in 8.3.1, then the overview of the temperature field and melting pool profile in three modellings are presented and discussed, which gives the basic overall pictures to introduce the LMwD processing in the three numerical modellings. Then for the experimental results, both the melting profiles in the processing and the temperature history results were compared and analyzed with each model in turn, the comparison results provided credible evidence to support the feasibility of each model, both from the processing procedure and the thermal-historical data aspects. In addition, the displacement and stress maps after the cooling time of the model were presented, which exhibits the mechanical behaviours affected by the LMwD processing.

8.3.1 Basic microstructure comparison

As the process carried out, the laser source was generated and input the energy into the system, which increases the temperature of both adding material and substrate. And depends on the energy reached, the material was melted (fusion zone) or metallurgically transformed (heat affected zone), then the latent heat and plastic energy dissipation interact into the manufacturing process. In the AM, the processing

is deeply coupled with all the aspects from mechanical behaviour (stress and strain), thermal behaviour (heat generation and transfer), and the metallurgical behaviour (phase transformation), and different behaviours also interacted with each other, and the effect of this has been defined as metallo-thermomechanical coupling [8.17, 8.18], and their relationships during the AM process are demonstrated in Fig 8.18.

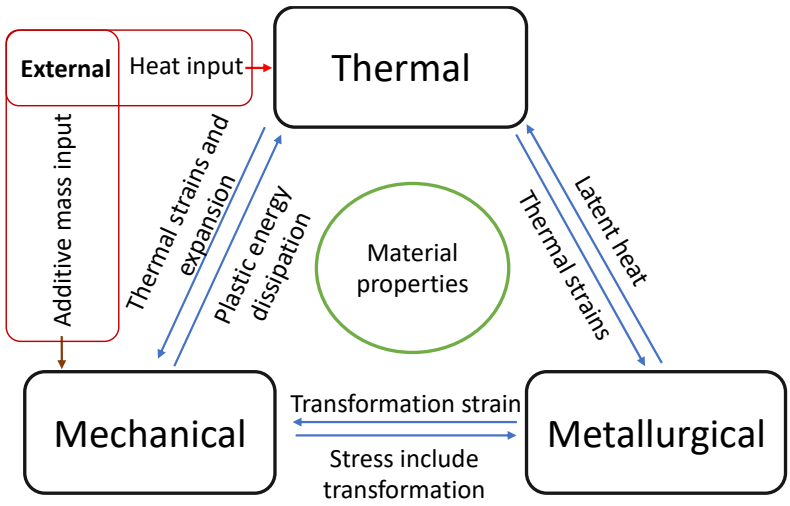

Figure 8.18 Metallo-thermomechanical coupling in AM process.

As the basic, the properties of materials are directly involved in the activities with all three behaviours. The thermal behaviour and external laser heat input influence the status of stress and strain by temperature increase and followed plastic deformation, it leads to the phase changes as well which driven by the metallurgical transformation kinetics. Normally, in subtractive manufacturing (turning, cutting, and drilling), the plastic deformation and friction in the process produce the energy effects in the thermal field, meanwhile, the strain influence the metallurgical transformation which is named strain-induced transformation [8.19]. However, due to the difference between the processing, AM affected by these mechanical factors is much reduced or even can be neglected along with decreasing of the material mass input. The phase changes lead to dilatation which is reacted into the mechanical field, meanwhile the latent heat also affected heat transfer during the solid-liquid transition in the thermal field. In addition, because of the transformation in the phase constituents, the thermomechanical features are significantly influenced which also affected the material performance in the process.

In this case, the overall temperature field can be measured through thermal couples, but due to the invalidation of thermal couples in the high temperature near or in the

melting pool, it is hard to obtain the thermal histories in the central area, thus the cross-section microstructure observation will be compared with the experimental results. Therefore, because these three fields are strongly coupled together as illustrated above, in the FEA model, if the temperature field (numerically calculated thermal historical curve) and metallurgical field (cross-section microstructure map) can be precisely simulated compared with the experimental results, the corresponding predicted mechanical behaviour will also provide a certain accuracy even without the experimental evaluation. This is also the basic condition is proved that the numerical model can perform its prediction function.

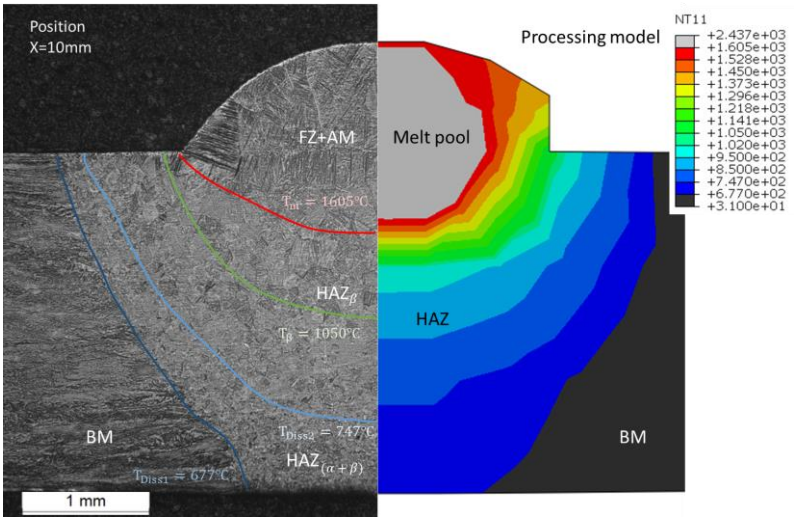

Figure 8.19 Straight-line sample cross-section (X=10mm) comparison between the experimental microstructure and numerical model.

Fig 8.19 shows the bead microstructure comparison, the cross-sections are taken at X=10mm (distance from the deposition start point) position same from the completed experiments and in-process numerical model respectively. The top area is the fusion zone (FZ) of the melting added material (AM) and the base substrate, in the numerical model, the grey area means the melting pool (over solidus temperature 1605℃) during the process, and the left side, above the red line, indicates the zone has melted the microstructure mainly consists of the basket-weave structure and prior β grain can be observed [8.20]. In the heat-affected zone (HAZ), T_β stands for the β transus temperature and T_{Diss} means the temperature point that α starts the dissolute to the β grain, so the area between the blue and red line is regarded as the $\mathrm{HAZ_\beta}$, and a clear trend is observed that the β fraction is increased from bottom to top along with the rise of temperature in the model map. Due to the α-dissolution temperature still is an

unconfirmed value which reported range from minimum 677℃ (T_{Diss1}) to maximum 747 ℃ (T_{Diss2}) [8.21, 8.22], so the zone marked $\mathrm{HAZ}_{(\alpha+\beta)}$ is the material start dissolute from α to β or little fraction has been partly transformed, which in the numerical map is the dark blue gap at the outer rainbow. Finally, the temperature below the lowest dissolution temperature T_{Diss2} was not affected by heat treatment labelled base material (BM), which coloured solid black in the processing model map.

The microstructure comparison results confirmed that compared with the experimental microstructure, the corresponding numerical processing model presents a high agreeable temperature map, and competitive similarities both in AM+FZ and HAZ areas. It needs to be noted that, the numerically calculated areas are all slightly smaller than the experimental microstructure, one explanation is in the modelling generation, the heat input is all considered as released on the substrate without wire absorption, so the melting pool in added material is smaller than real condition. Another reason is that the model shows the melting status of the experiment, the higher temperature would continue expanding in actual condition after the laser processing and enlarge the HAZ area. In sum, the contour map of numerical results still presents a reliable trend of metallurgical transformation from the view of thermal field compared to the experimental results.

8.3.2 Temperature field and melting pool profile

Fig 8.20 and Fig 8.21 below show the overview temperature fields and melting pool profiles of three models respectively, since the same pattern of the linear motion of the laser energy input, the map overview and melting pool of the straight-line model has a similar temperature map with laser welding model, the temperature distribution shows a high agreement with the welding FE model in [8.21]. The map shows a partial view in and around the deposition path, under the combined effect of heat source shape and laser travel direction, the temperature gradient curve elliptically spread from the central area to the outside, which is steep and confined to a central region around the heat source at the location of welding and deposition. In this model, the maximum temperature value is around $1870℃$, and the melting pool is bilaterally symmetrized since the thermal boundary condition setting.

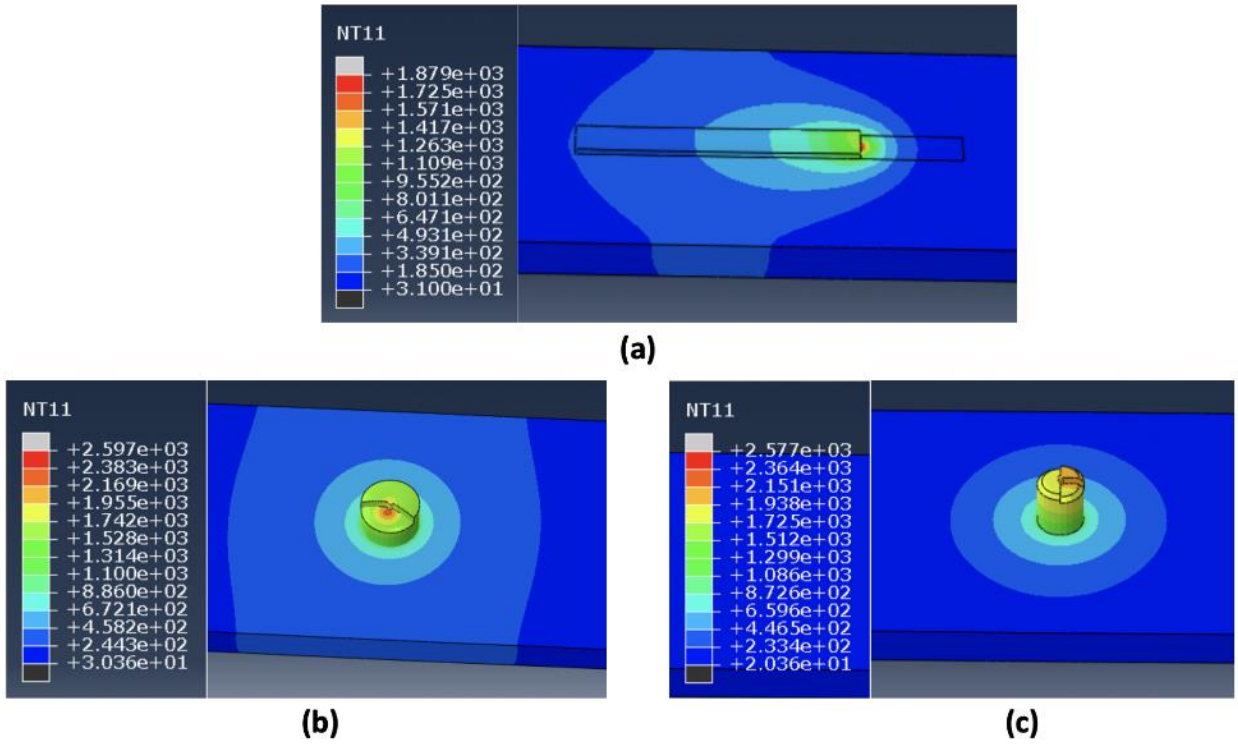

Figure 8.20 Temperature field of the numerical modellings: (a) Straight-line deposition model, (b) Normal deposition model, (c) HSCS deposition model.

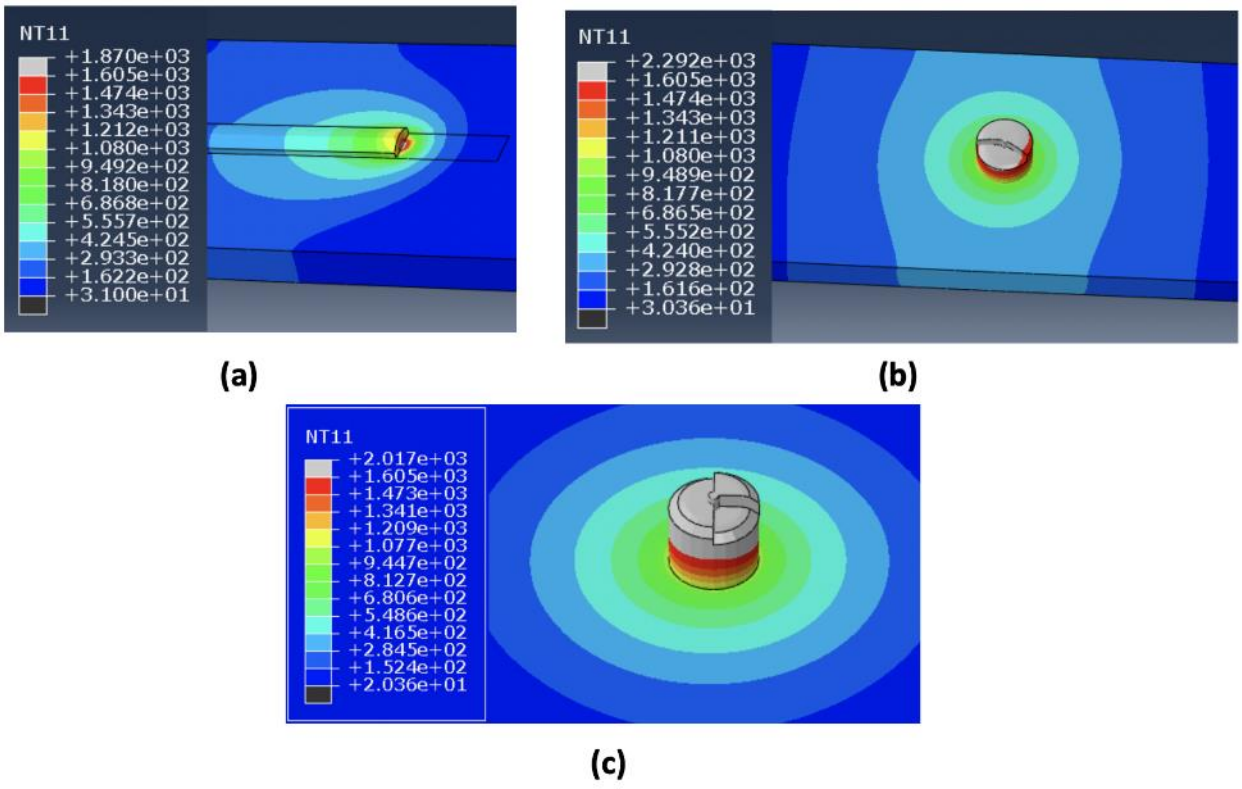

Figure 8.21 Melting pool profile in three numerical modellings: (a) Straight-line deposition model, (b) Normal deposition model, (c) HSS deposition model.

Figures above show the overview temperature fields and melting pool profiles of normal deposition and HSS deposition, when halfway through processing, both of their maps were obtained at the final layer deposition. For the temperature field in Fig 8.21 (b) and (c), the temperature gradient is still steep and confined to a central region around the heat source at the location of the deposition, which appears a similar presents ladder form decrease with straight-line deposition map. In another point of temperature distribution, because of the difference of laser deposition travel path strategy, the deposition processing has repeated the path of the cycles in the normal and HSS models, it leads the heat input accumulated in a certain area, consequently, the circular distribution is observed instead.

In addition, due to the energy accumulation difference in the deposition strategies, which directly influence the maximum value of temperature in Fig 8.21, the maximum temperature of the straight-line deposition is lower than which in the cylinder models, and because of the total processing time difference, the maximum temperature of normal deposition is slightly higher than it in HSS deposition. In another perspective, the deposition processing of HSS is completed in one short time, which efficiency is much higher than the normal deposition, so the temperature gradient curves are more intensive in the former model.

8.3.3 Experimental results comparison

Here, two aspects of the feasibility of the numerical modelling are checked with experimental records: the melting pool profile captured by the real-time camera, and the temperature history data collected by the thermal couples. Both of them are compared with three numerical models in turn, and the results will be presented and discussed in the following.

(1) Basic straight-line deposition

The comparison results of melting pool profile shown in Fig 8.22, the recorded photo is taken from calibration experiment shows in Fig 8.22(a), a laser melting area is observed at the bead of the deposition, and present a similar semi-ellipsoid melting zone, which also shows the similar shape of high-temperature curves in numerical

modelling in Fig 8.22(b). For the grey calculated melting pool profile, which is moderately smaller than it in experimental result, mainly because the heat flux path is the simplified ideal condition, which is set at the top of the substrate and the bottom of the additive material part, but in the real condition, laser beam directly covers the wire tip, added material top surface and part of the substrate. From the view of heat input, it would not cause a huge difference with experimental conditions.

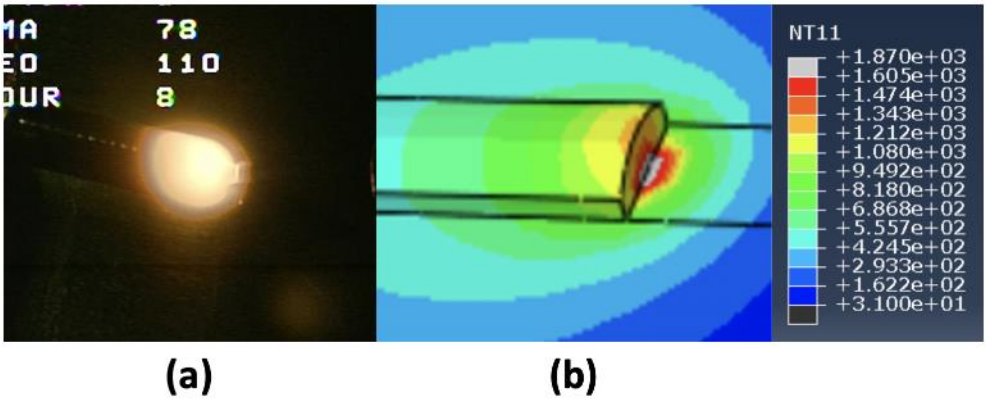

Figure 8.22 Record Melting pool profile comparison between the experimental and numerical results of straight-line deposition: (a) Real-time photograph, (b) FE model.

In the numerically calculated thermal history curves, two different thermal couples expected two curves with different times and peak values. The curve of PT2 position is rise later but faster and higher than which of PT1, affected by the joint actions of laser deposition travel path and the heat transfer in the substrate material. The comparison results show in Fig 8.23, compared with the experimental data, the calculated curve of PT1 position is slightly over the collected data from the thermal couple, but the curve of PT2 is equal to the experimental result. Therefore, the fitting curves provide a solid result for the accuracy of this basic straight-line model, which gives a general and fundamental guideline for the FE model of simple deposition additive manufacturing.

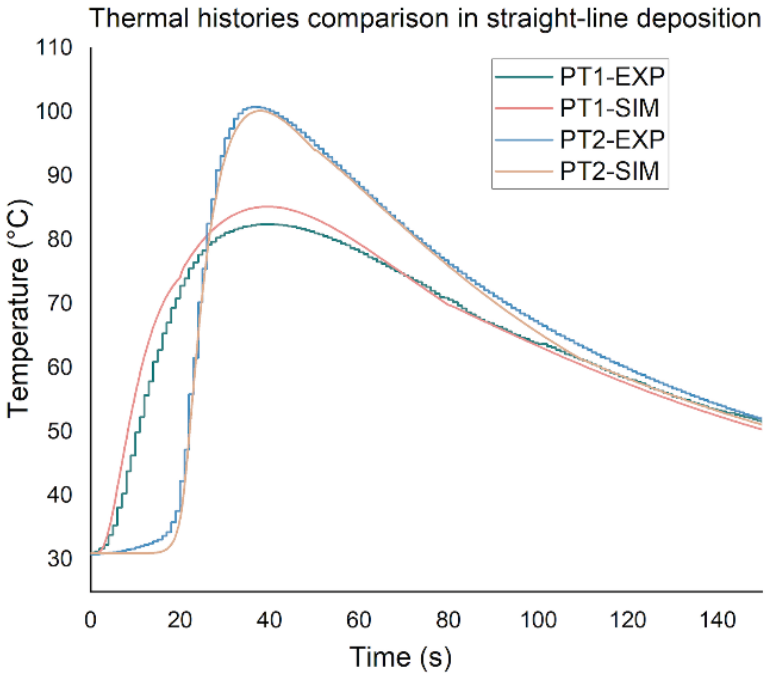

Figure 8.23 Numerically calculated thermal histories of single straight-line deposition calibrated by using thermocouples data.

(2) NM deposition

Fig 8.24 shows the melting pool profile at the 4th layer deposition processing, the deposited rivet is partly reheated and melted at the top in a certain area, and because of discontinuity cooling time break, the melted boundary can be clearly recognised on the deposited material, which presents a similar situation both in the recorded picture and the numerical model.

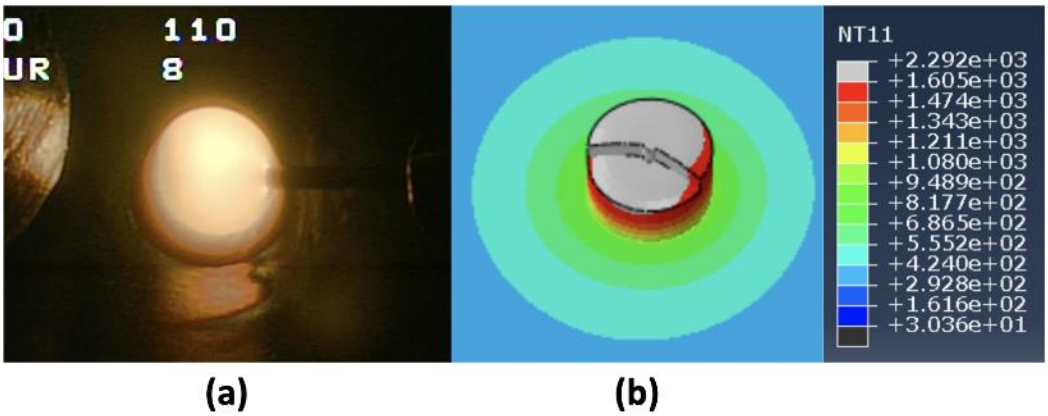

Figure 8.24 Record Melting pool profile comparison between the experimental and numerical results of 4-layer NM deposition: (a) Real-time photograph, (b) FE model.

The comparison results of thermal history curves between numerical and experimental data are shown in Fig 8.25 PT1 present similar trending and values with experimental data, each layer cycle contains one peak due to the discontinuity of the deposition, wash path and cooling step, there are 4 peaks (thermal cycles) and the fluctuation area range from $169 \sim 304$ ℃ during the deposition process. Because of farther distance from the central deposition position and heat transfer interaction, PT2 only went through one peak in the whole process, which numerically calculated peak (112.8℃) is slightly lower than experimental data, the relative error of two curves between the numerical and experimental results keep roughly less than 10%.

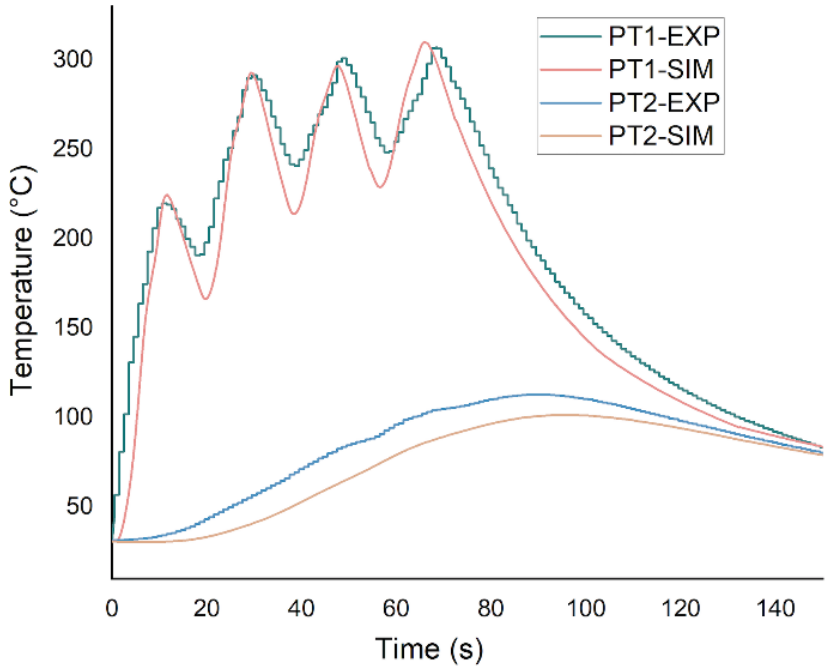

Figure 8.25 Numerically calculated thermal histories of 4-layer NM deposition calibrated by using thermocouples data.

(3) HSS deposition

Fig 8.26 shows the melting pool profile at the final layer during the HSS deposition, similar to the normal deposition above, the deposited rivet is heated and melted at the top, because the whole processing is continuous, the molten area is larger and has a lower unclear boundary line with solidified deposited material, the recorded picture and the numerical model map also shows the same status.

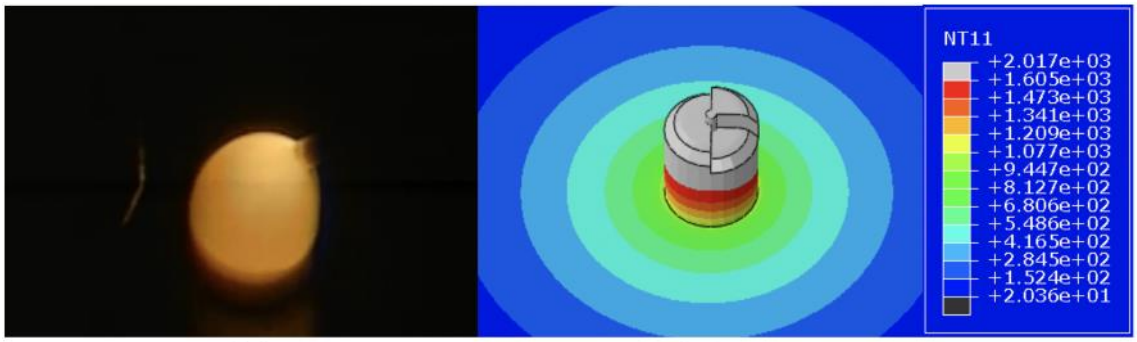

Figure 8.26 Melting pool profile recording comparisons between the experimental and numerical results of 6-layer HSS deposition: (a) Real-time photograph and (b) FE model.

Two trends of thermal history curves show in Fig 8.27, in the HSS deposition method, the deposition path is continuous at one time, for each curve only one peak appears in the whole processing. And since the high efficiency of the heat input, the PT1 curve increases significantly and reach the peak (286℃) in a short time in the deposition path and then cooling down, for the PT2 curve, it increases slower and the maximum value (83℃) is lower than the former due to the farther distance from the deposition position. Thanks to the simplified deposition method, both PT1 and PT2 values are almost equal to the collected data from the experiment, which means the successful development method, and provide solid evidence of validation results for the numerical model.

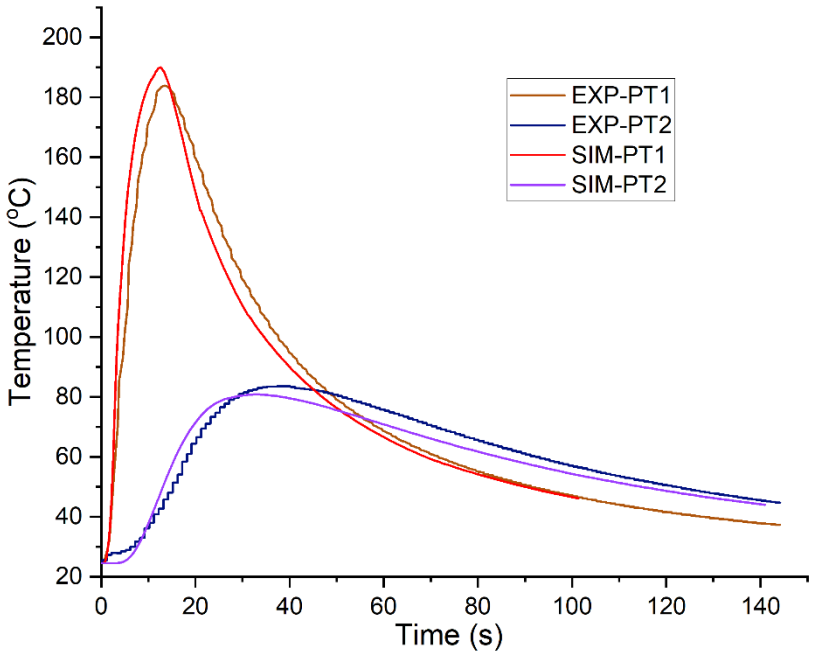

Fig 8.27 Numerically calculated thermal histories of 6-layer HSS deposition calibrated by using thermocouples data.

8.3.4 Overview of displacement and residual stress

Besides thermal analysis for the numerical modelling, their mechanical behaviours are measured and observed. As seen in Figures 8.28 and 8.29 shown below, displacement and stress maps have been obtained from the three modellings, they are observed after the cooling down steps to analyze the effect relate to residual stress.

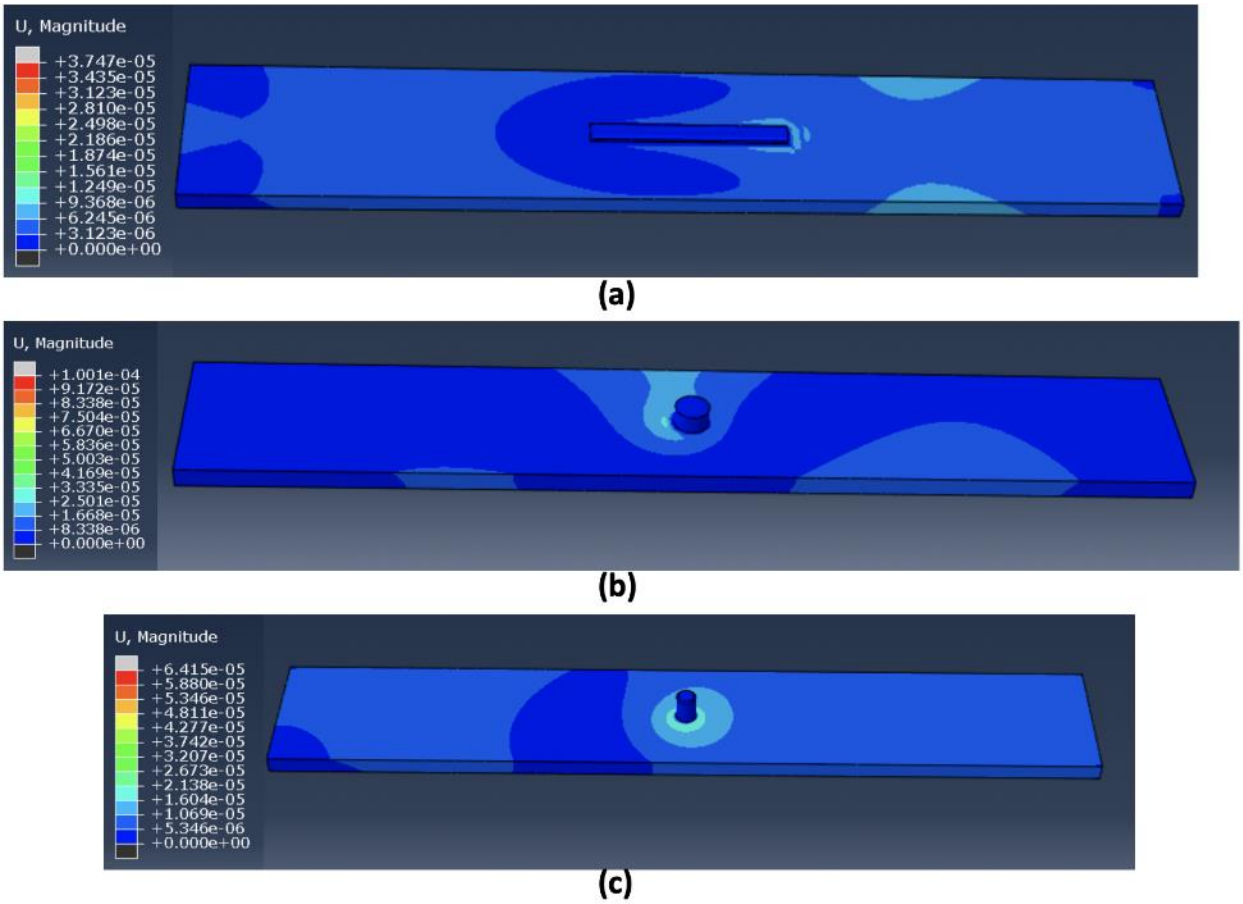

Figure 8.28 Displacement scale map after the cooling time of three numerical modellings: (a) Straight-line deposition model, (b) Normal deposition model, (c) HSS deposition model.

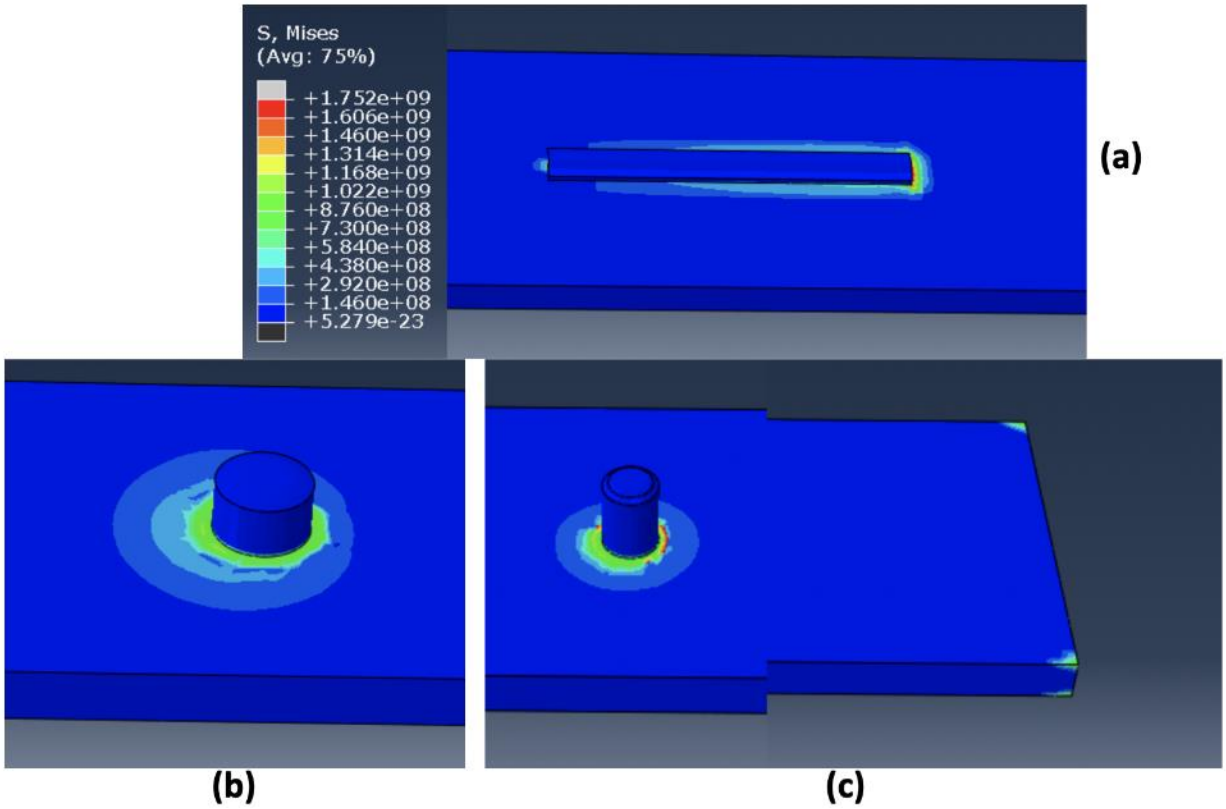

Figure 8.29 Stress field after the cooling time of three numerical modellings: (a) Straight-line deposition model, (b) Normal deposition model, (c) HSS deposition model.

Because of the special requirement boundary conditions for the deposition (welding) part and pinned edges, the deposition and rivets are encastred to avoid the excess distortion during the deposition processing. According to the measurement in Fig 8.29, most of displacement and distortion are concentrated in and around the deposition areas and the fixed points, where also be set to the mechanical boundaries and processing path. This trend of displacement and stress lies in the joints and fixed edges, affected by residual stress which shows a certain agreement with [8.5] and [8.22]. In this case, the displacement and stress values of the three models are kept at a low level, which for displacement is around $37.5{\sim}100.0\,\mu m$ and for stress is around 1606 MPa, and the maximum value is most influenced by the factor of energy accumulation mentioned above. However, it should be noticed that the whole processing time is quite short, it leads to a minor mechanical behaviour presented in this study, and it is affected by other factors like substrate dimensions, material properties and deposition strategies as well. Therefore, in further studies, stress and displacement field monitor and analysis are still required in multiple rivets deposition or other complex heat input cases.

8.4 Summary

In this study, applied with an inactive element method, though the introduction of each single modular of model generation, three Laser Metal wire Deposition numerical modelling are designed and accomplished: basic straight-line deposition, 4-layer normal deposition and 6-layer HSS deposition. Meanwhile, their corresponding experiments are conducted, calculated thermal history curves were obtained by thermal couples to calibrate the thermal analysis results from FE models developed.

The temperature field and melting pool profile of each model is captured when halfway through processing, the whole procedure shows a high agreement with the experiments in chapters 4 and 5. The temperature gradient curves distribution will be varied from elliptical to circle pattern, with the deposition direction changed from single straight-line to cylinder path. And the relationship between the path strategy and energy accumulation efficiency is confirmed in this case with three different models, which determines the density of temperature gradient curves and the maximum temperature during the processing.

Three numerical models are validated with corresponding experiments, all of their results show a high agreement with the experimental results, both calibrated by the melting pool profile photographed by a real-time camera and the temperature histories collected by thermal couples. The relative error in all of the models keeps roughly below 10% between the experimental and numerical results, which provide solid evidence of feasibility and the accuracy of thermal analysis for the developed FE models in this study, which means it can be used for further LMwD application experiment to assist with the investigation and better predict how the process would be affected by different deposition conditions.

Most displacement and residual stress occurred in and around the deposition processing area and the fixed edges since the boundary conditions, and their maximum values were directly influenced by the energy input efficiency and thermal history where the material went through. In addition, due to the total processing time being quite shorter compared with the large component fabricated by LMwD, in these

three models, the maximum stress and displacement keep at a certain low level after the cooling step, the maximum of stress measured in the models is 1606 MPa, but the mechanical observation and measurement still required for further studies with multiple rivets deposition or complex heat input.

Chapter remarks for research

Based on the literature and knowledge about the numerical simulation in section 2.3, in this chapter, follow the order of straight-line, NM, and HSS deposition experiments correspond to chapters 4 and 5, with the inactive element method for mass deposition and programmed heat flux, basic LMwD numerical models were developed.

The models were calibrated from microstructural maps, temperature fields, and thermal histories, the results show a high agreement (< 10% error) with the previous experimental records, which provide certain reliability for this thermal prediction in the LMwD research. And the deposition method will be applied in the next chapter for rivet building simulation.

Chapter 9 Numerical study of laser riveting for Ti6Al4V to AA6061 joining

The mass and heat input were simulated by the inactive element method and predefined DFLUX subroutine in the Abaqus, three primary LMwcD models had been developed in chapter 8. The numerical thermal gradient fields and temperature historical curves were validated by the corresponding experiments. As a result, a certain extent of accuracy of the numerical simulation was proved by the 10% maximum comparison error, which demonstrates the model can precisely calibrate and predict the LMwcD experimental process. Therefore, the developed simulations in the last chapter provide the primary guidelines and instructions for the LMwcD processing model creation, which can be applied to the deposition process of the further LR simulation.

Based on the theories and methodologies of previous LMwcD models, in this chapter, an LR model was developed for Ti6Al4V to AA6061 joining. In the 9.2 setup section, the interactive element method in the LMwcD model was applied to simulate the rivet deposition, an annular laser source was programmed by a user-defined DFLUX subroutine, which can better simulate the high-speed wash path in the post-process. Similar to the LMwcD modelling chapter, the developed LR simulation was validated with the corresponding experiment from the cross-section microstructure map and temperature field aspects, as well as the overall mechanical prediction, the results were analysed and discussed in 9.3 and concluded in 9.4.

9.1 Introduction

For the recent numerical research for joining techniques, [9.1] developed the traditional joining models of mechanical fasten (riveting) and adhesive bonding is studied, and [9.2] investigated that the dissimilar metals joined by the laser shock forming. Meanwhile, in the studies of laser profile and processing simulation, the dynamic behaviour in the molten pool and keyhole processing area is explained in

[9.3], the laser pulse width and energy ratio concluded as the most significant parameter to influence the dimensions of keyhole profile. Then, [9.4] demonstrated the molten pool measurement small scale and the overall thermal behaviour in macro-scale in the titanium welding process both from investigations of experiment and simulation.

And for the research of laser additive corresponded numerical simulation in recent years, [9.5] developed an LMwD modelling method by inactive elements in ABAQUS, and the results are evaluated by the experimental results from thermal history and mechanical behaviour. Moreover, a domain cubic mathematical model of the heat source region is designed and employed in the Al-Mg wire deposition simulation as instigated by [9.6], which accurately predict the temperature field near the processing area. However, there still has limited research about the LMwcD for the T6Al4V and no actual LMwcD and laser riveting experiment is conducted so far, thus the corresponded simulation of this application is still a blank area waiting for the investigation.

9.2 Methodology and model generations

In this section, a laser riveting numerical simulation was designed and developed step by step from the reference experiment to the laser model generation. At first, the experimental setup was introduced in 9.2.1, which provide the basic processing information for the corresponding model creation and result validation in 9.3. The LR simulation was divided into two parts, the basic rivet deposition model was generated according to the procedures of LMwcD modelling, 9.2.2 introduced the geometry, material properties, mesh distribution setups in detail, a deposited rivet was created inside the dissimilar materials joining model with the defined thermal interaction boundaries. In addition, in 9.2.3, annular heat flux was created by DFLUX subroutine to simulate the high-speed laser wash-path, which combined with the deposition model made up the LR processing simulation.

9.2.1 Experimental setup

In the dissimilar metals joining experiment, the 12s HS post-wash LR experiment of Ti6Al4V/AA6061 was selected as the original comparative experiment, to further assist develop the modelling generation and its results validation in this numerical simulation, both experiment and simulation were designed to collect the real-time data, then the results were compared to evaluate the reliability of the developed modelling.

As for the material selection, the substrate and feeding wire used Ti6Al4V, the upper joined sheet used AA6061, the dimensions of the substrate and upper sheet are $50mm \times 50mm \times 4mm$ and $50mm \times 50mm \times 2mm$ respectively, and the wire diameter is 0.8mm. The processing parameters were set to appreciate value level and same to the range in Chapter 6, all the processing parameters of the validation experiment shows table 9-1 below, the values also were applied into the numerical modelling developed in this chapter. For the thermal-history data collection preparation, TC-08 Thermocouple Data Logger (Pico Technology) is set with K-type thermal couples, which can measure the temperature value of the target area between 0 – 400℃.

Table 9-1. Processing parameters of HS-LR comparative experiment.

Process/Parameters	Deposition	Post-washing
Power (W)	600	450
WFS (mm/s)	4.1	N.A.
Travel speed (mm/s)	0.75	2000
Circular path diameter (mm)	1	1.7
Beam spot diameter (mm)	2	0.3
Cooling time (s)	233	206

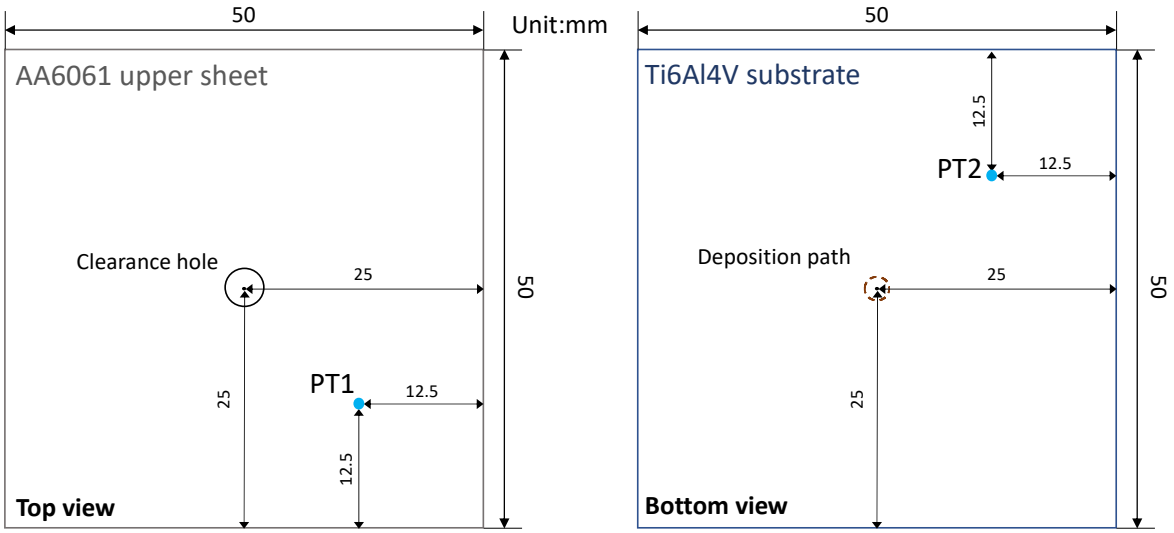

Figure 9.1 Sketch and dimensions of LR deposition experiment and the positions of thermal couples.

Same to the experiment setup in 6.4, in this simulation comparative test, Fig 9.1 shows positions of the thermal couples and the sketch dimensions, the LR deposition and wash-path was processed in the central point of the substrate. In order to validate both the temperature fields in the substrate and which in the upper sheet, and the heat transfer and interaction between them, two test points are located in the bottom of the substrate and the top surface of the upper sheet respectively, at the positions with the same distance from central rivet deposition point.

9.2.2 Model generations of Ti6Al4V/AA6061 laser riveting

In the modelling generation of the LR experimental process, similar to the previous LMwcD modelling, the LR FEA model development is divided into the following five modules: deposition geometry creation, materials properties thermophysical assignment, element type and mesh design, processing procedure step creation and interaction setup.

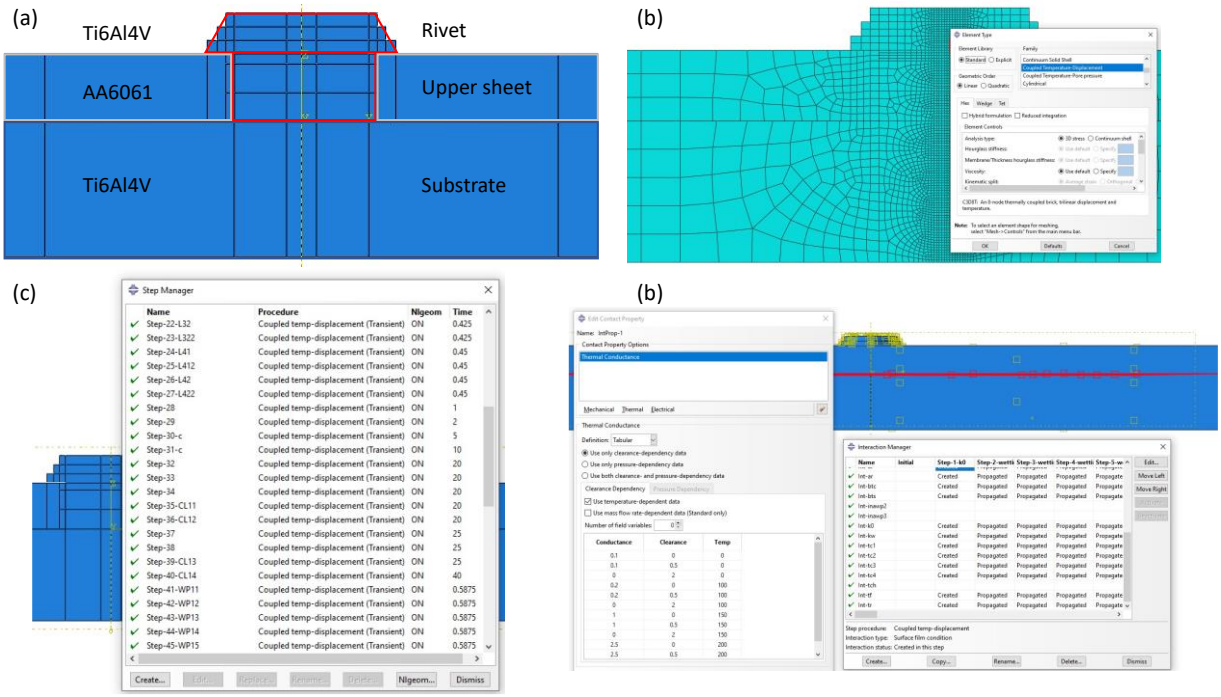

Figure 9.2 Generation setup of LR modelling: (a) geometrical parts creation, (b) element type and mesh design, (c) processing procedure steps creation and (d) interaction setup.

(1) Deposition geometry

The geometrical features of this model were designed and created according to the experimental outcome. In the deposition step, the whole model structure is divided into three main components: substrate and upper sheet and deposited rivet. Figure 9.2 (a) shows the geometry of the rivet zone, upper sheet, and substrate with created partitions, based on the different procedures in the experiment: deposition step, wash path step, cool down step, and four sets of cylinder geometries were defined as four layers in the deposition step, and the rivet cap divided into three different layers to descript the shape changes in the post-wash step.

(2) Materials properties

In this numerical simulation, the same Ti6Al4V material properties were applied to this LR model for the substrate and deposited rivet. In addition, the material property data of the AA6061 upper sheet was according to the existing experimental measurement and literature surveys [9.7-9.10]. In the mechanical property modulus, for both Ti6Al4V and AA6061 materials, the thermal and mechanical properties, including density, conductivity, elasticity, thermal expansion coefficient, plasticity and specific heat were

determined using values that were either fixed or temperature dependent, the same properties of Ti6Al4V employed in 8.2.3.2 was used in this modelling, part of key values of the AA6061 material thermophysical property data applied are shown in Fig 9.3 below.

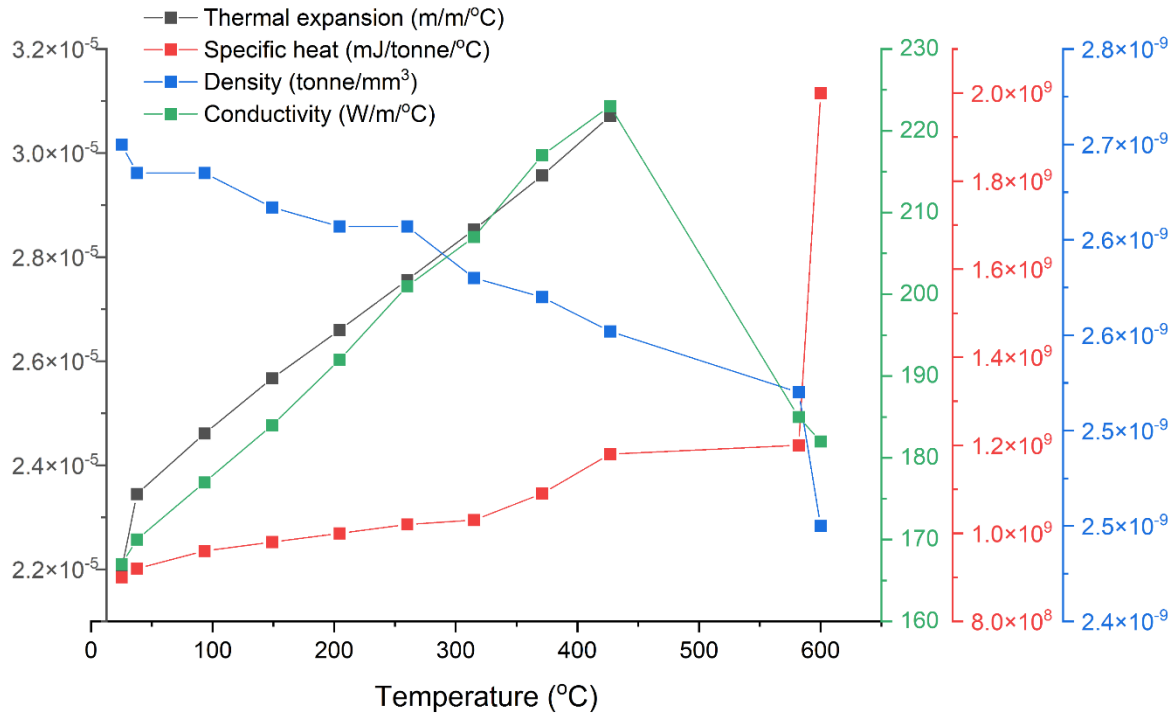

Figure 9.3 Thermophysical and mechanical properties for AA6061.

(3) Element type and mesh

A similar mesh optimization method of the previous HSS-LMwcD model in 8.2.2 was applied in this LR model, so the mesh distributions were decreased from coarse to fine sizes, which mainly refer to the distance from the deposited rivet and laser scanning position. In this model, a general mesh view and element type setup are shown above in Fig 9.2 (b), the overall seed size was divided into three parts, the seed size of far areas near the edge part is 1.2 mm, then the near parts between the hole edge and boundaries of the farm area, the mesh size was set to 0.44mm, in the central parts of substrate and the deposited rivet parts, the mesh size of them is 0.07mm. Following these mesh distribution rules, the whole mesh was constructed on the substrate and deposited rivet with a total of 55815 elements and 7993 elements of the upper sheet. In this study, the FEA model aims to predict the thermal stress analysis for the experiment, the Couple Temperature-Displacement (C3D8T) is chosen as the element

analysis type. Mesh shapes of all the assemblies are set to Hex, and the mesh distribution technique applied is the sweep method.

(4) Processing procedure steps

Based on the real experimental process, the whole LR model steps were divided into four separate procedures: one deposition, one post-wash and two cooling steps followed. In the deposition processing, similar to the HSS deposition modelling, four layers of spiral deposition steps were created, and then a cooling gap with 233s, the post-wash process divided into three small periods to describe the shape transformation of the rivet cap, finally followed with one more 206s cooling step of an agreement with the experimental processes. In this case, because the high heat input was needed to be noticed, each step time was kept in a proper short-range and the difference between the two steps was controlled as small as possible, in order to avoid the convergence issue when the job running, a part of steps setup interface in Fig 9.2(c).

(5) Interaction creation

The inactive element method was applied in this simulation to control the mass input and material changes in the process: in the deposition step, four layers of material were added orderly eight times to simulate the rivet depositing; and the cap was transformed in a flatter shape in three separate times in the post-wash step. In addition, in this LR joining model, differs from the previous LMwcD experiments, the heat transfer and interaction between the two different materials of the substrate and upper sheet were involved in the process, so the thermal conductance was defined at the interface between the Ti6Al4V substrate top surface and AA6061 sheet bottom surface, the value was dependent with both position and temperature, which increases with the temperature rise and decease of distance from central heat input point, the interface of thermal conductance setup is shown in Fig 9.2(d).

9.2.3 Laser heat flux modelling and boundary conditions

(1) Gaussian heat flux in the deposition process

In the deposition step of the LR experiment, the OSD strategy is different from the HSS method, but they still belong to the same LMwcD, and in the OSD experiment, 2-4 layers deposition process is the same as the HSS, thus in this case, the deposition process was simplified to a 4-layer HSS with a 2s wetting time in the beginning. The Gaussian distribution heat flux was applied in the deposition process, the detail sketch and parameters are presented in Fig 9.4 below. The mathematical form can be written as:

$$q(r) = \frac{3\eta_1 Q_1}{\pi r_0^2}\left(-\frac{3r^2}{r_0^2}\right) \qquad (15)$$

In this modelling, surface heat flux was considered as the most suitable energy model to simulate the laser interaction, where the laser beam power is $600W$ and the beam spot radius r_0 is $1mm$, the start point is same to the experimental at the middle point, and the absorptivity of laser power was set to $\eta = 0.3$ according to the previous LMwcD models.

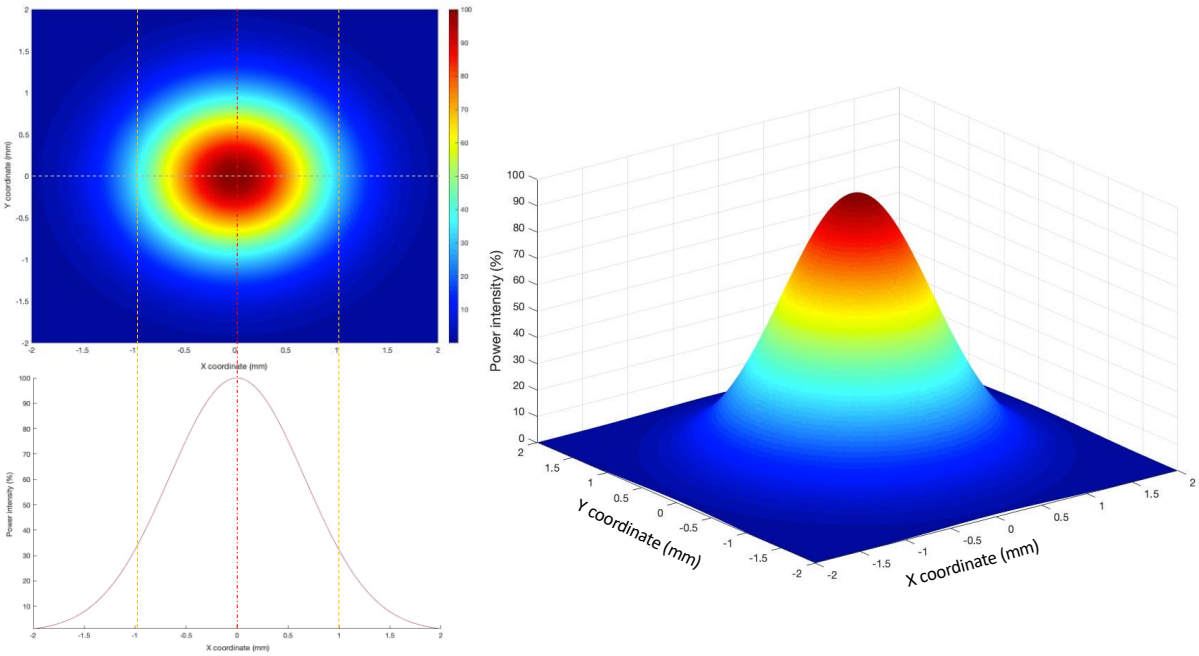

Figure 9.4 Sketch and dimensions of Gaussian laser distribution in LR deposition process.

(2) Annular heat flux in the post-wash process

Since the post-wash process with this extreme high travel speed, which involves several issues of laser interaction with materials and the dynamic problem, so it is hardly realised in the FEA model with a fast and small laser spot scanning by the traditional methodology. To properly simulate the high-speed post-wash process in this model, an annular laser heat source was designed and developed in this chapter, detail sketch and parameters are presented in Fig 9.5, the laser spot radius is 0.2mm and the circular path radius is 1.7mm, the absorptivity of laser power was set to $\eta = 0.06$ regarding the motion difference with the experimental situation.

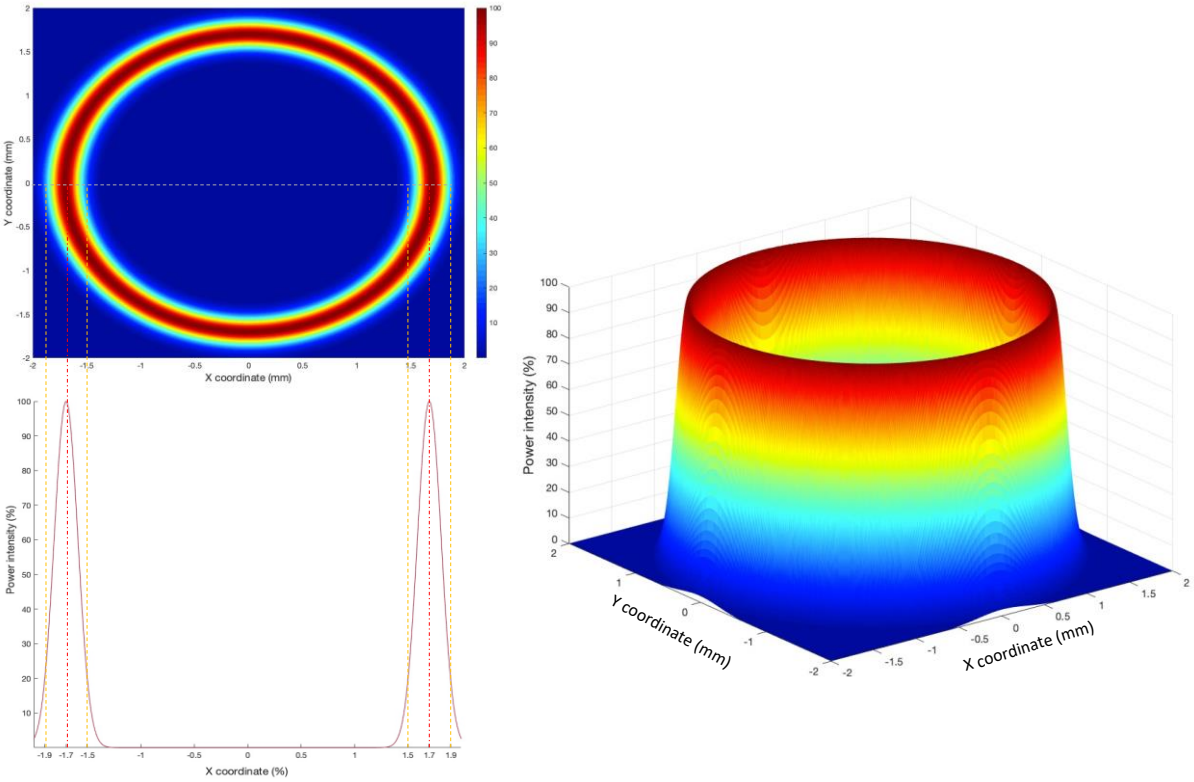

Figure 9.5 Sketch and dimensions of annular laser distribution in the post-wash process.

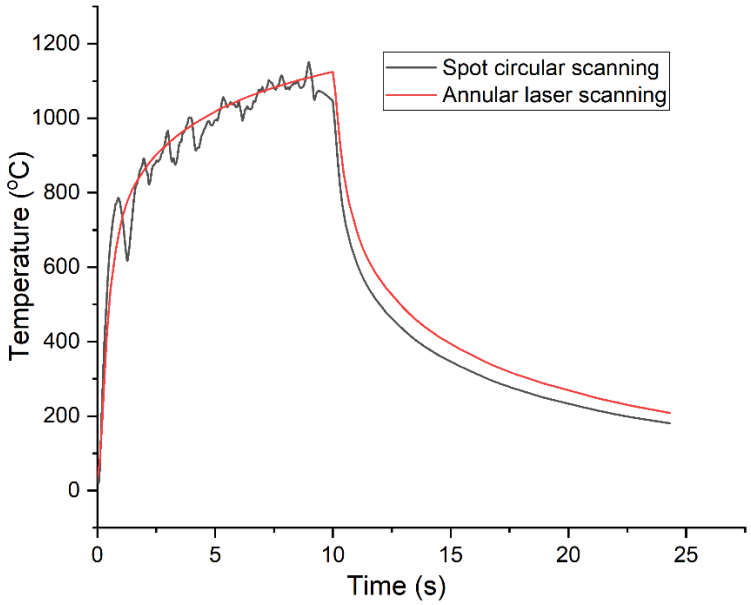

Figure 9.6 Temperature histories comparison results between traditional high-speed spots and annular heat source modelling.

In this model, compared to the normal moving laser source, the high-speed laser circular movement was simulated to a whole annular heat source to input the energy, the heat was distributed uniformly on the material. The example of comparison results is shown in Fig 9.6, because of the complexity of the laser extreme fast motion, and limited by the calculation capability of ABAQUS, the normal heat source presents a thermal history with severe fluctuations, on the contrary, the annular heat source presents a stable curve since the energy distribution. In addition, another benefit is that the normal circular moving model needs a long calculation time (24 cores with 46 hours in the example) but the annular model only takes a comparatively short time (1 hour) to complete the job running, which significantly reduces the processing time and improves the efficiency for the simulation works.

There are two parts of thermal load that are active during the deposition and post-wash period, and the setting surface on each layer of the rivet. Both user-defined DFLUX subroutine contents in deposition and post-wash processes were specified written by the Fortran codes, to simulate the laser source moving, on-and-off in the experimental process.

(3) Boundary conditions

According to the comparative experimental setup, in this numerical model, the mechanical boundary is pinned to the four corners and the ambient temperature is 34.9. Because the working experiment and materials used are similar to the previous LMwcD model, the film coefficient and emissivity at ambient temperature are set to 34.9 and 0.8, respectively. In addition, the same reason the varied thermal conductance, during the processing, because of the temperature change in the material, the surface film confidence will be adjusted to the higher value level corresponds to the actual condition. More setup detail was listed in the appendix.

9.3 Results and discussion

Microstructural, thermal, and mechanical behaviours of the FEA numerical model are related, reflected, and interacted with each other as illustrated in 8.3.1. Therefore, to effectively validate the reliability model, the local thermal gradient map was calibrated with the experimental cross-section structures. Afterwards, for the overall thermal analysis, the molten pool profiles during the process were observed and compared with the video records, and the comparison results of thermal historical curves were presented and discussed in detail in 9.3.2. Finally, the initial mechanical predictions of the LR model were presented and according to the results, further advice about the application was suggested in 9.3.3.

9.3.1 Microstructure and temperature field

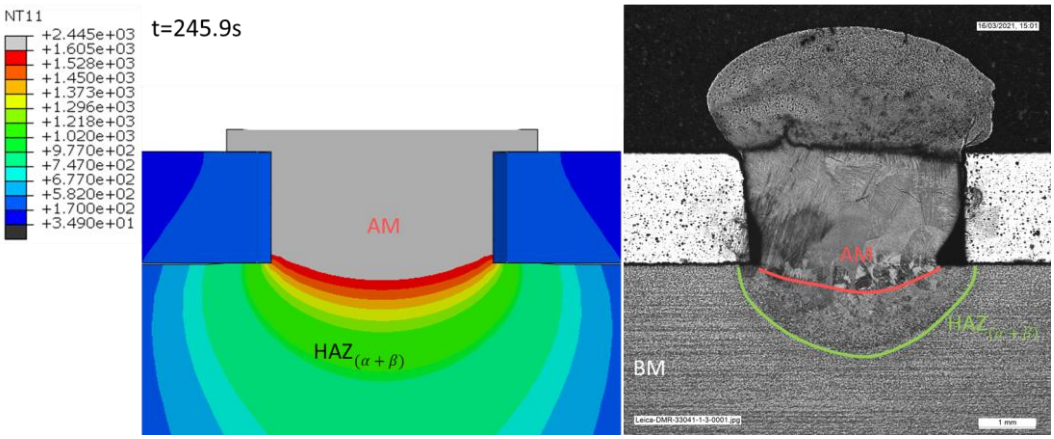

Figure 9.7 Numerical and experimental comparison results in cross-section microstructure overviews.

The microstructure evolution and grain structure introduction of Ti6Al4V deposition were explained in 6.5 and 8.4. In this simulation, the molten pool and heat-affected zone (HAZ) in the deposition cross-section were compared between numerical modelling and experimental map, the cross-sections were taken at the X=25mm which at the middle of the deposition. The left section view of Fig 9.7 shows the temperature map of numerical modelling at the end of the post-wash process, which demonstrates the thermal behaviour at the time point of highest heat accumulation before the cooling step. The molten pool profile in numerical modelling is the grey area with the temperature above the Ti6Al4V melting point (1605 ℃), it in LR experimental deposition is the fusion zone over the marked red line, where mainly is consisted of globular and columnar β grains near the welding area. Between the fusion zone and base material in the sectioned sample, the HAZ area marked above the green line went through the thermal field higher than the α-dissolution temperature and the α and β phase transformation can be observed, which is the green and red areas covered in the numerical temperature map.

As the results introduced above, the temperature fields in numerical modelling show a certain extent of agreement with the experimental microstructure overview. Infusion and added material zones, the calculated molten pool in the simulation is slightly smaller than the real condition because of the inherent deviation that existed in the wire deposition FEA model, which is explained in 7.3.1. In addition, the thermal conductance issue resulted in the difference presented at the HAZ, it can be clearly observed that the HAZ (red to green) area in the numerical model is wider than it in the experimental map, the reason in this case is the thermal conductance was only considering the heat transfer contact between the deposition and upper sheet under the general condition, but the melting material touched the hole caused a mass heat transfer, which led to a faster cooling rate and low energy accumulation in the actual experimental process. Due to this factor, the model is slightly inaccurate (~20% error) near the HAZ, but it still can provide the basic and general guidance for future experiments, and the error can be further reduced with the increase of the distance from the central position and the cooling time.

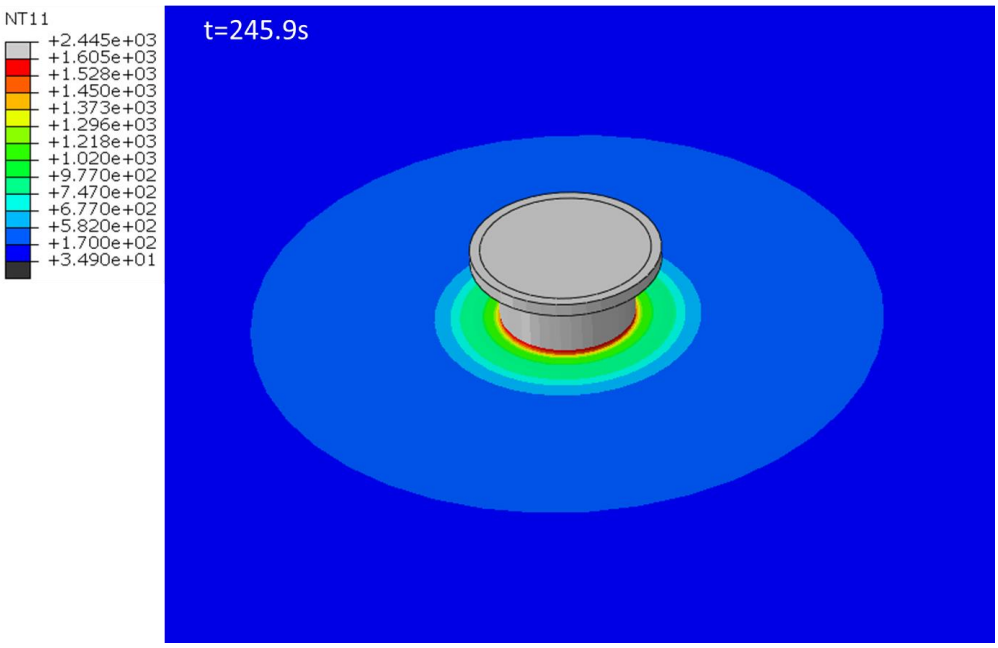

Figure 9.8 Temperature field of the substrate and rivet at the end of the post-wash process.

The corresponding temperature field of the deposited rivet and substrate is shown in Fig 9.8 above. From the left gradient contour, the maximum temperature of $2445℃$ can be obtained at the top surface of the rivet in the process. As the validation simulation result, the melting pool profile provides evidence that the originally deposited rivet would be remelted from the crown to the joining interface, consequently the welding area was expanded by melting liquid material. Besides, it needs to be noted that the temperature map of the substrate, also indicates that near the deposition (<5mm) the top surface can reach a comparatively high temperature (> $500℃$), which explains one of the reasons of the CFRP degradation and based on it gives the general ideas of design in composite joining experiments in Chapter7.

9.3.2 Processing records and thermal histories comparison

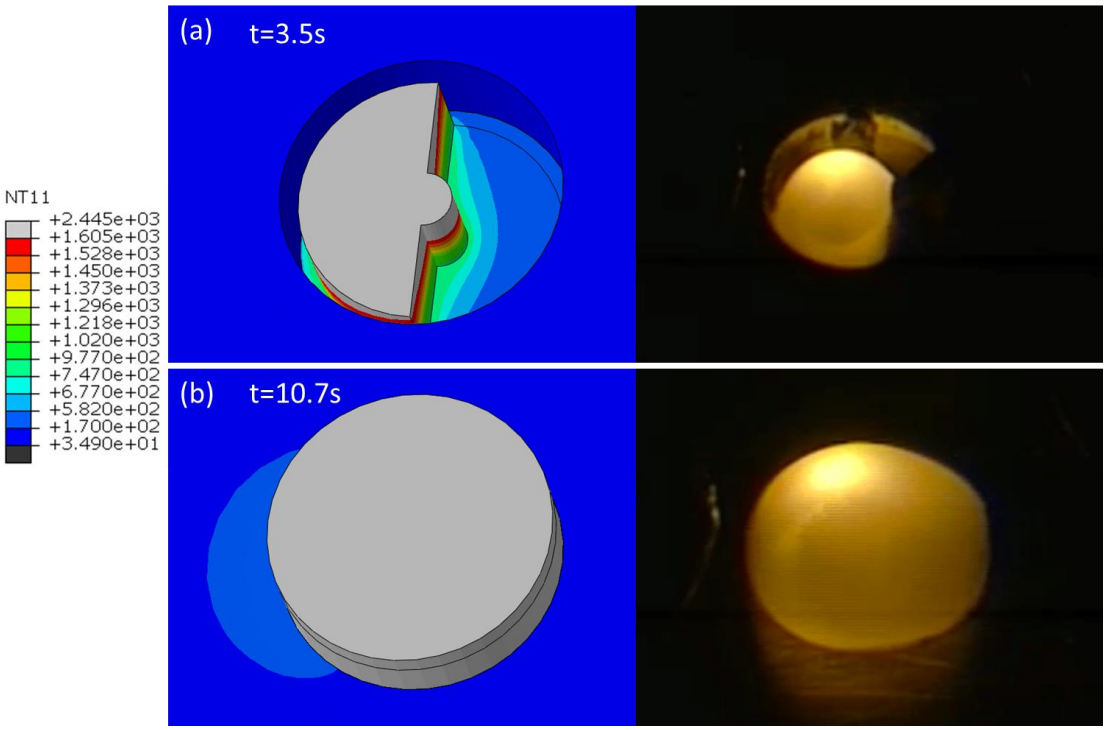

Figure 9.9 Melting pool profiles of the numerical modelling at (a) first and (b) final layer of the deposition process compared to the experimental records.

The process comparison of deposition and post-wash steps were shown in Fig 9.9 and Fig 9.10 to further validate the thermal behaviour numerical modelling in the fusion processing compared to the actual experimental record. When the deposition step start (9.9a), as presented in the interaction modulus, each layer was divided into left and right two half-cylinders, so the first added half-cylinder simulated the contacted droplet of the deposition in the initial layer but limited of mass and heat input expressions of the wire deposition model, the deposition was melted start from the top surface. The heat input increased to melt the added material, the whole new deposited layers were fully melted in the HSS deposition step, and which shows high agreement with the experimental record (Fig 9.9b).

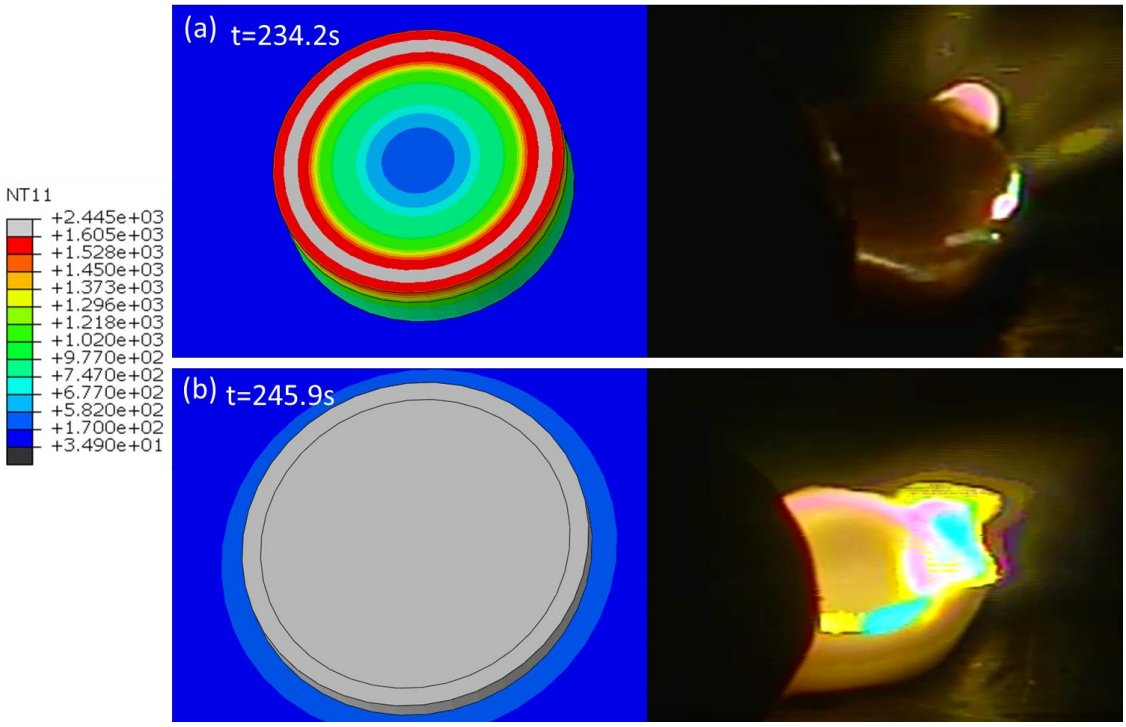

Figure 9.10 Record melting pool profile comparison between the experimental and numerical results at the (a) start and (b) end of the post-wash process.

After the cooling gap, at the beginning of the post-wash step, a smooth and uniform circular heat distribution was observed thanks to the design annular heat flux, and it is similar to the experimental deposition, then the rivet was remelted in the post-wash process (Fig 9.10) regarding the heat accumulation with the increase of scanning time (6-12s). Although the melting pool profile in the post-wash step shows a high agreement with it in the experimental record, the flame and flash around the cap edge in-process video indicate that the materials went through a violent interaction (cutting and drilling) with the laser beam due to the high speed at the focus position. However, it needs to be noticed that this simulation only considers the condition as the ideal thermal and mechanical environment, the laser interaction with the corresponding mass and heat loss was miscalculated in the process, but the results were not seriously affected thanks to the lower laser power input (450W) in the post-wash process.

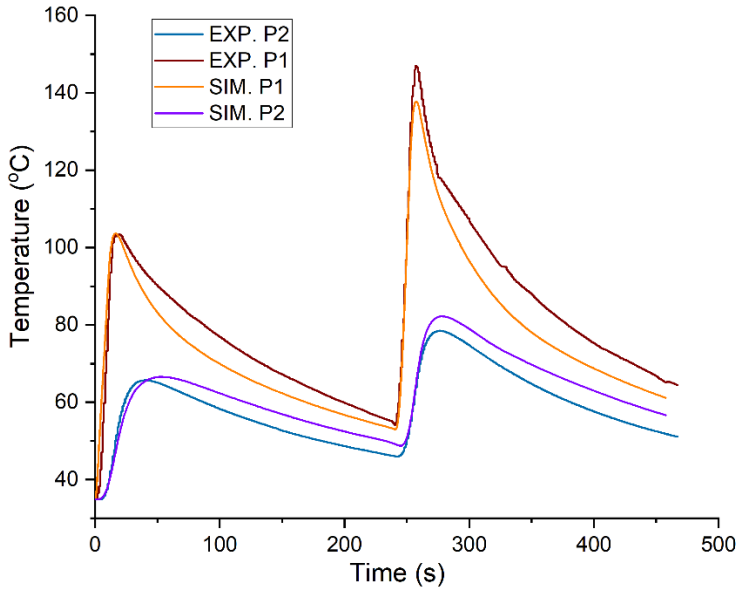

Figure 9.11 Numerically calculated thermal histories LR modelling calibrated by using thermocouples data.

The temperature histories comparison between numerical and experimental results was demonstrated in Fig 9.11 above, the thermal histories in both AA6061 upper sheet and Ti6Al4V were presented. The curves with consistent heating rates show a high agreement at the start of the deposition and post-wash steps, and the models collected the almost same peak temperatures at the substrate and upper sheet. Nevertheless, the post-wash peak temperatures of FEA P1 (137.4℃)) was lower than that of EXP P1 (146℃) with 5.9% error, and on contrary, the peak values of FEA P2 (82.2℃) was slightly higher than it in EXP P2 (78.5℃) with 4.7% error. It is mainly because of thermal conductance issue between the hole edge and melting deposition, combined with the potential deviation of the heat transfer in the LMwD model, which also explains the followed differences in the cooling step, the maximum error between numerical and experimental data were measured at t= 353s, the FEA P1 (77.3℃) is 10.8% lower than the EXP P1 (86.7℃), after this time point, the value differences of results were gradually decreased.

9.3.3 Mechanical predictions

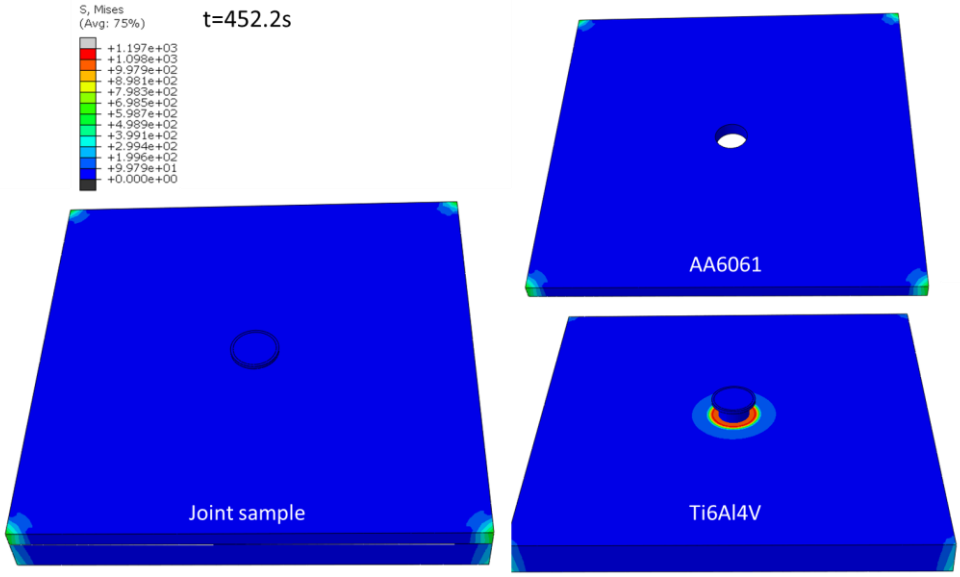

Figure 9.12 Initial stress field prediction in each component of the sample after the cooling time in the LR numerical modelling.

Besides thermal analysis for the numerical modelling, the mechanical behaviours of the LR model were measured and observed in this chapter. As shown in Fig 9.12 below, the stress maps have been obtained after the cooling step to predict the effect relate to residual stress. Due to the experimental simulated boundary conditions for the deposited rivet part and pinned edges of the substrate and upper sheet, the corners of components and rivet were encastred to avoid the exceed distortion during the processing. Therefore, the distortion and residual stresses were mostly observed near the corners of the substrate and upper sheet, and the amplitude in the aluminium sheet is slightly higher than substrate regarding a higher thermal history went through. The maximum stress was measured at the welding area in HAZ with 1197 MPA, and the comparative higher stress concentrated on the near area since the massive heat input in the process, the stress is reduced from the centre to the edge following the trend of temperature gradient map in the cooling step. In addition, it needs to be noted that, this numerical model only can provide the prediction to similar experimental single-rivet manufacturing, but in the mature industrial application, the further processing and boundaries parameters need to be adjusted depending on the actual situation.

9.4 Summary

The LR numerical modelling was developed to simulate the HSS-LR Ti6Al4V/AA6061 joining experiment, a similar model generation with an inactive element method were applied to realize the mass input and shape transformation process, and an annular laser source was developed to simulate the high-speed post-wash process.

Validated by experimental results, the numerical microstructure map shows a slightly smaller melting pool regarding the inherent problem of LMD modelling, but the HAZ comparison shows the heat-transfer difference between the actual process and simulation, due to the surface breaking and material interaction between the upper sheet and deposition, the actual heat loss in substrate and heat transfer to AA6061 sheet should be more than that presented in simulation.

The comparison results of temperature field maps and thermal historical curves illustrate the model shows a high agreement with the experimental results in the overall thermal trend and behaviour, the closer difference measured at peak temperatures provide certain reliability for the model, but as explained heat transfer issue, the simulation shows a 10.8% maximum error in the cooling step.

The mechanical results present a similar result with the previous LMwcD models, the residual stresses concentrate at the corners of the substrate and upper sheet and the area near the weld of deposition.

Chapter remarks for research

A Ti6Al4V/AA6061 LR joining simulation was developed in this chapter, the basic modelling creation method from LMwcD simulation was applied for the rivet building process, and an annular heat DFLUX was programmed to simulate the post-wash process.

The results show a certain agreement in the microstructure map, temperature fields, and the thermal histories with comparative experimental records. In this numerical

simulation work, the LMwcD and LR models also can provide the mechanical prediction to some extent according to the reliability of thermal results.

For further action, to improve the accuracy of the model, further specific relationships and parameter sets of materials thermal conductance, energy absorptivity dependent with temperature were required, and further mechanical validation and analysis can be testified and improved for the model in future work.

Chapter 10 Conclusions and recommendations

10.1 Conclusions for the research

10.1.1 LMwcD experiments

As an innovative dissimilar joining technique, the feasibility and parametric studies on the key factors of laser riveting were conducted and analysed. Numerical models on the process were also validated by corresponding experimental results and simulations carried out in this research.

In the studies on Ti6Al4V LMwcD, single circular depositions and cylindrical multiple layers building features were produced by ALM methods applied with both 3-arc and circular paths. The circular path deposition is free of the inside cavities, which were present in 3-arcs depositions caused by the wide-angle and stuck feeding issues. Compared with the straight-line thin wall deposition, similar grain structures were observed in HAZ and AM areas, but the mass deposition and the thermal history of LMwcD lead to a considerably more transverse orientation of grain growths.

Based on the results of the wire feeding/travel speed preliminary test, the designed HSS-CS deposition strategy not only significantly reduced the total processing time thus increased the productivity as approximately 8 times compared to the initial NM-ALM method, but it also can build up a similar deposition height regarding a better mass-heat input for melting and solidification balance. In addition, the parametric study finds that higher energy accumulation (higher power input, slower travel speed and faster wire feeding) increases the material deposition efficiency and intend to form the larger colony α inside equiaxed β grains instead of basket-weave structure, which enhances the local micro-hardness of the deposition from the crown to weld HAZ area.

This research developed the principal guidance for LMwcD potential applications, as a result, the HSS-CS deposition offers the highest productivity while the NM-ALM method can provide the strongest mechanical properties among different building strategies, as well as the basic relationship between the energy input and grain

evolution, was revealed in the Ti6Al4V deposition. According to this research, the specific deposition strategy can be designed and selected for exact actual demand.

Research values:

- Proved the cylindrical feature can be successfully built up by ALM-LMwD with circular deposition track.
- The quality and defect of LMwcD deposition can be improved by deposition track and wash path.
- Primary try-and-narrow experiments defined the influences of the key factors in the process.
- The productivity optimization of LMwcD was achieved by controlling the deposition speed, cooling step and deposition strategy, the final deposition method significantly improved the efficiency of the application.
- The microstructural analyses revealed the grain structure evolution with different LMwcD strategies regarding the varied thermal behaviour in titanium LMwD.
- The parametric study revealed the relationship and processing window between the deposition features and specific processing factors (power, travel speed and height adjustment).

10.1.2 LR dissimilar joining experiments

In the Ti6Al4V/AA6061 joining study, the OSD-LMwcD method was applied to the LR concept can avoid the wire feeding and hole edge obstruct issues. The initially deposited rivet presents microstructure as well as microhardness similar to HSS-LMwcD deposition, and its shear strength is already close to the comparative blind rivet. In addition, the rivet strength can be increased by the post-wash process, the rivet was remelted thus the welding area and wetting angle were improved. The post-wash parametric study found that:

- For circular motion, in this case, the focused beam spot and faster beam scanning speed can obtain a competitive high energy input, furthermore,

increasing heat input not only can improve the morphology of the rivet and expand the FZ area and depth to increase the rivet shear strength, but also can promote the grain evolution for a stronger local microhardness which also shows an agreement with the previous LMwcD research.

- The equiaxed primary α would be formed in a fast-scanning speed (~1000m/s) with a certain period (>8s) processing, after the formation threshold, and the grain size and density are increased along with increased speed and prolonged processing time, but the structure should be avoided regarding the defect normally formed along the grain boundaries.
- The high-energy LR process breaks the surface tension quickly to fully remelt and reform the rivet, the welding area and depth significantly increased thus it can achieve the highest maximum shear load with 3.59KN, which is 180.4% higher than the initial rivet.

From the morphological and microstructural analysis, the feasibility of this innovative LR concept was proved, and mechanical evaluation demonstrates the post-washed rivet can provide a 146% higher shear strength with the current blind rivet, and it also has the flexibility and efficiency benefits compared with the adhesive method. In addition, the processing parameters and strategy can be adjusted to fulfil the desired application demands, therefore, LR is a suitable joining technique in certain conditions instead of the traditional methods.

For LR dissimilar materials application exploration, although the HSS-LR was directly applied into the Ti6Al4V/CFRP joining can successfully build up the rivet, the contamination and oxidation issues were occurred due to the degradation of the CFRP sheet. The microstructural and chemical analysis present that the PD and PS-LR method prevent contamination in the process since heat accumulation and the transfer was reduced in the CFRP. The shear failure mode also can be improved from the deposition failure in HSS-LR to CFRP failure in post-processed LR, which doubled the strength. Last but not least, the PS and PD method can provide the basic strength for the joint, but the post-process method still needs more comprehensive investigation and optimization on the rivet morphology to get the superior interlock and strength for metal/composite materials.

Research values:

- The Ti6Al4V/AA6061 joints were successfully developed and built up applied by the OSD-LR method.
- The parametric study further revealed the relationships between processing parameters and welding conditions and microstructural changes.
- In general, increasing the heat input promotes the formation of the equiaxed α grains with enhanced microstructure, and enlarged the welding area with improved shear joining strength.
- The Ti6Al4V/CFRP joint can be successfully built up applied by the LMwcD-LR method, however, the contamination and oxidation caused by CFRP degradation weakened the deposition strength.
- Post-processed LR rivet resolved the processing issues and improved strength in titanium/composite joint, microstructural analysis and shear tests provided detailed information and evidence.
- In PS riveting method, the joint strength increases with the thickness of the CFRP sheet, and a certain (>3s) scanning time can reform a flatter cap can better interlock the sheet better.

10.1.3 Numerical simulation

To validate the experimental results and predict the thermal and mechanical behaviour of deposition and joints in the future potential experiments. The corresponding straight-line, NM and HSS of LMwcD experiments were selected as the references, the element inactive method and surface Gaussian heat flux subroutine were applied into FEA models to simulate the mass and heat input respectively, the calculated results show a high agreement both in HAZ local microstructural map and global thermal field with experimental observation, and the numerical temperature-historical curves show the same trend and measured maximum approximate 10% error compared with the experimental data. In sum, the high agreement of calculated results has provided certain reliability for the related LMwcD experimental prediction and offered the recommendations for further parameters adjustment.

The annular heat flux can properly simulate the post-wash process in LR numerical model, but because of the inherent heat transfer problem between the melting deposited rivet and upper aluminium sheet, the numerical HAZ area are slightly mismatched with the actual numerical cross-section map. The calculated melting pool profile and thermal historical curves are still consistent with the experimental results regarding the accurate overall performance. Therefore, further improvement of materials interaction would be required in future work to validate and predict the LR process more precisely.

Both in LMwcD and LR models, the mechanical analysis results show that most of the residual stress and distortion concentrate on the fixed corners and at the HAZ area of deposition, the highest value measured at the welding interface on the substrate. However, it needs to be noted that the mechanical behaviour was indirectly reckoned by thermal analysis but not directly validated by experimentally measured values, so is it only suitable for rough prediction in current models.

Research values:

- Three LMwcD numerical simulations of feasibility and parametric studies were developed to better understand the experimental result, assist with the investigation and better predict the process affected by different welding conditions.
- The numerical modelling of the Ti6Al4V LR experiment was developed as well to further simulate the processing behaviour in the LR experiment.
- The deposition and post-wash procedures were simplified to the experimental conditions and a new annular heat source was created to simulate the laser circular wash processing.
- All the models show high agreements with the validated experimental results, with a maximum 10% calculated error, which proved certain reliability for the numerical work in the thesis.
- LMwcD and following LR models were compared to the experimental results in the thermal behaviours, subsequently predicting the mechanical performance for the samples.

10.2 Recommendations for future work

10.2.1 LMwcD research

Based on the LMwcD study in this thesis, besides the micro-hardness, other mechanical properties like tensile and shear strength in the deposition also can be evaluated, and their relationship with energy input and processing parameters. It is helpful to further understand the overall and local mechanical performance for potential applications, for example, the strength component repair and laser riveting relate to weld area strength, but the deposition trunk strength is more concerned for the component fabrication.

Limited by the time and final objective for LR application in this thesis, current LMwcD research only applied on the minor scale applications (diameter<5mm), and the small range parameters were investigated in the LMwcD experiments. But AM is widely applicable to the automatic and aerospace sectors, and the fabrication of the large components is highly demanded, consequently, the macro LMwcD processing is one of industrial demand for manufacturers.

Another valuable research interest of LMwcD study is its special deposition-path strategies, further complex deposition routes and shape can be tested, depending on the specific condition, due to a sounder deposition quality and higher manufacturing efficiency, part of original LPDed components might be replaced by LMwD through the process development. Moreover, the preprogrammed deposition path can repair the defect, for instance, LMwcD can fill the holes and cracks can be fixed by matched curve-path deposition, but this specific application needs a further systematically investigation to achieve a comprehensive understanding and applicable quality.

10.2.2 LR joining research

A Ti6Al4V/AA6061 joint was built in this study which proved the feasibility of the LR concept, and competitive high shear strength was measured. However, due to the limitation of the wire processing system and melting material surface tension, there

still has a little void gap between the deposition and hole edge from the cross-section observation which is a risk to harm the production cycle life and fatigue strength.

There are two main considerable research directions to optimize this weakness factor: first is implement the experiment with a more suitable LMD processing system with coaxial wire feeder, the setup can deposit wire vertically to avoid the angle issue, and another ideal situation is that design the different multiple-layer ALM deposition strategy for initial rivet building, but the post-wash needs to be implemented on each layer to break the surface tension and increase the wetting angle to melt the material fit in the hole. But both two scenarios required further experimental development to testify and evaluate their feasibility and joint quality.

The production materials decide its usage, the Ti6Al4V/AA6061 LR joining studied in this thesis is mainly used in aerospace applications. For other material selections, the feasibility of 304L steel/AA6061 LR joining had been proved by the preliminary trial in this research, and it can be applied as an innovative joining technique into the automotive industry after the systematic process development and quality evaluations. And other dissimilar metals joining also can be developed for the specific desired purpose.

The post-processed rivet can provide the basic strength for titanium/composite joint, but it is hard to reform a proper and flatter cap shape to obtain a better interlock regarding the huge melting temperature difference between the titanium and composite, and the shear test results show that brittle ceramic insert bush weakened the strength of joint. Hence, a considerable solution is to select titanium as the bush material meanwhile increasing bush thickness and reshaping it to the flanged bush, although which is increased the manufacturing cost, rivet pulling strength, weldability with joining strength can be significantly improved and applied for the special field, from this view, the specific experimental development is required for further investigation.

10.2.3 Numerical simulations

Both LMwcD and LR models can describe rough trend and temperature histories in the global thermal field, but due to the most of thermal interactive parameters (like power absorptivity, heat transfer and film coefficient, etc.) in the model were predefined and dependent on the time according to the reference experimental record. In future work, the specific relationship between the values in interactive and boundary modules and material temperature need to be found out, and their mathematical expressions programmed into the user subroutine can more precisely predict the thermal behaviours.

Moreover, the residual stress and distortion level in the fusion process is one of the vital factors concerned in the industrial application, another research recommendation for this numerical simulation study is the mechanical prediction, because, in the ideal experimental condition, only a little heat input in the single deposition/rivet was built up in the model, the stress and displacement were hardly measured in the specimens. Therefore, in future simulation work from the industrial view, multiple rivets processing model can be developed to simulate the actual product line manufacturing and calibrated with the corresponding experimental sample to preliminary predict the mechanical influences of distortion and residual stress for the industrial product.

Therefore, about future work on this project, for the further mechanical study on the LMwcD, a particular experiment can be designed and conducted, then based on the current model, the specific investigation on the residual stress could be carried out. In addition, a parameters adjustment study can be designed to find the parameter influence in the LMwcD, to find out key factors that affect the deposition quality and processing efficiency for the experiment and then assist with the investigation and better predict how the process would be affected by different deposition conditions. Next, as follow the experiment parts, the numerical modelling of dissimilar joining between the dissimilar materials need to be investigated and developed, meanwhile conduct the calibration experiment to validate the FE model. Afterwards, for this thesis target, the dissimilar joining between the metal and composite also will be investigated by numerical model step by step.

Reference

Chapter 1

[1.1] Vasiliev, V. & Morozov, E.V. 2018, Advanced mechanics of composite materials and structures, Elsevier, Amsterdam, Netherlands.

[1.2] Wang, W., Fan, D., Huang, J., Li, C., Yang, J. & Chen, S. 2018, "Microstructural mechanism and mechanical properties of Cf/SiC composite/TC4 alloy joints composite-diffusion brazed with TiZrCuNi + TiCp composite filler", Materials Science & Engineering A, vol. 728, pp. 1-9.

[1.3] Sun, J., Li, H., Han, L. and Song, Q., 2019. Enhancing both strength and toughness of carbon/carbon composites by heat-treated interface modification. Journal of materials science & technology, 35(3), pp.383-393.

[1.4] Regulation, E.C., 2009. Regulation (EC) No 443/2009 of the European Parliament and of the Council of 23 April 2009 setting emission performance standards for new passenger cars as part of the Community's integrated approach to reduce CO2 emissions from light-duty vehicles. Official Journal of the European Union L, 140, pp.5-6.

[1.5] Goldberg, P.K., 1998. The effects of the corporate average fuel efficiency standards in the US. The Journal of Industrial Economics, 46(1), pp.1-33.

[1.6] Williams, G., Trask, R. and Bond, I., 2007. A self-healing carbon fibre reinforced polymer for aerospace applications. Composites Part A: Applied Science and Manufacturing, 38(6), pp.1525-1532.

[1.7] Jasmin Stein, 2018. Research committee summary 2018. TWI reports.

[1.8] Meng, H., Liao, J., Zhou, Y. & Zhang, Q. 2009, "Laser micro-processing of cardiovascular stent with fiber laser cutting system", Optics and Laser Technology, vol. 41, no. 3, pp. 300-302.

[1.9] Kannatey-Asibu Jr, E., 2009. Principles of laser materials processing (Vol. 4). John Wiley & Sons.

[1.10] Davies, P., Cantwell, W.J., Jar, P.Y., Bourban, P.E., Zysman, V. and Kausch, H.H., 1991. Joining and repair of a carbon fibre-reinforced thermoplastic. Composites, 22(6), pp.425-431.

[1.11] Seaman, F.D., 1977. The Role of Shielding Gas in High Power CO 2 (CW) Laser Welding. Technical Paper MR77-982, Society of Manufacturing Engineers, Dearborn, Michigan.
[1.12] Piancastelli, L., Frizziero, L., Rocchi, I., Zanuccoli, G. and Daidzic, N.E., 2013. The “C-triplex” approach to design of CFRP transport-category airplane structures. International Journal of Heat and Technology, 31(2), pp.51-59.
[1.13] Chen, S., Li, L., Chen, Y., & Huang, J. (2011). Joining mechanism of Ti/Al dissimilar alloys during laser welding-brazing process. Journal of Alloys and Compounds, 509(3), 891-898.
[1.14] Huang, Y., Wang, J., Wan, L., Meng, X., Liu, H., & Li, H. (2016). Self-riveting friction stir lap welding of aluminium alloy to steel. Materials Letters, 185, 181-184.
[1.15] Wang, H., Yuan, X., Li, T., Wu, K., Sun, Y., & Xu, C. (2018). TIG welding-brazing of Ti6Al4V and Al5052 in overlap configuration with assistance of zinc foil. Journal of Materials Processing Technology, 251, 26-36.
[1.16] Brown N and Worrall C, 2015. Development of a Thermally-Assisted Piercing (TAP) process for forming holes in thermoplastic composites. TWI Members report 1062/2015.

Chapter 2

[2.1] Siegman, A.E., 1998, January. How to (maybe) measure laser beam quality. In Diode Pumped Solid State Lasers: Applications and Issues (p. MQ1). Optical Society of America.
[2.2] Steen, W.M. and Mazumder, J., 2010. Laser material processing. springer science & business media.
[2.3] Majumdar, J & Manna, I. (2003). Laser processing of materials.
[2.4] Dawes, C.T., 1992. Laser welding: a practical guide. Woodhead Publishing.
[2.5] Kannatey-Asibu Jr, E., 2009. Principles of laser materials processing (Vol. 4). John Wiley & Sons.
[2.6] Charschan, S.S., 1972. Lasers in industry. Van Nostrand Reinhold Co.
[2.7] Ready, J.F., 1975. Lasers: Their Unusual Properties and Their Influence on Applications. Society of Manufacturing Engineers.
[2.8] Migliore, L.R., 1996. Laser materials processing. CRC Press.

[2.9] Hughes, T.P., 1975. Plasmas and laser light. New York, Halsted Press, 1975. 539 p.
[2.10] Allison, A. and Scudamore, R., 2014. Strategic Research Agenda: Joining: Joining Sub-platform.
[2.11] Stürmer, E. and von Allmen, M., 1978. Influence of laser-supported detonation waves on metal drilling with pulsed CO2 lasers. Journal of Applied Physics, 49(11), pp.5648-5654.
[2.12] Duley, W.W., 1986. Laser processing and analysis of materials, 1983. New York, Plenum Press.
[2.13] Khaskin, V.Y., Korzhik, V.N., Chizhskaya, T.G., Sidorets, V.N. and ZIE, L., 2016. Effect of laser radiation absorption on efficiency of laser welding of copper and its alloys. The Paton Welding Journal, 11.
[2.14] Sokolov, M. and Salminen, A., 2014. Improving laser beam welding efficiency. Engineering, 6(09), p.559.
[2.15] Williams, S.W., Martina, F., Addison, A.C., Ding, J., Pardal, G. and Colegrove, P., 2016. Wire+ arc additive manufacturing. Materials Science and Technology, 32(7), pp.641-647.
[2.16] Gu, J., Cong, B., Ding, J., Williams, S.W. and Zhai, Y., 2014, August. Wire+ arc additive manufacturing of aluminium. In Proceedings of the 25th Annual International Solid Freeform Fabrication Symposium, Austin, TX, USA (pp. 4-6).
[2.17] Syed, W.U.H., Pinkerton, A.J. and Li, L., 2005. A comparative study of wire feeding and powder feeding in direct diode laser deposition for rapid prototyping. Applied surface science, 247(1-4), pp.268-276.
[2.18] Dubourg, L. and Archambeault, J., 2008. Technological and scientific landscape of laser cladding process in 2007. Surface and Coatings Technology, 202(24), pp.5863-5869.
[2.19] Ding, D., Pan, Z., Cuiuri, D. and Li, H., 2015. Wire-feed additive manufacturing of metal components: technologies, developments and future interests. The International Journal of Advanced Manufacturing Technology, 81(1-4), pp.465-481.
[2.20] Gu, D.D., Meiners, W., Wissenbach, K. and Poprawe, R., 2012. Laser additive manufacturing of metallic components: materials, processes and mechanisms. International materials reviews, 57(3), pp.133-164.

[2.21] Motta, M., Demir, A.G. and Previtali, B., 2018. High-speed imaging and process characterization of coaxial laser metal wire deposition. Additive Manufacturing, 22, pp.497-507.
[2.22] Froend, M., Riekehr, S., Kashaev, N., Klusemann, B. and Enz, J., 2018. Process development for wire-based laser metal deposition of 5087 aluminium alloy by using fibre laser. Journal of Manufacturing Processes, 34, pp.721-732.
[2.23] Abioye, T.E., Folkes, J. and Clare, A.T., 2013. A parametric study of Inconel 625 wire laser deposition. Journal of Materials Processing Technology, 213(12), pp.2145-2151.
[2.24] Liu, W. and DuPont, J.N., 2003. Fabrication of functionally graded TiC/Ti composites by laser engineered net shaping. Scripta Materialia, 48(9), pp.1337-1342.
[2.25] Manvatkar, V.D., Gokhale, A.A., Reddy, G.J., Venkataramana, A. and De, A., 2011. Estimation of melt pool dimensions, thermal cycle, and hardness distribution in the laser-engineered net shaping process of austenitic stainless steel. Metallurgical and materials transactions A, 42(13), pp.4080-4087.
[2.26] Liu, S. and Shin, Y.C., 2019. Additive manufacturing of Ti6Al4V alloy: A review. Materials & Design, 164, p.107552.
[r2.27] Carroll, B.E., Palmer, T.A. and Beese, A.M., 2015. Anisotropic tensile behavior of Ti–6Al–4V components fabricated with directed energy deposition additive manufacturing. Acta Materialia, 87, pp.309-320.
[2.28] Griffith, M.L., Schlienger, M.E., Harwell, L.D., Oliver, M.S., Baldwin, M.D., Ensz, M.T., Essien, M., Brooks, J., Robino, C.V., Smugeresky, E.J. and Hofmeister, W.H., 1999. Understanding thermal behavior in the LENS process. Materials & design, 20(2-3), pp.107-113.
[2.29] Wu, X., 2007. A review of laser fabrication of metallic engineering components and of materials. Materials Science and Technology, 23(6), pp.631-640.
[2.30] Qian, L., Mei, J., Liang, J. and Wu, X., 2005. Influence of position and laser power on thermal history and microstructure of direct laser fabricated Ti–6Al–4V samples. Materials science and technology, 21(5), pp.597-605.
[2.31] Pratt, P., Felicelli, S.D., Wang, L. and Hubbard, C.R., 2008. Residual stress measurement of laser-engineered net shaping AISI 410 thin plates using neutron diffraction. Metallurgical and Materials Transactions A, 39(13), pp.3155-3163.

[2.32] Kelly, S.M. and Kampe, S.L., 2004. Microstructural evolution in laser-deposited multilayer Ti-6Al-4V builds: Part II. Thermal modeling. Metallurgical and Materials Transactions A, 35(6), pp.1869-1879.
[2.33] Wang, F., Williams, S., Colegrove, P. and Antonysamy, A.A., 2013. Microstructure and mechanical properties of wire and arc additive manufactured Ti-6Al-4V. Metallurgical and materials transactions A, 44(2), pp.968-977.
[2.34] Zhang, X., Martina, F., Ding, J., Wang, X. and Williams, S.W., 2017. Fracture toughness and fatigue crack growth rate properties in wire+ arc additive manufactured Ti-6Al-4V. Fatigue & Fracture of Engineering Materials & Structures, 40(5), pp.790-803.
[2.35] Bai, X., Colegrove, P., Ding, J., Zhou, X., Diao, C., Bridgeman, P., roman Hönnige, J., Zhang, H. and Williams, S., 2018. Numerical analysis of heat transfer and fluid flow in multilayer deposition of PAW-based wire and arc additive manufacturing. International Journal of Heat and Mass Transfer, 124, pp.504-516.
[2.36] Ho, A., Zhao, H., Fellowes, J.W., Martina, F., Davis, A.E. and Prangnell, P.B., 2019. On the origin of microstructural banding in Ti-6Al4V wire-arc based high deposition rate additive manufacturing. Acta Materialia, 166, pp.306-323.
[2.37] Demir, A.G., 2018. Micro laser metal wire deposition for additive manufacturing of thin-walled structures. Optics and Lasers in Engineering, 100, pp.9-17.
[2.38] Al-Jamal, O.M., Hinduja, S. and Li, L., 2008. Characteristics of the bond in Cu–H13 tool steel parts fabricated using SLM. CIRP annals, 57(1), pp.239-242.
[2.39] Katayama, S. 2004, "Laser welding of aluminium alloys and dissimilar metals", Welding International, vol. 18, no. 8, pp. 618-625.
[2.40] Martinsen, K., Hu, S.J. and Carlson, B.E., 2015. Joining of dissimilar materials. CIRP Annals, 64(2), pp.679-699.
[2.41] Sierra, G., Wattrisse, B. and Bordreuil, C., 2008. Structural analysis of steel to aluminium welded overlap joint by digital image correlation. Experimental Mechanics, 48(2), pp.213-223.
[2.42] Eelman DA, Dahn JR, MacKay GR, Dunlap RA. An investigation of mechanically alloyed Fe–Al. J Alloys Compd 1998; 266: 234–40.
[2.43] Lee, W.B., Schmuecker, M., Mercardo, U.A., Biallas, G. and Jung, S.B., 2006. Interfacial reaction in steel–aluminium joints made by friction stir welding. Scripta Materialia, 55(4), pp.355-358.

[2.44] Brockmann, R., Dickmann, K., Radscheit, C., Schubert, E. and Sepold, G., 1996. Method for the laser beam joining of aluminium and steel in the thin sheet range. Weld Cutt, 3, pp.46-7.
[2.45] Soltan Ali Nezhad M, Haerian Ardakani A. A study of joint quality of aluminium and low carbon steel strips by warm rolling. Mater Des 2009; 30: 1103–9.
[2.46] Barney, J.B., 1997. Gaining and sustaining competitive advantage.
[2.47] Netland, T., Ravn, J.E., Knutstad, G. and Skjelstad, L., 2011. IDEALFACTORY@ XPS: A Manufacturing Concept for High-Tech Norwegian Companies.
[2.48] Sakundarini, N., Taha, Z., Abdul-Rashid, S.H. and Ghazila, R.A.R., 2013. Optimal multi-material selection for lightweight design of automotive body assembly incorporating recyclability. Materials & Design, 50, pp.846-857.
[2.49] Wargnier, H., Kromm, F.X., Danis, M. and Brechet, Y., 2014. Proposal for a multi-material design procedure. Materials & Design (1980-2015), 56, pp.44-49.
[2.50] Zenkert, D., 1995. An introduction to sandwich construction. Engineering materials advisory services.
[2.51] Pflug, J. and Verpoest, I., 2006. Sandwich materials selection charts. Journal of Sandwich Structures & Materials, 8(5), pp.407-421.
[2.52] Shim, H., McCullough, E.A. and Jones, B.W., 2001. Using phase change materials in clothing. Textile Research Journal, 71(6), pp.495-502.
[2.53] Levy, G.N., Schindel, R. and Kruth, J.P., 2003. Rapid manufacturing and rapid tooling with layer manufacturing (LM) technologies, state of the art and future perspectives. CIRP annals, 52(2), pp.589-609.
[2.54] Bahraminasab, M., Sahari, B.B., Edwards, K.L., Farahmand, F., Hong, T.S., Arumugam, M. and Jahan, A., 2014. Multi-objective design optimization of functionally graded material for the femoral component of a total knee replacement. Materials & Design, 53, pp.159-173.
[2.55] Wargnier, H., Kromm, F.X., Danis, M. and Brechet, Y., 2014. Proposal for a multi-material design procedure. Materials & Design (1980-2015), 56, pp.44-49.
[2.56] Sakundarini, N., Taha, Z., Abdul-Rashid, S.H. and Ghazila, R.A.R., 2013. Optimal multi-material selection for lightweight design of automotive body assembly incorporating recyclability. Materials & Design, 50, pp.846-857.
[2.57] Michelangelo, M., 2016. laser offset welding an innovative technique for joining lightweight dissimilar al-ti metal alloys. PhD thisis, Faculty of Politecnico di bari.

[2.58] Rathbun, H.J., Fredette, L.F., Scott, P.M., Csontos, A.A. and Rudland, D.L., 2011, January. NRC welding residual stress validation program international round robin program and findings. In ASME 2011 Pressure vessels and piping conference (pp. 1539-1545). American Society of Mechanical Engineers.
[2.59] AOZM, 2013. Super Light-weight (Super LIGHT-Car) Car Research and Development. Available from https://www.azom.com/article.aspx?ArticleID=9249 [13.03.2019].
[2.60] Miller, W.S., Zhuang, L., Bottema, J., Wittebrood, A., De Smet, P., Haszler, A. and Vieregge, A., 2000. Recent development in aluminium alloys for the automotive industry. Materials Science and Engineering: A, 280(1), pp.37-49.
[2.61] Zhang, J., Ma, M. and Lu, H., 2013. The Study of the Impact of Aluminium Formability Parameters on its Stamping Formability. In Proceedings of the FISITA 2012 World Automotive Congress (pp. 1491-1500). Springer, Berlin, Heidelberg.
[2.62] Yu, Z., Lin, Z. and Zhao, Y., 2007. Evaluation of fracture limit in automotive aluminium alloy sheet forming. Materials & design, 28(1), pp.203-207.
[2.63] Toros, S., Ozturk, F. and Kacar, I., 2008. Review of warm forming of aluminium–magnesium alloys. Journal of materials processing technology, 207(1-3), pp.1-12.
[2.64] Hao, X., Dong, H., Li, P. and Xia, Y., 2019. Dissimilar joining of TC4 alloy to ST16 steel by GTAW. Journal of Manufacturing Processes, 37, pp.413-417.
[2.65] Kayhan, E. & Kaftanoglu, B. 2018, "Experimental investigation of non-isothermal deep drawing of DP600 steel", The International Journal of Advanced Manufacturing Technology, vol. 99, no. 1-4, pp. 695-706.
[2.66] Li, Z., Li, Q., Li, S., Li, H., Yu, G. & He, X. 2019, "Study of thermal behavior and solidification characteristics during laser welding of dissimilar metals", Results in Physics, vol. 12, pp. 1062-1072.
[2.67] Jia, Q., Guo, W., Wan, Z., Peng, Y., Zou, G., Tian, Z. and Zhou, Y.N., 2018. Microstructure and mechanical properties of laser welded dissimilar joints between QP and boron alloyed martensitic steels. Journal of Materials Processing Technology, 259, pp.58-67.
[2.68] Chen, H.C., Pinkerton, A.J. and Li, L., 2011. Fibre laser welding of dissimilar alloys of Ti-6Al-4V and Inconel 718 for aerospace applications. The International Journal of Advanced Manufacturing Technology, 52(9-12), pp.977-987.
[2.69] Gao, X.L., Liu, J. and Zhang, L.J., 2018. Dissimilar metal welding of Ti6Al4V and Inconel 718 through pulsed laser welding-induced eutectic reaction technology.

The International Journal of Advanced Manufacturing Technology, 96(1-4), pp.1061-1071.
[2.70] Kulkarni, N., Mishra, R.S. and Yuan, W., 2015. Friction stir welding of dissimilar alloys and materials. Butterworth-Heinemann.
[2.71] Allison, A. and Scudamore, R., 2014. Strategic Research Agenda: Joining: Joining Sub-platform.
[2.72] Zhang, G., Su, W., Zhang, J., & Wei, Z. (2011). Friction stir brazing: a novel process for fabricating Al/steel layered composite and for dissimilar joining of Al to steel. Metallurgical and Materials Transactions A, 42(9), 2850-2861.
[2.73] Gulbrandsen-Dahl, S., Moen, K. E., Ehlers, F. J., Marioara, C. D., Pedersen, K. O., & Marthinsen, K. (2010). Matrix Coherency Strain and Hardening of Al-Mg-Si. In Materials Science Forum (Vol. 638, pp. 229-234). Trans Tech Publications Ltd.
[2.74] Ninive, P. H., Strandlie, A., Gulbrandsen-Dahl, S., Lefebvre, W., Marioara, C. D., Andersen, S. J., ... & Løvvik, O. M. (2014). Detailed atomistic insight into the β'' phase in Al–Mg–Si alloys. Acta Materialia, 69, 126-134.
[2.75] Cai, X., Sun, D., Li, H., Meng, C., Wang, L., & Shen, C. (2019). Dissimilar joining of TiAl alloy and Ni-based superalloy by laser welding technology using V/Cu composite interlayer. Optics & Laser Technology, 111, 205-213.
[2.76] Donachie, M.J., 2000. Titanium: a technical guide. ASM international.
[2.77] Morita, T., Hatsuoka, K., Iizuka, T. and Kawasaki, K., 2005. Strengthening of Ti–6Al–4V alloy by short-time duplex heat treatment. Materials transactions, 46(7), pp.1681-1686.
[2.78] Zhang, S., Lin, X., Chen, J. and Huang, W., 2009. Heat-treated microstructure and mechanical properties of laser solid forming Ti-6Al-4V alloy. Rare metals, 28(6), pp.537-544.
[2.79] Zhong, C., Liu, J., Zhao, T., Schopphoven, T., Fu, J., Gasser, A. and Schleifenbaum, J.H., 2020. Laser metal deposition of Ti6Al4V—a brief review. Applied Sciences, 10(3), p.764.
[2.80] Ervin, J.K., 2008. Post Heat Treatment Effects of Ti-6Al-4V Produced via Solid Freeform Electron Beam Melting.
[2.81] Xu, C. and Peng, C., 2020. Mechanical properties and microstructure analysis of welding-brazing of Al/Ti butt joint with Zn foil additive. Materials Research Express, 7(2), p.026542.

[2.82] Fergus, J.W., 2010. High temperature corrosion of intermetallic alloys.
[r20] Sepold, G., 1999. Laser beam joining of dissimilar materials. IIW, IV, 1999, 734, pp.1-10.
[2.83] Kreimeyer, M., Wagner, F. and Vollertsen, F., 2005. Laser processing of aluminum–titanium-tailored blanks. Optics and Lasers in Engineering, 43(9), pp.1021-1035.
[2.84] Chen, Y., Chen, S. and Li, L., 2010. Influence of interfacial reaction layer morphologies on crack initiation and propagation in Ti/Al joint by laser welding–brazing. Materials & Design, 31(1), pp.227-233.
[2.85] Alhazaa, A.N. and Khan, T.I., 2010. Diffusion bonding of Al7075 to Ti–6Al–4V using Cu coatings and Sn–3.6 Ag–1Cu interlayers. Journal of Alloys and Compounds, 494(1-2), pp.351-358.
[2.86] Song, Z., Nakata, K., Wu, A. and Liao, J., 2013. Interfacial microstructure and mechanical property of Ti6Al4V/A6061 dissimilar joint by direct laser brazing without filler metal and groove. Materials Science and Engineering: A, 560, pp.111-120.
[2.87] Su, J., Tan, C., Wu, Z., Wu, L., Gong, X., Chen, B., Song, X. and Feng, J., 2020. Influence of defocus distance on laser joining of CFRP to titanium alloy. Optics & Laser Technology, 124, p.106006.
[2.88] Tan, C., Su, J., Zhu, B., Li, X., Wu, L., Chen, B., Song, X. and Feng, J., 2020. Effect of scanning speed on laser joining of carbon fiber reinforced PEEK to titanium alloy. Optics & Laser Technology, 129, p.106273.
[2.89] Wang, H., Chen, Y., Guo, Z. and Guan, Y., 2019. Porosity elimination in modified direct laser joining of Ti6Al4V and thermoplastics composites. Applied Sciences, 9(3), p.411.
[2.90] Zou, P., Zhang, H., Lei, M., Cheng, D., Huang, S. and Yang, F., 2021. Interfacial Microstructure and Formation of Direct Laser Welded CFRP/Ti-6Al-4V Joint. Metals, 11(9), p.1398.
[2.91] Savage, G., 1993. Applications of Carbon-carbon composites. In Carbon-Carbon Composites (pp. 323-359). Springer, Dordrecht.
[2.92] Delhaes, P., 2002. Chemical vapor deposition and infiltration processes of carbon materials. carbon, 40(5), pp.641-657.
[2.93] Jacobson, N.S. and Curry, D.M., 2006. Oxidation microstructure studies of reinforced carbon/carbon. Carbon, 44(7), pp.1142-1150.

[2.94] Abdo, J., Shamseldeen, E. and Lafdee, K., 2008. Humidity effects on carbon–carbon composites (fiber pre-form+ CVI). Materials Science and Engineering: A, 472(1-2), pp.2-14.
[2.95] Archive, 2019, The Jump to a Composite Plane. [online] Available at: https://archive.nytimes.com/www.nytimes.com/interactive/2013/07/29/business/The-Jump-to-a-Composite-Plane.html [Accessed 17.03.2019].
[2.96] Katayama, S. and Kawahito, Y., 2008. Laser direct joining of metal and plastic. Scripta materialia, 59(12), pp.1247-1250.
[2.97] Jung, K.W., Kawahito, Y., Takahashi, M. and Katayama, S., 2013. Laser direct joining of carbon fiber reinforced plastic to aluminium alloy. Journal of Laser Applications, 25(3), p.032003.
[2.98] Andrés, M., Ferros, M. and Liébana, F., 2018. Influence of temperature and clamping force on the strength of the joint over different composite-metal combinations joined by laser. Procedia CIRP, 74, pp.506-510.
[2.99] Woizeschke, P. and Wottschel, V., 2013. Recent developments for laser beam joining of CFRP-aluminium structures. Procedia Materials Science, 2, pp.250-258.
[2.100] Bashford, D.P., 1986. Basic aspects of joining technology for fibre reinforced plastics. In Developments in Reinforced Plastics—5 (pp. 205-232). Springer, Dordrecht.
[2.101] Davies, P., Cantwell, W.J., Jar, P.Y., Bourban, P.E., Zysman, V. and Kausch, H.H., 1991. Joining and repair of a carbon fibre-reinforced thermoplastic. Composites, 22(6), pp.425-431.
[2.102] Groß, A. and Schäfer, H., 1990. Fügeverfahren von Faserverbundwerkstoffen. Ingenieur-Werkstoffe, 2(1), p.2.
[2.103] Ucsnik, S., Scheerer, M., Zaremba, S. & Pahr, D.H. 2010, "Experimental investigation of a novel hybrid metal–composite joining technology", Composites Part A, vol. 41, no. 3, pp. 369-374.
[2.104] Kinloch, A.J., 2012. Adhesion and adhesives: science and technology. Springer Science & Business Media.
[2.105] Hart-Smith, L.J., 1973. Adhesive-bonded double-lap joints. NASA contract report.
[2.106] Baker, A.A., Rose, L.F. and Jones, R. eds., 2003. Advances in the bonded composite repair of metallic aircraft structure. Elsevier.

[2.107] Jahn, J., Weeber, M., Boehner, J. and Steinhilper, R., 2016. Assessment strategies for composite-metal joining technologies–a review. Procedia CIRP, 50, pp.689-694.
[2.108] Grant, L.D.R., Adams, R.D. and da Silva, L.F., 2009. Experimental and numerical analysis of single-lap joints for the automotive industry. International journal of adhesion and adhesives, 29(4), pp.405-413.
[2.109] Belingardi, G. and Chiandussi, G., 2004. Stress flow in thin-walled box beams obtained by adhesive bonding joining technology. International journal of adhesion and adhesives, 24(5), pp.423-439.
[2.110] Goglio, L., Rossetto, M. and Dragoni, E., 2008. Design of adhesive joints based on peak elastic stresses. International Journal of Adhesion and Adhesives, 28(8), pp.427-435.
[2.111] De Morais, A.B., Pereira, A.B., Teixeira, J.P. and Cavaleiro, N.C., 2007. Strength of epoxy adhesive-bonded stainless-steel joints. International journal of adhesion and adhesives, 27(8), pp.679-686.
[2.112] Rudawska, A., 2010. Adhesive joint strength of hybrid assemblies: Titanium sheet-composites and aluminium sheet-composites—Experimental and numerical verification. International Journal of Adhesion and Adhesives, 30(7), pp.574-582.
[2.113] Pramanik, A., Basak, A.K., Dong, Y., Sarker, P.K., Uddin, M.S., Littlefair, G., Dixit, A.R. and Chattopadhyaya, S., 2017. Joining of carbon fibre reinforced polymer (CFRP) composites and aluminium alloys–A review. Composites Part A: Applied Science and Manufacturing, 101, pp.1-29.
[2.114] Lee, S.H., Lee, C.J., Lee, K.H., Lee, J.M., Kim, B.M. and Ko, D.C., 2014. Influence of tool shape on hole clinching for carbon fiber-reinforced plastic and SPRC440. Advances in Mechanical Engineering, 6, p.810864.
[2.115] Tu, W., Wen, P.H., Hogg, P.J. and Guild, F.J., 2011. Optimisation of the protrusion geometry in Comeld™ joints. Composites Science and Technology, 71(6), pp.868-876.
[2.116] Woizeschke, P. and Vollertsen, F., 2015. Fracture Analysis of Competing Failure Modes of Aluminium-CFRP Joints Using Three-Layer Titanium Laminates as Transition. Journal of Materials Engineering and Performance, 24(9), pp.3558-3572.
[2.117] Pecat, O. and Brinksmeier, E., 2014. Low damage drilling of CFRP/titanium compound materials for fastening. Procedia Cirp, 13, pp.1-7.

[2.118] Löbel, T., Kolesnikov, B., Scheffler, S., Stahl, A. and Hühne, C., 2013. Enhanced tensile strength of composite joints by using staple-like pins: working principles and experimental validation. Composite Structures, 106, pp.453-460.
[2.119] Kashaev, N., Ventzke, V., Riekehr, S., Dorn, F. and Horstmann, M., 2015. Assessment of alternative joining techniques for Ti–6Al–4V/CFRP hybrid joints regarding tensile and fatigue strength. Materials & Design, 81, pp.73-81.
[2.120] Caccese, V., Berube, K.A., Fernandez, M., Melo, J.D. and Kabche, J.P., 2009. Influence of stress relaxation on clamp-up force in hybrid composite-to-metal bolted joints. Composite Structures, 89(2), pp.285-293.
[2.121] Fink, A., Camanho, P.P., Andrés, J.M., Pfeiffer, E. and Obst, A., 2010. Hybrid CFRP/titanium bolted joints: Performance assessment and application to a spacecraft payload adaptor. Composites Science and Technology, 70(2), pp.305-317.
[2.122] Kolesnikov, B., Herbeck, L. and Fink, A., 2008. CFRP/titanium hybrid material for improving composite bolted joints. Composite Structures, 83(4), pp.368-380.
[2.123] Gery, D., Long, H. and Maropoulos, P., 2005. Effects of welding speed, energy input and heat source distribution on temperature variations in butt joint welding. Journal of materials processing technology, 167(2-3), pp.393-401.
[2.124] Han, L. and Liou, F.W., 2004. Numerical investigation of the influence of laser beam mode on melt pool. International journal of heat and mass transfer, 47(19-20), pp.4385-4402.
[2.125] Piekarska, W., Kubiak, M. and Saternus, Z., 2012. Numerical modelling of thermal and structural strain in laser welding process/Modelowanie Numeryczne Odkształceń Cieplnych I Strukturalnych W Procesie Spawania Techniką Laserową. Archives of Metallurgy and Materials, 57(4), pp.1219-1227.
[2.126] Chang, W.S. and Na, S.J., 2002. A study on the prediction of the laser weld shape with varying heat source equations and the thermal distortion of a small structure in micro-joining. Journal of materials processing technology, 120(1-3), pp.208-214.
[2.127] Piekarska, W. and Kubiak, M., 2013. Modelling of thermal phenomena in single laser beam and laser-arc hybrid welding processes using projection method. Applied Mathematical Modelling, 37(4), pp.2051-2062.
[2.128] Lacki, P. and Adamus, K., 2011. Numerical simulation of the electron beam welding process. Computers & Structures, 89(11-12), pp.977-985.

[2.129] Piekarska, W. and Kubiak, M., 2012. Theoretical investigations into heat transfer in laser-welded steel sheets. Journal of thermal analysis and calorimetry, 110(1), pp.159-166.
[2.130] Song, X.L., Li, B.B., Guo, Z., Wang, S.Y., Cai, D.F. and Wen, J.G., 2009. Influences of pump beam distribution on thermal lensing spherical aberration in an LD end-pumped Nd: YAG laser. Optics Communications, 282(24), pp.4779-4783.
[2.131] Pfistner, C., Weber, R., Weber, H.P., Merazzi, S. and Gruber, R., 1994. Thermal beam distortions in end-pumped Nd: YAG, Nd: GSGG, and Nd: YLF rods. IEEE Journal of Quantum Electronics, 30(7), pp.1605-1615.
[2.132] Weber, R., Neuenschwander, B., Mac Donald, M., Roos, M.B. and Weber, H.P., 1998. Cooling schemes for longitudinally diode laser-pumped Nd: YAG rods. IEEE Journal of Quantum Electronics, 34(6), pp.1046-1053.
[2.133] Kim, H.S., Yang, J.M. and Lim, C., 2009. Dependence of the Temperature of a Yb: YAG Disk Laser Crystal on the Pump Laser's Spot Size and the Disk's Thickness. Journal of the Korean Physical Society, 55(4), pp.1425-1429.
[2.134] Xie, W., Tam, S.C., Lam, Y.L., Liu, J., Yang, H., Gu, J. and Tan, W., 2000. Influence of the thermal effect on the TEM 00 mode output power of a laser-diode side-pumped solid-state laser. Applied optics, 39(30), pp.5482-5487.
[2.135] Yilbas, B.S., 1997. Laser heating process and experimental validation. International journal of heat and mass transfer, 40(5), pp.1131-1143.
[2.136] Doan, H.D., Akamine, Y. and Fushinobu, K., 2012. Fluidic laser beam shaper by using thermal lens effect. International Journal of Heat and Mass Transfer, 55(11-12), pp.2807-2812.
[2.137] Jin, X., Li, L. and Zhang, Y., 2003. A heat transfer model for deep penetration laser welding based on an actual keyhole. International Journal of Heat and Mass Transfer, 46(1), pp.15-22.
[2.138] Sundqvist, J., Kaplan, A.F.H., Shachaf, L. and Kong, C., 2017. Analytical heat conduction modelling for shaped laser beams. Journal of Materials Processing Technology, 247, pp.48-54.
[2.139] Kaplan, A., 1994. A model of deep penetration laser welding based on calculation of the keyhole profile. Journal of Physics D: Applied Physics, 27(9), p.1805.
[2.140] Kaplan, A.F., 2011. Modelling the primary impact of an Yb: fibre laser beam profile on the keyhole front. Physics Procedia, 12, pp.627-637.

[2.141] Buvanashekaran, G., Siva Shanmugam, N., Sankaranarayanasamy, K., Sabarikanth, R., 2009. A study of laser welding modes with varying beam energy levels. Proc. Inst. Mech. Eng. Part C: J. Mech. Eng. Sci. 223, 1141–1156.
[2.142] Assuncao, E., Williams, S., Yapp, D., 2012. Interaction time and beam diameter effects on the conduction mode limit. Opt. Laser. Eng. 50, 823–828.
[2.143] Sanchez-Amaya, J.M., Delgado, T., Gonzalez-Rovira, L., Botana, F.J., 2009. Laser welding of aluminium alloys 5083 and 6082 under conduction regime. Appl. Surf. Sci. 255,
9512–9521.
[2.144] Dal, M. and Fabbro, R., 2016. An overview of the state of art in laser welding simulation. Optics & Laser Technology, 78, pp.2-14.
[2.145] Anca, A., Cardona, A., Risso, J. and Fachinotti, V.D., 2011. Finite element modelling of welding processes. Applied Mathematical Modelling, 35(2), pp.688-707.
[2.146] Lee, J.Y., Ko, S.H., Farson, D.F. and Yoo, C.D., 2002. Mechanism of keyhole formation and stability in stationary laser welding. Journal of Physics D: Applied Physics, 35(13), p.1570.
[2.147] Cho, J.H. and Na, S.J., 2006. Implementation of real-time multiple reflection and Fresnel absorption of laser beam in keyhole. Journal of Physics D: Applied Physics, 39(24), p.5372.
[2.148] Cho, W.I., Na, S.J., Thomy, C. and Vollertsen, F., 2012. Numerical simulation of molten pool dynamics in high power disk laser welding. Journal of Materials Processing Technology, 212(1), pp.262-275.
[2.149] Han, S.W., Ahn, J. and Na, S.J., 2016. A study on ray tracing method for CFD simulations of laser keyhole welding: progressive search method. Welding in the World, 60(2), pp.247-258.
[2.150] Medale, M., Xhaard, C. and Fabbro, R., 2007. A thermo-hydraulic numerical model to study spot laser welding. Comptes Rendus Mécanique, 335(5-6), pp.280-286.
[2.151] Hirt, C.W., Amsden, A.A. and Cook, J.L., 1997. An arbitrary Lagrangian–Eulerian computing method for all flow speeds. Journal of computational physics, 135(2), pp.203-216.
[2.152] M. Medale, C. Touvrey, R. Fabbro, An axi-symmetric thermo-hydraulic model to better understand spot laser welding, Eur. J. Comput. Mech. 17 (5–7) (2008) 795–806.

[2.153] Medale, M., Touvrey, C. and Fabbro, R., 2008. An axi-symmetric thermo-hydraulic model to better understand spot laser welding. European Journal of Computational Mechanics/Revue Européenne de Mécanique Numérique, 17(5-7), pp.795-806.
[2.154] Otto, A. and Schmidt, M., 2010. Towards a universal numerical simulation model for laser material processing. Physics Procedia, 5, pp.35-46.
[2.155] Otto, A., Koch, H. and Vazquez, R.G., 2012. Multiphysical simulation of laser material processing. Physics Procedia, 39, pp.843-852.
[2.156] Wong, K.V. and Hernandez, A., 2012. A review of additive manufacturing. ISRN Mechanical Engineering, 2012.
[2.157] Huang, S.H., Liu, P., Mokasdar, A. and Hou, L., 2013. Additive manufacturing and its societal impact: a literature review. The International Journal of Advanced Manufacturing Technology, 67(5-8), pp.1191-1203.
[2.158] Tawfik, S.M., Nasr, M.N. and El Gamal, H.A., 2018. Finite element modelling for part distortion calculation in selective laser melting. Alexandria Engineering Journal.
[2.159] Toyserkani, E., Khajepour, A. and Corbin, S.F., 2004. Laser cladding. CRC press.
[2.160] Toyserkani, E., Khajepour, A. and Corbin, S., 2004. 3-D finite element modelling of laser cladding by powder injection: effects of laser pulse shaping on the process. Optics and lasers in engineering, 41(6), pp.849-867.
[2.161] Cho, C., Zhao, G., Kwak, S.Y. and Kim, C.B., 2004. Computational mechanics of laser cladding process. Journal of materials processing technology, 153, pp.494-500.
[2.162] Kumar, S. and Roy, S., 2006. Development of theoretical process maps to study the role of powder preheating in laser cladding. Computational Materials Science, 37(4), pp.425-433.
[2.163] Nickel, A.H., Barnett, D.M. and Prinz, F.B., 2001. Thermal stresses and deposition patterns in layered manufacturing. Materials Science and Engineering: A, 317(1-2), pp.59-64.
[2.164] Vasinonta, A., Beuth, J.L. and Griffith, M., 1999, August. Process maps for laser deposition of thin-walled structures. In Solid Freeform Fabrication Proceedings (pp. 383-391). The University of Texas at Austin, August.

[2.165] Tobar, M.J., Suárez-Díaz, A., Álvarez, J.C., Amado, J.M. and Yáñez, A., 2007. A 3D transient FEM analysis of residual stress generation during laser cladding. In Proceedings of the LANE (Vol. 2007).
[2.166] Zhao, H.Y., Zhang, H.T., Xu, C.H. and Yang, X.Q., 2009. Temperature and stress fields of multi-track laser cladding. Transactions of Nonferrous Metals Society of China, 19, pp. s495-s501.
[2.167] Suárez, A., Tobar, M.J., Yáñez, A., Pérez, I., Sampedro, J., Amigó, V. and Candel, J.J., 2011. Modelling of phase transformations of Ti6Al4 V during laser metal deposition. Physics Procedia, 12, pp.666-673.
[2.168] Wei, S., Wang, G., Shin, Y.C. and Rong, Y., 2018. Comprehensive modelling of transport phenomena in laser hot-wire deposition process. International Journal of Heat and Mass Transfer, 125, pp.1356-1368.
[2.169] Sussman, M., Almgren, A.S., Bell, J.B., Colella, P., Howell, L.H. and Welcome, M.L., 1999. An adaptive level set approach for incompressible two-phase flows. Journal of Computational Physics, 148(1), pp.81-124.
[2.170] Ferreira, R.B., Falcão, D.S., Oliveira, V.B. and Pinto, A.M.F.R., 2015. Numerical simulations of two-phase flow in proton exchange membrane fuel cells using the volume of fluid method–A review. Journal of Power Sources, 277, pp.329-342.
[2.171] Sun, D.L. and Tao, W.Q., 2010. A coupled volume-of-fluid and level set (VOSET) method for computing incompressible two-phase flows. International Journal of Heat and Mass Transfer, 53(4), pp.645-655.
[2.172] Nichita, B.A., Zun, I. and Thome, J.R., 2010. A level set method coupled with a volume of fluid method for modelling of gas-liquid interface in bubbly flow. Journal of fluids engineering, 132(8), p.081302.
[2.173] Wang, Z., Yang, J., Koo, B. and Stern, F., 2009. A coupled level set and volume-of-fluid method for sharp interface simulation of plunging breaking waves. International Journal of Multiphase Flow, 35(3), pp.227-246.
[2.174] Nie, Z., Wang, G., McGuffin-Cawley, J.D., Narayanan, B., Zhang, S., Schwam, D., Kottman, M. and Rong, Y.K., 2016. Experimental study and modelling of H13 steel deposition using laser hot-wire additive manufacturing. Journal of Materials Processing Technology, 235, pp.171-186.

Chapter 3

[3.1] Li, C., Muneharua, K., Takao, S. and Kouji, H., 2009. Fiber laser-GMA hybrid welding of commercially pure titanium. Materials & Design, 30(1), pp.109-114.

[3.2] Li, R., Li, Z., Zhu, Y. and Rong, L., 2011. A comparative study of laser beam welding and laser–MIG hybrid welding of Ti–Al–Zr–Fe titanium alloy. Materials Science and Engineering: A, 528(3), pp.1138-1142.

[3.3] Li, Z., Gobbi, S.L., Norris, I., Zolotovsky, S. and Richter, K.H., 1997. Laser welding techniques for titanium alloy sheet. Journal of Materials Processing Technology, 65(1-3), pp.203-208.

[3.4] Lee, H.K., Han, H.S., Son, K.J. and Hong, S.B., 2006. Optimization of Nd: YAG laser welding parameters for sealing small titanium tube ends. Materials Science and Engineering: A, 415(1-2), pp.149-155.

[3.5] Gao, X.L., Liu, J., Zhang, L.J. and Zhang, J.X., 2014. Effect of the overlapping factor on the microstructure and mechanical properties of pulsed Nd: YAG laser welded Ti6Al4V sheets. Materials Characterization, 93, pp.136-149.

[3.6] Ramachandrula, S., 2014. Effect of Aluminium Enclosures on Induced EMF. Procedia materials science, 6, pp.444-449.

[3.7] Nandy, S., Bakkar, M.A. and Das, D., 2015. Influence of ageing on mechanical properties of 6063 Al alloy. Materials Today: Proceedings, 2(4-5), pp.1234-1242.

[3.8] Khadyko, M., Marioara, C.D., Dumoulin, S., Børvik, T. and Hopperstad, O.S., 2017. Effects of heat-treatment on the plastic anisotropy of extruded aluminium alloy AA6063. Materials Science and Engineering: A, 708, pp.208-221.

[3.9] Khalifa, T.A. and Mahmoud, T.S., 2009. Elevated temperature mechanical properties of Al alloy AA6063/SiCp MMCs. In Proceedings of the world congress on engineering (Vol. 2, pp. 1-3).

[3.10] Tao, X., Chang, Y., Guo, Y., Li, W. and Li, M., 2018. Microstructure and mechanical properties of friction stir welded oxide dispersion strengthened AA6063 aluminium matrix composites enhanced by post-weld heat treatment. Materials Science and Engineering: A, 725, pp.19-27.

[3.11] Asm (2019). ASM Material Data Sheet. [online] Available at: http://asm.matweb.com/search/SpecificMaterial.asp?bassnum=MA6063T6 [Accessed 11 Jun. 2019].

[3.12] Chen, T., Wang, X. and Qi, M., 2018. Fatigue improvements of cracked rectangular hollow section steel beams strengthened with CFRP plates. Thin-Walled Structures, 122, pp.371-377.
[3.13] Machado, J.J.M., Gamarra, P.R., Marques, E.A.S. and da Silva, L.F., 2018. Numerical study of the behaviour of composite mixed adhesive joints under impact strength for the automotive industry. Composite Structures, 185, pp.373-380.
[3.14] Yanzhong, Z. and Rongchang, N., 1996. STUDY ON DELAMINATION OF CFRP LAMINATES SUBJECTED BY DROP-WEIGHT IMPACT. JOURNAL OF AERONAUTICAL MATERIALS, (2), p.02.
[3.15] Shi, Q., Liu, J., Liu, W., Wang, F. and Wang, Y., 2019. Barker-coded modulation laser thermography for CFRP laminates delamination detection. Infrared Physics & Technology, 98, pp.55-61.
[3.16] Chen, Y., Yang, X., Li, M., Wei, K. and Li, S., 2019. Mechanical behavior and progressive failure analysis of riveted, bonded and hybrid joints with CFRP-aluminium dissimilar materials. Thin-Walled Structures, 139, pp.271-280.
[3.17] Khan, M.I., Kuntz, M.L., Su, P., Gerlich, A., North, T. and Zhou, Y., 2007. Resistance and friction stir spot welding of DP600: a comparative study. Science and Technology of Welding and Joining, 12(2), pp.175-182.
[3.18] Arcelormittal (2019). Dual Phase steels. [online] Available at: https://automotive.arcelormittal.com/DP [Accessed 11 Jun. 2019].
[3.19] Calcagnotto, M., Adachi, Y., Ponge, D. and Raabe, D., 2011. Deformation and fracture mechanisms in fine-and ultrafine-grained ferrite/martensite dual-phase steels and the effect of aging. Acta Materialia, 59(2), pp.658-670.

Chapter 4

[4.1] Gu, D.D., Meiners, W., Wissenbach, K. and Poprawe, R., 2012. Laser additive manufacturing of metallic components: materials, processes and mechanisms. International materials reviews, 57(3), pp.133-164.
[4.2] Syed, W.U.H. and Li, L., 2005. Effects of wire feeding direction and location in multiple layer diode laser direct metal deposition. Applied Surface Science, 248(1-4), pp.518-524.

[4.3] Abioye, T.E., Folkes, J. and Clare, A.T., 2013. A parametric study of Inconel 625 wire laser deposition. Journal of Materials Processing Technology, 213(12), pp.2145-2151.
[4.4] Bambach, M., Sizova, I., Silze, F. and Schnick, M., 2018. Comparison of laser metal deposition of Inconel 718 from powder, hot and cold wire. Procedia CIRP, 74, pp.206-209.
[4.5] Baufeld, B., Brandl, E. and Van der Biest, O., 2011. Wire based additive layer manufacturing: Comparison of microstructure and mechanical properties of Ti–6Al–4V components fabricated by laser-beam deposition and shaped metal deposition. Journal of Materials Processing Technology, 211(6), pp.1146-1158.
[4.6] Ding, D., Pan, Z., Cuiuri, D. and Li, H., 2015. Wire-feed additive manufacturing of metal components: technologies, developments and future interests. The International Journal of Advanced Manufacturing Technology, 81(1-4), pp.465-481.
[4.7] Demir, A.G. 2018, "Micro laser metal wire deposition for additive manufacturing of thin-walled structures", Optics and Lasers in Engineering, vol. 100, pp. 9-17.
[4.8] Brandl, E., Michailov, V., Viehweger, B. and Leyens, C., 2011. Deposition of Ti–6Al–4V using laser and wire, part II: Hardness and dimensions of single beads. Surface and Coatings Technology, 206(6), pp.1130-1141.
[4.9] Torkamany, M., Kaplan, A., Ghaini, F., Vänskä, M., Salminen, A., Fahlström, K. and Hedegård, J. (2015). Wire deposition by a laser-induced boiling front. Optics & Laser Technology, 69, pp.104-112.
[4.10] Allison, A. and Scudamore, R., 2014. Strategic Research Agenda: Joining: Joining Sub-platform.
[4.11] Welsch, G., Boyer, R. and Collings, E.W. eds., 1993. Materials properties handbook: titanium alloys. ASM international.
[4.12] Ho, A., Zhao, H., Fellowes, J.W., Martina, F., Davis, A.E. and Prangnell, P.B., 2019. On the origin of microstructural banding in Ti-6Al4V wire-arc based high deposition rate additive manufacturing. Acta Materialia, 166, pp.306-323.
[4.13] Ye, H., Ye, K., Guo, B.G., Le, F.B., Wei, C., Sun, X., Wang, G.Y. and Liu, Y., 2020. Effects of combining ultrasonic micro-forging treatment with laser metal wire deposition on microstructural and mechanical properties in Ti–6Al–4V alloy. Materials Characterization, 162, p.110187.

[4.14] Wang, J., Lin, X., Wang, J., Yang, H., Zhou, Y., Wang, C., Li, Q. and Huang, W., 2018. Grain morphology evolution and texture characterization of wire and arc additive manufactured Ti-6Al-4V. Journal of Alloys and Compounds, 768, pp.97-113.
[4.15] Demir, A.G. and Biffi, C.A., 2019. Micro laser metal wire deposition of thin-walled Al alloy components: Process and material characterization. Journal of Manufacturing Processes, 37, pp.362-369.

Chapter 5

[5.1] Abioye, T.E., Folkes, J. and Clare, A.T., 2013. A parametric study of Inconel 625 wire laser deposition. Journal of Materials Processing Technology, 213(12), pp.2145-2151.
[5.2] Froend, M., Riekehr, S., Kashaev, N., Klusemann, B. and Enz, J., 2018. Process development for wire-based laser metal deposition of 5087 aluminium alloy by using fibre laser. Journal of Manufacturing Processes, 34, pp.721-732.
[5.3] Williams, S.W., Martina, F., Addison, A.C., Ding, J., Pardal, G. and Colegrove, P., 2016. Wire+arc additive manufacturing. Materials Science and Technology, 32(7), pp.641-647.
[5.4] Baufeld, B., Van der Biest, O., & Gault, R. (2009). Microstructure of Ti-6Al-4V specimens produced by shaped metal deposition. International Journal of Materials Research, 100(11), 1536-1542.
[5.5] Demir, A. G. (2018). Micro laser metal wire deposition for additive manufacturing of thin-walled structures. Optics and Lasers in Engineering, 100, 9-17.
[5.6] Brandl, E., Michailov, V., Viehweger, B., & Leyens, C. (2011). Deposition of Ti–6Al–4V using laser and wire, part I: Microstructural properties of single beads. Surface and Coatings Technology, 206(6), 1120-1129.
[5.7] Ho, A., Zhao, H., Fellowes, J. W., Martina, F., Davis, A. E., & Prangnell, P. B. (2019). On the origin of microstructural banding in Ti-6Al4V wire-arc based high deposition rate additive manufacturing. Acta Materialia, 166, 306-323.
[5.8] Lütjering, G. (2003). u. JC Williams: Titanium.
[5.9] Abbas, A., Seif, A., El-Mahallawi, I., & Khalifa, W. (2017). Microstructure and Hardness of Subzero Quenched and Heat Treated Ti-6Al-4V Alloy. In Proceedings of the 3rd Pan American Materials Congress (pp. 379-391). Springer, Cham.

[5.10] Li, J., & Zuo, D. (2021). Laser polishing of additive manufactured Ti6Al4V alloy: a review. Optical Engineering, 60(2), 020901.
[5.11] Ho, A., Zhao, H., Fellowes, J. W., Martina, F., Davis, A. E., & Prangnell, P. B. (2019). On the origin of microstructural banding in Ti-6Al4V wire-arc based high deposition rate additive manufacturing. Acta Materialia, 166, 306-323.
[5.12] Czichos, H., Hütte eV, A.V. and Hennecke, M. eds., 2007. Hütte-Das Ingenieurwissen. Springer-Verlag.
[5.13] Pardal, G., Martina, F. and Williams, S., 2019. Laser stabilization of GMAW additive manufacturing of Ti-6Al-4V components. Journal of Materials Processing Technology, 272, pp.1-8.
[5.14] Escobar-Palafox, G., Gault, R. and Ridgway, K., 2011, December. Preliminary empirical models for predicting shrinkage, part geometry and metallurgical aspects of Ti-6Al-4V Shaped Metal Deposition builds. In IOP Conference Series: Materials Science and Engineering (Vol. 26, No. 1, p. 012002). IOP Publishing.
[5.15] Jhavar, S., Jain, N.K. and Paul, C.P., 2014. Development of micro-plasma transferred arc (μ-PTA) wire deposition process for additive layer manufacturing applications. Journal of Materials Processing Technology, 214(5), pp.1102-1110.

Chapter 6

[6.1] Braga, D.F., Tavares, S.M.O., Da Silva, L.F., Moreira, P.M.G.P. and De Castro, P.M., 2014. Advanced design for lightweight structures: Review and prospects. Progress in Aerospace Sciences, 69, pp.29-39.
[6.2] Mendez, P.F. and Eagar, T.W., 2001. Welding processes for aeronautics. Advanced materials and processes, 159(5), pp.39-43.
[6.3] Kulkarni, N., Mishra, R.S. and Yuan, W., 2015. Friction stir welding of dissimilar alloys and materials. Butterworth-Heinemann.
[6.4] He, X., Wang, Y., Lu, Y., Zeng, K., Gu, F. and Ball, A., 2015. Self-piercing riveting of similar and dissimilar titanium sheet materials. The International Journal of Advanced Manufacturing Technology, 80(9), pp.2105-2115.
[6.5] Rendigs, K.H., 1997. Aluminium structures used in aerospace-status and prospects. In Materials Science Forum (Vol. 242, pp. 11-24). Trans Tech Publications Ltd.

[6.6] Lei, Z., Li, P., Zhang, X., Wu, S. and Nannan, L., 2019. Microstructure and mechanical properties of welding–brazing of Ti/Al butt joints with laser melting deposition layer additive. Journal of Manufacturing Processes, 38, pp.411-421.
[6.7] Casalino, G., Mortello, M. and Peyre, P., 2015. Yb–YAG laser offset welding of AA5754 and T40 butt joint. Journal of materials processing technology, 223, pp.139-149.
[6.8] Zhao, L., He, X., Xing, B., Zhang, X., Cheng, Q., Gu, F. and Ball, A., 2017. Fretting behavior of self-piercing riveted joints in titanium sheet materials. Journal of Materials Processing Technology, 249, pp.246-254.
[6.9] Mucha, J., 2015. The failure mechanics analysis of the solid self-piercing riveting joints. Engineering Failure Analysis, 47, pp.77-88.
[6.10] Geyer, M., Vidal, V., Pottier, T., Boher, C. and Rezai-Aria, F., 2021. Investigations on the material flow and the role of the resulting hooks on the mechanical behaviour of dissimilar friction stir welded Al2024-T3 to Ti-6Al-4V overlap joints. Journal of Materials Processing Technology, 292, p.117057.
[6.11] Lambiase, F. and Di Ilio, A., 2018. Joining Aluminum with Titanium alloy sheets by mechanical clinching. Journal of Manufacturing Processes, 35, pp.457-465.
[6.12] Lißner, M., Erice, B., Alabort, E., Thomson, D., Cui, H., Kaboglu, C., Blackman, B.R.K., Gude, M. and Petrinic, N., 2020. Multi-material adhesively bonded structures: Characterisation and modelling of their rate-dependent performance. Composites Part B: Engineering, 195, p.108077.
[6.13] Boyer, R.R., 1996. An overview on the use of titanium in the aerospace industry. Materials Science and Engineering: A, 213(1-2), pp.103-114.
[6.14] Wang, S.F., Zhang, J.H., Liu, Z.G., Zhang, X.W., Hong, J., Nan, K.G. and Wang, W., 2015. Riveting parameter design that satisfies requirements for driven rivet head dimensions. Proceedings of the Institution of Mechanical Engineers, Part C: Journal of Mechanical Engineering Science, 229(13), pp.2412-2432.
[6.15] Zhu, Z.S., Wang, X.N. and Shang, G.Q., 2014. Studies of New-Type Titanium Alloys for Aviation Applications in China. In Applied Mechanics and Materials (Vol. 687, pp. 4362-4366). Trans Tech Publications Ltd.
[6.16] Ni, R., Liu, L., Shen, Y., Cao, F., Yan, Y. and Liu, W., 2021. Friction forge riveting of AA6061-T6 and TA2 plates with large diameter TA2 titanium rivets. Journal of Materials Processing Technology, 294, p.117119.

[6.17 25] Baufeld, B., Brandl, E. and Van der Biest, O., 2011. Wire based additive layer manufacturing: Comparison of microstructure and mechanical properties of Ti–6Al–4V components fabricated by laser-beam deposition and shaped metal deposition. Journal of Materials Processing Technology, 211(6), pp.1146-1158.

[6.18 27] Demir, A.G. and Biffi, C.A., 2019. Micro laser metal wire deposition of thin-walled Al alloy components: Process and material characterization. Journal of Manufacturing Processes, 37, pp.362-369.

[6.19] Von Fraunhofer, J.A., 2012. Adhesion and cohesion. International journal of dentistry, 2012.

[6.20] Wang, J., Lin, X., Wang, J., Yang, H., Zhou, Y., Wang, C., Li, Q. and Huang, W., 2018. Grain morphology evolution and texture characterization of wire and arc additive manufactured Ti-6Al-4V. Journal of Alloys and Compounds, 768, pp

[6.21] Sun, X., Stephens, E. V., & Khaleel, M. A. (2008). Effects of fusion zone size and failure mode on peak load and energy absorption of advanced high strength steel spot welds under lap shear loading conditions. Engineering Failure Analysis, 15(4), 356-367.

[6.22] Pouranvari, M., & Marashi, S. P. H. (2013). Critical review of automotive steels spot welding: process, structure and properties. Science and Technology of welding and joining, 18(5), 361-403.

[6.23] Lin, S. H., Pan, J., Wu, S. R., Tyan, T., & Wung, P. (2002). Failure loads of spot welds under combined opening and shear static loading conditions. International Journal of Solids and Structures, 39(1), 19-39.

[6.24] Song, J. H., & Huh, H. (2011). Failure characterization of spot welds under combined axial–shear loading conditions. International Journal of Mechanical Sciences, 53(7), 513-525.

[6.25] Li, G., Renaud, G., & Liao, M. (2021). Assessing the riveting process and the quality of riveted lap joints in aerospace and other applications. In Welding and joining of aerospace materials (pp. 383-426). Woodhead Publishing.

[6.26] Momeni, A., & Abbasi, S. M. (2010). Effect of hot working on flow behavior of Ti–6Al–4V alloy in single phase and two phase regions. Materials & Design, 31(8), 3599-3604..97-113.

[6.27] Damisih, D., Jujur, I. N., Sah, J., & Prajitno, D. H. (2018). Effect of heat treatment temperature on microstructure characteristic and hardness properties of casted Ti-6Al-4V ELI. Widyariset, 4(2), 153-162.

[6.28] Liu, J., Gao, X. L., Zhang, L. J., & Zhang, J. X. (2014). A study of fatigue damage evolution on pulsed Nd: YAG Ti6Al4V laser welded joints. Engineering Fracture Mechanics, 117, 84-93.
[6.29] Wojtaszek, M., Korpała, G., Śleboda, T., Zyguła, K., & Prahl, U. (2020). Hot Processing of Powder Metallurgy and Wrought Ti-6Al-4V Alloy with Large Total Deformation: Physical Modelling and Verification by Rolling. Metallurgical and Materials Transactions A, 51(11), 5790-5805.
[6.30] Chu, M. Q., Zhang, S. Y., Su, G. Q., Ding, R. G., Wang, L., & Padde, S. (2020). Research on Post-processing Microstructure and Property of Titanium Components with Selective Laser Melting (SLM). In IOP Conference Series: Materials Science and Engineering (Vol. 751, No. 1, p. 012079). IOP Publishing.

Chapter 7

[7.1] Zhou, X., Yang, H., Chen, F., Han, Y.H., Lee, J. and Huang, Q., 2016. Joining of carbon fiber reinforced carbon composites with Ti3SiC2 tape film by electric field assisted sintering technique. Carbon, 102, pp.106-115.
[7.2] Wang, M., Hu, X., Xu, X., Yun, Z., Liu, J., Du, H. and Guo, A., 2015. A user-friendly heat-resistant modified polymer-based adhesive for joining and repair of carbon/carbon composites. Materials & Design, 86, pp.709-713.
[7.3] Meireman, T., Daelemans, L., Van Verre, E., Van Paepegem, W. and De Clerck, K., 2020. Nanofibre toughening of dissimilar interfaces in composites. Materials & Design, 195, p.109050.
[7.4] Wargnier, H., Kromm, F.X., Danis, M. and Brechet, Y., 2014. Proposal for a multi-material design procedure. Materials & Design (1980-2015), 56, pp.44-49.
[7.5] Hadibeyk, S., Beidokhti, B. and Sajjadi, S.A., 2018. Effect of bonding time and homogenization heat treatment on the microstructure and mechanical properties of the transient liquid phase bonded dissimilar GTD-111/FSX-414 TLP superalloys. Journal of Alloys and Compounds, 731, pp.929-935.
[7.6] Zhang, Y., Luo, Z., Li, Y., Liu, Z. and Huang, Z., 2015. Microstructure characterization and tensile properties of Mg/Al dissimilar joints manufactured by thermo-compensated resistance spot welding with Zn interlayer. Materials & Design, 75, pp.166-173.

[7.7] Lin, T., Yang, M., He, P., Huang, C., Pan, F. and Huang, Y., 2011. Effect of in situ synthesized TiB whisker on microstructure and mechanical properties of carbon–carbon composite and TiBw/Ti–6Al–4V composite joint. Materials & Design, 32(8-9), pp.4553-4558.
[7.8] Song, X.G., Chai, J.H., Hu, S.P., Cao, J., Feng, J.C. and Tang, D.Y., 2017. A novel metallization process for soldering graphite to copper at low temperature. Journal of Alloys and Compounds, 696, pp.1199-1204.
[7.9] Zhou, Y.H., Liu, D., Niu, H.W., Song, X.G., Yang, X.D. and Feng, J.C., 2016. Vacuum brazing of C/C composite to TC4 alloy using nano-Al2O3 strengthened AgCuTi composite filler. Materials & Design, 93, pp.347-356.
[7.10] MURAKAMI, S., OZAKI, K., ONO, K. and ITSUMI, Y., 2011. Effect of Alloying Elements on Machinability and Hot Workability of α-β Titanium Alloy Containing Fe and C. Feature-ｌ Material Processing Technologies, p.13.
[7.11] Kashaev, N., Ventzke, V., Riekehr, S., Dorn, F. and Horstmann, M., 2015. Assessment of alternative joining techniques for Ti–6Al–4V/CFRP hybrid joints regarding tensile and fatigue strength. Materials & Design, 81, pp.73-81.
[7.12] Woizeschke, P. and Wottschel, V., 2013. Recent developments for laser beam joining of CFRP-aluminium structures. Procedia Materials Science, 2, pp.250-258.
[7.13] Bashford, D.P., 1986. Basic aspects of joining technology for fibre reinforced plastics. In Developments in Reinforced Plastics—5 (pp. 205-232). Springer, Dordrecht.
[7.14] Davies, P., Cantwell, W.J., Jar, P.Y., Bourban, P.E., Zysman, V. and Kausch, H.H., 1991. Joining and repair of a carbon fibre-reinforced thermoplastic. Composites, 22(6), pp.425-431.
[7.15] Groß, A. and Schäfer, H., 1990. Fügeverfahren von Faserverbundwerkstoffen. Ingenieur-Werkstoffe, 2(1), p.2.
[7.16] Higgins, A., 2000. Adhesive bonding of aircraft structures. International Journal of Adhesion and Adhesives, 20(5), pp.367-376.
[7.17] Molitor, P., Barron, V. and Young, T., 2001. Surface treatment of titanium for adhesive bonding to polymer composites: a review. International Journal of Adhesion and Adhesives, 21(2), pp.129-136.

[7.18] Schimanski, K., von Hehl, A. and Zoch, H.W., 2013. Failure behavior of diffusion bonded transition structures for integral FRP-Aluminium compounds. Procedia Materials Science, 2, pp.189-196.
[7.19] Kwakernaak, A., Hofstede, J., Poulis, J. and Benedictus, R., 2012. Improvements in bonding metals for aerospace and other applications. In Welding and Joining of Aerospace Materials (pp. 229-275). Woodhead Publishing.
[7.20] Wang, J., Li, K., Song, X., Guo, L., Li, W. and Li, Z., 2012. The study on joining carbon/carbon composites using Ti–Ni–Si compound. Materials Science and Engineering: A, 547, pp.12-18.
[7.21] Qin, Y. and Feng, J., 2009. Active brazing carbon/carbon composite to TC4 with Cu and Mo composite interlayers. Materials Science and Engineering: A, 525(1-2), pp.181-185.
[7.22] White, J.D., Simpson, A.H., Shteinberg, A.S. and Mukasyan, A.S., 2008. Combustion joining of refractory materials: Carbon–carbon composites. Journal of Materials Research, 23(1), pp.160-169.
[7.23] Chueh, Y.H., Wei, C., Zhang, X. and Li, L., 2020. Integrated laser-based powder bed fusion and fused filament fabrication for three-dimensional printing of hybrid metal/polymer objects. Additive Manufacturing, 31, p.100928.
[7.24] Chen, Y., Yang, X., Li, M., Wei, K. and Li, S., 2019. Mechanical behavior and progressive failure analysis of riveted, bonded and hybrid joints with CFRP-aluminium dissimilar materials. Thin-Walled Structures, 139, pp.271-280.
[7.25] Cui, J., Gao, S., Jiang, H., Huang, X., Lu, G. and Li, G., 2020. Adhesive bond-electromagnetic rivet hybrid joining technique for CFRP/Al structure: Process, design and property. Composite Structures, 244, p.112316.
[7.26] Kashaev, N., Ventzke, V., Riekehr, S., Dorn, F. and Horstmann, M., 2015. Assessment of alternative joining techniques for Ti–6Al–4V/CFRP hybrid joints regarding tensile and fatigue strength. Materials & Design, 81, pp.73-81.

Chapter 8

[8.1] Michaleris, P., 2014. Modelling metal deposition in heat transfer analyses of additive manufacturing processes. Finite Elements in Analysis and Design, 86, pp.51-60.
[8.2] Patankar, S.V., 2018. Numerical heat transfer and fluid flow. CRC press.

[8.3] Song, J., Shanghvi, J.Y. and Michaleris, P., 2004. Sensitivity analysis and optimization of thermo-elasto-plastic processes with applications to welding side heater design. Computer methods in applied mechanics and engineering, 193(42-44), pp.4541-4566.
[8.4] Goldak, J., Chakravarti, A. and Bibby, M., 1984. A new finite element model for welding heat sources. Metallurgical transactions B, 15(2), pp.299-305.
[8.5] Nie, Z., Wang, G., McGuffin-Cawley, J.D., Narayanan, B., Zhang, S., Schwam, D., Kottman, M. and Rong, Y.K., 2016. Experimental study and modelling of H13 steel deposition using laser hot-wire additive manufacturing. Journal of Materials Processing Technology, 235, pp.171-186.
[8.6] Thompson, S.M., Bian, L., Shamsaei, N. and Yadollahi, A., 2015. An overview of Direct Laser Deposition for additive manufacturing; Part I: Transport phenomena, modelling and diagnostics. Additive Manufacturing, 8, pp.36-62.
[8.7] Tan, P., Shen, F., Li, B. and Zhou, K., 2019. A thermo-metallurgical-mechanical model for selective laser melting of Ti6Al4V. Materials & Design, 168, p.107642.
[8.8] Boivineau, M., Cagran, C., Doytier, D., Eyraud, V., Nadal, M.H., Wilthan, B. and Pottlacher, G., 2006. Thermophysical properties of solid and liquid Ti-6Al-4V (TA6V) alloy. International journal of thermophysics, 27(2), pp.507-529.
[8.9] Hodge, N.E., Ferencz, R.M. and Solberg, J.M., 2014. Implementation of a thermomechanical model for the simulation of selective laser melting. Computational Mechanics, 54(1), pp.33-51.
[8.10] Yadroitsev, I. and Yadroitsava, I., 2015. Evaluation of residual stress in stainless steel 316L and Ti6Al4V samples produced by selective laser melting. Virtual and Physical Prototyping, 10(2), pp.67-76.
[8.11] Zhang, Z., Huang, Y., Kasinathan, A.R., Shahabad, S.I., Ali, U., Mahmoodkhani, Y. and Toyserkani, E., 2019. 3-Dimensional heat transfer modelling for laser powder-bed fusion additive manufacturing with volumetric heat sources based on varied thermal conductivity and absorptivity. Optics & Laser Technology, 109, pp.297-312.
[8.12] Rosenthal, D., 1941. Mathematical theory of heat distribution during welding and cutting. Welding journal, 20, pp.220-234.
[8.13] Teixeira, P.R.D.F., Araújo, D.B.D. and Cunda, L.A.B.D., 2014. Study of the gaussian distribution heat source model applied to numerical thermal simulations of TIG welding processes.

[8.14] D'Ostuni, S., Leo, P. and Casalino, G., 2017. FEM simulation of dissimilar aluminium titanium fiber laser welding using 2D and 3D Gaussian heat sources. Metals, 7(8), p.307.
[8.15] Villa, M., 2016. Metallurgical and mechanical modelling of Ti-6Al-4V for welding applications (Doctoral thesis, University of Birmingham).
[8.16] Yang, J., Sun, S., Brandt, M. and Yan, W., 2010. Experimental investigation and 3D finite element prediction of the heat affected zone during laser assisted machining of Ti6Al4V alloy. Journal of Materials Processing Technology, 210(15), pp.2215-2222.
[8.17] Inoue, T., 2002. Metallo-thermo-mechanics: Application to Quenching. Handbook of Residual Stress and Deformation of Steel, pp.296-311.
[8.18] Denis, S., Archambault, P., Gautier, E., Simon, A. and Beck, G., 2002. Prediction of residual stress and distortion of ferrous and non-ferrous metals: current status and future developments. Journal of materials engineering and performance, 11(1), pp.92-102.
[8.19] Ding, H. and Shin, Y.C., 2012. A metallo-thermomechanically coupled analysis of orthogonal cutting of AISI 1045 steel. Journal of manufacturing science and engineering, 134(5).
[8.20] Brandl, E., Michailov, V., Viehweger, B. and Leyens, C., 2011. Deposition of Ti–6Al–4V using laser and wire, part I: Microstructural properties of single beads. Surface and Coatings Technology, 206(6), pp.1120-1129.
[8.21] Katzarov, I., Malinov, S. and Sha, W., 2002. Finite element modelling of the morphology of β to α phase transformation in Ti-6Al-4V alloy. Metallurgical and materials transactions A, 33(4), pp.1027-1040.
[8.22] Ahn, J., He, E., Chen, L., Wimpory, R.C., Dear, J.P. and Davies, C.M., 2017. Prediction and measurement of residual stresses and distortions in fibre laser welded Ti-6Al-4V considering phase transformation. Materials & Design, 115, pp.441-457.

Chapter 9

[9.1] Potgorschek, L., Domitner, J., Hönsch, F., Sommitsch, C. and Kaufmann, S., 2020. Numerical simulation of hybrid joining processes: self-piercing riveting combined with adhesive bonding. Procedia Manufacturing, 47, pp.413-418.

[9.2] Wang, X., Ji, Z., Zheng, C. and Liu, R., 2020. Joining similar and dissimilar material combinations by laser shock forming. Journal of Manufacturing Processes, 60, pp.318-327.
[9.3] Akman, E.R.H.A.N., Demir, A., Canel, T.I.M.U.R. and Sınmazçelik, T., 2009. Laser welding of Ti6Al4V titanium alloys. Journal of materials processing technology, 209(8), pp.3705-3713.
[9.4] Akbari, M., Saedodin, S., Toghraie, D., Shoja-Razavi, R. and Kowsari, F., 2014. Experimental and numerical investigation of temperature distribution and melt pool geometry during pulsed laser welding of Ti6Al4V alloy. Optics & Laser Technology, 59, pp.52-59.
[9.5] Nie, Z., Wang, G., McGuffin-Cawley, J.D., Narayanan, B., Zhang, S., Schwam, D., Kottman, M. and Rong, Y.K., 2016. Experimental study and modelling of H13 steel deposition using laser hot-wire additive manufacturing. Journal of Materials Processing Technology, 235, pp.171-186.
[9.6] Bock, F.E., Herrnring, J., Froend, M., Enz, J., Kashaev, N. and Klusemann, B., 2021. Experimental and numerical thermo-mechanical analysis of wire-based laser metal deposition of Al-Mg alloys. Journal of Manufacturing Processes, 64, pp.982-995.
[9.7] Martinsen, K., Hu, S.J. and Carlson, B.E., 2015. Joining of dissimilar materials. Cirp Annals, 64(2), pp.679-699.
[9.8] Frazier, W.E., 2014. Metal additive manufacturing: a review. Journal of Materials Engineering and Performance, 23(6), pp.1917-1928.
[9.9] Syed, W.U.H. and Li, L., 2005. Effects of wire feeding direction and location in multiple layer diode laser direct metal deposition. Applied Surface Science, 248(1-4), pp.518-524.
[9.10] Abioye, T.E., Folkes, J. and Clare, A.T., 2013. A parametric study of Inconel 625 wire laser deposition. Journal of Materials Processing Technology, 213(12), pp.2145-2151.

Appendix A. LMwcD potential applications

A-1 Steel cylindrical deposition

In this case, mild steel and 304L stainless steel was applied to ALM and CS deposition and successfully build up the cylinder feature, Fig A.1 (a) shows the CS different multi-layer deposition, the substrate is 304L stainless steel and the wire used is mild steel, it demonstrates the feasibility for other materials, and it also provides the possibility of the application for the automotive sector. The processing parameter needs to be reidentified depending on the thermoplastic properties of the material, the values of absorptivity, specific heat, conductivity and fluidity of liquid are all key factors that influence the processing parameters. Moreover, another benefit of stainless steel is more commercial to investigate the deposition processing strategies instead of titanium alloy.

Figure A.1 LMwD cylinder feature further studies: (a) steel deposition (304L stainless steel substrate and mild steel feeding wire), (b) dissimilar joinings for Ti6Al4V to DP600 steel, (c) Ti6Al4V to AA6061 alloy and (d) 304L steel to AA6061 alloy.

A-2 Dissimilar joining

As one of the suitable options, advanced dissimilar joining is a promising technique to achieve the goal of lightweight structure, hence which is widely used in the aerospace industry. Moreover, hybrid materials joining by LMwcD can make full use of the benefits of both low-cost manufacture and lightweight structure. In further studies, the small-scale cylinder depositions of Ti6Al4V and steel for the dissimilar joining

applications are designed and developed, these introduce a novel technique – laser riveting, the initial concept is employing the LMwD build up a cylinder on a metal substrate, and through a hole of the metal upper sheet, and two sheets will be interlocked with the deposited mushroom ‘rivet’ feature, the detail of this application has been investigated in further studies. The different sizes of metal joints of Ti6Al4V/AA6061, Ti6Al4V/DP600 and AA6061/304 steel are presented in Fig A.1(b), (c) and (d). After the deposition step, the laser washing procedure is implemented to form a proper crown for improvement on the rivet.

A-3 Hole and cavity repair

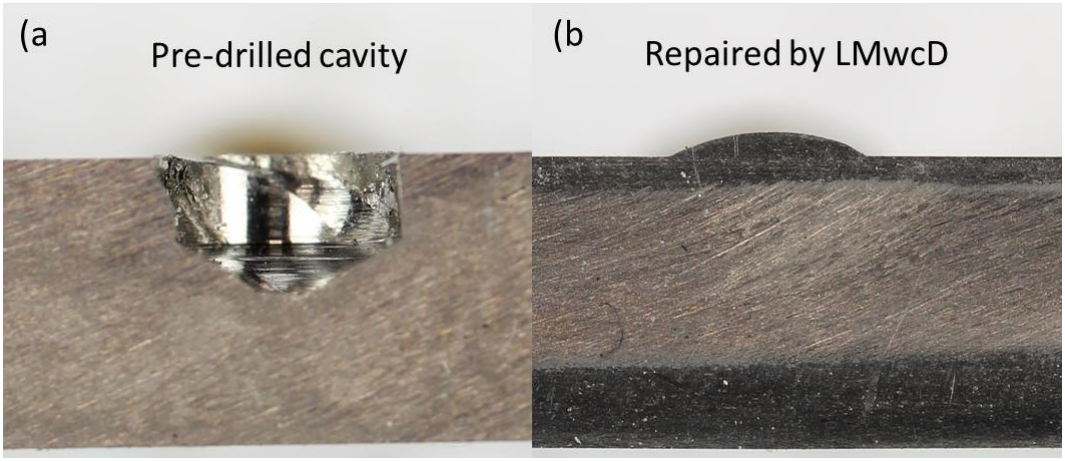

Figure A.2 LMwcD application of cavity repair on the Ti6Al4V sheet.

Another potential application of LMwD for designed curve multilayer deposition is repairing the defects such as holes and cavities in the aircraft or automobile components and structures, the cavity repair cross-section comparison shown in Fig 5.14. The damaged components normally can be replaced directly, however, regarding the considerations of commercial, environmental and efficiency, essential and valuable components are usually repaired by suitable techniques and then return to use. In the LMwcD processing, thanks to its high efficiency and flexibilities of both deposition and track strategies, it can be easily employed to repair the small-scale dents, holes and cavities on the components or body frames. In addition, depending on the weldabilities in processing and the production demand, the processed structures can be improved or even improved through selecting the suitable material for filling wire.

Appendix B. Supplementary analysis results of LMwcD experiments.

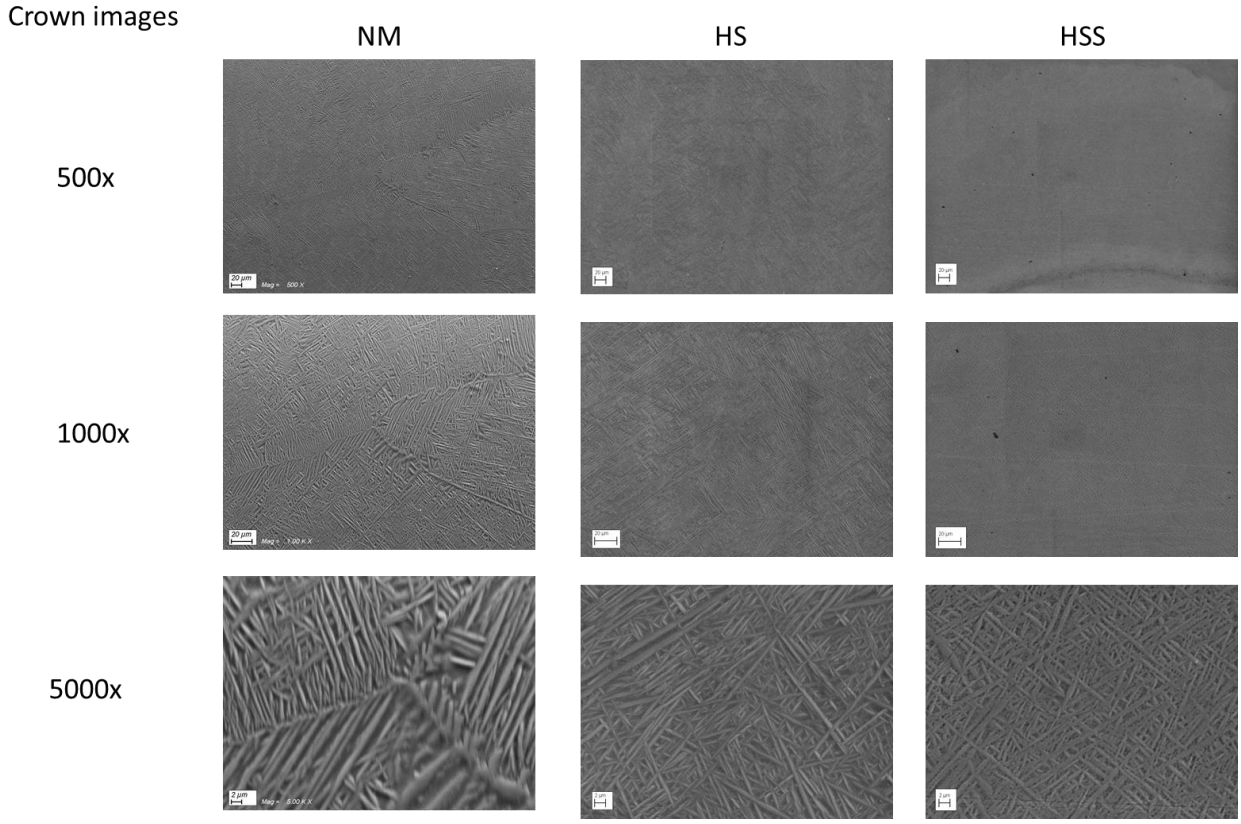

Figure B.1 SEM images of LMwcD depositions at the crown area with extra lower and higher magnifications.

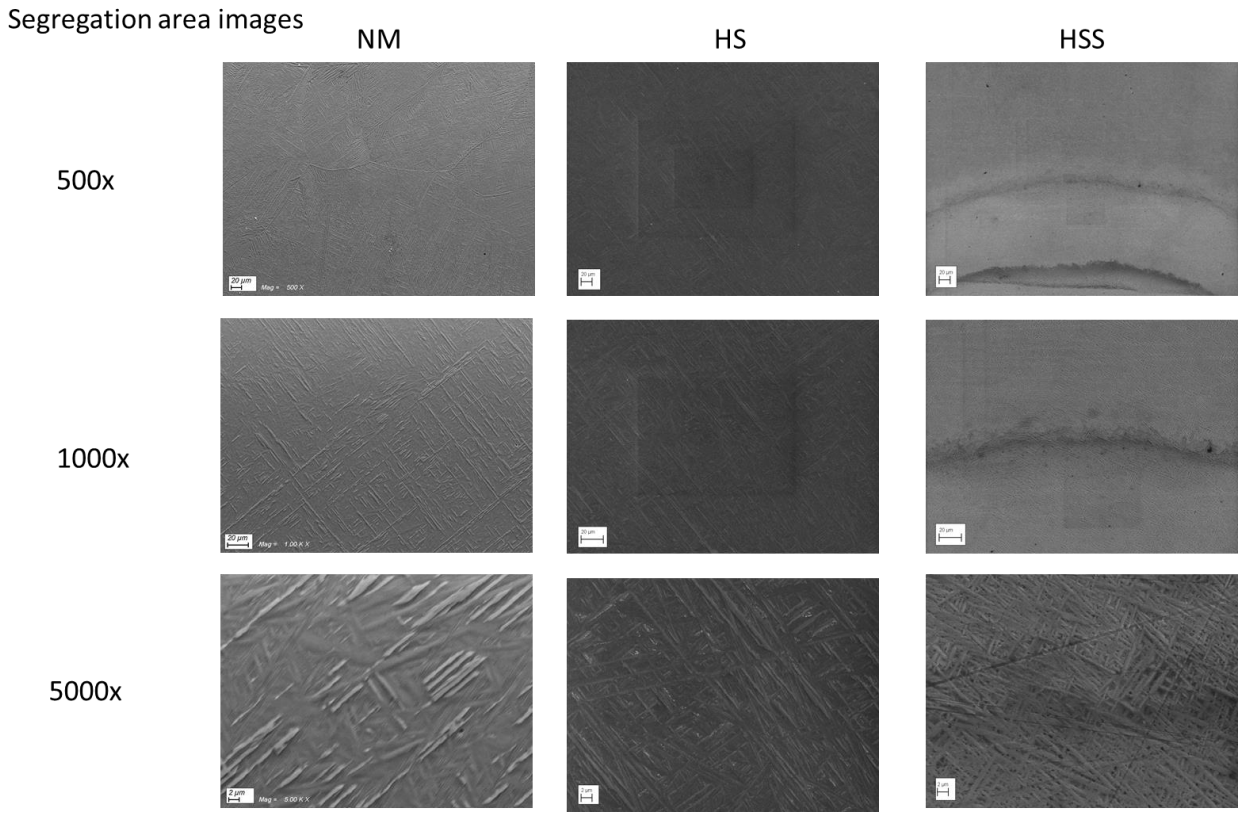

Figure B.2 SEM images of LMwcD depositions at segregation band area with extra lower and higher magnifications.

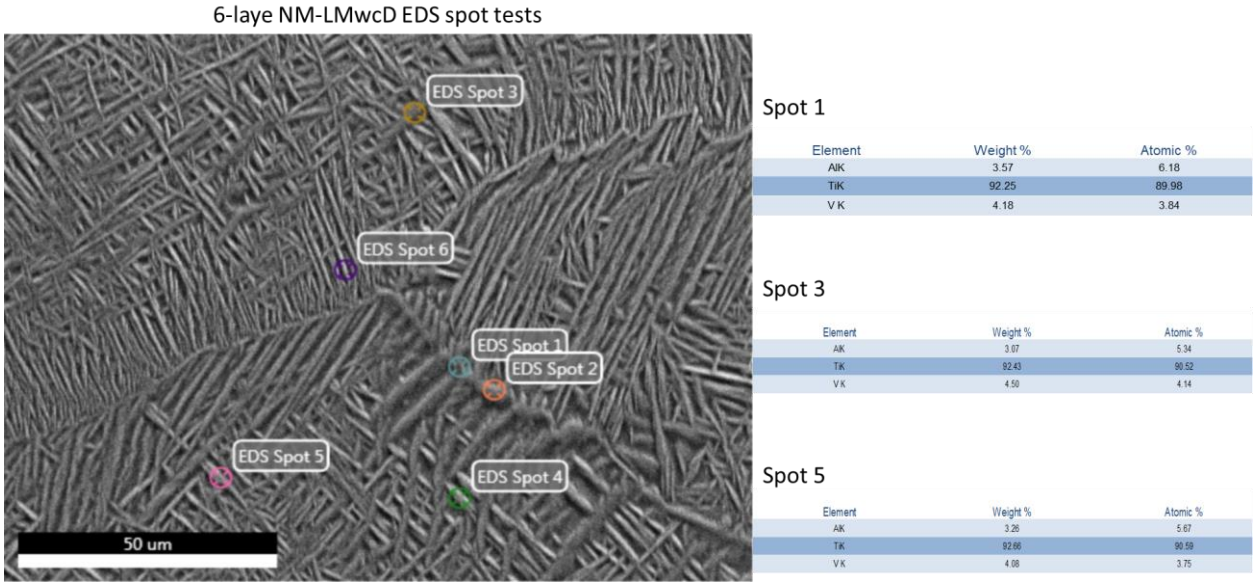

Figure B.3 EDS spots analysis of HSS-LMwcD depositions at the crown area.

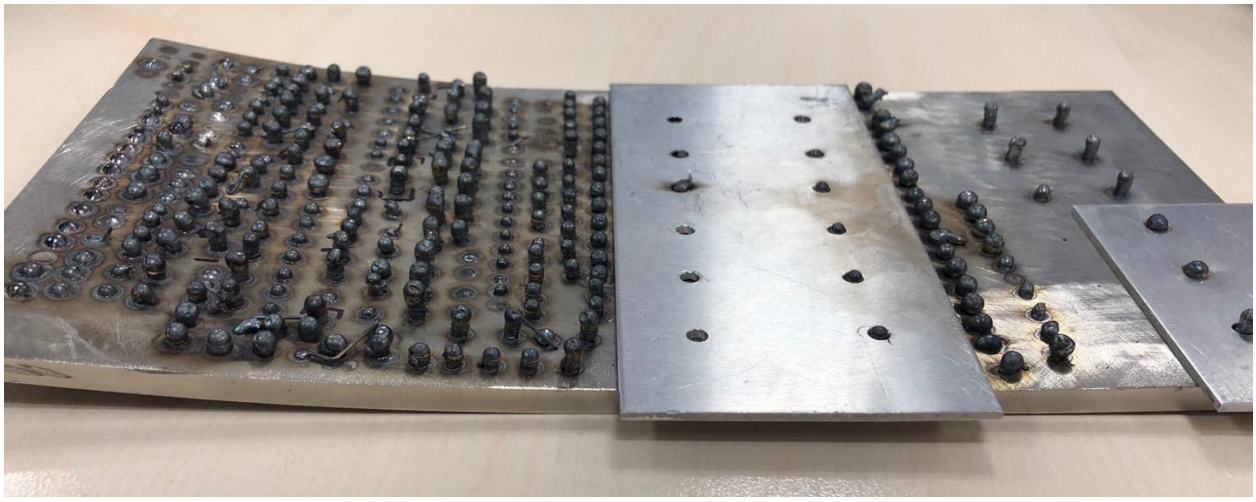

Figure B.4 LMwcD and LR trials on 304L steel.

Fig B.1 and B.2 provide the further overall and detailed microstructure appearances of different deposition in LMwcD parametric studies, such as the clearer alpha and beta grains structures and the segregation band in a wider view. Fig B.3 provides the detailed spot chemical analysis on the primary α and basket-weave structures, which proves that very few differences can be found in the LMwcD deposition in Section 5.4. Furthermore, Fig B.4 shows the steel deposition trials plate, after the try-and-narrow experiments, the steel deposition can be properly applied by LMwcD and LR methods through the processing parameters development.

Appendix C. Supplementary analysis results and trials of LR experiments.

Further overall and detailed microstructure appearances of different Ti6Al4V/AA6061 HS-LR joints from trunk to crown areas are presented below:

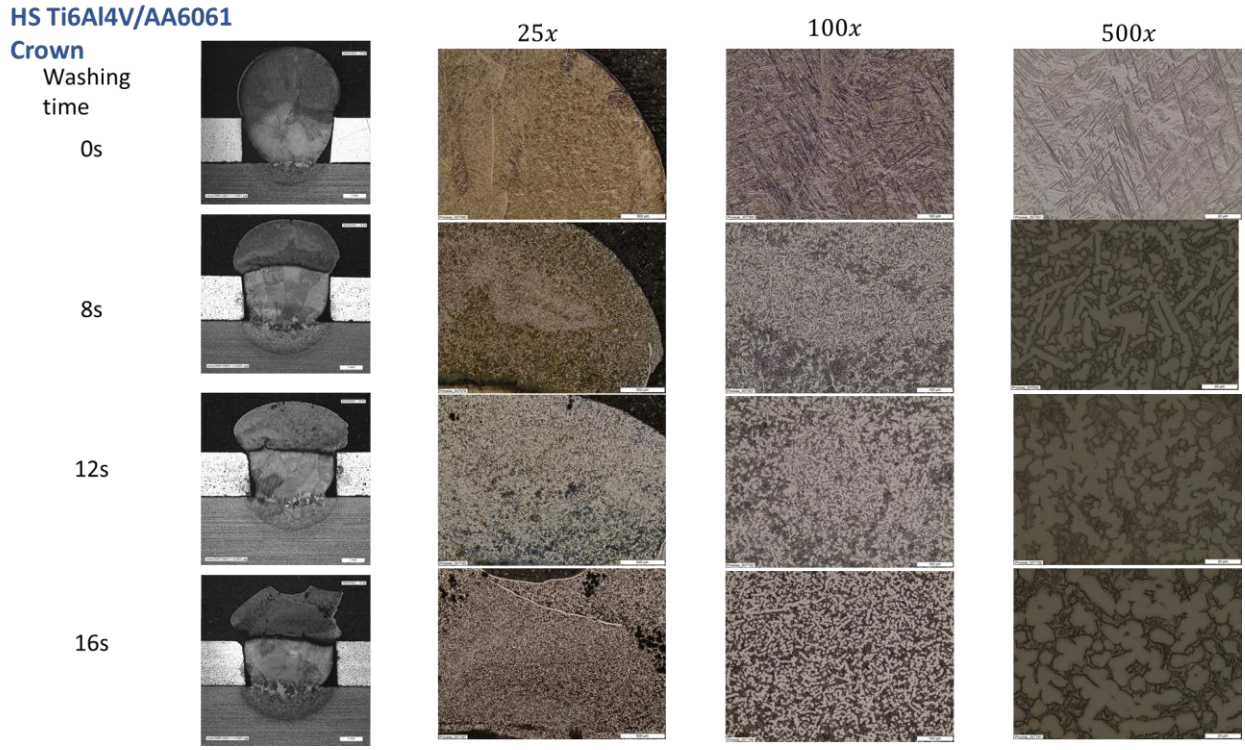

Figure C.1 Microstructure images of Ti6Al4V/AA6061 HS-LR joints at the crown area with varied magnifications.

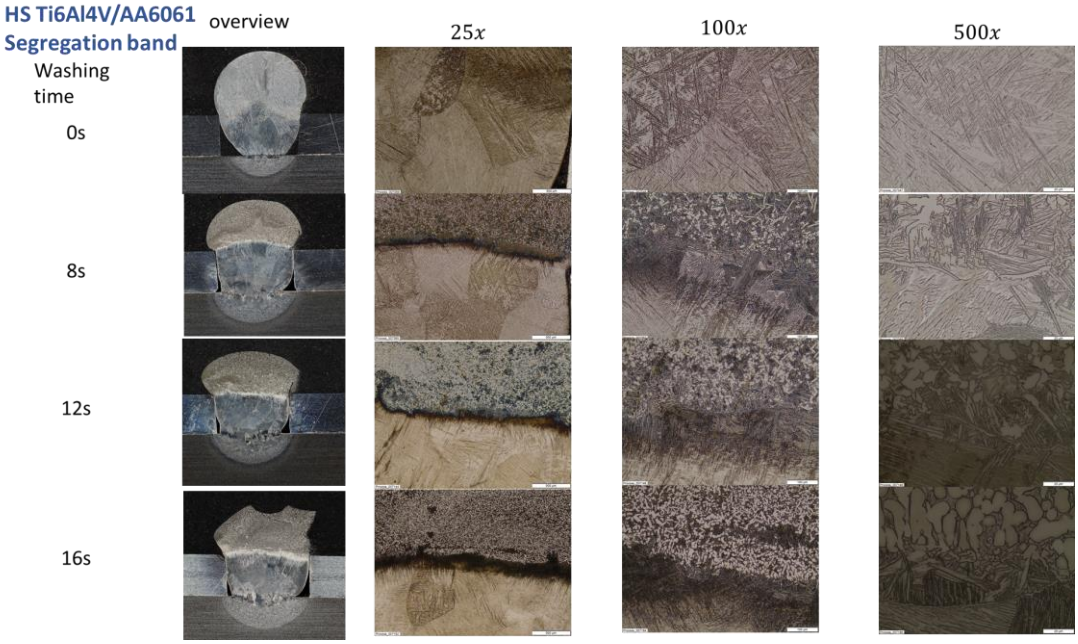

Figure C.2 Microstructure images of Ti6Al4V/AA6061 HS-LR joints at segregation band area with varied magnifications.

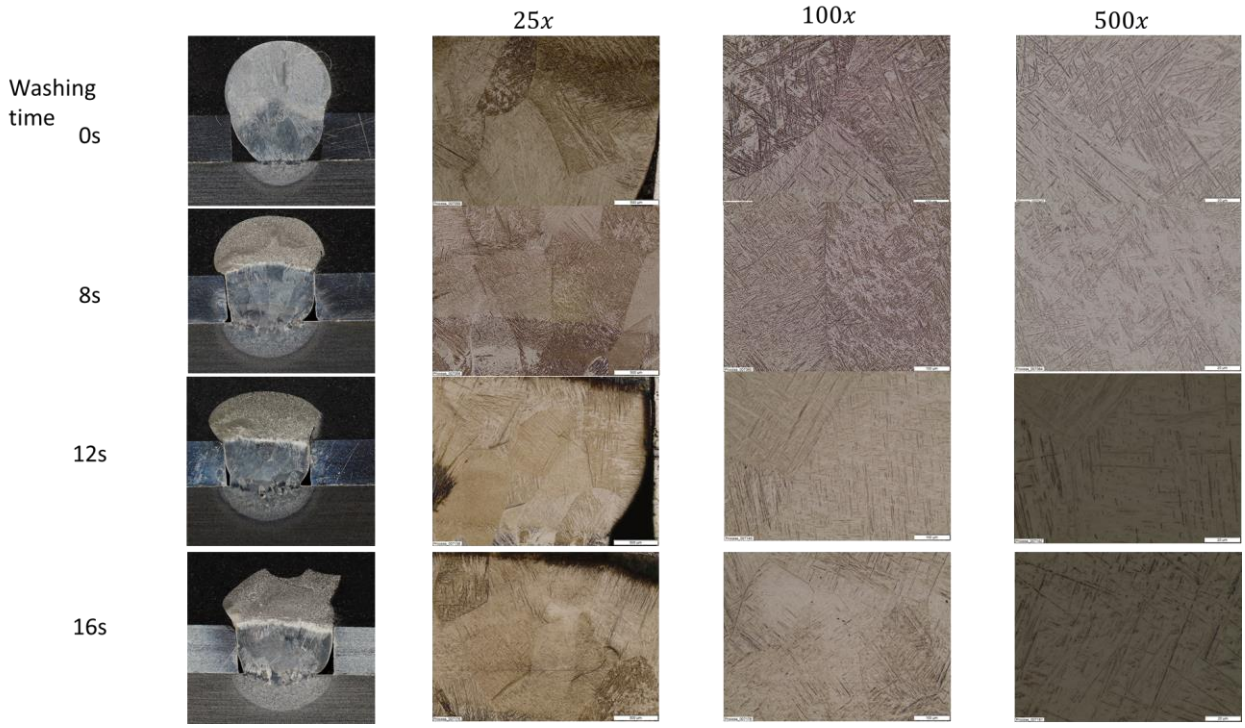

Figure C.3 Microstructure images of Ti6Al4V/AA6061 HS-LR joints at rivet trunk area with varied magnifications.

In Fig C.4, to further investigate the relationship between wetting conditions and rivet deposition strategies, a 2-layer post-processing deposition method was tested, but it only improved the welding area a little and its shear test results were an average level of parametric studies.

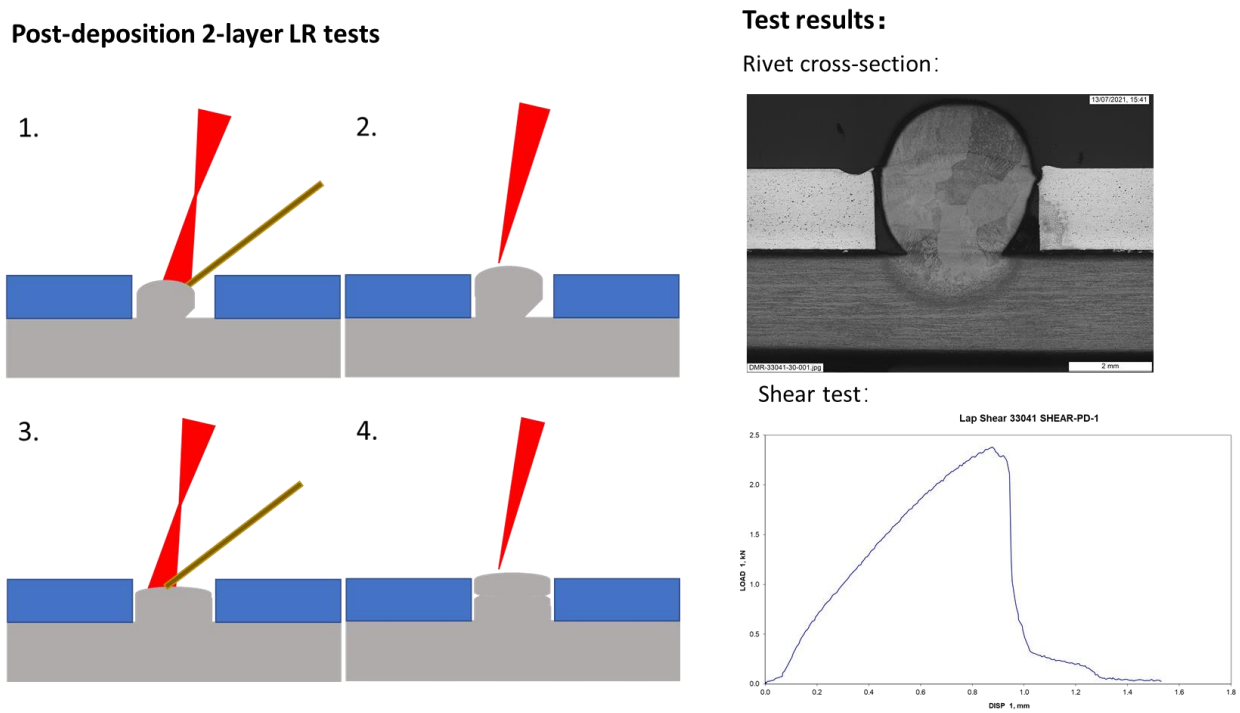

Figure C.4 2-layer post-processing deposition method and its results.

In Fig C.5, to further investigate the influence of washing path patterns on the surface tension breaking, different scanning patterns were designed and implemented on the same deposition, the results concluded that there has a very limited impact of it on the cap reforming.

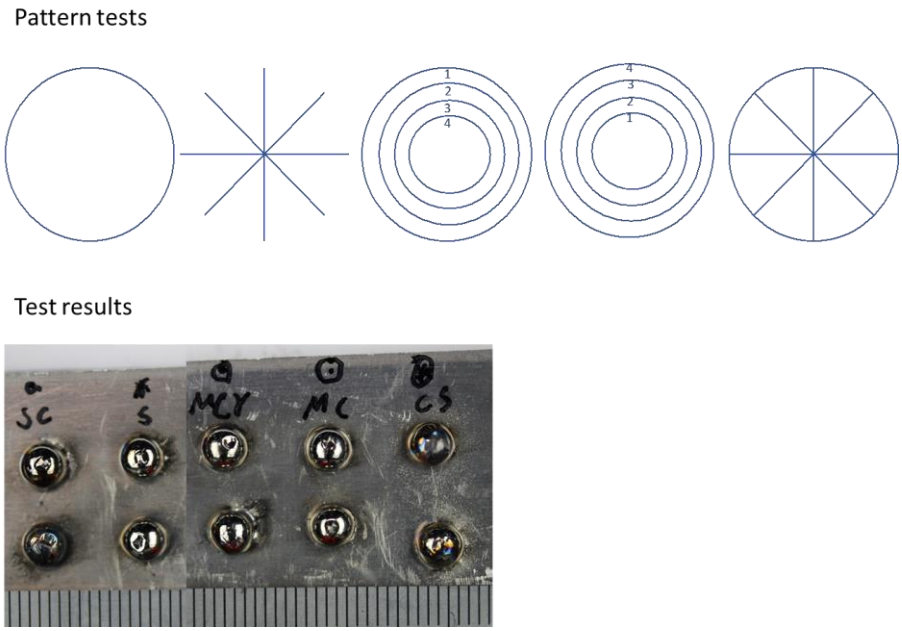

Figure C.5 Laser washing on the rivets with different path patterns.

To prove the primary equiaxed α grains formation caused by the cooling difference between substrate and Al upper sheet but not the laser processing, the same processing was carried out on the titanium deposition, the results show only the colony α grains were formed like in NM method, which confirmed the cause discussed in Section 6.4.2.

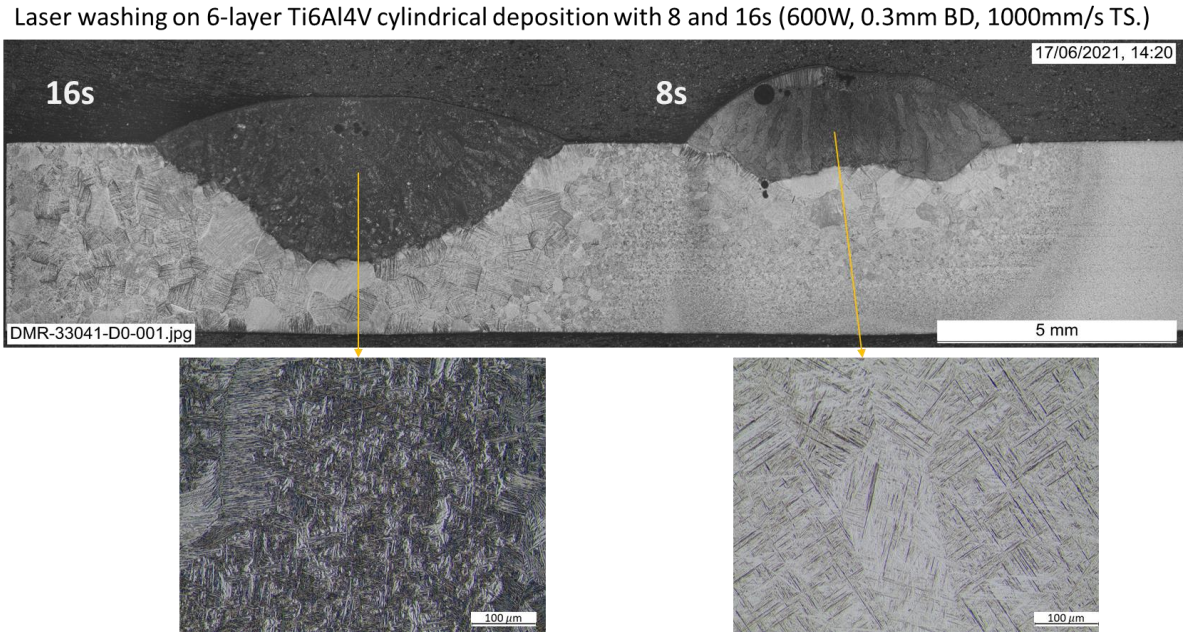

Figure C.6 HS wash-path implemented on the titanium depositions without Al sheets involved.

Besides the Al/Ti joining, the dissimilar joining for titanium to steel was explored, the HS-LR method was applied and successfully built up the joints shown in Fig C.7, but it still needs further parametric development and optimization to create a sound joint.

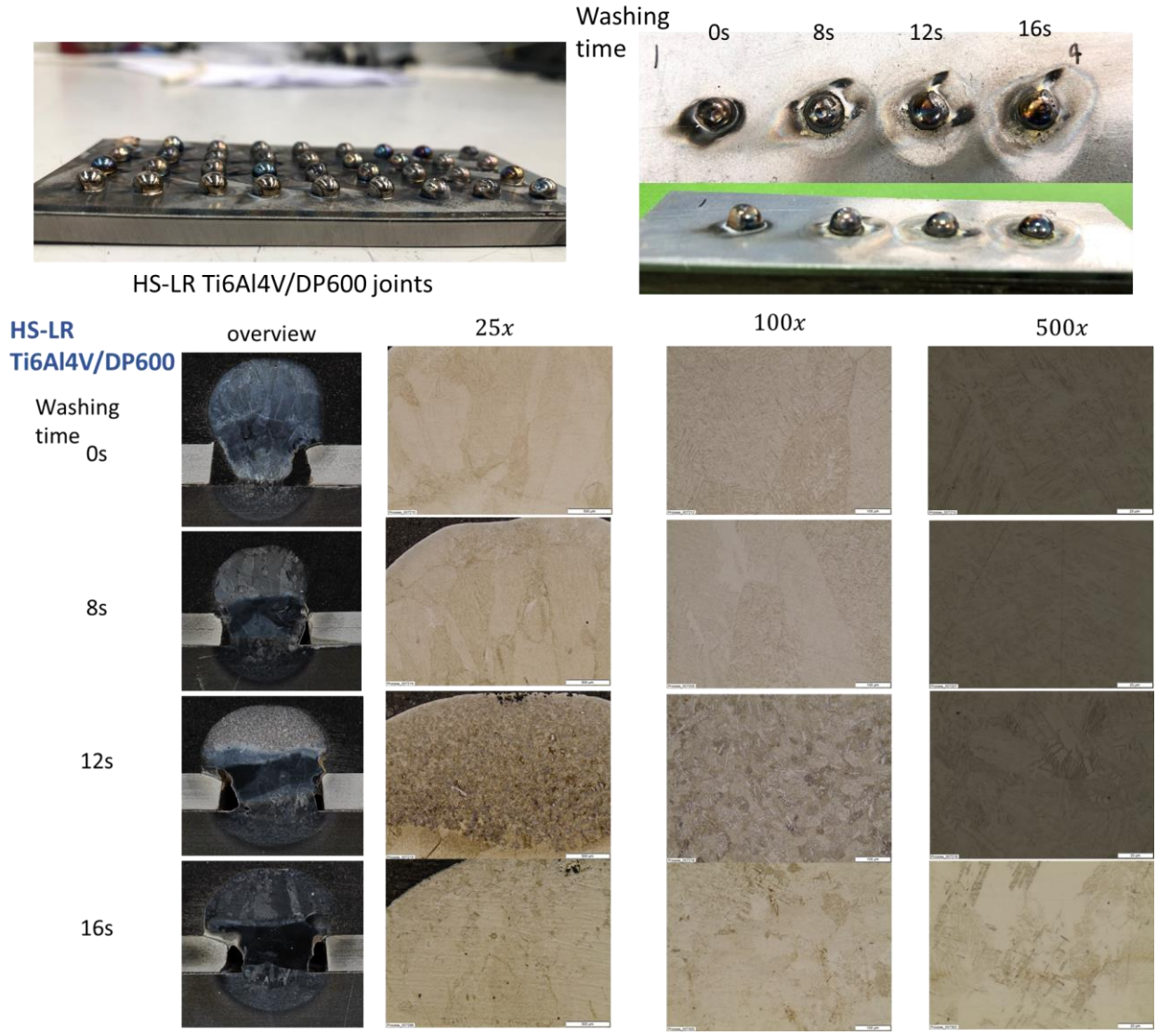

Figure C.7 outlooks and microstructure overviews of Ti6Al4V/DP600 joints.

In the LMwcD-LR composite joining experiment, to exclude the processing cause for the deposition contamination and oxidation, the same processing was carried out in the AA6061 sheet, the results (Figure C.8) show an intact cross-section, which indicates the composite upper sheet is the main reason of the issues.

HSS-LR

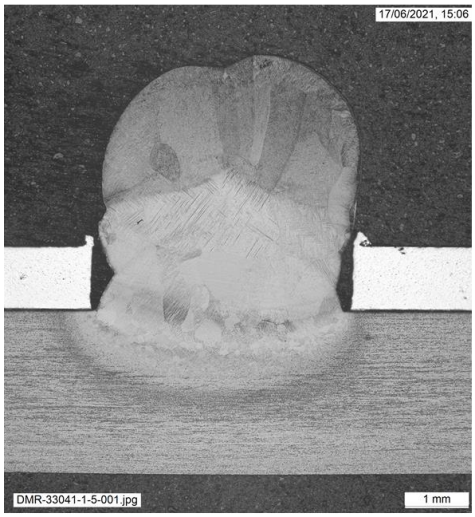

HS-LR

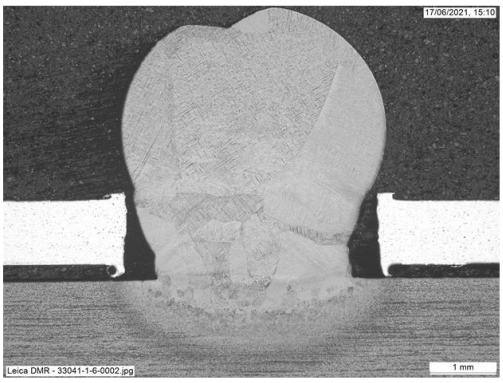

Comparative HSS and HS-LR forTi6Al4V/AA6061 joining results

Figure C.8 cross-section overviews of LMwcD rivets for Ti6Al4V/AA6061 joining.

Appendix D. Material properties and user-subroutines in numerical modelling

D-1 Material property tables

Table D-1 Ti6Al4V properties input in the modelling

latent heat J/kg	Liquidus Temp oC	Solidus temp oC				heat transfer coefficientJ/m2/s/oC	radiation heat transfer			absolute zero oC	boltzmann constant				
3.65E+05	1605	1660				1	0.85			-273.15	5.67E-08				
3.65E+11						0.001					5.67E-11				
thermal conductivity W/m/oC	Temp oC	mW/mm/C		tonne/mm3	Density kg/m3	Temp		Mpa	Elastic modulus Pa	Poisson ratio	Temp oC		mm/mm/C	Thermal expansion m/m/oC	Temp oC
7.07	20	=		4.48E-09	4480	20		1.14E+05	1.14E+11	0.31	20		=	8.70E-06	20
9.44	200			4.43E-09	4430	200		1.10E+05	1.10E+11	0.315	100			8.80E-06	200
11.8	400			4.38E-09	4380	600		1.05E+05	1.05E+11	0.32	300			9.00E-06	300
14.5	600			4.33E-09	4330	1000		1.00E+05	1.00E+11	0.325	500			1.00E-05	400
17.4	800			4.25E-09	4250	1500		8.00E+04	8.00E+10	0.337	800			1.05E-05	500
19.79	1000			4.2E-09	4200	1878		7.00E+04	7.00E+10	0.345	1000			1.12E-05	800
25	1200			3.89E-09	3890	1928		6.50E+04	6.50E+10	0.375	1200			1.18E-05	1000
27.5	1500			3.65E-09	3650	2300		3.50E+04	3.50E+10	0.4	1500			1.22E-05	1200
28.5	1800			3.5E-09	3500	2500		1.00E+04	1.00E+10	0.41	1600			1.27E-05	1500
67.5	1928			3.25E-09	3250	3000		0.00E+00	0.00E+00	0.425	1850			1.29E-05	1800
6.85E+01	2150							0.00E+00	0.00E+00	0.435	2000			1.29E-05	2000
71.5	2300							0.00E+00	0.00E+00	0.45	2500			1.31E-05	2300
73	2500							0.00E+00	0	0.45	3000			1.32E-05	2500
77	3000													1.32E-05	3000
				mj/tonne/c	specific heat J/kg/oC	Temp oC		Mpa	Yield stress Pa	Plastic strain	Temp			1.33E-05	3500
				580000000	580	20		1.10E+03	1.10E+09	0	20				
				610000000	610	200		9.80E+02	9.80E+08	0	200				
				650000000	650	400		7.40E+02	7.40E+08	0	500				
				720000000	720	600		5.00E+02	5.00E+08	0	800				
				765000000	765	800		2.30E+02	2.30E+08	0	1000				
				936000000	936	1000		1.70E+02	1.70E+08	0	1200				
				1.016E+09	1016	1200		5.00E+01	5.00E+07	0	1500				
								1.00E+01	1.00E+07	0	1700				

Table D-2 AA6061 properties input in the modelling

latent heat J/kg	Solidus temp oC	Liquidus Temp oC			heat transfer coefficientJ/m2/s/oC	radiation heat transfer			absolute zero oC	boltzmann constant
2.90E+05	582	652			1	0.85			-273.15	5.67E-08
2.90E+11					0.001					5.67E-11
thermal conductivity W/m/oC	Temp oC		tonne/mm3	Density kg/m3	Temp		Elastic modulus Mpa	Elastic modulus GPa	Poisson ratio	Temp oC
167	25		2.7E-09	2700	25		6.80E+04	6.80E+01	0.33	25
170	37.8		2.685E-09	2685	37.8		6.79E+04	6.79E+01	0.331	37.8
177	93.3		2.685E-09	2685	93.3		6.70E+04	6.70E+01	0.333	93.3
184	148.9		2.667E-09	2667	148.9		6.45E+04	6.45E+01	0.335	148.9
192	204.4		2.657E-09	2657	204.4		6.20E+04	6.20E+01	0.338	204.4
201	260		2.657E-09	2657	260		6.05E+04	6.05E+01	0.342	260
207	315		2.63E-09	2630	315		5.90E+04	5.90E+01	0.345	315
217	371		2.62E-09	2620	371		5.40E+04	5.40E+01	0.348	371
223	426.7		2.602E-09	2602	426.7		5.20E+04	5.20E+01	0.35	426.7
185	582		2.57E-09	2570	582		4.30E+04	4.30E+01	0.365	582
1.82E+02	600		2.5E-09	2500	600		4.00E+04	4.00E+01	0.368	600
mj/tonne	specific heat J/kg/oC	Temp oC		Thermal expansion m/m/oC	Temp oC					
900000000	900	25		2.20E-05	25					
920000000	920	37.8		2.35E-05	37.8					
960000000	960	93.3		2.46E-05	93.3					
980000000	980	148.9		2.57E-05	148.9					
1000000000	1000	204.4		2.66E-05	204.4					
1020000000	1020	260		2.76E-05	260					
1030000000	1030	315		2.85E-05	315					
1090000000	1090	371		2.96E-05	371					
1180000000	1180	426.7		3.07E-05	426.7					
1400000000	1400	550								
1200000000	1200	582								
2000000000	2000	600								

D.2 DFLUX user-subroutine codes

Straight-line LMwcD:

```
      SUBROUTINE DFLUX(FLUX,SOL,KSTEP,KINC,TIME,NOEL,NPT,COORDS,JLTYP,
     1                 TEMP,PRESS,SNAME)

      INCLUDE 'ABA_PARAM.INC'
      DIMENSION COORDS(3),FLUX(2),TIME(2)
      CHARACTER*80 SNAME

       v=0.0015
       d1=v*TIME(2)

       x=COORDS(1)
       y=COORDS(2)
       z=COORDS(3)

      JLTYP=0
       pi=3.1415
       IF (KSTEP.GT.2.AND.KSTEP.LT.61) THEN
       Qs=180
       x0=0.086
       y0=0.0045
       z0=0
           fa=2;     rs=0.001
          FLUX(1)=(fa*Qs/(pi*rs*rs))*exp(-1*fa*((x-x0-d1)**2+
     $        (y-y0)**2)/(rs**2))
       ENDIF

      RETURN
      END
```

NM-LMwcD modelling:

```
      SUBROUTINE DFLUX(FLUX,SOL,KSTEP,KINC,TIME,NOEL,NPT,COORDS,JLTYP,
     1                 TEMP,PRESS,SNAME)

      INCLUDE 'ABA_PARAM.INC'


      DIMENSION COORDS(3),FLUX(2),TIME(2)
      CHARACTER*80 SNAME

      real Qs,rs,pi,r,v,fa,rs,x0,y0,z0

      if (kstep.ge.2.and.kstep.le.34)then
          x0=-0.00075;  y0=0; z0=0; r=0.00075; v=0.00075;
          Qs=200
      endif
      if (kstep.ge.35.and.kstep.le.35)then
          x0=-0.001;  y0=0; z0=0.0008; r=0.001; v=0.0014;
          Qs=200
      endif

      if (kstep.ge.37.and.kstep.le.69)then
          x0=-0.00075;  y0=0; z0=0.0008; r=0.00075; v=0.00075;
          Qs=200
      endif
```

```
      if (kstep.ge.70.and.kstep.le.70)then
          x0=-0.001;  y0=0; z0=0.0016; r=0.001; v=0.0014;
          Qs=200
      endif

      if (kstep.ge.72.and.kstep.le.104)then
          x0=-0.00075;  y0=0; z0=0.0016; r=0.00075; v=0.00075;
          Qs=200
      endif
      if (kstep.ge.105.and.kstep.le.105)then
          x0=-0.001;  y0=0; z0=0.0024; r=0.001; v=0.0014;
          Qs=200
      endif

      if (kstep.ge.107.and.kstep.le.139)then
          x0=-0.00075;  y0=0; z0=0.0024; r=0.00075; v=0.00075;
          Qs=200
      endif
      if (kstep.ge.140.and.kstep.le.140)then
          x0=-0.001;  y0=0; z0=0.0032; r=0.001; v=0.0014;
          Qs=200
      endif

      pi=3.14
      omega=-v/r
      theta=omega*TIME(1)
      x=COORDS(1)*cos(theta)+COORDS(2)*sin(theta)
      y=COORDS(2)*cos(theta)-COORDS(1)*sin(theta)
      z=COORDS(3)

      JLTYP=0
      fa=2;   rs=0.001
      FLUX(1)=(fa*Qs/(pi*rs*rs))*exp(-1*fa*((x-x0)**2+
     $        (y-y0)**2)/(rs**2))

      ENDIF

      RETURN
      END
```

HSS-LMwcD modelling:

```
SUBROUTINE DFLUX(FLUX,SOL,KSTEP,KINC,TIME,NOEL,NPT,COORDS,JLTYP,
     1                 TEMP,PRESS,SNAME)

      INCLUDE 'ABA_PARAM.INC'
      parameter(one=1.d0)
      DIMENSION COORDS(3),FLUX(2),TIME(2)
      CHARACTER*80 SNAME

       Q_1=200
      Q_2=155
      Q_3=140
      Q_4=140
      Q_5=140
      Q_6=115

       PI=3.1415
      Rh=0.001

      R_1=0.001
```

```
      R_2=0.001

       x=COORDS(1)
       y=COORDS(2)
       z=COORDS(3)

      JLTYP=0
È
       IF (KSTEP.GE.2.AND.KSTEP.LE.9) THEN
           x_1=-R_1*COS(2*PI/2.66*TIME(2))
            y_1=R_1*SIN(2*PI/2.66*TIME(2))
           R=sqrt((x-x_1)**2+(y-y_1)**2)
           FLUX(1)=(2*Q_1/(PI*Rh**2))*exp(-2*R**2/Rh**2)

       ELSEIF(KSTEP.GE.10.AND.KSTEP.LE.17) THEN
           x_1=-R_2*COS(2*PI/2*(TIME(2)-2.66))
            y_1=R_2*SIN(2*PI/2*(TIME(2)-2.66))
           R=sqrt((x-x_1)**2+(y-y_1)**2)
           FLUX(1)=(2*Q_2/(PI*Rh**2))*exp(-2*R**2/Rh**2)

       ELSEIF(KSTEP.GE.18.AND.KSTEP.LE.25) THEN
           x_1=-R_1*COS(2*PI/1.83*(TIME(2)-4.66))
            y_1=R_1*SIN(2*PI/1.83*(TIME(2)-4.66))
          R=sqrt((x-x_1)**2+(y-y_1)**2)
          FLUX(1)=(2*Q_3/(PI*Rh**2))*exp(-2*R**2/Rh**2)

       ELSEIF(KSTEP.GE.26.AND.KSTEP.LE.33) THEN
           x_1=-R_1*COS(2*PI/1.5*(TIME(2)-6.49))
            y_1=R_1*SIN(2*PI/1.5*(TIME(2)-6.49))
          R=sqrt((x-x_1)**2+(y-y_1)**2)
           FLUX(1)=(2*Q_4/(PI*Rh**2))*exp(-2*R**2/Rh**2)

       ELSEIF(KSTEP.GE.34.AND.KSTEP.LE.41) THEN
          x_2=-R_2*COS(2*PI/1.5*(TIME(2)-7.99))
            y_2=R_2*SIN(2*PI/1.5*(TIME(2)-7.99))
           R=sqrt((x-x_2)**2+(y-y_2)**2)
           FLUX(1)=(2*Q_5/(PI*Rh**2))*exp(-2*R**2/Rh**2)

       ELSEIF(KSTEP.GE.42.AND.KSTEP.LE.49) THEN
          x_2=-R_2*COS(2*PI/1.5*(TIME(2)-9.49))
            y_2=R_2*SIN(2*PI/1.5*(TIME(2)-9.49))
           R=sqrt((x-x_2)**2+(y-y_2)**2)
           FLUX(1)=(2*Q_6/(PI*Rh**2))*exp(-2*R**2/Rh**2)

       ENDIF

      RETURN
      END
```

LR modelling:

```
      SUBROUTINE DFLUX(FLUX,SOL,KSTEP,KINC,TIME,NOEL,NPT,COORDS,JLTYP,
     1                 TEMP,PRESS,SNAME)

      INCLUDE 'ABA_PARAM.INC'
      parameter(one=1.d0)
      PARAMETER(pi=3.14159,Qs=0,fa=2,rs=1)

      PARAMETER(Qh=20000,fr=2,rr=0.4)

      PARAMETER(x0=0,y0=0,z0=0,v=0)
```

```
PARAMETER(RL1=0.1,RL2=0.4,D=1.4)
real Sx,R0,R1,RC
DIMENSION COORDS(3),FLUX(2),TIME(2)
CHARACTER*80 SNAME

Q_2=200000
Q_1=200000

Rh1=1
Rh2=0.2
R_1=1

Sx=v*TIME(2)

 x=COORDS(1)
 y=COORDS(2)
 z=COORDS(3)

JLTYP=0

 IF (KSTEP.GE.2.AND.KSTEP.LE.9) THEN
     x_1=-R_1*COS(2*pi/10000*TIME(2))
      y_1=R_1*SIN(2*pi/10000*TIME(2))
     R=sqrt((x-x_1)**2+(y-y_1)**2)
     FLUX(1)=(2*Q_2/(pi*Rh1**2))*exp(-2*R**2/Rh1**2)

 ELSEIF(KSTEP.GE.10.AND.KSTEP.LE.11) THEN
     x_1=-R_1*COS(2*pi/10000*(TIME(2)-2))
      y_1=R_1*SIN(2*pi/10000*(TIME(2)-2))
     R=sqrt((x-x_1)**2+(y-y_1)**2)
     FLUX(1)=(2*Q_1/(pi*Rh1**2))*exp(-2*R**2/Rh1**2)

 ELSEIF(KSTEP.GE.12.AND.KSTEP.LE.13) THEN
     x_1=-R_1*COS(2*pi/2*(TIME(2)-3.5))
      y_1=R_1*SIN(2*pi/2*(TIME(2)-3.5))
     R=sqrt((x-x_1)**2+(y-y_1)**2)
     FLUX(1)=(2*Q_1/(pi*Rh1**2))*exp(-2*R**2/Rh1**2)

 ELSEIF(KSTEP.GE.14.AND.KSTEP.LE.15) THEN
     x_1=-R_1*COS(2*pi/2.2*(TIME(2)-4.5))
      y_1=R_1*SIN(2*pi/2.2*(TIME(2)-4.5))
    R=sqrt((x-x_1)**2+(y-y_1)**2)
    FLUX(1)=(2*Q_1/(pi*Rh1**2))*exp(-2*R**2/Rh1**2)

 ELSEIF(KSTEP.GE.16.AND.KSTEP.LE.19) THEN
     x_1=-R_1*COS(2*pi/1.6*(TIME(2)-5.6))
      y_1=R_1*SIN(2*pi/1.6*(TIME(2)-5.6))
    R=sqrt((x-x_1)**2+(y-y_1)**2)
     FLUX(1)=(2*Q_1/(pi*Rh1**2))*exp(-2*R**2/Rh1**2)

 ELSEIF(KSTEP.GE.20.AND.KSTEP.LE.23) THEN
    x_2=-R_1*COS(2*pi/1.7*(TIME(2)-7.2))
      y_2=R_1*SIN(2*pi/1.7*(TIME(2)-7.2))
     R=sqrt((x-x_2)**2+(y-y_2)**2)
     FLUX(1)=(2*Q_1/(pi*Rh1**2))*exp(-2*R**2/Rh1**2)

 ELSEIF(KSTEP.GE.24.AND.KSTEP.LE.27) THEN
    x_2=-R_1*COS(2*pi/1.8*(TIME(2)-8.9))
      y_2=R_1*SIN(2*pi/1.8*(TIME(2)-8.9))
     R=sqrt((x-x_2)**2+(y-y_2)**2)
     FLUX(1)=(2*Q_1/(pi*Rh1**2))*exp(-2*R**2/Rh1**2)
```

```
 ELSEIF(KSTEP.GE.41.AND.KSTEP.LE.66) THEN
     R0 = SQRT((x-x0-Sx)**2+(y-y0)**2)
          IF (R0 .LE. RL1) THEN
              FLUX(1)=(fa*Qs/(pi*rs*rs))*exp(-1*fa*R0**2/(rs**2))
          ELSEIF ((R0 .GE. (RL1+D)) .AND. (R0 .LE. (RL1+D+2*RL2))) THEN

                 RC = RL1+RL2+D
                 R1 = RC-R0
                 FLUX(1)=(fr*Qh/(pi*rr*rr))*exp(-1*fr*R1**2/(rr**2))
       ELSE
                 FLUX(1)=0.0
          ENDIF

 ENDIF

RETURN
END
```